On the metallicity of pseudo-bulges in the CALIFA galaxy Survey

Iris Pereira Breda

Mestrado em Astronomia
Departamento de Física e Astronomia
2014

Orientador
Polychronis Papaderos,
Investigador Coordenador, Centro de Astrofísica da Universidade do Porto

Coorientador
Jean Michel Gomes,
Investigador, Centro de Astrofísica da Universidade do Porto

U.PORTO

FACULDADE DE CIÊNCIAS
UNIVERSIDADE DO PORTO

Todas as correções determinadas pelo júri, e só essas, foram efetuadas.

O Presidente do Júri,

Porto, _____/_____/_____

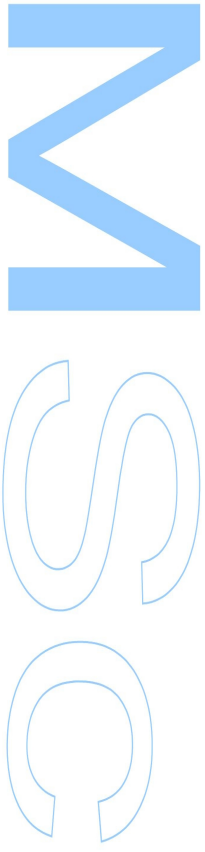

◦Master in Astronomy Dissertation

On the metallicity of pseudo-bulges in the CALIFA galaxy Survey

Author:

Iris Pereira Breda[1,2]

Supervisors:

Polychronis Papaderos[1,2] and Jean Michel Gomes[1,2]

Affiliations:

[1]Instituto de Astrofísica e Ciências do Espaço - Centro de Astrofísica da Universidade do Porto, Rua das Estrelas, 4150-762 Porto, Portugal

[2]Departamento de Física e Astronomia, Faculdade de Ciências, Universidade do Porto, Rua do Campo Alegre, 4169-007 Porto, Portugal

Acknowledgements

I would like to express my deepest gratitude to PD Dr. Polychronis Papaderos and Dr. Jean Michel for their valuable contribution and constructive suggestions, making possible the development and conclusion of this work, with special attention to Polychronis who generously dedicated his time and attention to the issues and new ideas encountered during this stage. I would also like to extend my thanks to my family and friends for their support, patience and encouragement, specifically to my father for the interesting discussions and useful criticisms. Finally, I would like to thank Sandra Reis and all the team at IA-CAUP. I also acknowledge funding from the FCT project "An exploration of the assembly history of galaxies with the novel concept of self consistent spectral synthesis (FADO)" (FCOMP-01-0124-FEDER-029170 & PTDC/FIS-AST/3214/2012) and SELGIFS (Study of emission line galaxies with integral field spectroscopy) (P7-PEOPLE-2013-IRSES) project.

Abstract

A sample of 66 late-type galaxies included both in the CALIFA Integral Field Spectroscopy (IFS) Galaxy Survey and SDSS has been subject of a thorough investigation that combined surface photometry with spectral synthesis techniques. The main goal of this project was to determine the stellar and gas-phase metallicity in galaxy bulges and explore possible physical relations between these quantities and the photometric/structural characteristics of the bulge and the underlying disk component.

After spaxel-by-spaxel processing of CALIFA IFS data with the IA-CAUP spectral synthesis pipeline Porto3D (Papaderos & Gomes), a suite of auxiliary codes was used to determine the radial distribution of various quantities inferred from it. These include, besides the stellar and gas-phase metallicity, the $H\alpha$ flux and equivalent width, the mass fraction of stars formed over the recent past (100 Myr), the stellar V-band extinction and the Balmer decrement. This way metallicity gradients could be determined both in the bulge and the disk permitting for the first time a systematic analysis on the basis of robust statistics.

Through a hybrid 1D/2D surface photometry technique that was substantially improved in the framework of this MSc project, the sample galaxies were decomposed into their disk and bulge emission, with the significant addition of the inclusion of a bar component for barred galaxies. Fitting these photometric components with a generalized exponential Sérsic law has permitted the determination of their structural characteristics which were correlated both with integral and photometric characteristics and various quantities determined with Porto3D (e.g., luminosity-weighted stellar metallicity). Adopting the definition proposed by Kormendy & Kennicutt (2004), 63 of the sample galaxies were found to host a pseudo-bulge.

Due to the fact that a substantial fraction of late-type galaxies exhibits active star formation

(SF) in the disk, whereas star forming activity is weak or absent in the bulge, and, following a proposal by Papaderos et al. (2014, in prep.), this project has addressed the question of whether the SF-elevated surface brightness of the disk can systematically bias state-of-the-art $bulge + disk$ decomposition analyses.

Thanks to the code $RemoveYoung$ (RY; Gomes et al. 2014, in prep.) it has been possible to determine the surface brightness enhancement of the disk due to recent and ongoing SF activity and correct surface brightness profiles for this effect. A repetition of the profile decomposition analysis, after removal of the luminosity contribution from the young ($\leq$30 Myr) ionizing stellar component has indeed led to a substantially improved determination of the photometric properties of the bulge. More specifically, a comparison of the bulge structural properties before and after application of RY has shown that correction for the surface brightness enhancement of the disk on average yields a larger luminosity contribution and isophotal extent for the bulge.

On the other hand, it has to be noted that this project has merely provided a proof of concept for RY, with its narrow time framework not permitting to fully exploit its potential for refining structural analyses of galaxies. Furthermore, several relations between photometric/structural and evolutionary/chemical characteristics of the bulge were investigated (see Chapter 7), revealing in some cases clear trends, in others an equally important lack of any correlation.

Some of the main conclusions drawn from this parameter study may be summarized as follows: The absolute magnitude of the bulge correlates with the total galaxy absolute magnitude ($R^2 \sim$ 0.64; 0.70, before and after applying RY, respectively), but there is no clear correlation between the bulge-to-total ratio (B/T) and the total absolute magnitude ($R^2 \sim$ 0.16; 0.15). It was further found that the absolute magnitude of the bulge is strongly correlated with the mean stellar surface density μ_{80} within the radius R_{80} encircling 80% of the bulge total luminosity ($R^2 \sim$ 0.61; 0.58), whereas no obvious correlation is apparent between the bulge luminosity and its Sérsic index η ($R^2 \sim$ 0.22; 0.19). The present analysis neither reveals any clear correlation between η and the B/T ($R^2 \sim$ 0.24; 0.20). μ_{80} was found to correlate with the total absolute magnitude ($R^2 \sim$ 0.47; 0.53).

The Porto3D pipeline and a suite of additional codes have permitted the derivation of 2D maps and radial profiles for several physical characteristics of the stellar and ionized gas component.

Among other tasks, the mean value for the stellar and gas-phase metallicity within the isophotal extent of the bulge were compared with photometric/structural quantities (see Chapter 6). It was found that the mean luminosity- and mass-weighted stellar metallicity within the bulge is correlated with the total absolute magnitude ($R^2 \sim 0.46$; 0.55, respectively), the total stellar mass ($R^2 \sim 0.36$; 0.50), bulge absolute magnitude ($R^2 \sim 0.49$; 0.51) and μ_{80} ($R^2 \sim 0.39$; 0.40). The difference between gas-phase and stellar metallicity within the bulge was found to be correlated with the bulge absolute magnitude ($R^2 \sim 0.44$; 0.46), total stellar mass ($R^2 \sim 0.30$; 0.34) and bulge mean stellar metallicity ($R^2 \sim 0.76$; 0.70).

Since a parallel MSc project by S. Reis at IA-CAUP has dealt with the stellar age and age gradients for the same galaxy sample, it was possible to use the results from it for an extended analysis combining information on metallicity, age and structural galaxy properties. Quite importantly, it was found that the studied sample can be subdivided into four physically similar main classes, based on luminosity-weighted stellar metallicity and age gradients within the bulge (see Chapter 6, 7 and App. D). It was further found that these classes describe a clear sequence, which suggests that metallicity and age gradients within the bulge may provide sensitive indicators of the evolutionary stage and star formation history of a normal late-type galaxy.

Keywords

Surface Photometry and Photometric Decomposition, Integral Field Spectroscopy, CALIFA Survey, Galactic bulge, Metallicity gradients, Pseudo-bulge

Resumo

Uma amostra de 66 galáxias "late-type", incluídas tanto no Survey de Espectroscopia de Campo Integral CALIFA como no Survey SDSS, foi objecto de uma investigação minuciosa que combinou técnicas de fotometria de superfície com síntese espectral. O principal objetivo deste projeto foi determinar metalicidades estelar e do gás ionizado em bojos de galáxias espirais e explorar possíveis relações físicas entre essas quantidades e características estruturais/fotométricas do bojo e do componente do disco subjacente.

Após o processamento spaxel-a-spaxel de dados IFS-CALIFA usando o "pipeline" de síntese espectral Porto3D (Papaderos & Gomes, IA-CAUP), um conjunto de códigos auxiliares foi utilizado para determinar a distribuição radial de diversas quantidades estimadas. Estes incluem, além das metalicidades estelar e em fase gasosa, o fluxo de $H\alpha$ e largura equivalente, a fração de massa estelar formada no passado recente (100 Myr), a extinção estelar na banda V e o decréscimo de Balmer. Desta forma foram determinados os gradientes de metalicidade, tanto no bojo como no disco, permitindo pela primeira vez, uma análise sistemática destas quantidades, com base em dados estatísticos robustos.

Através de uma técnica de fotometria de superfície híbrida 1D/2D que foi substancialmente melhorada no âmbito deste projeto de mestrado, as galáxias da amostra foram decompostas em disco e bojo, com a inclusão de uma componente de barra para galáxias barradas. O ajuste destes componentes fotométricos a uma lei de Sérsic exponencial generalizada permitiu a determinação das suas características estruturais que foram correlacionadas com características integrais e fotométricas e com várias quantidades determinadas com o Porto3D (ex., metalicidade estelar ponderada em luminosidade). Adoptando a definição proposta por Kormendy & Kennicutt (2004), 63 das galáxias da amostra contêm um pseudo-bojo.

Devido ao facto de uma fração substancial de galáxias "late-type" exibir formação estelar (FS) no disco, enquanto que no bojo a mesma é escassa ou ausente, e, por proposta Papaderos et al. (2014, em prep.), foi abordada a questão de verificar se o brilho de superfície em regiões do disco de FS-elevada pode comprometer sistematicamente métodos "state-of-the-art" de decomposição $bojo + disco$.

Com auxílio do código $RemoveYoung$ (RY; Gomes et al, 2014, em prep.), foi possível determinar o aumento no brilho de superfície do disco, devido à atividade de FS recente e em curso, e perfis de brilho de superfície corrigidos deste efeito. Uma repetição da decompsição dos perfis de brilho de superfície, após remoção da contribuição do componente estelar jovem ($\sim$ 30 Myr), levou a uma melhoria substancial da determinação das propriedades fotométricas do bojo. Mais especificamente, uma comparação das propriedades estruturais do bojo, antes e após a aplicação do RY mostrou que a correcção para o aumento do brilho da superfície do disco, em média, transcreve-se numa contribuição maior da luminosidade e extensão isofotal do bojo.

Por outro lado, e devido à limitação de tempo, é de salientar que este projecto forneceu apenas uma prova de conceito para o RY, não permitindo explorar plenamente o seu potencial para a refinação de análise estrutural de galáxias. Além disso, foram investigadas várias relações entre parametros fotométricos/estruturais e características evolutivas/químicas do bojo (ver Capítulo 7), revelando em alguns casos, tendências claras, em outros – igualmente importante – falta de correlações.

Algumas das principais conclusões deste estudo podem ser resumidas da seguinte forma: A magnitude absoluta do bojo correlaciona-se com a magnitude absoluta total da galáxia ($R^2 \sim$ 0,64; 0,70, antes e após a aplicação do RY, respectivamente), não existindo nenhuma correlação clara entre o bojo-para-total (B/T) e a magnitude absoluta total ($R^2 \sim$ 0,16; 0,15). Verificou-se, ainda, que a magnitude absoluta do bojo está fortemente correlacionada com a densidade estelar superficial média μ_{80} dentro do raio R_{80}, que contem 80% da luminosidade total do bojo ($R^2 \sim$ 0,61; 0,58), ao passo que nenhuma correlação óbvia é aparente entre a luminosidade do bojo e o seu índice de Sérsic η ($R^2 \sim$ 0,22; 0,19). A presente análise não revela qualquer correlação clara entre η e o B/T ($R^2 \sim$ 0,24; 0,20). μ_{80} correlaciona-se com a magnitude absoluta total ($R^2 \sim$ 0,47; 0,53).

O "pipeline" Porto3D e um conjunto de códigos adicionais permitiram a derivação de mapas 2D e perfis radiais de várias características físicas dos componentes estelar e gás ionizado. Entre outras tarefas, o valor médio para as metalicidades estelar e em fase gasosa dentro da extensão isofotal do bojo foram comparados com quantidades estruturais/fotométricas (ver Capítulo 6). Verificou-se que a metalicidade estelar média ponderada em luminosidade e em massa dentro do bojo está correlacionada com a magnitude absoluta total ($R^2 \sim$ 0,46; 0,55, respectivamente), a massa estelar total ($R^2 \sim$ 0,36; 0,50), magnitude absoluta do bojo ($R^2 \sim$ 0,49; 0,51) e μ_{80} ($R^2 \sim$ 0,39; 0,40). A diferença entre as metalicidades da fase gasosa e estelar no bojo pode também ser correlacionada com a magnitude absoluta do bojo ($R^2 \sim$ 0,44; 0,46), massa estelar total ($R^2 \sim$ 0,30; 0,34) e metalicidade estelar no bojo ($R^2 \sim$ 0,76; 0,70).

Uma vez que o projeto de mestrado que está a decorrer paralelamente no IA-CAUP de S. Reis lida com idades e gradientes de idade estelares para a mesma amostra de galáxias, foi possível utilizar os seus resultados para uma análise mais extensa, combinando informação sobre metalicidade, idade e propriedades estruturais. De salientar que a amostra estudada pode ser subdividida em quatro classes principais fisicamente semelhantes, com base nos gradientes de metalicidade e idade estelar, ponderados em luminosidade, dentro do bojo (ver Capítulo 6, 7 e Ap. D). Concluiu-se que essas classes descrevem uma sequência clara, o que sugere que os gradientes de metalicidade e idade dentro do bojo podem ser indicadores sensíveis da história de formação estelar e estágio evolutivo de uma galáxia "late-type" normal.

Palavras chave

Fotometria de Superfície e Decomposição Fotométrica, Espectroscopia de Campo Integral, CALIFA Survey, Bojo galáctico, Gradientes de metalicidade, Pseudo-bojo

Contents

List of Figures

List of Tables

Chapter 1.

Introduction

We are now witnessing an epic era of remarkable discoveries in astronomy, leading to a vast expansion of the knowledge and insight into the Cosmos. In the last few decades, the development of high-resolution instruments is allowing to perform a detailed examination of all types of astronomical objects, providing the Astronomer with the means to acquire a deeper understanding of the Universe. The field of Extragalactic Astronomy, which is the scientific branch dedicated to the study of the galactic objects external to our own galaxy – the Milky Way – is extremely important when it comes to unravel the mysteries behind the collective physical processes that gave origin to the Universe we see today. By studying the formation and evolution of galaxies by means of structural and stellar population properties – stellar populations, $inter\text{-}stellar\ medium$ (ISM), $active\ galactic\ nucleus$ (AGN), clustering of galaxies – carefully analyzing their physical properties – kinematics, photometric and spectroscopic attributes – one can give answers to very fundamental questions related with the evolution of galaxies both generally and specifically for the target galactic system. For instance, one can collect crucial information about the nature and shape of $dark\ matter\ halos$, acknowledge how the galaxies aggregate themselves in the cosmic filamentary necklaces, and on the other hand, decipher the behavior and physical characteristics of the stellar, gas and dust components of a galaxy, or analyze the presence and feedback processes of AGNs and how will they influence the properties of the host galaxy.

In the Universe, one can find an authentic zoo of galaxies. The two main types of Hubble-type galaxies are elliptical – early-type – and spiral – late-type. Furthermore, one can identify

several other types of galaxies (morphologically: lenticular, irregular, dwarf; by activity type: active forming and starburst galaxies, AGN; etc.). These classes differentiate themselves not only in their morphology, but also in their dominant physical properties, suggesting that they followed different paths of evolution, possibly having distinct formation histories. This work is mainly focused on late-type, spiral galaxies, which are, in most cases, highly complex systems. In the simplest case, these galaxies are constituted by a central stellar system – the bulge – surrounded by a complex star-forming disk. The main goal of this work is to shed some light into the mysteries of the formation and evolution of the bulge of spiral galaxies, relating their physical properties with the same of the other components of the galaxy, in special the $metallicity$ (Z) of both stellar populations and ionized gas.

The main motivation behind this study was the recent change of paradigm about the interpretation of the formation histories and physical properties of the central region of these galaxies. Over the last few years, the analysis of high-resolution ground-based and satellite multi-wavelength data had revealed the existence of a vast diversity of structural and kinematic properties of bulges. The traditional overview that adopts a very simplistic conception of these stellar structures, due to their commonly featureless appearance and resemblance to elliptical systems, is now considered as one of the two possible pathways for the nature of bulges. The current view discriminates between $classical\ bulges$ (CB), formed through violent processes that fall within the traditional overview, and $pseudo\text{-}bulges$ (PB), which assembled gradually in the course of secular galactic evolution. The necessity for this ramification emerged a few years ago, being first pointed out by Kormendy (1993). It is thought that the physical properties of these two classes are very distinct, for instance, while CBs are mostly composed of old, low-mass stars without showing signs of recent star-formation, PBs seems to be constituted by young stars, gas and dust presenting ongoing star-formation. The formation histories and dependence on the properties of the host galaxy of PBs is still an open question.

In order to conduct this study, both photometric and spectroscopic data are used. While the first technique measures the intensity or flux of an astronomical object's electromagnetic radiation over large wavelength bands, the latest measures the spectral distribution of the same flux of electromagnetic radiation. Combining these two techniques, it is possible to achieve a deep

understating of the physical properties of galaxies. As photometric data, it is used the r band SDSS-DR7, which provides high quality images in the five bands - u, g, r, i and z. For the spectroscopic data one will use $Integral\ Field\ Unit\ Spectroscopy$ (IFS) from the $Calar\ Alto\ Legacy\ Integral\ Field\ Area$ (CALIFA) Survey, which provides high precision spatially-resolved spectral data. When completed, this survey will provided the community detailed spatially resolved spectral data for 600 local ($0.005 \leq z \leq 0.03$) galaxies, covering all of the Hubble types, enabling Astronomers to study the observed galaxies over a large field of view, highly in detail. The main tool one will use to investigate this data is PORTO3D pipeline, an automated pipeline for post-processing and spectral synthesis of IFU data cubes that was developed at CAUP by PD Dr. Polychronis Papaderos and Dr. Jean Michel Gomes. The target sample is constituted by 66 face-on or nearly face-on late-type galaxies that were both observed by the CALIFA Survey and by the SDSS.

This work is primarily focused on the radial metallicity distribution – both in stellar populations and the nebular component – mainly in the PBs, with the purpose of acquiring tight observational constrains which will enable theoreticians to investigate how the chemical evolution occurs in late-type galaxies and how can it be related with the nature of the bulge. This is done by using PORTO3D that estimates $star\ formation\ histories$ (SFH), metallicities and ages, for each spaxel of the IFU data by using $stellar\ population\ synthesis\ codes$ (SPSC) like STARLIGHT, enabling to estimate, among other physical quantities, mass and light weighted stellar metallicities. The gas-phase metallicities are estimated by applying semi-empirical $strong\ line\ methods$ (SLM).

The photometric data is used for the decomposition of late-type galaxies into $bulge + disk$, or in some cases $bulge + bar + disk$, using 1D surface photometry techniques. Furthermore, key physical parameters are investigated – both integral (e.g., total absolute magnitude) and structural properties (e.g., bulge Sérsic index, disk, bar and bulge absolute magnitudes) – and correlations between them. A robust photometric analysis allows to estimate several physical quantities for every component of the galaxy distinctively, that indicates how the light is distributed throughout the galactic system. It is assumed that the disk follows an exponential luminosity profile, where the surface brightness is linearly correlated to the radius. Following a proposal by Papaderos et al. (2014, in prep.), in order to get a better estimate of the disk continuum that dominates

the mass – the light it would emit if the disk was free from recent star formation (SF) episodes – one will combine photometric with spectroscopic techniques. By removing from the IFS data-cube the light contribution of young stars, one will estimate the shift in magnitudes the disk has to be scaled down and apply this correction to the decomposition process ($RemoveYoung$ (RY) routine, Gomes et al., 2014, in prep.). When a bar is present after removing the disk contribution, its $surface\ brightness\ profile$ (SBP) will be approximated by a Sérsic model (Sérsic, 1963) with $\eta \leq 0.4$. The SBP of the bulge will be the result of the subtraction of the fitted disk – and bar if it is a barred galaxy – from the total flux emission. The remaining SBP is then fitted with a Sérsic model. For this task it was developed a innovating method to estimate the Sérsic index (η) – more stable and independent on the settings made by the user than the traditional method – strongly alleviating the degeneracy between the scalength (α) and the η, two of the three free parameters of the Sérsic model. In this approach, η is estimated by using observed quantities – the effective radius (R_{mod} or R_{50}) of the bulge and the surface brightness (μ_{mod} or μ_{50}) at R_{mod}. Besides the aforementioned ones, the principal photometric structural and integral properties that were measured and studied in this work were the absolute magnitude, effective radius of the galaxy (R_{eff}), mean stellar surface density (μ_{80}) within the radius that encompasses 80% of the total flux (R_{80}) of the bulge and bulge-to-total (B/T) ratio.

As for the spatially-resolved spectroscopic data, the output from PORTO3D pipeline – a data-cube in FITS format with several layers where the spatial maps of different spectroscopic quantities are stored (e.g., emission-line maps, ages, metallicities, etc..) – will be translated into radial profiles by using the irregular isophotal annuli method (Papaderos et al., 2002). From the radial profiles it were measured several key parameters, as the mean values and the slope of the linear fit (gradient) in the different galactic components for several physical quantities – for instance, luminosity and mass weighted stellar metallicity, gas-phase metallicity, and the logarithm of the stellar mass the galaxy presently contains – and then compared with the previously estimated photometric quantities (namely total and bulge absolute magnitude and μ_{80}).

1.1 MORPHOLOGICAL CLASSES OF GALAXIES AND THEIR MAIN PHYSICAL PROPERTIES

There are many types of galaxies in the Universe. The simplest way to classify these objects is by analyzing their visual appearance, doing a morphological classification. In 1936 Edwin Hubble proposed the first morphological classification scheme for galaxies - the $Hubble\ Sequence$ (HS).

The Hubble's scheme divides the galaxies into 3 principal classes - ellipticals, lenticulars and spirals – and one extra class – the irregulars – to note that there are several other exotic types of galaxies in the Universe which do not fit in the context of this work.

Elliptical Galaxies

The elliptical galaxies, also called by early-type galaxies – denoted in the HS by Ex ($spherical$ $0 \leq x \leq 7$ $oblong$) – are triaxial systems, at first sight very homogeneous, presenting a featureless SBP, in most cases described by the Sérsic model with $\eta \sim 4$ (De Vaucouleurs' law). They are composed of an old stellar component with kinematics dminated by random motions, as evident from its large velocity dispersion (σ_*), being characterized as passive galaxies, that stopped their star formation long ago in the cosmic time-scale. Generally, the most massive galaxies in the Universe belong to this morphological class. They host a $super\text{-}massive\ black\ hole$ (SMBH) in their core, that in some cases is accreting matter at a high rate, becoming what is known as an AGN, which feedback processes – observed in spectra as nonthermal radiation – can be extremely energetic (to note that the presence of an AGN is not exclusive of this morphological class). One of the many explanations for the commonly observed absence of gas in this type of galaxies is that feedback processes, caused by the presence of an AGN, may drive the gas as outflows to the $inter\text{-}galactic\ medium$ (IGM), or inject kinetic energy into the system, heating the gas, preventing it to collapse and form new stars. Another explanation comes from the theory that states that elliptical galaxies are the result of merger processes: the occurrence of violent mergers can easily force an intense burst of star formation, transforming most of the gas into stars, ejecting part of the gas into the IGM via galactic winds. In the monolithic collapse scenario, the ellipticals are among the first galaxies to emerge in the Cosmos, resulting from the quick collapse of the most

massive initially gravitationally bounded structures. Due to their deep gravitational potential well, these galaxies are preferentially found at the center of galaxy clusters and are usually surrounded by galaxy satellites.

Spiral Galaxies

The spiral galaxies, also designated by late-type galaxies – denoted in the HS by Sx or SBx when barred (x from a to c, by decreasing the prominence of spiral-arms/bar) – are, at first sight, more complex systems when compared to the ellipticals. These are composed by a central bulge, where older stars are sometimes highly concentrated, surrounded by a flattened rotating disk with spiral features, dominated by young stellar populations. Occasionally they also present other features like bars, rings, etc.. Each of the structural components that constitute a spiral galaxy has different physical properties and formation histories.

The spiral arms are composed by gas, dust and young, metal-rich stars, and are currently actively forming stars. Usually, the disk presents high flux of $ultra\text{-}violet$ (UV) – emitted by the young, hot OB stars – and $far\text{-}infrared$ (FIR) radiation – re-emitted by the dust after absorbing low- to high-energy photons. In a face-on spiral galaxy, the disk continuum can usually be described as an exponential luminosity profile, where the surface brightness is linearly correlated to the radius.

Regarding the bar, it is thought that bar-like structures – quasi-elliptical structures which are present in many of the spiral galaxies (Marinova & Jogee, 2007; Menéndez-Delmestre et al., 2007) – have an important role in the evolution of a galaxy – to note that the bar feature is commonly observed not only in spiral, but also in elliptical and lenticular galaxies. Numerical simulations have shown that rotating disks are very unstable, spontaneously forming bars as a result of slightly higher density zones at the disk. The simulations also show that the DMH that surrounds the galaxy will stabilize the spiral disk preventing the formation of prominent bars. Hereupon, one important factor when it comes to determine the probability of having a barred galaxy is the disk-to-halo mass (this is known as the Ostriker-Peebles criterion). This probability decreases with increasing $redshift$ (z): at $z \sim 1$ - approximately 8 Gyr ago - only 11% of the spiral galaxies had bars, by $z \sim 0.2$ - 2.5 Gyrs ago - the quantity of bared galaxies doubled and at the present day $\sim 22\%$ of the observed spiral galaxies are bared (Melvin et al., 2014) – the observed

bar fractions in the local universe range from 25 to 70% depending on several selection effects: bar classification method; prominence of the bar; observed wavelength.

The presence of a bar is also related with the total mass of the galaxy, since the probability of having a bared galaxy increases with its mass. It is thought that the bar is related to the quenching of the galaxy: observations have shown that the more prominent is the bar, the less likely is the existence of ongoing star forming activity. This might be related with the fact that strong, prominent bar-like features can drive interstellar gas towards the center of the galaxy, depleting the spiral arms. Stellar bars have been recognized as the most important internal factor in redistributing the angular momentum of the baryonic and dark matter components in disk galaxies (Athanassoula & Misiriotis, 2002; Berentzen et al., 2006; Debattista & Sellwood, 1998; Weinberg, 1985). Observations of local galaxies support the scenario where bars drive gas from the outer disk to the central part of the galaxy, feeding central starbursts (Elmegreen, 1994; Jogee et al., 2005). The SBP of this component it is usually approximated to a Sérsic model with a $\eta \leq 0.4$.

This work aims to give a better understanding on the nature of the central part of late-type galaxies - the bulge. The classical view of the central region of spiral and lenticular galaxies had radically changed over the past few years. In 1926 Edwin Hubble suggests that the central part of these galaxies is very similar to an elliptical system, creating the traditional and simplified view that a spiral galaxy is composed by a scale down elliptical at its center, surrounded by a star forming disk. Although, recent ground-based and satellite multi-wavelength data of high resolution revealed that some of the nuclear regions of disky galaxies do not fall within this traditional connotation, emerging the necessity to elaborate a physically motivated definition of this nuclear stellar systems, relating the characteristics of the bulge with the different physical properties of the surrounding disk and the other galactic components. Today, one can find in the literature two main categories of bulges which are structurally, photometrically and kinematically distinct: the classical/bona fide bulges which lie in the traditional definition, and the pseudo-bulges which present significant different physical characteristics.

Classical Bulge

According to our current understanding, CBs are largely similar to normal elliptical galaxies with regard to their stellar kinematics and formation history. They present a spheroidal shape and are composed by old, low-mass stellar populations, with smoothed/featureless SBPs, in most cases being described by the De Vaucouleurs' law. They are kinematically hot, being dynamically supported by the σ_*, depleted in gas and dust, presenting reddish colors and no significant star forming activity. Most of them host a SMBH at its core, and have a deep and steep gravitational potential well. Through observations is known that CBs follow relatively tight physical correlations between the mass of the $black\ hole$ (BH), the total mass of the bulge (M_B), the luminosity of the bulge (L_B) and the σ_* (e.g., Gültekin et al., 2009). There are currently two scenarios to explain the formation history of this class of bulges: they were formed via several mergers, by the accretion of smaller external units during its life time (Aguerri et al., 2001; Bournaud et al., 2007), or they could be formed by a quasi-monolithic collapse via major mergers (Eggen et al., 1962). These proposals are encouraged by the fact that galaxies which host a CB are mostly found in clusters, where merger episodes are more likely to happen.

Pseudo-bulge

These stellar systems can be also refereed as disk-like bulges, since they share some physical characteristics with a disky system. According to Kormendy & Kennicutt (2004), observations show that PBs preserve a memory of their disk origin, presenting one or more of the following characteristics: flatter shapes compared to CBs, large ratios of ordered to random velocities – being gravitationaly supported by the rotation of their stars (V_{rot}) – indicating disk dynamics, smaller σ_* than the predicted by the Faber-Jackson relation (Faber-Jackson, 1976) σ_* – L_B (bulge luminosity), spiral structure and/or nuclear bars, nearly exponential SBPs described by a Sérsic model with $\eta \leq 2$ (e.g., Drory & Fisher, 2007), dominated by Population I material (young stars, gas and dust) with no signs of merging episodes. Kormendy et al. (2011) shows that PBs do not follow the same correlations between the physical quantities of the bulge and BH as the CBs, indicating different formation histories, although, even $bulgeless$ galaxies contain a central low-mass ($10^5 - 10^6$ $M_\odot$) BH (e.g., Kormendy & Ho, 2013). Gadotti 2008 shows that CBs follow a correlation between

Sérsic index and bulge-to-total ratio (B/T) whereas PBs does not, and that PBs follow a mass-size relation different from that of the CBs, similar to that of bars. Fisher & Drory (2008) present a new method to distinguish PBs from CBs: they show that the half-light radius of PBs correlates with the scale-length of the disk whereas in the case of a CB this correlation is absent.

In the current framework, PBs were formed over larger time-scales evolving secularly – slow, steady evolution that can be either the result of long-term interactions between the galaxy and its environment or induced by internal processes such as the actions of spiral arms or bars – without being perturbed by mergers, in a continuous and smooth process of aging, in contrast with CBs which are merger-built bulges. It is thought that PBs may be the result of disk instabilities and bar-driven gas inflows. Such instabilities will redistribute the angular momentum along the galaxy, forcing part of the gas – and possibly some of the stars – of the disk to migrate to the central region of the galaxy (Athanassoula, 2003). When the inner component becomes massive enough, new stars are born, originating a PB (Athanassoula, 1992; Heller & Shlosman, 1994; Wada & Habe, 1992). Semi-analytical bulge formation models, where the bulge is built via disk instabilities – despite being still very crude (Athanassoula, 2008; De Lucia et al., 2011; Guo et al., 2011) – show that in the case of bar-unstable disks, a large fraction (13%) of the disk mass is transferred to the bulge (Gadotti, 2008).

Combes & Sanders (1981) and Pfenniger & Norman (1990) discuss the building of bulges by bars by two independent processes: the inward transport of gas by bars and ovals and dissipationless processes that might yield vertically thickened central components when bars suffer buckling instabilities and when disk stars scatter off of bars and are heated in the axial direction. Both processes can occur in the same galaxy and produce bulge-like components out of disk material trough the bar component.

PBs are mostly found in low density environments (Durbala et al., 2008) – at the periphery of clusters – or in the field.

Lenticular Galaxies

In the Hubble Sequence, a lenticular galaxy – denoted by S0 – lies between elliptical and spiral galaxies. Although their properties are simultaneously similar to both spiral and elliptical systems

– indicating they might be a transitional phase from spiral to elliptical within the process of galactic evolution – it is a subject of an intense debate how their physical properties may be linked to those of the other galaxy types. They are composed mostly by old stars, resembling at first sight spiral galaxies that had partially lost their disk component. The disk of a S0 galaxy is usually gas depleted, showing none or very little ongoing star formation, with high quantities of dust. The bulge component is usually prominent and dominant, being, in most of the cases, classified as CB. This class have much higher bulge-to-disk ratios when compared with typical spiral galaxies and may exhibit a prominent central bar (Binney & Merrifield, 1998).

1.2 METALLICITY AND EVOLUTION OF GALAXIES

In Astronomy, the metallicity (Z) of a celestial object is a measure of the quantity of chemical elements other than Hydrogen and Helium. There are several ways to quantify this characteristic, depending on the subject and aim of the study. According to the Big Bang theory, the $primordial\ nucleosynthesis$ filled up the Universe with Hydrogen and Helium, and vestigial traces of Lithium and Beryllium. All the observed heavier elements in the Universe were created subsequently by nuclear fusion, in the core of stars or during the explosion of $supernova$ (SNe). Part of this heavy elements were then ejected back into the ISM via SNe explosions and/or stellar winds, enriching the surrounding environment, being later integrated into new stars. A galaxy is a very complex system, mainly composed by its stellar populations plus gas and dust, being possible to estimate the amount of metals in both components.

The Z is a fundamental aspect of the galaxies properties. This key parameter will provide information about the object's former evolution, since it traces the star formation history (SFH) of the galaxy, linking three key processes in galaxy evolution: star formation, gas accretion and galactic outflows (Peng & Maiolino, 2013). It also permits to determine UV, optical and NIR colors at a given age (e.g., Leitherer et al., 1999), nucleosynthetic yields (e.g., Woosley & Weaver, 1995), dust-to-gas ratios (e.g., Hirashita et al., 2001) and shapes of the interstellar extinction curve (e.g., Piovan et al., 2006). Since the heavy chemical elements have a high atomic number, the amount of metals in the diffuse gas will also determine the cooling rate and consequently the ability of

galaxies to form new stars.

The metal enrichment of a galaxy is a very complex phenomenon, depending on many internal and external processes that occur during galactic evolution. In order to deeply understand it, it is necessary to take into account for physical processes such as inflows and outflows of poor/rich gas, the depletion of the metal gas phase by dust, being latter returned to the ISM when the dust is destroyed, the role of the gravitational potential well of the galactic system, the mass and star formation rate (SFR) of the stars which are formed in the galaxy, and many other parameters – which is only possible by using chemical evolution models that are not employed in this work. Hereupon Z is in fact, a key parameter when the purpose is to understand the evolution of galactic systems, since it can be correlated with several other physical quantities like $luminosity$ (L), $stellar\ mass$ (M_*) and $star\ formation\ rates$ (SFR).

Metallicity Relations

Luminosity-Metallicity Relation

The first time the $luminosity$-$metallicity$ $(L-Z)$ relation was observationally established was in 1979 in a seminal work by Lequeux in the context of dwarf elliptical systems. Due to the fact that these are vital parameters when it comes to understand galactic evolution, since that time this relation has been extensively studied (e.g., Skillman et al., 1989; Tremonti et al., 2004). It was established by various authors a tight correlation between the blue luminosity (L_B) and the Z for dwarf irregulars (dIs), spirals and ellipticals (Garnett & Shields, 1987; Lamareille et al., 2004; Lee et al., 2003; Melbourne & Salzer, 2002; Salzer et al., 2005; Skillman et al., 1989; Tremonti et al., 2004; van Zee & Haynes, 2006; Zaritsky et al., 1994), but there are still disagreements due to some contradictory results in some of the morphological classes.

According to standard scenarios of chemical evolution in galaxies, the $L-Z$ relation reflects the behavior of galactic winds (induced by SNe) and feedbacks, which withdraw the gas of the ISM before its conversion into stars (Dekel & Silk, 1986; Lynden-Bell, 1992; Tinsley & Larson, 1979). Ultimately, the $L-Z$ relation arises as a consequence of another well defined dependence, which is the $mass$-to-$light\ ratio$ (M_*/L), together with the M_*-Z relation. Since it is easier to measure L rather then M_*, this dependence is often used rather than the last.

As it was mentioned above, the $L - Z$ relation depends greatly on the morphological class of the galactic system, and its still target of study, but generally, and also due to the fact that $M_* - Z$ and M_*/L are direct dependencies, the trend evolves in a way that the galaxies tend to be redder from lower to higher L or Z.

Mass-Metallicity Relation

It has been well established in literature the correlation between M_* of the galactic system and its Z (e.g., Peng & Maiolino, 2013). The interest in the relation between these two quantities ($M_* - Z$) suggested first by Larson (1974), where he attempted to explain this trend in elliptical galaxies. Till that time, several studies have demonstrated that, in fact, the M_* and the Z of a galaxy are two dependent parameters.

Tremonti et al. (2004) studied 53,000 SDSS galaxies and found a steep correlation between M_* and Z for galactic masses $\leq 10^{10.5}\ M_\odot$, followed by a flattening for higher masses. These authors explain their observations assuming that low mass galaxies are more likely to loose their produced metals by outflows (since their gravitational potential wells are more shallow), requiring lower escape velocities to break free from the gravitational embrace of the galaxy than in high mass galaxies. To note that this explanation is the most accepted but not the only one (for instance, a galaxy mass dependent $initial\ mass\ function$ (IMF) has been proposed as an alternative).

In addition, there are other processes which are assumed to have an important role in the $M_* - Z$ dependence, like the scenario where less massive galaxies take longer time scales to convert their gas into stars, having higher gas-to-stellar mass ratios, presenting lower Z values (Brooks et al., 2007).

Recently it was proposed that the $M_* - Z$ relation arises as a consequence of a fundamental relation between M_*, gas-phase metallicity (Z_N) and SFR. This was realized by several authors – Lara-López et al. (2010); Mannucci et al. (2010) – and its called by "$fundamental\ metallicity\ relation$" (FMR). The FMR relates these three key quantities in a 3D parameter space, exhibiting a tight correlation, being the residual Z dispersion of local SDSS galaxies of about 0.05 dex. According to these authors, the solid correlation of these three parameters strongly suggests the existence of highly efficient mechanisms which regulate the galactic system. These authors

justify the FMR by a well regulated balance between pristine inflows and metal-rich outflows, where metal poor gas is captured by the galaxy halo, acting both by boosting star formation and dilute the ISM gas, decreasing its mean Z. The outflows driven by the newly formed stars will then remove the enriched gas at a rate which is dependent of the SFR. The combination of these two effects will produce the observed correlation between the three parameters.

Local Mass-Metallicity-SFR Relation

Using spatially-resolved optical spectroscopy of 2573 HII regions of 38 local galaxies, Rosales-Ortega et al. (2012) show that there is a $local$ correlation between galaxy surface mass density, gas-phase metallicity – estimated using the O3N2 calibrator ($\equiv$ to the ratio between the flux of the emission-lines [OIII] and [NII], with some variations) (Pettini & Pagel, 2004) and SFRs. The local $M_* - Z$ relation is very tight - being the 1σ scatter of the data about the median $\pm$ 0.14 dex – and notably similar to the $global$ $M_* - Z$ relation. These authors also found a more general relation between mass surface density, metallicity and the equivalent width of Hα, a measure of the SFR per unit luminosity (Kennicutt, 1998). The value of $|EW(H\alpha)|$ is inversely proportional to mass and metallicity. They interpret this local $M_* - Z - EW(H\alpha)$ relation as being a consequence of a more subtle relation between mass, metallicity and SFH of the galaxy, where the inner regions of the galaxy form first and faster, increasing the gas metallicity of the surroundings. As the galaxy evolves, the star-formation progresses radially, creating a radial metallicity gradient in the disk. The mass is progressively accumulated at the inner regions of the galaxy, rising the surface mass density and creating the bulge where the metallicity is high and the SFRs are low. This explication can be seen as a combination of two scenarios: the $inside - out$ galaxy disk growth and a local $downsizing$ effect – more massive regions form stars faster, presenting higher SFRs.

Sánchez et al. (2013) studied both local and global $M_* - Z$ relation based on spatially-resolved data, analyzing 150 galaxies with masses higher than $\sim 10^{9.5} M_\odot$ from CALIFA DR1 and exploring relations between stellar mass, oxygen abundance and SFRs. They found a tight direct relation between the integrated stellar mass and the gas-phase metallicity, with a dispersion of $\sim$ 0.07 dex which is inside the typical error derived for their oxygen abundances. However these authors did not found any secondary relation with the SFR, contradicting the results of Mannucci et al.

(2010) and Lara-López et al. (2010) that present a trend for which galaxies with stronger star-formation show lower oxygen abundances for the same mass range. These authors justify this discrepancy by the strong aperture biases that the single aperture spectroscopic technique of the SDSS is subjected. The obtained results are consistent with the $quiescent\ evolution$ scenario in late-type galaxies, in which gas recycling, both locally and globally, is much faster than other typical timescales (Silk, 1993) - like that of the gas accretion by inflow and/or metal loss due to outflows - implying that the galaxies behave locally in a similar manner than globally: they present a radial mass distribution that follows the potential well of the matter, with an inside-out growth that is regulated by gas inflow and local downsizing star-formation. These authors conclude that the dominant parameter that defines the stellar metallicity is the stellar mass.

◦ SFR-Metallicity Relation

There are several studies where it was found an anti-correlation between SFR and Z_N at low mass regime (Yates & Kauffmann, 2014). Ellison et al. (2008a) related the Z_N both with SFR and R_{50} at low mass regimes, finding an anti-correlation between these parameters. The authors justify this trend with the observational fact that more compact galaxies at the present day present lower star formation efficiencies comparing with rapid star formation systems at early times which is believed to consume their cold gas rapidly. In this scenario, the galaxies at high redshift, which present high SFR, are less metallic due to the abundant presence of metal-poor gas. As for the local galaxies, which present lower SFR and had depleted its metal-poor gas, have higher Z_N.

The FMR by Mannucci et al. (2010) justify this observed anti-correlation between SFR and Z_N in low mass regime assuming a scenario where active star forming galaxies will produce stronger galactic winds which will efficiently remove metals from their gravitational potential wells.

In a recent study by Yates, Kauffman & Guo (2012) of SDSS-DR7 galaxies it was also found a reversal in the dependence SFR$-Z_N$ from low to high stellar mass (an anti-correlation between SFR and Z_N in low mass regimes and a direct correlation between this two parameters at high mass regime). They found that at low masses, low SFR galaxies have higher Z_N compared to active star forming galaxies. The authors justify these observations by considering that at low mass regimes, where outflows are more effective on removing the gas of the ISM, low SFR galaxies produce fewer SNe, being less effective in removing their metals. In the high mass

regime, where the outflows become weaker, low SFR galaxies produce less metals comparing with active star forming galaxies in the same mass regime. Summarizing, these authors suggests that the two factors which determine these relations are the galactic outflows and the gravitational potential well of the galactic system. In the low mass regime, the winds are stronger, playing an important role depleting the ISM from metals, due to the low potential well. As for the higher mass regimes, the winds are weaker and the potential wells deeper, being harder to the galactic system to expel its metals to the IGM.

Age-Metallicity Relation

It might seem reasonable to expect the existence of a direct correlation between Z_* and $stellar\ age$ (A_*) of the system, since the older the system, the more available time to create heavier chemical elements and enrich the medium and the stars. But this might not be true, since early systems assembled in a time where the medium was poor in metals, some of them presenting today very low values of Z_*.

There are several studies which tried to proof or disproof the existence of an $A - Z$ relation in galaxy disks, and till today this question is still open to debate. Examples of this disagreement are the studies by Jønch-Sørensen (1995); Meusinger et al. (1991); Twarog (1980), which concluded that the A_* and Z_* of the Milky Way disk stars are tightly correlated (decreasing Z_* with increasing A), and Edvardsson et al. (1993); Feltzing et al. (2001) which found a large scatter in Z_* at all A_*.

As for $A - Z$ studies of galaxies, in the study conducted by Sreedhar et al. (2012) it was suggested that the quantities A_*, Z_* and M_* correlate well between each other: statistically, the low mass galaxies are metal poor and younger, whereas the metal rich galaxies are more massive and older.

One of the most notorious bias in astronomy is the $age\text{-}metallicity\ degeneracy$ (AMD). As the galaxy ages, its colors become redder, due to the migration of it stars to the giant branch and the increasing Z_*. The observable effects of increasing the age can be simulated by decreasing the Z_*: a younger metal-rich system resembles a older metal-poor one, and vice-versa. Worthey (1994) estimated that, in the optical regime, a change of A_* by a factor of 3 corresponds to a change of Z_* by a factor of 2 (what is known by the $3/2$ law).

As one can see, this aspect is till target of debate, presenting very different results in the literature. However, Reis (2014) found an interesting correlation between the mean stellar age and the luminosity-weighted mean stellar metallicity within the bulge: the older stellar populations are more metal-enriched, whereas the young stellar populations are more metal-poor.

On the Estimation of Stellar Metallicities

There are several methods that can be used in order to estimate the $stellar\ metallicity$ (Z_*) in a galaxy. The adopted diagnostic should depend on the chief goal of the study and on the type of the available observational data. Generally, in order to estimate Z_* it is used the absorption lines produced by the different stellar populations that compose the galaxy, since the spectroscopic mark of the Z_* arise mainly in the chromosphere of stars, where the present chemical elements will absorb their specific photons created by the star. It is also known that Z_* is strongly correlated with the luminosity, circular velocity and stellar masses (e.g., Gallazzi et al., 2005; Garnett, 2002; Lequeux et al., 1979; Tremonti et al., 2004), although the physical processes behind this trend are not yet completely understood.

In this work, the observed spectra are fitted using linear combinations of stellar populations with different characteristics – ages and metallicities – by means of the spectral population synthesis code STARLIGHT (Cid Fernandes et al., 2005). Is a Fortran 77 program created to fit an observed spectrum with a model which adds up N_* spectral populations from a pre-defined set of base spectra. The spectral base can be made up of observed templates (e.g., individual stars, globular clusters) or evolutionary synthesis models (Bruzual & Charlot, 2003), individual stars (for e.g. for velocity dispersion estimates, as in Barbosa et al. (2006); Garcia-Rissman et al. (2005); Vega (2004) or whatever might be relevant for the specific application. This code was designed to be as general as possible, permitting to derive properties of the stellar population mixtures, to produce a stellar-template to aid emission line measurements, to estimate velocity dispersions, etc..

In the context of this work, the STARLIGHT code will be used to estimate A_*, Z_* and star formation histories (SFH).

On the Estimation of Gas-Phase Metallicities

As the stellar component, there are a variety of diagnostic methods to estimate the $metallicity\ of\ the\ nebular/gas\ component$ (Z_N) of the galactic system. In this work, in order to estimate Z_N, it is used optical emission lines, which are emitted by the nebular component.

To determine chemical abundances in nebulae, it is often used the oxygen, since beside being one of the most abundant metals, its emission lines are the most notable in the optical spectrum of a HII region (Saviane et al., 2007).

To estimate Z_N one can use empirical methods, which can be direct or statistical, and model fitting methods. The most precise technique to estimate chemical abundances in HII regions is the electron temperature method (T_e), which is empirical and direct. In order to estimate the T_e its required the detection of the [OIII]λ4363 line, which only appears in high excitation spectra of oxygen-rich nebular regions, being weak or unobservable in star forming regions with high Z or/and low excitation (Díaz et al., 2007; Dors et al., 2008).

In the case where it is not possible to detect the [OIII]λ4363 emission with a high signal-to-noise (S/N), one adopts empirical calibrations of strong emission lines which are easily observable - the strong line methods (empirical, statistical) - such as the R_{23}, P, N_2, $O3N2$ and S_{23} methods (Charlot & Longhetti, 2001; Díaz & Pérez-Montero, 2000; Kobulnicky, Kennicutt & Pizagno, 1999; Pagel et al., 1979; Pilyugin et al., 2001; Tremonti et al., 2004; Vílchez & Esteban, 1996). These empirical statistical methods have first been introduced by Pagel et al. (1979) to derive the Z in giant extragalactic HII regions.

Since, in general, the CALIFA data presents lower S/N values for the [OIII]λ4363 emission line, the adopted method used to estimate Z_N was the SLM. To estimate the radial distribution of the $12 + log(O/H)$ it will be used a new semi-empirical metallicity calibration based on CALIFA data from Marino et al. (2013).

One must bear in mind that the obtained Z estimates depend greatly on the elected method. There are studies in the literature which compare the several methods between each other, to understand which are the most reliable (e.g., Hughes, 2010, PhD Thesis).

Metallicity Gradients

A gradient is here defined as the slope of the fitted linear regression to the data that is plotted against the galactocentric radius of the galaxy. It indicates if the quantity is increasing or decreasing from the center to the periphery of the galaxy or of the target component. By studying this parameter one can perceive how physical quantities like age and metallicity are distributed throughout the galactocentric radius, permitting a detailed and spacial analysis of the galaxy.

Sánchez et al. (2013) analyzes $\sim$ 5000 HII regions of 227 galaxies from the CALIFA sample, of different morphological types and evenly distributed along the color-magnitude diagram. Their results show that disk galaxies in the local Universe present a common or characteristic gradient in the oxygen abundance of $\alpha_{O/H} = -0.1$ dex/r_e up to $\sim$ 2 disk effective radii - with a small dispersion which is compatible with being produced by random fluctuations - and a flattening of the abundance gradient at the outer regions. The trend is independent of the morphological type, presence or absence of bars, absolute magnitude and/or stellar mass, deviating from the common slope only for galaxies with evident interaction or undergoing mergers, which present a clearly flatter oxygen abundance distribution in agreement with the results obtained by Kewley et al. (2010) and Rich et al. (2012), indicating that these dynamical processes can effectively mix the metals. These authors conclude that the common slope suggests that the chemical evolution of galaxies is very similar in all disk galaxies, being compatible with a "modified" closed-box model, in which the disk is formed via continuous accretion of gas, driven by the gravitational force. In this scenario, both stellar mass and chemical enrichment would be proportional to the time for a given halo mass, assuming the amount of primordial gas is proportional to the depth of the potential well and the efficiency of the SFR is the same for all galaxies. Under this assumption all galaxies should present an universal gradient of their oxygen abundance with its zero-point proportional to the total mass. As for the flattening in the outer regions – which is also an universal property of disk galaxies – these authors suggest that it is related to secular evolution of galaxies, involving processes like radial migration or the capture of evolved satellite galaxies. They also present observational evidence for a decrease of the oxygen abundance in the central region of some particular galaxies, being more frequent in non-barred systems and absent in interacting galaxies. The authors justify this effect by associating the drop in oxygen abundance with central

star-forming rings, where the radial flow of gas induced by resonances in the disk pattern speed would produce both features.

1.3 IFU SPECTROSCOPY

The traditional long-slit or single-fiber spectroscopic analysis is based on single aperture or long-slit spectroscopy, where the object is observed through a single fiber or an elongated slit aperture, respectively. When the object of study is a galaxy, the slit is usually centered at the galaxy's nucleus, losing most of the area of the galaxy, allowing only a fraction of the light to pass through. Obviously this technique has some limitations when it comes to galactic systems analysis (specially spiral galaxies which are disk-like systems and very heterogeneous), since it disregards the external parts of the galaxy. Furthermore, these techniques are subjected to aperture effects due to the limited - and z dependent - coverage of the individual galaxies, causing a lost of a significant fraction of the total flux at all wavelengths. Several studies of aperture effects have been carried out (e.g., Brinchmann et al., 2004; Ellis et al., 2005; Gerssen et al., 2012; Hopkins et al., 2013; Iglésias-Páramo et al., 2013; Kewley et al., 2005; Kronberger et al., 2008; Salim et al., 2007; Zahid et al., 2013), but there is still no satisfactory recipe to correct the data for this effect. The unwanted effect is produced by two main issues: the size of the projection on the sky of the aperture relative to the physical dimensions of the galaxy and the precise position of the aperture relative to the galactic center, which will affect spectral stacking studies, since the fraction of a galaxy covered by a fixed aperture varies with z. In the study carried out by Gerssen et al. (2012), it was analyzed a reduced SDSS star-forming galaxies sample using the VIMOS integral field spectrograph (Le Fèvre et al., 2003) to map some properties related to star formation diagnostics. The authors found a large dispersion when comparing their results with color-based SDSS extrapolations, suggesting that full spatial coverage is essential to produce proper corrections for emission-line intensities. Iglésias-Páramo et al. (2013) investigates the aperture size effect on derived galaxy properties for 104 spiral galaxies from the CALIFA survey. They found the Hα flux (f(Hα)) growth curve follows a well defined sequence with aperture radius showing low dispersion around the median value. Taking properly into account the stellar absorption, they

found that the $f(\mathrm{H}\alpha)/f(\mathrm{H}\beta)$ ratio growth curve shows a smooth decline, pointing towards the absence of differential dust attenuation as a function of radius. They also found that the $EW(\mathrm{H}\alpha)$ growth curve increases with the size of the aperture and shows a very large dispersion for small apertures, preventing the use of reliable aperture corrections for this specific quantity. This result suggests that by using the $EW(\mathrm{H}\alpha)$ observed through small apertures to classify the galaxies into star-forming/quiescent, will likely result in low $EW(\mathrm{H}\alpha)$ star-forming galaxies to be wrongly classified as quiescent.

Integral Field Unit (IFU) spectroscopy - also known as IFS - attempts to solve the main disadvantages of the traditional spectroscopy. These new instruments permits to gather several spectra of the sky over a two-dimensional field of view, usually producing a data-cube with three axes (x, y and z), where x and y regards to the spacial axes (RA and Dec) and z the observed wavelength. This new technology permits to obtain spatially resolved spectra, allowing to study galactic systems with a precision never archived before. It produces a spectrum for every spatial pixel (spaxel) allowing for the astronomers to gather detailed information over that particular area of the object. However, IFS techniques are subjected to resolution limitations. Mast et al. (2014) analyzes how the information loss due to spatial resolution degradation will affect an hypothetical IFS survey at higher z. They use a sample of five PINGS galaxies (Z0, $z \leq 0.0025$) and simulated two z regimes - one associated with the ongoing CALIFA survey (Z1, $0.003 \leq z \leq 0.014$) and the other with an hypothetical higher z survey (Z2, $0.01 \leq z \leq 0.06$) - without taking into account the surface brightness dimming or increase of noise. They study the behavior of the radial metal abundance (O3N2), BPT diagrams, D4000, Hα emission and the morphology. These authors found that Z1 is able to reproduce all morphological signatures visible at lower z, despite the loss of details, but not Z2, where the identification of morphological features is only possible when is a global scale feature; in Z1 only 1/3 of the original HII regions from Z0 are detectable, while in Z2 only $\sim$ 1/15 of Z0 HII regions where detected; Z1 is able to reproduce with acceptable accuracy the shape of the Z0 BTP and in Z2 only the most populated regions of the lower z regime are mapped; the flat inner part of the abundance distribution presented in the Z0 galaxies is observable in Z1 and Z2, although with smoothed values; Z1 is capable of reproducing the fine structure of the Z0 D4000 distributions. As a global conclusion, these authors show that the information loss will depend

on the level of detail contained in the analyzed feature. They conclude that the CALIFA survey will be able to analyze to an acceptable scale, with a good level of detail, all desired magnitudes, permitting a robust characterization of the local Universe.

In order to conduct this study, it is going to be used IFU data, specifically from the CALIFA Survey, as the spectroscopic data and SDSS-DR7 data as photometric data.

Chapter 2.

The Galaxy Sample

The chosen sample is composed of 66 face-on and/or nearly face-on spiral galaxies observed by the CALIFA Survey. They were selected by Sandra Reis – who is working at CAUP under Jean Michel supervision, doing research on PB with main focus on their stellar ages – from the 337 observed CALIFA galaxies early on 2014. The selection criteria, which are specified in detail in Reis (2014, Msc Thesis), are focused on selecting face-on, late-type galaxies without AGN in their nuclei. In the Table 2.1 it is presented, for each galaxy of the sample, the most common name, examples of surveys in which the galaxy was observed that were considered relevant, right ascension and declination, redshift, distance in Mpc, morphological classification as published in NED, activity type, inclination in degrees, foreground galactic extinction in mag in the V band and computed absolute magnitude in the r-band within the extinction corrected 24 mag/arcsec^2. The specifications were obtained in the NED database. The inclination was computed based on the galactic major and minor axis, available in the NED database, by applying the following equation (see e.g., Sánchez et al., 2013)[1]:

$$i = \arccos^{1/2}\left(\frac{1-q^2-\varepsilon^2}{1-q^2}\right), \tag{2.1}$$

[1] The paper has a small error in the median ellipticity (ε), equation 3: $\varepsilon^2 = 1-(b/a)^2$.

where,

i – inclination,

$\varepsilon^2 = 1 - (b/a)^2$ – median ellipticity where a and b are the semi-major and minor axis of the galaxy, r

$q = 0.13$ – intrinsic ellipticity for galaxies (Giovanelli et al., 1995, 1997)

CALIFA Survey

The Calar Alto Legacy Integral Field Area Survey (Sánchez et al., 2012a, hereafter S12) is an large-scale project which is conducted at Centro Astronómico Hispano-Alemán at the Calar Alto Observatory. By the end of the project, the Survey will comprise integral field spectroscopic data of 600 local galaxies ($0.005 \leq z \leq 0.03$) which where observed with the $Potsdam\ Multi\ Aperture\ Spectrograph$ (PMAS, Roth et al., 2005), mounted to the 3.5 m telescope, utilizing the large (74" x 64") hexagonal field-of-view (FoV) offered by the PPak fiber bundle (Kelz et al., 2006; Verheijen et al., 2004). Two spectral setups are available for each observed galaxy: V500 - low-resolution setup covering the nominal wavelength from 3745 to 7500 Å, with a spectral resolution of 6.0 Å(FWHM) - and V1200 - medium-resolution setup covering the nominal wavelength range 3650 to 4840 Å, with a spectral resolution of 2.3 Å(FWHM). The median limiting continuum sensitivity of the data corresponds to a surface brightness of 23.6 mag/arcsec^2 in the r band for the V500 setup and 23.4 mag/arcsec^2 in the g band for the V1200 setup. The CALIFA mother sample (MS) comprises galaxies with a wide range of properties, covering different morphological types as elliptical, lenticular, spiral and ongoing mergers. The galaxies were selected from the SDSS DR7 photometric catalog in order to fulfill certain characteristics, being the main feature of this sample that it has been selected by diameter to fill the field of view of the IFU. The observed sample is a randomly selected subset of the MS, sharing all its properties. Walcher et al. (2014) describe the statistical properties of the MS: it is representative of the Hubble-type galaxy population with -19.0 to -23.1 as absolute magnitude limits for the r-band, 1.7 to 11.5 kpc in half light radii and 9.7 to 11.4 in $\log(M_*/M_\odot)$; more than 97% of the CALIFA galaxies are covered out to more than $2R_{50}$ at a typical mean spatial resolution of 1kpc; the sample covers all environments, from isolated to interacting merging galaxies; the final observed sample will contain approximately 30 Seyfert galaxies. Hereupon, this survey offers an excellent opportunity to extend our understanding on

galactic physical properties, and shed some light on the broader context of galactic evolution. The data is distributed within the CALIFA collaboration in regular public data releases, after being processed with the CALIFA IFS reduction pipeline (now v1.3c), that calibrates the flux to a precision better than $\sim 15\%$, corrects for foreground Galactic extinction (Husemann et al., 2013) and render information about error statistics for each spaxel and a detailed quality control. Some of the studies the CALIFA collaboration has performed in its first science publication in K12 are dedicated to, e.g., aperture effects (Iglésias-Páramo et al., 2013) and the spatial resolution of IFS data (Mast et al., 2013), stellar age gradients in galaxies (González-Delgado et al., 2014; Pérez et al., 2013; Sánchez-Blázquez et al., 2014) and the uncertainties in their determination from spectral fitting (Cid Fernandes et al., 2014), the mass-metallicity relation (Sánchez et al., 2013), the presence of universal metallicity gradients in galaxies (Sánchez et al., 2014b; Sánchez, 2014a), the spatial distribution and excitation mechanisms of nebular emission in ETGs and other LINER galaxies (Singh et al., 2013, P13), stellar and gas kinematics (Barrera-Ballesteros et al., 2014; Falcón-Barroso et al., 2014; García-Lorenzo et al., 2013) and devised a new semi-empirical metallicity calibration based on the largest hitherto compiled sample of HII regions in late-type galaxies (Marino et al., 2013) that is going to be used in this work to derive nebular metalicities.

In this work it will be used the low resolution V500 datacubes, since it covers the entire optical spectral range.

Table 2.1: It is listed – from left to right – galaxy name, relevant surveys where the galaxy is included, right ascension, declination, distance in Mpc, morphological class, activity, inclination, Galactic extinction in the V-band and r-band total absolute magnitude

Galaxy	Surveys	RA	DEC	z	Distance	Morph. Class.	Activity	Inclination	Gal. Ext. V-band	r-band Abs. mag
IC0776	HIPASS J121ALFA 3-21	12h19m02.90s	+08d51m22.0s	0.008232	40.20	Sdm	HII	62.76	0.06	-18.96
IC1256	KIG; UZC	17h23m47.31s	+26d29m11.5s	0.015778	72.10	Sb	-	59.78	0.13	-21.15
IC4566	USGC	15h36m42.16s	+43d32m21.6s	0.01926	86.30	Sab	-	59.23	0.07	-21.71
NGC0001	ALFALFA; KPG	00h07m15.84s	+27d42m29.1s	0.015177	61.60	SA(s)b:	-	56.79	0.17	-21.43
NGC0023	ALFALFA; KUG	00h09m53.41s	+25d55m25.6s	0.015231	61.70	SB(s)a	Sbrst	62.48	0.11	-22.28
NGC0160	UZC	00h36m04.06s	+23d57m28.4s	0.017525	70.50	(R)SA0$^+$ pec	-	64.22	0.09	-21.96
NGC0165	NVSS	00h36m28.92s	-10d06m22.2s	0.019617	78.90	SB(rs)bc	-	56.41	0.10	-21.35
NGC0171	HIPASS; VV	00h37m21.53s	-19d56m03.3s	0.013043	52.80	SB(r)ab	-	45.01	0.06	-21.67
NGC0180	HIPASS	00h37m57.70s	+08d38m06.7s	0.017616	70.60	SB(rs)bc	-	54.41	0.15	-22.11
NGC0214	ALFALFA; CXO	00h41m28.03s	+25d29m58.0s	0.015134	61.00	SAB(r)c	-	57.47	0.10	-22.04
NGC0237	HIPASS; GALEXASC ; [VCV2006]	00h43m27.84s	-00d07m29.7s	0.013926	55.90	SAB(rs)cd	Sy?; LINER	64.35	0.05	-20.88
NGC0257	NVSS; GALEXASC	00h48m01.51s	+08d17m49.5s	0.017592	70.40	Scd:	-	59.93	0.16	-22.00
NGC0477	NVSS	01h21m20.37s	+40d29m17.5s	0.0196	79.10	SAB(s)c	-	64.86	0.15	-21.47
NGC0776	NVSS J015954+233839; UZC	01h59m54.49s	+23d38m39.8s	0.016415	65.50	SAB(rs)b	-	54.89	0.27	-21.81
NGC1093	NVSS; UZC	02h48m16.15s	+34d25m11.2s	0.017646	70.80	SABab?	-	62.76	0.24	-21.40
NGC1645	GALEXASC	04h44m06.38s	-05d27m56.2s	0.016345	65.90	(R')SB0$^+$(rs) pec	-	67.67	0.15	-21.67
NGC2253	NVSS; [RC2]	06h43m41.84s	+65d12m22.6s	0.011885	51.30	Scd:	-	57.65	0.19	-21.44
NGC2347	MRK; NVSS; KPG	07h16m03.69s	+64d42m32.1s	0.014747	63.00	(R')SA(r)b:	-	58.20	0.22	-21.89
NGC2639	[VCV2001]; CXO; NVSS	08h43m38.08s	+50d12m20.0s	0.011128	49.60	(R)SA(r)a:?	LINER; Sy1.9	61.65	0.07	-22.09
NGC2730	NVSS	09h02m15.83s	+16d50m17.9s	0.012782	56.70	SBdm:	-	55.99	0.08	-20.66
NGC2906	NVSS; UZC	09h32m06.22s	+08d26m30.4s	0.007138	33.50	Scd:	-	61.60	0.13	-20.71
NGC2916	HIPASS; UZC	09h34m57.60s	+21d42m19.0s	0.012442	56.00	SA(rs)b?	-	64.23	0.07	-21.91
NGC3057	DDO; UZC	10h05m39.36s	+80d17m08.5s	0.005084	25.90	SB(s)dm	-	63.44	0.07	-18.81
NGC3300	GALEXASC; UZC	10h36m38.44s	+14d10m16.0s	0.01027	48.00	SAB(r)0^0:?	-	66.04	0.10	-21.27
NGC3381	[BKD2008]; NVSS	10h48m24.82s	+34d42m41.1s	0.005434	28.80	SB pec	WR; HII	36.58	0.06	-19.83
NGC3614	GALEXASC; UZC	11h18m21.32s	+45d44m53.6s	0.007782	38.40	SAB(r)c	-	64.60	0.04	-20.79

Table 2.1 Continued.

NGC3687	MRK; GALEXASC	11h28m00.61s	+29d30m39.8s	0.008362	41.10	(R')SAB(r)bc?	-	53.39	0.06	-20.66
NGC4003	NVSS; GALEXASC; KPG	11h57m59.04s	+23d07m29.6s	0.021712	96.60	SB0	-	63.14	0.07	-21.77
NGC4047	NVSS; GALEXASC	12h02m50.68s	+48d38m10.3s	0.011375	53.30	(R)SA(rs)b:	-	57.65	0.06	-21.67
NGC4185	HIJASS; UZC	12h13m22.20s	+28d30m39.5s	0.013022	61.00	Sbc	-	57.78	0.06	-21.67
NGC4210	NVSS; UZC	12h15m15.83s	+65d59m07.2s	0.009113	43.20	SB(r)b	-	60.66	0.05	-20.83
NGC4961	FAUST; [MO2001]; NFGS	13h05m47.57s	+27d44m02.9s	0.008456	42.50	SB(s)cd	-	59.78	0.03	-19.99
NGC5000	GALEXASC; FIRST; VV; ABELL	13h09m47.49s	+28d54m25.0s	0.018706	84.90	SB(rs)bc	Sbrst	59.35	0.02	-21.45
NGC5016	HIPASS; KIG	13h12m06.68s	+24d05m42.0s	0.008713	43.50	SAB(rs)c	SBNG	55.99	0.04	-20.86
NGC5205	UZC	13h30m03.58s	+62d30m41.7s	0.005891	30.90	Sbc	-	65.28	0.06	-19.89
NGC5320	UZC	13h50m20.38s	+41d21m58.4s	0.008736	43.60	SAB(rs)c:	-	66.11	0.02	-20.85
NGC5378	UZC-CG	13h56m51.02s	+37d47m50.1s	0.010147	49.60	(R')SB(r)a	-	53.80	0.04	-21.10
NGC5406	GALEXASC; NVSS	14h00m20.12s	+38d54m55.5s	0.017352	79.00	SAB(rs)bc	-	65.04	0.03	-22.32
NGC5480	NVSS; KPG	14h06m21.58s	+50d43m30.4s	0.006191	32.90	SA(s)c:	-	56.87	0.05	-20.54
NGC5614	FIRST; VV; ARP	14h24m07.59s	+34d51m31.9s	0.012982	61.40	SA(r)ab pec	-	57.60	0.04	-22.41
NGC5656	GALEXASC ; NVSS	14h30m25.51s	+35d19m15.7s	0.010551	51.40	Saab	LINER	60.33	0.04	-21.45
NGC5735	UZC	14h42m33.24s	+28d43m35.2s	0.012482	59.60	SB(rs)bc	-	54.41	0.05	-21.18
NGC5772	GALEXASC; FIRST; KIG	14h51m38.88s	+40d35m57.0s	0.016345	74.80	SA(r)b:	-	66.31	0.05	-22.00
NGC5829	HIPASS; ARP; HCG	15h02m42.01s	+23d20m01.0s	0.018797	85.80	SA(s)c	HII	58.62	0.12	-21.35
NGC6004	UZC	15h50m22.72s	+18d56m21.4s	0.012762	60.80	SAB(rs)bc	-	46.13	0.11	-21.68
NGC6032	[WB92]; UZC	16h03m01.12s	+20d57m21.4s	0.014283	67.00	SB(rs)b:	-	66.80	0.25	-21.13
NGC6154	UZC	16h25m30.48s	+49d50m24.9s	0.020064	88.70	SB(r)a	-	55.77	0.06	-21.79
NGC6186	GALEXASC; ADBS	16h34m25.48s	+21d32m27.2s	0.009797	48.10	(R')SB(s)a	-	66.48	0.13	-21.11
NGC6278	CXO; GALEXASC	17h00m50.33s	+23d00m39.7s	0.009447	45.80	S0	-	67.19	0.17	-21.45
NGC6941	HIPASS; NVSS	20h36m23.47s	-04d37m07.5s	0.020761	88.60	SAB(rs)b	-	62.51	0.17	-22.22
NGC7321	NVSS	22h36m28.02s	+21d37m18.5s	0.023833	97.90	SB(r)b	-	59.78	0.13	-22.32
NGC7489	NVSS; UZC	23h07m32.71s	+22d59m52.8s	0.020811	85.10	Sd	-	65.47	0.63	-22.27
NGC7625	1WGA; NVSS; VV; ARP; CGPG	23h20m30.13s	+17d13m32.0s	0.005447	23.70	SA(rs)a pec	HII	48.11	0.07	-20.14

Table 2.1 Continued.

NGC7653	TXS; GALEXASC	23h24m49.36s	+15d16m32.1s	0.014227	58.30	Sb	-	56.87	0.18	-21.50
NGC7691	UZC	23h32m24.42s	+15d50m52.2s	0.013479	55.20	SAB(rs)bc	-	56.87	0.17	-21.01
NGC7716	HIPASS; KIG	23h36m31.45s	+00d17m50.2s	0.008604	35.60	SAB(r)b:	-	49.69	0.09	-20.79
NGC7738	2XMM; NVSS; KIG	23h44m02.06s	+00d30m59.9s	0.022556	91.40	SB(rs)b	-	69.79	0.07	-21.86
NGC7819	NVSS; KUG	00h04m24.54s	+31d28m19.4s	0.016538	67.20	SB(s)b	HII	53.88	0.16	-20.83
UGC07012	KUG; UZC	12h02m03.15s	+29d50m52.8s	0.010277	49.40	Scd:	-	65.32	0.06	-19.62
UGC08234	UZC; [RC2]	13h08m46.49s	+62d16m18.2s	0.027025	116.10	S0/a	-	69.07	0.04	-22.60
UGC08733	UZC	13h48m38.90s	+43d24m44.6s	0.007799	39.70	Sbcd:	Sbrst	61.24	0.05	-19.33
UGC09067	NVSS; GALEXASC	14h10m45.46s	+15d12m33.9s	0.026151	116.30	Sab	-	66.11	0.05	-21.69
UGC09291	LCSB; UZC	14h28m36.89s	+38d59m56.9s	0.009657	47.60	Sd	-	67.48	0.04	-20.29
UGC09476	UZC; KPG	14h41m32.02s	+44d30m45.9s	0.010881	52.30	SAB(rs)c	-	63.42	0.05	-20.75
UGC10796	KUG; UZC	17h16m47.73s	+61d55m12.5s	0.010271	48.00	SB(s)b	-	68.62	0.05	-19.28
UGC12224	HIPASS; GALEXASC; KIG	22h52m38.30s	+06d05m37.2s	0.011695	48.70	Scd:	-	45.01	0.24	-20.63

Chapter 3.

Adopted Methodology

This Chapter is dedicated to the detailed explanation of the methodology adopted to achieve the goals defined for this MSc project, with special attention on the surface photometry techniques, since they were developed in the context of this work. Almost the totality of the data analysis was conducted by using several stand-alone routines that were written both in ESO-MIDAS and Fortran 90 scripts, that are combined into a surface photometry code. The 66 galaxies selected from the CALIFA sample were submitted to an intense analysis, were the ultimate goal is to understand what is behind the nature of their bulges.

3.1 PHOTOMETRIC DATA

The photometric analysis was done by using data from the SDSS-DR7, giving greater emphasis on the r band (from the five SDSS filters, the r band is the one with higher filter transmission and that includes the $H\alpha$ emission-line). The main purpose is to decompose the galaxies of the sample in its main components, in order to study them individually. The developed code allows to divide the $surface\ brightness\ profile$ (SBP) of the object into its three main components – bulge, bar and disk. These physical components will then be studied separately by estimating a series of structural parameters – a list of all of the structural parameters that where estimated is presented in Tables 5.1 and 5.2.

Photometric Data Reduction

Data reduction transforms raw images taken by the telescopes into calibrated images free from instrumental signatures and artifacts. It involves the removal of instrumental signatures (e.g., bias, flatfield), masking unwanted signals (e.g., cosmic rays, hot/cold pixels) and the application of photometric and astrometric calibrations.

The used fits from SDSS-DR7 were already corrected, having been bias subtracted, flat-fielded, sky-fitted and with bad pixels replaced by interpolated values. To complete the full reduction, the images were subtracted from the sky contribution, rotated according to the camera position angle with respect to the North, corrected from the Galactic extinction produced by the Milky Way (the correction values were acquired in the NED database for each galaxy – Schlafly & Finkbeiner (2011), recalibration of the Schlegel, Finkbeiner & Davis (1998)) co-aligned and background subtracted. The co-alignment of the images in the three photometric bands was done by matching the gaussian center of at least three Galactic bright stars that were previously chosen in each of the three images, and align them relatively to the g-band image. Finally the images were corrected for the presence of some external light sources – like contaminating stars of the Milky Way – by substituting the projected area of the undesired light source on the image by the closest uncontaminated area (see Reis, 2014, MSc Thesis for full explanation).

Photometric Decomposition

The total SBP of the galaxy is computed by fitting ellipses to the isophotes of the object (in a 2D frame). The algorithm is based on the formulas of Bender & Moellenhoff (1987). Applying equation 3.1, the flux will be converted into surface brightness units – surface brightness [mag/arcsec^2] versus the photometric radius R [arcsec] within the galaxy:

$$\mu(R) = -2.5 \log_{10} \left(\frac{k(R)}{S^2} \right) + C, \tag{3.1}$$

where,

$\mu(R)$ - surface brightness at radius R [mag/arcsec^2],
$k(R)$ - isophote levels for each radius R [mag/pixel^2],
S - natural scale of SDSS = 0.396127 arcsec/pixel,
C - constant which is the subtraction between the calibration constant [mag] and the galactic extinction for the SDSS photometric bands [mag] from Schlafly & Finkbeiner (2011).

To convert the data into counts, it is used the following equation:

$$I(R) = 2\pi R 10^{[(\mu(R)-C)/-2.5]}, \tag{3.2}$$

where,

$I(R)$ – intensity of the flux at radius R [counts].

In order to integrate the SBP, one will use a spline transformation by applying a 4^{th} order polynomial regression to the data. By applying this transformation one will have the distribution of light throughout the photometric radius of the object. The next step is to integrate this distribution which is already in a polynomial form:

$$\begin{aligned} I_{tot} &= 2\pi \int_0^{R_{max}} RI(R)dR \\ &= \int_0^{R_{max}} a + bR + cR^2 + dR^3 dR \\ &= aR_{max} + \tfrac{b}{2}R_{max}^2 + \tfrac{c}{3}R_{max}^3 + \tfrac{b}{4}R_{max}^4, \end{aligned} \tag{3.3}$$

where,

I_{tot} – total integrated flux of the SBP [$counts$],

a, b, c, d – coefficients of the polynomial regression,

R_{max} – maximum radius of the SBP.

To convert the I_{tot} into apparent magnitude, one should use the following equation:

$$m_{tot} = -2.5 \log_{10}(I_{tot}) + C, \tag{3.4}$$

and for the absolute magnitude:

$$M_{tot} = m_{tot} - 5(\log_{10}(D_L) - 1), \tag{3.5}$$

where,

m_{tot} – apparent magnitude of the total integrated flux of the SBP [mag],

M_{tot} – absolute magnitude of the total integrated flux of the SBP [mag],

D_L – galaxy's luminosity distance [parsec].

To note that in this work, all of the estimated magnitudes were obtained by integrating the SBP to 24 mag/arcsec^2, which is a proxy to the limiting surface brightness of the SDSS before the errors become prohibiting large.

By using this approach, parameters like R_{20}, R_{50}, and R_{90} – which are the photometric radii that include 20, 50, 80 and 90 $\%$ of the total flux of the SBP, respectively – and μ_{20}, μ_{50}, μ_{90} – the values for the surface brightness at each of this radii – are easily estimated.

This methodology will be applied not only for the total SBP of the galaxy, but also to its individual components, permitting to estimate the aforementioned physical quantities for the bulge, bar and

disk, separately. In the simplest case, the SBPs of galaxies are decomposed into $bulge + disk$. When an additional bar-feature is evident in the SBP after removing the disk component, the SBP will be decomposed into $bulge + bar + disk$.

Surface Brightness Profile of the Disk

Freeman (1970) was the pioneer in the investigation of disk parameters. He concluded that the disk's light profile is generally represented by an exponential law – the Sérsic model with $\eta = 1$ – in agreement with the results obtained by de Vaucouleurs (1959) – the reasons for this behavior are not yet clearly understood:

$$I(R) = I_0 \exp\left(-\frac{R}{\alpha}\right), \tag{3.6}$$

where,

- $I(R)$ – intensity of the flux in the disk component [counts],
- I_0 – intensity of the flux of the disk in the center of the galaxy [counts],
- α – scale length of the disk [arcsec].

Although the exponential law is usually a good approximation of the SBP of the galactic disk, in some cases, in the outer regions of the disk, it is possible to identify a radial truncation of the SBP. Many authors have discussed about what can be the origin of this radial truncation. Among many distinct hypothesis: it is possible that star formation is regulated by disk instabilities (Kennicutt, 1989), and the truncation radius is where the density of the gas drops to a critical value for star formation – which is consistent with the dependence on density of the SFR (e.g., Schmidt, 1959). Pohlen & Trujillo (2006) propose a scheme of three classes according to the light distribution in the outer regions of disks: Type I show a single untruncated exponential disk out to the limit of the photometry; Type II present an inner exponential disk breaking to a steeper exponential disk in the outer regions; Type III present two exponential components and the outer component has a higher α than the inner. Erwin et al. (2008) presents a truncated exponential function which was

designed to fit the SBP of disks which are not single exponential. This new function is similar to the original exponential function, but it has two exponential radial zones with different α, joined by a transition region at R_b of variable sharpness:

$$I(R) = SI_0^{-R/h_1}[1+^{\alpha(R-R_b)}]^{\frac{1}{\alpha}(\frac{1}{h_1}-\frac{1}{h_2})}, \tag{3.7}$$

where,

$S = (1+\exp^{-\alpha R_b})^{-\frac{1}{\alpha}(\frac{1}{h_1}-\frac{1}{h_2})}$	–	scaling factor,
$h_1 and h_2$	–	inner and outer scale lengths of the disk [arcsec],
R_b	–	break radius [arcsec],
α	–	parameterizes the sharpness of the break [arcsec].

Another example of a modified exponential function was developed by Papaderos et al. (1996a) to describe the SBPs of $blue\ compact\ dwarfs$ (BCDs) with a central flattened exponential light distribution:

$$I(R) = I_0^{\left(-\frac{R}{\alpha}\right)}(1-q^{-P_3(R)}), \tag{3.8}$$

where,

$P_3(R) = \left(\frac{R}{b\alpha}\right)^3 + \left(\frac{R}{\alpha}\frac{1-q}{q}\right)$,

$q = \delta I/I_0$,

$b = 3q$.

The intensity of the flux per unit of area and the surface brightness are interconnected, which is evident making use of equation 3.4. Applying this logaritmization, it is obtained a linear relation

between the surface brightness and the photometric radius:

$$\mu(R) = \mu_0 + \frac{2.5}{ln(10)}\frac{R}{\alpha} + C, \tag{3.9}$$

where,

$\mu_0 = -(2.5/ln(10))\log_{10}(I_0)$ – surface brightness of the disk at the center of the galaxy.

The code will ask the user to choose the radial range that is going to be used to fit the disk exponential profile, simultaneously presenting the color map $r - i$ for that SBP. By interactively choosing the radius range in the disk where the color gradients become minimal, and the colors level off to a nearly constant value, one can obtain a reasonable estimate on the galactocentric radius beyond which the disk component dominates. The next step is to do a linear regression between the surface brightness and respective radius of the points that lie in the selected range, obtaining:

$$y(x) = b + mx, \tag{3.10}$$

where,

$y(x) = \mu(R)$

$b = \mu_0 + C$

$m = 2.5/ln(10)\alpha$

At this point it is obtained the surface brightness of the disk at the center of the galaxy and the scale length of the disk component. By subtracting the modeled disk from the observed SBP, it will remain the excess flux, corresponding to the emission of $bar + bulge$ or only $bulge$.

It is important to notice that the SBP of the disk can deviate from the exponential law in the presence of extended extranuclear star-forming zones, which introduce significant uncertainties in the disk fitting process. To estimate the real continuum emission of the disk it is adopted an innovative approach that combines spectroscopic and photometric techniques. The spectral synthesis analysis code called $RemoveYoung$ (Gomes et al. in prep.) permits to remove from the IFU spectra the light contribution of young stellar populations – in this work, it was adopted a cut of age of $A_* \leq 30\text{x}10^6$ years – by using SPSC to compute the SFH spaxel-by-spaxel, and translate it to how much magnitudes the total SBP should be scaled down in order to obtain the real continuum emission, without the contamination of prominent active star forming regions.

SBP of the Bar

According to some published studies, $\sim 50\%$ of the nearby disk galaxies in the optical (Aguerri et al., 2008; Barazza et al., 2008; Marinova & Jogee, 2007) and $\sim 70\%$ in the near infrared (Eskridge et al., 2000; Menéndez-Delmestre et al., 2007) host a bar. In order to perform a robust photometrical decomposition and derive structural parameters, it is imperative to take it into account.

After removing the disk, when a bar-feature is evident within the excess emission, one should fit a low η – ≤ 0.4 – Sérsic model to account for this extra component. In surface brightness units the Sérsic equation will have the form:

$$\mu(R) = \mu_0 + \frac{2.5}{ln(10)} \left(\frac{R}{\beta}\right)^{1/\eta}, \tag{3.11}$$

where,

β – pseudo scale-length.

Providing a radial range for the bar-feature, the code will compute the free parameters of the equation by interactively doing linear regressions between the observed $\mu(R)$ and $R^{1/\eta}$, adopting

different values for η in each iteration. It will assume as the right η the one which provides the lower $standard\ error\ of\ constant\ term$ for the linear regression. Once it converges, the modeled bar will be subtracted to the remaining excess emission – the total SBP subtracted by the modeled disk. After this process, one will have the emission of the bulge component.

SBP of the Bulge

The Sérsic model - in surface brightness units - can also be written as:

$$\mu(R) = \mu_{mod} + \frac{2.5 b_\eta}{ln(10)} \left[\left(\frac{R}{R_{mod}} \right)^{1/\eta} - 1 \right], \tag{3.12}$$

where,

R_{mod} - photometric radius that encloses 50 % of the total emitted light when the SBP is integrated to infinity,
μ_{mod} - surface brightness at R_{mod} when the SBP is integrated to infinity,
b_η - the value of b_η is such that $\Gamma(2\eta) = 2\gamma(2\eta, b_\eta)$ with Γ and γ being the incomplete and complete gamma functions, respectively (Ciotti, 1991). This way its ensured that the radius R_{mod} encloses half of the total luminosity of the SBP. It was addopted $b_\eta = 1.9992\eta - 0.3271$.

The traditional method invoked to estimate the η of a SBP – total or of an individual component – follows the methodology aforementioned adopted for the bar component. However, this procedure has many flaws concerning the stability and robust estimation of the parameters from the Sérsic model. Some of the deficiencies of Sérsic fits that can be found in the literature are related to the degeneracy between η and the pseudo-scale length β in equation 2.9 (e.g., Lang et al., 2014; Noeske et al., 2003). Papaderos & Östlin (2012) have shown that the superposition of two exponentials with different μ_0 and β can perfectly reproduce a Sérsic model with a high (> 3) η, and that the derived η increases with the limiting surface brightness the SBP is fitted; the central points of the SBP (with high seeing) strongly affects both 1D and 2D surface photometry techniques based in the χ^2 minimization.

Driven by the necessity of estimating stable and precise Sérsic parameters for the bulge component, it was developed an alternative approach that overcomes some of these problems, specially with regard to the $\eta - \beta$ degeneracy.

In equation 3.11 the Sérsic model is rewritten into a form that is dependent on the physical quantities R_{mod} and μ_{mod} of the SBP of the bulge component. By integrating the SBP of the bulge as explained in the beginning of the section, one will get the physical quantities integrated to the maximum photometic radius of the galaxy (R_{50} and μ_{50}) or some previously chosen radius. Graham et al. (2005) shows that for $0.1 < \eta < 10$, R_{mod} can be approximated in terms of Petrosian concentration by the expression:

$$R_{mod} \sim \frac{R_{50}}{1 - P_3(R_{90}/R_{50})^{P_4}}, \tag{3.13}$$

where,

$P_3 = 8.0\text{x}10^{-6}$,
$P_4 = 8.47$,
R_{50} and R_{90} - the photometric radius that encloses 50 and 90 % of the total light of the SBP integrated to $2R_p$, where R_p is the Petrosian radius with $\eta_p = 5$, being η_p the Petrosian index (this R_p encloses about 90 % of the total light of the SBP).

Using equation 3.12 it is possible to estimate the effective radius of the SBP if integrated to infinity, and the corresponding surface brightness, fixing two of the tree free parameters of the Sérsic model.

Substituting R per R_{50} in equation 3.11 one obtains:

$$\Delta\mu_{mod} = \mu_{50} - \mu_{mod} = \frac{2.5b_\eta}{ln(10)} \left[\left(\frac{R_{50}}{R_{mod}} \right)^{1/\eta} - 1 \right]. \tag{3.14}$$

The former equation allows to estimate the theoretical difference between the observed surface brightness at R_{50} and the model surface brightness at R_{mod}. The code will then compute the difference between the two estimated quantities μ_{50} and μ_{mod} ($\Delta\mu_{obs}$), and the theoretical difference $\Delta\mu_{mod}$, using R_{50} and R_{mod}, for all the possible range of η:

$$\xi = \Delta\mu_{mod} - \Delta\mu_{obs}. \tag{3.15}$$

The η that produces the closest values between the theoretical and observed quantities – the absolute minimum of ξ – is assumed to be the one that will correctly model the data. To identify it, the code will look for the η for which the derivative of ξ relative to η changes its sign.

By using this approach, the user does not need to chose points to fit the data; after the subtraction of the other components, the user will be prompted to choose the physical limit of the bulge and the estimation of the modeled bulge will then occur completely automatic.

3.2 IFS DATA

The spectroscopic analysis was done by using IFS data, specifically, the reduced V500 datacubes from CALIFA Survey. The main goal of this analysis is to understand how the metallicity is distributed throughout the galactic radius. By combining these results with the ones obtained trough photometric analysis, it is expected to obtain a deeper perception of how the chemical enrichment occurs and how are these processes related to physical aspects of the galactic system, specially in the context of pseudo bulges.

PORTO3D

The datacubes were processed, spaxel-by-spaxel, with the most recent version of PORTO3D (v.2) pipeline. This pipeline was developed at CAUP by Polychronis Papaderos and Jean Michel

Gomes, to post-process the flux calibrated IFS data-cubes and perform automated spectral fitting. It combines modules written in ESO-MIDAS and in GNU Fortran 2008, with peripheral modules using CFITSIO and PGplot routines. The spectral fitting is done by invoking STARLIGHT (v.4 - public available version). A description of the code is given in Cid Fernandes et al. (2005, 2007); and subsequent publications of the SEAGal collaboration. It was also published a detailed manual for its application. PORTO3D permits the estimation of uncertainties in emission-line fluxes and equivalent widths (EWs), being composed by three main modules: m.1 that performs data quality assessment and initial statistics, and extracts individual spectra from the flux-calibrated CALIFA datacubes, converting them into a suitable format for STARLIGHT; m.2 will extract emission lines, after the subtraction of the best-fitting stellar SED, determines emission line fluxes and kinematics and computes several secondary quantities from the STARLIGHT models (e.g., SFH, mean stellar ages, metallicities and ages weighted by mass and light); m.3 determines the Balmer line luminosities implied by the best-fitting population vector. This module is being used in the context of studies of early-type galaxies by the CAUP team (see Gomes et al., 2014; Kehrig et al., 2012; Papaderos et al., 2013, for details). A suit of auxiliary codes to PORTO3D permits the execution of various other tasks, such as the error-weighted combination of emission-line maps and the derivation of radial profiles for various quantities obtained from spectral synthesis (e.g., luminosity- and mass-weighted stellar metallicity and age). For a detailed description of PORTO3D pipeline see Gomes et al. (2014).

Estimating Metallicities with PORTO3D

It will be computed both stellar metallicity gradients and nebular metallicity gradients. As it was already mentioned in Chapter 1, the $Z_*(R)$ will be estimated by STARLIGHT which is invoked in the m.1 of PORTO3D, whereas the $Z_N(R)$ will be estimated by applying SLM to the output of the m.2 of PORTO3D.

◦ Stellar Metallicities

After the extraction of the spectra from the IFS data-cube and the error spectrum and bad pixel map provided by the CALIFA data reduction pipeline, the correction for z and wavelength,

rebinned to 1 Å/pixel, the selection of spaxels according to their $signal\text{-}to\text{-}noise$ (S/N) and flagging the emission lines, the spectra will be stored in ascii format and its ready to be analyzed with STARIGHT, that decomposes the observed spectrum into a linear combination of its $simple\ stellar\ populations$ (SSP) spectra. The $population\ vector$, besides the derived intrinsic V band extinction and velocity dispersion of the stellar component, encloses all the information of the best-fitting model spectrum M_λ:

$$M_\lambda = M_{\lambda_0} \left[\sum_{j=1}^{N_*} x_j b_{j,\lambda} r_\lambda \right] \otimes G(v_*, \sigma_*), \tag{3.16}$$

where,

$b_{j,\lambda} = L_\lambda^{SSP}(t_j, Z_j)/L_{\lambda_0}^{SSP}(t_j, Z_j)$ - spectrum of the j^{th} SSP normalized at λ_0,
$r_\lambda = 10^{-0.4(A_\lambda - A_{\lambda_0})}$ - reddening term,
x - population vector,
M_{λ_0} - synthetic flux at the normalization wavelength,
N_* - total number of SSPs,
$G(v_*, \sigma_*)$ - line-of-sight stellar velocity distribution modeled as a Gaussian centered at velocity v_* with standard deviation of σ_*.

The code converges to a solution by the standard χ^2 minimization with respect to the observed spectrum O_λ:

$$\chi^2(x, M_{\lambda_0}, A_V, v_*, \sigma_*) = \sum_{\lambda=1}^{N_\lambda} [(O_\lambda - M_\lambda) w_\lambda]^2, \tag{3.17}$$

where spectral weights w_λ are the inverse of the error spectrum e_λ.

◦ Nebular Metallicities

To obtain the emission-line maps, as first step, the m.2 of PORTO3D will estimate the pure emission-line spectrum, by subtracting the best fit from the observed spectrum O_λ. In order to accurately recover faint ($EW \sim 1$ Å) emission lines that are hidden within broader stellar absorption features and noisy the continuum, PORTO3D rectifies the rest-continuum (i.e., $O_\lambda - M_\lambda$), based on an 1D adaptation of the flux-conserving unsharp masking technique developed by Papaderos et al. (1998), permitting the determination of a smooth version of the rest-continuum which will be subsequently subtracted from the input data array, yielding a net emission-line spectrum with zero as its mean value when its absent of emission-lines. The determination of emission-line fluxes from rectified net spectra is based on the combination of two techniques: the first (el1) utilizes standard Gaussian line fitting/deblending with the Levenberg-Marquardt non-linear fitting algorithm and the second (el2) a simple summation of the flux within pre-defined spectral windows centered on the laboratory wavelength of up to 50 emission-lines, after the correction for local motions. The output is in the format of data-cubes, with spatially resolved information about the emission of the galaxy.

To compute the gas-phase metallicity from the emission-line maps from the output of PORTO3D, it was developed a MIDAS code based in SLMs, inspired in a Fortran code previously developed by Dr. Jean Michel Gomes, that computes several metallicity indexes. Although, in this work it was used only the Marino et al. (2013) calibration that has developed specifically for CALIFA data:

$$O3N2 = \frac{[OIII]5007}{H\beta}\frac{H\alpha}{[NII]6584},$$
$$12 + log(O/H) = 8.533(\pm 0.012) - 0.214(\pm 0.012)O3N2.$$

To compute the radial profiles it was adopted the isophotal annuli method (Papaderos et al., 2002, referred to as meth. iv). Its principal concept consists in the determination of photon statistics within equidistant logarithmic portions of a galaxy image, with each of these regular portions faithfully reproducing the morphology of a galaxy within each intensity interval that corresponds to a well-defined photometric radius.

Chapter 4.

Observational Motivation for $RemoveYoung$

Figs. 4.1 to 4.4 illustrate the output from RY. The best-fitting $population\ vector$ computed by the spectral synthesis code STARLIGHT encodes the mass percentage, age and metallicity of those library SSPs evaluated by the code, in addition to the extinction and velocity dispersion required for the full characterization of the best-fitting model to a spectrum.

In principle, the construction of the best-fitting model as a linear superposition of SSPs permits to address the question "how would the spectrum under study look like, if the best-fitting population vector would be stripped off SSPs with an age between $t_{\rm min}$ and $t_{\rm max}$"? Likewise, it is a straightforward task to recompute a model spectrum by filtering out those SSP elements within a metallicity range from $Z_{\rm min}$ to $Z_{\rm max}$. The 2D extension of this technique to spaxel-by-spaxel processing of IFU spectral data is obviously a manageable task.

In practice, however, the re-computation of a model spectrum after removal of a subset of SSP elements from the original best-fitting population vector from a STARLIGHT fit requires a careful treatment of various technical issues. This task was recently accomplished in Gomes et al. (2014, in prep.) and will soon lead to the publicly available code $RemoveYoung$. RY uses as input the best-fitting population vector (from STARLIGHT, obviously also from any other code storing a spectral fit in an equivalent data format) and re-computes from it a synthetic spectrum from which the contribution of SSPs younger than a time cutoff ($t_{\rm min}$) is excluded. Currently, the code permits to set $t_{\rm min}$ between 1 Myr and 1 Gyr. It also exports into ascii and FITS format several other quantities, such as, e.g., the luminosity fraction (in units of mag) of SSP younger than $t_{\rm min}$ in the

standard photometric bands (e.g., Johnson-Cousins, Bessel, SDSS, and others).

Coming to the question of the motivation behind RY, one may consider various applications. As an example, removal of stellar populations younger than an age $t_{\rm min}$ is a necessary – yet not sufficient – step for reconstructing the stellar mass surface density of a galaxy at the age $t_{\rm Hubble}$ – $t_{\rm min}$, i.e. for a study of the mass assembly history of galaxies as a function of cosmic time (see discussion in Gomes et al., 2014). Note that attempts in this direction were made, e.g., in the framework of IFU spectroscopy studies with CALIFA data.

Another argument that motivated the development of RY is the bulge/disk decomposition bias described in Papaderos et al. (2014, in prep.): As argued there, the standard technique of subtracting an exponential fit to the disk from a galaxy profile in order to isolate the residual emission of the bulge (and eventually of the the bar) is strictly valid only when the star formation rate (SFR) surface density $\Sigma_{\rm SFR}$ (in units of $M_\odot$ yr^{-1} kpc^{-2}) scales with the $local$ surface density $\Sigma_\star$ of older stars with an overall constant proportionality factor. For a geometrically thin, face-on disk such a proportionality would imply, among other things,a spatially constant Hα intensity and $EW(H\alpha)$, as well as M_{100}.

However, from a review of Figs. 4.1 to 4.4 it is apparent that this is not generally the case. In fact, Hα maps for most of the analyzed galaxies indicate that the disk is forming stars more actively than the bulge and the ratio $\Sigma_{SFR}/\Sigma_\star$ shows a significant radial gradient across galactic disks, as it will be discussed in further detail in a forthcoming publication by our team. As argued in Papaderos et al. (2014, in prep.), the elevated surface brightness of the disk due to ongoing star-forming activity together with the virtual absence star-forming activity in the bulge, will result in an over-subtraction of the disk beneath the bulge when standard bulge-disk decomposition techniques are used. This will in turn lead to an observational bias, systematically reducing both the total luminosity and the isophotal radius of the bulge. Evidently, the graveness of this bias is expected to be anti-correlated with the luminosity and compactness of bulges, rendering intrinsically faint and diffuse ones almost undetectable after disk-bulge profile decomposition.

In the framework of this study, the sample of CALIFA galaxies was processed spaxel-by-spaxel by RY using a $t_{\rm min}$ of 30 Myr, 100 Myr and 1 Gyr in order to evaluate the impact of the, respectively,

very young, pre-AGB and intermediately old stellar population on the observed r band surface brightness of the bulge and the disk. The three lower panels of Figs. 4.1 to 4.4 show that this effect increases with $t_{\rm min}$, as expected, ranging in the case of a time cutoff at 30 Myr from δ(30 Myr) $\sim$0.2 mag to $\sim$0.8 mag, and generally showing a strong dependence on galactocentric radius.

Following the illustrative discussion here, the profile decomposition in Chapter 5 was carried out both in the standard manner and after correction of SBPs for the above bias, whereby a $t_{\rm min}$ of 30Myr was adopted (referred to in the following as dmr30M). This conservative time cutoff is meant to eliminate the luminosity contribution of the ionizing stellar component only, yielding the minimal possible intervention to the SBPs. For further details on the adopted methodology see Gomes et al. (2014) and Papaderos et al. (2014, in prep.).

$H\alpha$ Maps and Radial Profiles

IC1256

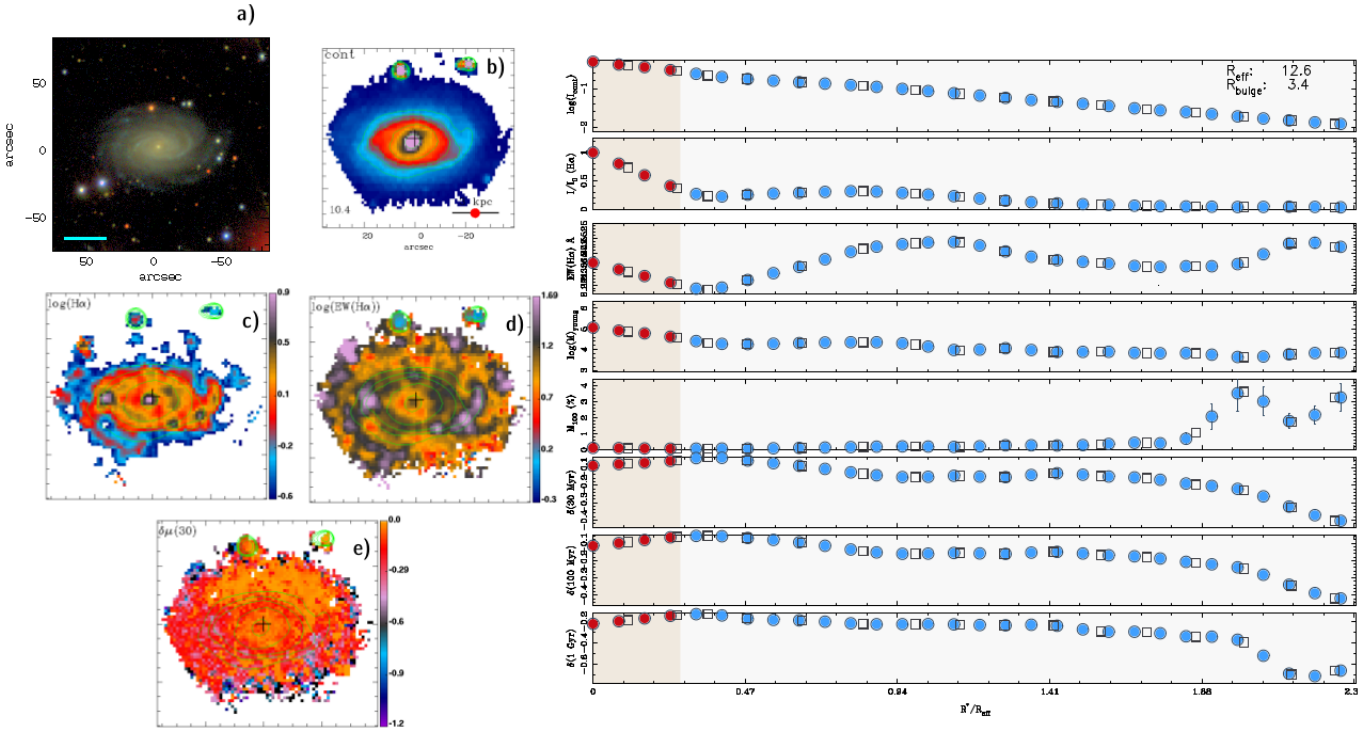

Figure 4.1: Maps and radial profiles of IC1256.

Left-hand side panel:

a) true color image of each galaxy, composed through combination of SDSS images in the $ugriz$ bands;

b) map of the emission-line free continuum in the spectral range between 6390 Å and 6490 Å;

c) logarithmic representation of the Hα flux in units of 10^{-16} erg s^{-1} cm^{-2};

d) logarithmic representation of the equivalent width (in units of Å) of the Hα emission line;

e) contribution $\delta\mu$(30) of stars younger than 30 Myr to the observed SDSS r surface brightness (in units of mag), as derived from CALIFA IFU data after spaxel-by-spaxel application of *RemoveYoung* (RY).

Note that in all maps the cross indicates the maximum of the emission-line free stellar continuum. The morphology of the latter is delineated by the overlaid contours (spacing of 0.5 dex).

Right-hand side panel:

Radial profiles derived with the *isophotal annuli method* (Papaderos et al., 2002, 2013) after

normalization to the effective radius in the SDSS r band. The shaded area depicts the radial extent of the bulge component, as derived from SBP fitting and decomposition prior to RY. Open squares correspond to the mean values within irregular annuli and circles to spline-interpolated values. Vertical error bars show the standard deviation about the mean ($\sigma/\sqrt{\mathrm{N}}$) of the N spaxels considered in each isophotal annulus.

From top to bottom:

Logarithm of the intensity of the emission-line free continuum between 6390 Å and 6490 Å, after normalization to the intensity maximum; The effective radius R_{eff} and isophotal radius of the bulge R_{bulge} in arcsec is indicated at the upper-right; Radial intensity of the Hα Balmer line, normalized to the Hα intensity I_0 that is determined at the maximum of the emission-line free continuum (i.e. the value at the photometric radius $R^{\star}$=0 arcsec) $EW(H\alpha)$ in Å; Logarithm of the mass surface density (in $\mathrm{M}_{\odot}$/arcsec^2) of stars younger than 100 Myr; Mass fraction (in $\%$) of stars younger than 100 Myr; $three\ lower\ panels$: contribution (in mag) of stars younger than 30 Myr, 100 Myr and 1 Gyr to the observed SDSS r surface brightness, as inferred by RY.

NGC0023

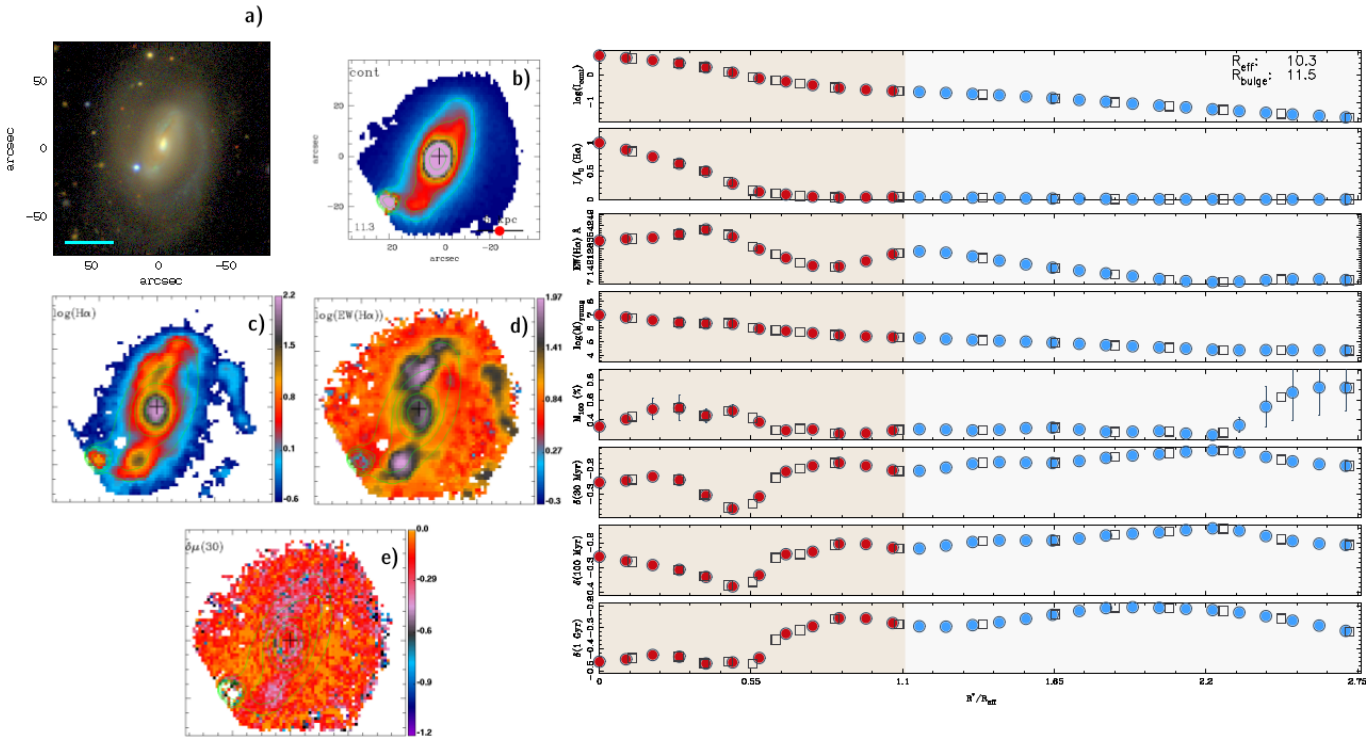

Figure 4.2: Maps and radial profiles of NGC0023.

NGC3057

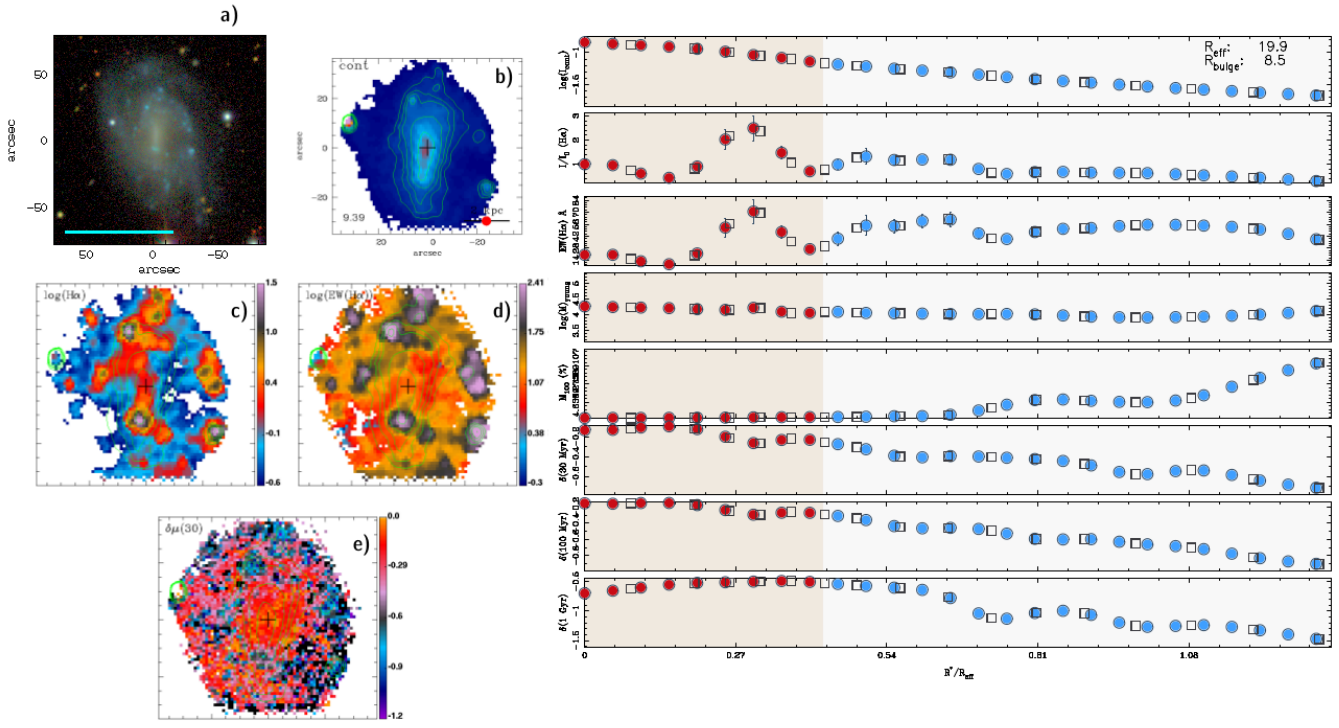

Figure 4.3: Maps and radial profiles of NGC3057.

NGC6154

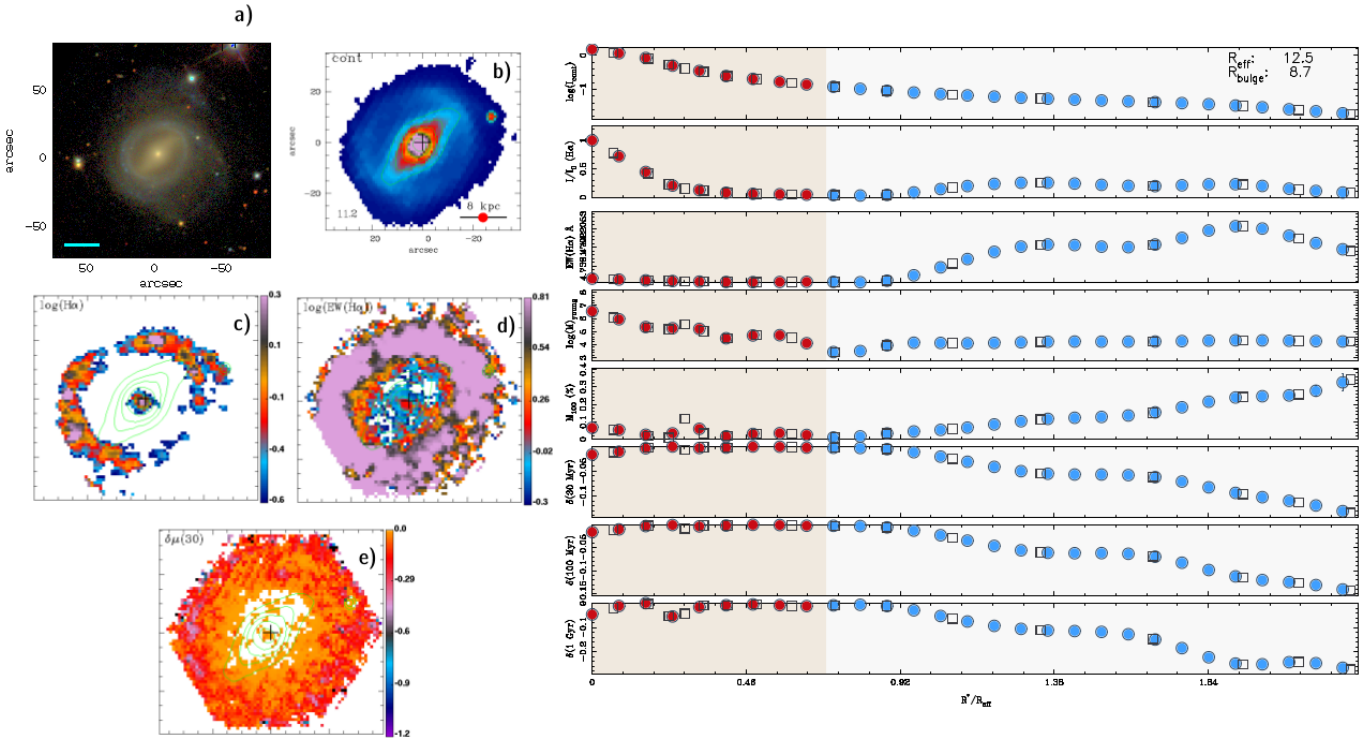

Figure 4.4: Maps and radial profiles of NGC6154.

Table 4.1: It is listed – from left to right – galaxy name, and the estimated quantities for: $H\alpha$ in the bulge (mean ($<>$), standard deviation (σ), mean standard deviation ($<\sigma>$), intercept of the linear regression (b), intercept error (b_{err}), slope of the linear regression (gradient) (m) and slope error (m_{err})), $H\alpha$ in the disk ($<>$, σ and $<\sigma>$), equivalent width of $H\alpha$ in the bulge ($<>$, σ, $<\sigma>$, b, b_{err}, m and m_{err}), equivalent width of $H\alpha$ in the disk ($<>$, σ and $<\sigma>$) and the logarithm of the mass of the stars younger than 100 Myr in the bulge and disk ($<>$, σ and $\sigma>$).

Galaxy	$H\alpha$ Bulge							$H\alpha$ Disk			$EW(H\alpha)$ Bulge							$EW(H\alpha)$ Disk			$log(M_{young})$ Bulge			$log(M_{young})$ Disk		
	$<>$	σ	$<\sigma>$	b	b_{err}	m	m_{err}	$<>$	σ	$<\sigma>$	$<>$	σ	$<\sigma>$	b	b_{err}	m	m_{err}	$<>$	σ	$<\sigma>$	$<>$	σ	$<\sigma>$	$<>$	σ	$<\sigma>$
IC0776	0.60	0.32	0.14	0.977	0.028	-3.052	0.187	0.19	0.20	0.04	53.02	20.27	9.06	78.383	1.497	-	9.978	45.49	16.90	3.60	4.39	0.05	0.02	4.17	0.14	0.03
IC1256	0.70	0.27	0.13	0.999	0.004	-2.476	0.027	0.16	0.15	0.03	11.42	2.34	1.17	14.043	0.002	-21.946	0.013	15.00	3.58	0.70	4.85	0.19	0.10	4.03	0.26	0.05
IC4566	0.47	0.37	0.17	0.918	0.080	-2.696	0.398	0.16	0.17	0.03	1.33	0.43	0.19	1.756	0.114	-2.616	0.565	6.21	3.33	0.68	5.41	0.35	0.16	4.52	0.21	0.04
NGC0001	0.32	0.32	0.08	0.761	0.070	-0.475	0.064	0.02	0.15	0.04	15.45	3.48	0.84	11.139	1.025	4.622	0.938	26.40	16.45	4.25	5.23	0.44	0.11	4.51	0.21	0.05
NGC0023	0.37	0.37	0.11	0.894	0.066	-0.989	0.106	0.01	0.15	0.04	28.39	8.14	2.35	37.997	2.895	-18.058	4.609	13.55	6.70	1.63	6.09	0.57	0.16	4.72	0.38	0.09
NGC0160	0.35	0.27	0.08	0.690	0.080	-0.824	0.166	0.24	0.14	0.03	0.81	0.45	0.13	0.166	0.070	1.575	0.146	5.07	1.95	0.46	5.07	0.45	0.12	5.35	0.18	0.04
NGC0165	0.32	0.39	0.14	0.818	0.108	-2.107	0.382	0.02	0.15	0.04	17.73	12.24	4.33	34.508	2.312	-71.204	8.213	10.63	2.69	0.63	5.50	0.71	0.25	4.32	0.22	0.05
NGC0171	0.42	0.28	0.08	0.707	0.114	-0.984	0.332	0.45	0.20	0.05	2.01	1.76	0.49	0.380	0.769	5.583	2.237	10.60	2.10	0.50	4.79	0.65	0.18	4.33	0.21	0.05
NGC0180	0.70	0.28	0.11	0.969	0.130	-2.387	0.972	0.03	0.11	0.02	16.43	4.16	1.70	19.272	2.803	-25.692	20.903	8.02	4.01	0.84	6.21	0.29	0.12	4.52	0.18	0.04
NGC0214	0.62	0.24	0.10	0.846	0.122	-1.382	0.605	0.43	0.32	0.06	3.71	1.54	0.63	2.229	0.833	8.921	4.136	16.56	3.18	0.64	5.68	0.30	0.12	5.32	0.16	0.03
NGC0237	0.80	0.17	0.07	0.974	0.020	-0.713	0.067	0.33	0.31	0.07	11.91	2.84	1.16	8.470	0.666	14.136	2.256	27.00	4.96	1.06	5.36	0.13	0.05	4.69	0.44	0.09
NGC0257	0.91	0.25	0.09	1.216	0.083	-1.433	0.324	0.27	0.16	0.03	10.67	4.62	1.63	4.486	1.092	28.689	4.240	19.11	3.18	0.66	5.80	0.19	0.07	5.33	0.16	0.03
NGC0477	0.71	0.28	0.13	1.025	0.035	-2.522	0.231	0.13	0.12	0.02	11.25	1.57	0.70	12.503	0.671	-10.134	4.417	15.61	4.93	1.01	5.49	0.34	0.15	4.65	0.14	0.03
NGC0776	0.57	0.38	0.16	1.061	0.047	-3.009	0.239	0.06	0.13	0.03	14.29	4.12	1.68	17.942	2.412	-22.375	12.216	15.27	4.81	0.96	5.79	0.53	0.22	4.53	0.30	0.06
NGC1093	0.52	0.27	0.10	0.736	0.159	-0.689	0.430	0.18	0.19	0.04	4.14	2.35	0.89	2.127	1.371	6.529	3.696	11.43	1.39	0.30	4.74	0.23	0.09	4.37	0.28	0.06
NGC1645	0.32	0.31	0.10	0.714	0.101	-0.845	0.183	0.09	0.13	0.03	1.27	0.45	0.14	0.958	0.223	0.675	0.406	7.30	5.04	1.16	5.02	0.62	0.20	4.57	0.25	0.06
NGC2253	0.34	0.38	0.14	0.815	0.114	-2.183	0.438	0.06	0.13	0.03	10.17	5.79	2.19	17.379	1.869	-33.272	7.180	20.15	4.50	0.90	5.50	0.65	0.25	4.81	0.27	0.05
NGC2347	1.54	0.37	0.15	1.087	0.080	2.017	0.296	0.45	0.44	0.09	8.62	5.77	2.36	1.018	0.639	33.938	2.356	18.76	3.43	0.70	5.76	0.13	0.05	5.09	0.29	0.06
NGC2639	0.15	0.25	0.05	0.404	0.082	-0.297	0.081	0.00	0.15	0.04	4.60	1.77	0.39	4.116	0.749	0.555	0.743	2.23	0.81	0.23	4.61	1.76	0.38	3.84	0.45	0.13
NGC2730	1.04	0.28	0.11	1.211	0.156	-1.254	0.953	0.44	0.26	0.05	19.19	5.83	2.38	12.920	2.629	46.389	16.059	31.60	6.50	1.30	5.10	0.13	0.05	4.77	0.22	0.04
NGC2906	0.83	0.17	0.06	0.863	0.111	-0.142	0.450	1.00	0.78	0.15	2.37	1.56	0.59	0.475	0.540	9.215	2.186	14.16	7.17	1.41	4.49	0.29	0.11	4.01	0.56	0.11
NGC2916	0.40	0.35	0.13	0.868	0.083	-2.611	0.386	0.49	0.22	0.05	1.27	0.39	0.14	1.704	0.098	-2.427	0.456	15.89	7.20	1.50	5.26	0.65	0.23	4.73	0.27	0.06
NGC3057	1.18	0.69	0.23	0.800	0.416	1.892	1.738	0.74	0.37	0.09	31.25	20.72	6.91	13.505	11.006	88.213	45.971	50.40	6.93	1.63	4.19	0.07	0.02	4.01	0.09	0.02
NGC3300	1.32	0.66	0.27	1.593	0.414	-1.205	1.501	0.29	0.21	0.04	0.18	0.21	0.08	0.101	0.066	0.335	0.241	0.61	0.54	0.11	5.02	0.34	0.14	3.73	0.32	0.06
NGC3381	0.39	0.38	0.14	0.868	0.084	-3.014	0.438	0.02	0.12	0.02	73.01	47.41	17.92	137.143	7.700	-	40.100	24.23	4.07	0.80	4.87	0.33	0.13	3.92	0.32	0.06
NGC3614	0.43	0.38	0.14	0.913	0.082	-4.660	0.650	0.28	0.14	0.03	4.58	2.67	1.01	8.049	0.562	-33.256	4.479	16.96	4.91	0.96	4.24	0.47	0.18	3.95	0.16	0.03
NGC3687	0.36	0.30	0.10	0.655	0.136	-1.016	0.390	0.35	0.23	0.05	2.34	2.03	0.64	0.286	0.924	7.008	2.656	15.05	3.37	0.70	4.00	0.53	0.17	3.94	0.31	0.07
NGC4003	0.35	0.38	0.13	0.850	0.084	-1.238	0.173	0.01	0.14	0.03	4.98	3.14	1.11	9.279	0.567	-10.562	1.166	2.53	1.07	0.24	6.19	0.36	0.13	4.85	0.55	0.13
NGC4047	0.93	0.10	0.04	0.983	0.024	-0.362	0.135	0.30	0.30	0.06	10.40	2.51	1.12	7.463	0.450	20.165	2.520	18.28	4.61	0.86	5.71	0.08	0.04	4.86	0.58	0.11
NGC4185	1.01	0.13	0.04	0.888	0.048	0.709	0.236	0.91	0.16	0.03	2.91	1.59	0.53	0.647	0.212	13.365	1.052	9.72	2.66	0.56	4.50	0.27	0.09	4.21	0.15	0.03
NGC4210	0.71	0.22	0.09	0.863	0.144	-1.148	0.899	1.77	0.40	0.08	1.15	0.73	0.30	0.396	0.367	5.682	2.288	14.14	4.37	0.91	4.04	0.54	0.22	4.24	0.20	0.04
NGC4961	1.35	0.27	0.11	1.075	0.067	1.169	0.233	0.58	0.52	0.11	15.40	6.70	2.73	6.619	0.398	36.983	1.384	35.93	3.61	0.75	0.06	0.01	0.00	0.02	0.02	0.00
NGC5000	0.65	0.38	0.22	1.001	0.002	-4.485	0.018	0.02	0.12	0.02	15.92	7.75	4.47	33.462	1.009	-95.814	9.928	10.73	4.81	0.94	6.24	0.28	0.16	4.73	0.17	0.03
NGC5016	0.83	0.18	0.09	1.000	0.001	-1.701	0.011	0.16	0.17	0.03	21.25	1.47	0.74	21.300	0.038	-0.496	0.300	18.68	1.51	0.28	5.23	0.09	0.04	4.65	0.22	0.04
NGC5205	0.68	0.21	0.07	0.768	0.124	-0.328	0.377	0.69	0.31	0.07	1.86	1.27	0.42	0.296	0.440	5.661	1.334	11.73	2.87	0.60	3.76	0.28	0.09	3.88	0.18	0.04
NGC5320	0.79	0.13	0.05	0.872	0.073	-0.525	0.381	0.82	0.27	0.05	4.11	1.48	0.56	2.266	0.450	11.515	2.336	20.70	7.03	1.41	4.58	0.04	0.01	4.32	0.18	0.04
NGC5378	0.40	0.33	0.11	0.852	0.069	-2.108	0.269	0.11	0.13	0.03	1.10	0.16	0.05	1.124	0.041	-0.127	0.161	4.03	1.54	0.33	3.40	3.20	1.07	3.67	0.43	0.09
NGC5406	0.44	0.37	0.15	0.895	0.088	-2.968	0.473	0.35	0.18	0.04	0.77	0.16	0.07	0.876	0.052	-0.661	0.276	9.56	4.05	0.84	4.92	0.32	0.13	4.57	0.17	0.04
NGC5480	0.39	0.35	0.13	0.823	0.104	-2.690	0.535	0.04	0.12	0.02	39.56	7.94	3.00	48.399	3.450	-54.659	17.742	27.65	8.33	1.63	5.24	0.29	0.11	4.52	0.21	0.04

Table 4.1 Continued.

NGC5614	0.15	0.23	0.05	0.402	0.066	-0.271	0.060	0.02	0.28	0.14	2.43	0.60	0.12	1.523	0.084	0.963	0.076	3.81	0.45	0.22	4.55	0.67	0.13	3.83	0.47	0.24
NGC5656	1.97	0.58	0.17	1.125	0.062	2.044	0.126	0.86	0.85	0.18	10.88	8.18	2.47	-1.298	0.771	29.326	1.570	20.25	6.80	1.45	5.13	0.13	0.04	4.47	0.39	0.08
NGC5735	0.44	0.37	0.17	0.870	0.113	-4.033	0.866	0.19	0.13	0.03	4.55	2.01	0.90	6.610	0.695	-21.139	5.305	15.03	5.07	1.01	4.94	0.40	0.18	4.25	0.15	0.03
NGC5772	0.29	0.29	0.09	0.568	0.133	-0.731	0.300	0.11	0.15	0.03	3.34	2.92	0.88	-0.339	0.955	9.825	2.158	10.28	2.92	0.67	4.89	0.53	0.16	4.48	0.28	0.06
NGC5829	0.81	0.24	0.14	0.998	0.005	-2.982	0.066	0.25	0.15	0.03	12.60	1.22	0.70	12.543	0.079	0.942	0.976	29.54	18.21	3.57	5.63	0.08	0.05	5.19	0.19	0.04
NGC6004	0.25	0.30	0.09	0.562	0.118	-1.196	0.386	0.06	0.12	0.03	10.11	4.45	1.28	8.034	2.401	7.981	7.821	12.92	2.28	0.49	4.95	0.54	0.15	4.40	0.17	0.04
NGC6032	0.39	0.42	0.19	0.872	0.113	-3.419	0.650	0.01	0.14	0.03	25.16	16.94	7.58	46.339	2.031	-	11.647	7.69	2.58	0.53	5.25	0.98	0.44	4.67	0.40	0.08
NGC6154	0.30	0.35	0.12	0.752	0.106	-1.396	0.277	0.17	0.16	0.03	0.95	0.34	0.11	1.352	0.090	-1.267	0.235	8.51	4.47	1.00	5.15	0.75	0.25	4.14	0.32	0.07
NGC6186	0.92	0.20	0.11	0.997	0.006	-0.950	0.059	0.06	0.16	0.03	34.62	4.00	2.31	31.567	0.306	36.318	2.816	12.05	6.33	1.24	5.93	0.08	0.04	4.19	0.51	0.10
NGC6278	0.15	0.29	0.08	0.460	0.107	-0.395	0.116	0.01	0.13	0.03	0.53	0.30	0.08	0.594	0.136	-0.085	0.147	2.32	2.72	0.64	3.93	0.94	0.24	3.15	0.34	0.08
NGC6941	0.46	0.39	0.16	0.960	0.053	-3.317	0.287	0.09	0.12	0.02	2.84	1.49	0.61	4.765	0.140	-12.701	0.760	9.78	7.13	1.32	5.47	0.57	0.23	4.47	0.19	0.03
NGC7321	0.65	0.31	0.14	1.018	0.023	-2.226	0.114	0.29	0.21	0.04	3.23	0.69	0.31	3.912	0.138	-4.136	0.681	15.04	5.26	1.10	5.68	0.31	0.14	4.92	0.32	0.07
NGC7489	0.90	0.14	0.08	1.000	0.001	-1.429	0.010	0.27	0.20	0.04	16.22	1.28	0.74	15.568	0.103	9.635	1.172	30.69	9.73	1.75	6.55	0.30	0.17	5.50	0.23	0.04
NGC7625	1.00	0.15	0.06	1.083	0.074	-0.424	0.305	0.10	0.19	0.04	37.18	10.89	4.44	23.140	1.881	70.323	7.780	16.58	14.76	2.74	0.29	0.04	0.02	-69.61	45.50	8.45
NGC7653	1.04	0.29	0.11	0.780	0.148	1.039	0.500	0.61	0.54	0.10	6.19	5.97	2.26	-1.231	1.976	30.118	6.675	25.02	4.16	0.82	5.40	0.46	0.17	4.67	0.30	0.06
NGC7691	0.77	0.28	0.14	1.041	0.059	-3.790	0.659	0.28	0.14	0.03	10.29	1.61	0.80	11.322	0.843	-14.416	9.422	16.74	5.27	1.03	5.18	0.10	0.05	5.17	0.11	0.02
NGC7716	0.51	0.29	0.08	0.583	0.160	-0.189	0.331	0.46	0.20	0.04	2.81	3.36	0.97	-1.441	1.069	10.371	2.211	16.30	3.89	0.83	3.30	2.67	0.77	4.04	0.37	0.08
NGC7738	0.57	0.38	0.19	0.996	0.006	-2.797	0.032	0.01	0.12	0.02	32.28	12.56	6.28	46.637	1.558	-94.773	8.246	7.93	5.28	1.04	6.87	0.70	0.35	4.50	0.35	0.07
NGC7819	0.34	0.40	0.14	0.854	0.104	-2.067	0.353	0.01	0.15	0.04	39.66	20.79	7.35	67.979	4.210	-	14.251	17.74	3.34	0.79	5.53	0.66	0.23	4.37	0.22	0.05
UGC07012	0.83	0.16	0.07	1.007	0.012	-0.639	0.037	0.23	0.23	0.05	28.92	6.79	2.77	20.086	0.919	32.397	2.782	38.11	8.53	2.01	4.92	0.09	0.04	4.42	0.31	0.07
UGC08234	1.01	0.42	0.19	1.249	0.209	-0.673	0.478	0.16	0.16	0.03	0.23	0.28	0.12	0.076	0.026	0.426	0.059	1.18	0.64	0.13	5.55	0.31	0.14	4.30	0.35	0.07
UGC08733	1.04	0.39	0.16	1.285	0.204	-1.784	1.201	0.47	0.23	0.05	17.43	4.72	1.93	17.327	3.447	0.762	20.342	25.77	5.50	1.20	4.24	0.16	0.07	3.78	0.17	0.04
UGC09067	0.95	0.21	0.12	0.999	0.002	-0.423	0.016	0.27	0.26	0.06	12.35	2.71	1.57	10.363	0.028	16.902	0.182	20.62	3.04	0.66	4.28	0.01	0.01	3.37	0.45	0.10
UGC09291	1.00	0.10	0.05	1.028	0.032	-0.230	0.240	0.66	0.25	0.05	8.00	1.79	0.80	5.904	0.137	19.569	1.041	19.56	4.49	0.88	4.61	0.09	0.04	4.09	0.14	0.03
UGC09476	0.61	0.30	0.13	0.965	0.044	-3.107	0.319	0.21	0.17	0.03	13.55	2.20	0.99	15.809	0.873	-19.939	6.293	19.37	5.97	1.15	5.11	0.22	0.10	4.37	0.29	0.06
UGC10796	0.77	0.26	0.13	1.017	0.024	-1.821	0.141	0.08	0.14	0.03	29.00	4.77	2.38	23.863	0.347	37.568	2.036	18.50	5.18	1.22	0.08	0.05	0.02	0.02	0.05	0.01
UGC12224	0.46	0.38	0.17	0.928	0.075	-5.152	0.678	0.10	0.12	0.02	12.22	7.15	3.20	21.093	1.122	-98.357	10.161	16.18	4.79	0.86	4.67	0.29	0.13	4.33	0.24	0.00

Table 4.2: It is listed – from left to right – galaxy name, and the estimated quantities for: logarithm of the mass of stars younger than 100 million years in the bulge ($<>$, σ and $\bar{\sigma}$), logarithm of the mass of stars younger than 100 million years in the disk ($<>$, σ and $\bar{\sigma}$), scale-down in magnitudes the profile will suffer by removing the contribution light of stars younger than: 30 million years in the bulge and disk ($<>$, σ, $\bar{\sigma}$, b, b_{err}, m and m_{err}); 100 million years in the bulge and disk ($<>$, σ and $\bar{\sigma}$) and 1Gyr in the bulge and disk ($<\mu>$, σ and $\bar{\sigma}$).

Galaxy	M_{100} Bulge			M_{100} Disk			$d30$ Bulge							$d30$ Disk							$d100$ Bulge			$d100$ Disk			$d1Gy$ Bulge			$d1Gy$ Disk		
	$<>$	σ	$\bar{\sigma}$	$<>$	σ	$\bar{\sigma}$	$<>$	σ	$\bar{\sigma}$	b	b_{err}	m	m_{err}	$<>$	σ	$\bar{\sigma}$	b	b_{err}	m	m_{err}	$<>$	σ	$\bar{\sigma}$	$<>$	σ	$\bar{\sigma}$	$<>$	σ	$\bar{\sigma}$	$<>$	σ	$\bar{\sigma}$
IC0776	0.48	0.13	0.06	6.37	8.58	1.83	-0.27	0.03	0.01	-0.308	0.008	0.330	0.055	-0.41	0.07	0.02	-0.322	0.029	-0.094	0.028	-0.27	0.03	0.01	-0.46	0.10	0.02	-0.37	0.04	0.02	-0.82	0.27	0.06
IC1256	0.10	0.07	0.04	0.80	1.09	0.21	-0.08	0.01	0.01	-0.088	0.001	0.110	0.005	-0.17	0.09	0.02	0.005	0.020	-0.130	0.014	-0.09	0.02	0.01	-0.18	0.10	0.02	-0.18	0.03	0.02	-0.30	0.17	0.03
IC4566	0.04	0.05	0.02	0.46	0.61	0.10	-0.02	0.01	0.00	-0.030	0.002	0.065	0.011	-0.09	0.05	0.01	0.018	0.011	-0.081	0.007	-0.02	0.01	0.00	-0.10	0.06	0.01	-0.03	0.01	0.00	-0.16	0.07	0.01
NGC0001	0.22	0.11	0.03	4.13	4.66	1.20	-0.14	0.05	0.01	-0.069	0.008	-0.081	0.008	-0.33	0.17	0.04	0.248	0.172	-0.207	0.061	-0.15	0.05	0.01	-0.35	0.17	0.04	-0.24	0.05	0.01	-0.48	0.16	0.04
NGC0023	0.38	0.14	0.04	0.38	0.19	0.05	-0.24	0.06	0.02	-0.283	0.028	0.073	0.045	-0.17	0.06	0.02	-0.206	0.022	0.021	0.011	-0.27	-0.60	0.02	-0.18	0.06	0.02	-0.38	0.09	0.03	-0.25	0.08	0.02
NGC0160	0.12	0.12	0.03	3.33	2.30	0.54	-0.04	0.03	0.01	0.002	0.008	-0.104	0.017	-0.53	0.15	0.04	-0.279	0.140	-0.169	0.092	-0.04	0.03	0.01	-0.53	0.15	0.04	-0.05	0.03	0.01	-0.54	0.15	0.04
NGC0165	0.26	0.20	0.07	0.32	0.30	0.07	-0.15	0.10	0.04	-0.260	0.047	0.462	0.166	-0.09	0.09	0.02	0.030	0.009	-0.109	0.008	-0.18	0.11	0.04	-0.11	0.09	0.02	-0.23	0.12	0.04	-0.28	0.18	0.04
NGC0171	0.09	0.11	0.03	1.03	1.06	0.25	-0.02	0.01	0.00	-0.021	0.007	0.006	0.019	-0.13	0.08	0.02	0.118	0.034	-0.240	0.031	-0.03	0.01	0.00	-0.15	0.08	0.02	-0.07	0.03	0.01	-0.33	0.14	0.03
NGC0180	0.33	0.13	0.05	0.29	0.36	0.07	-0.21	0.08	0.03	-0.315	0.016	0.977	0.118	-0.08	0.07	0.02	0.016	0.006	-0.122	0.008	-0.25	0.11	0.05	-0.09	0.08	0.02	-0.26	0.12	0.05	-0.17	0.12	0.03
NGC0214	0.11	0.07	0.03	2.63	3.04	0.61	-0.07	0.02	0.01	-0.072	0.019	0.019	0.096	-0.16	0.25	0.05	0.127	0.020	-0.494	0.015	-0.08	0.02	0.01	-0.18	0.25	0.05	-0.12	0.03	0.01	-0.55	0.26	0.05
NGC0237	0.23	0.13	0.05	2.83	2.36	0.50	-0.12	0.06	0.02	-0.045	0.013	-0.322	0.043	-0.29	0.08	0.02	-0.290	0.034	-0.003	0.020	-0.14	0.06	0.02	-0.32	0.08	0.02	-0.32	0.07	0.03	-0.60	0.11	0.02
NGC0257	0.25	0.15	0.05	2.24	1.70	0.35	-0.13	0.06	0.02	-0.049	0.008	-0.371	0.031	-0.49	0.20	0.04	0.049	0.012	-0.464	0.010	-0.16	0.06	0.02	-0.51	0.20	0.04	-0.23	0.08	0.03	-0.62	0.23	0.05
NGC0477	0.14	0.11	0.05	1.09	1.58	0.32	-0.07	0.01	0.01	-0.084	0.008	0.095	0.055	-0.19	0.13	0.03	0.087	0.022	-0.275	0.020	-0.10	0.02	0.01	-0.22	0.15	0.03	-0.15	0.03	0.01	-0.39	0.25	0.05
NGC0776	0.13	0.09	0.04	0.23	0.09	0.02	-0.09	0.02	0.01	-0.117	0.011	0.150	0.058	-0.11	0.04	0.01	-0.103	0.014	-0.005	0.011	-0.12	0.04	0.02	-0.12	0.05	0.01	-0.16	0.06	0.02	-0.22	0.08	0.02
NGC1093	0.04	0.06	0.02	0.82	1.41	0.30	-0.03	0.02	0.01	-0.012	0.011	0.047	0.029	-0.15	0.11	0.02	0.044	0.049	-0.110	0.026	-0.03	0.02	0.01	-0.17	0.12	0.03	-0.06	0.04	0.01	-0.32	0.16	0.03
NGC1645	0.05	0.02	0.01	7.21	5.97	1.37	-0.01	0.01	0.00	-0.016	0.006	0.011	0.011	-0.26	0.11	0.03	0.070	0.047	-0.167	0.023	-0.01	0.01	0.00	-0.26	0.11	0.03	-0.03	0.01	0.00	-0.31	0.13	0.03
NGC2253	0.15	0.10	0.04	0.83	0.77	0.15	-0.11	0.05	0.02	-0.171	0.017	0.300	0.064	-0.25	0.08	0.02	-0.148	0.026	-0.076	0.018	-0.13	0.06	0.02	-0.29	0.08	0.02	-0.20	0.09	0.03	-0.48	0.16	0.03
NGC2347	0.13	0.10	0.04	4.23	5.91	1.21	-0.09	0.05	0.02	-0.034	0.015	-0.243	0.057	-0.40	0.19	0.04	0.034	0.041	-0.271	0.024	-0.10	0.06	0.02	-0.42	0.20	0.04	-0.12	0.07	0.03	-0.47	0.21	0.04
NGC2639	0.08	0.05	0.01	0.57	0.71	0.20	-0.04	0.02	0.01	-0.013	0.007	-0.033	0.006	-0.05	0.05	0.01	0.084	0.028	-0.060	0.012	-0.05	0.03	0.01	-0.06	0.06	0.02	-0.07	0.04	0.01	-0.24	0.16	0.05
NGC2730	0.28	0.18	0.07	4.81	1.70	0.34	-0.18	0.04	0.01	-0.133	0.007	-0.352	0.040	-0.42	0.09	0.02	-0.437	0.042	0.021	0.040	-0.19	0.04	0.02	-0.46	0.10	0.02	-0.35	0.01	0.00	-0.76	0.13	0.03
NGC2906	0.03	0.05	0.02	0.22	0.14	0.03	-0.02	0.01	0.00	-0.005	0.005	-0.065	0.020	-0.11	0.06	0.01	-0.172	0.030	0.044	0.021	-0.03	0.01	0.00	-0.12	0.07	0.01	-0.05	0.01	0.00	-0.17	0.08	0.02
NGC2916	0.15	0.14	0.05	0.95	1.05	0.22	-0.04	0.04	0.01	-0.039	0.025	0.023	0.116	-0.20	0.12	0.02	0.097	0.018	-0.302	0.018	-0.04	0.04	0.01	-0.23	0.13	0.03	-0.07	0.05	0.02	-0.39	0.21	0.04
NGC3057	0.73	0.13	0.04	5.30	4.09	0.96	-0.17	0.06	0.02	-0.094	0.025	-0.370	0.104	-0.49	0.14	0.03	-0.098	0.026	-0.445	0.028	-0.21	0.06	0.02	-0.61	0.18	0.04	-0.56	0.08	0.03	-1.04	0.30	0.07
NGC3300	0.04	0.11	0.04	1.04	2.19	0.43	-0.01	0.00	0.00	-0.008	0.002	0.010	0.006	-0.05	0.07	0.01	0.082	0.023	-0.078	0.013	-0.01	0.01	0.00	-0.05	0.07	0.01	-0.03	0.03	0.01	-0.09	0.08	0.02
NGC3381	0.61	0.22	0.08	0.79	0.34	0.07	-0.39	0.15	0.06	-0.581	0.039	1.193	0.203	-0.23	0.08	0.02	-0.275	0.013	0.039	0.012	-0.41	0.14	0.05	-0.26	0.08	0.02	-0.54	0.08	0.03	-0.75	0.18	0.04
NGC3614	0.06	0.05	0.02	0.34	0.22	0.04	-0.04	0.03	0.01	-0.079	0.007	0.334	0.057	-0.12	0.05	0.01	-0.034	0.007	0.129	0.010	-0.05	0.03	0.01	-0.14	0.05	0.01	-0.07	0.04	0.01	-0.29	0.12	0.02
NGC3687	0.03	0.03	0.01	0.28	0.15	0.03	-0.01	0.02	0.01	0.005	0.007	-0.058	0.020	-0.12	0.03	0.01	-0.115	0.012	0.000	0.009	-0.01	0.02	0.01	-0.13	0.03	0.01	-0.02	0.03	0.01	-0.32	0.11	0.02
NGC4003	0.06	0.05	0.02	0.21	0.33	0.08	-0.04	0.03	0.01	-0.079	0.012	0.089	0.025	-0.05	0.05	0.01	0.043	0.004	-0.046	-0.002	-0.05	0.03	0.01	-0.05	0.05	0.01	-0.10	0.04	0.01	-0.10	0.06	0.01
NGC4047	0.18	0.09	0.04	0.65	0.54	0.10	-0.10	0.03	0.01	-0.063	0.001	-0.247	0.005	-0.22	0.05	0.01	-0.252	0.015	0.026	0.010	-0.13	0.03	0.01	-0.26	0.05	0.01	-0.23	0.02	0.01	-0.37	0.04	0.01
NGC4185	0.04	0.03	0.01	0.13	0.06	0.01	-0.02	0.01	0.00	-0.007	0.003	-0.104	0.016	-0.07	0.03	0.01	-0.017	0.006	-0.066	0.007	-0.03	0.02	0.01	-0.08	0.04	0.01	-0.03	0.02	0.01	-0.14	0.05	0.01
NGC4210	0.03	0.06	0.02	0.26	0.12	0.02	-0.01	0.01	0.00	-0.012	0.005	-0.009	0.033	-0.13	0.05	0.01	-0.029	0.011	-0.110	0.011	-0.02	0.01	0.00	-0.15	0.05	0.01	-0.02	0.01	0.00	-0.25	0.11	0.02
NGC4961	0.47	0.33	0.13	11.55	7.28	1.52	-0.22	0.07	0.03	-0.123	0.007	-0.391	0.025	-0.49	0.09	0.02	-0.469	0.039	-0.010	0.022	-0.23	0.08	0.03	-0.52	0.09	0.02	-0.63	0.07	0.03	-0.85	0.09	0.02
NGC5000	0.22	0.12	0.07	1.33	1.83	0.36	-0.14	0.01	0.01	-0.156	0.010	0.138	0.103	-0.19	0.14	0.03	0.060	0.024	-0.205	0.018	-0.18	0.04	0.02	-0.20	0.14	0.03	-0.21	0.06	0.04	-0.29	0.20	0.04
NGC5016	0.14	0.08	0.04	6.47	9.55	1.77	-0.14	0.00	0.00	-0.131	0.000	-0.050	0.001	-0.25	0.08	0.01	-0.138	0.025	0.094	0.019	-0.14	0.01	0.00	-0.27	0.09	0.02	-0.14	0.01	0.01	-0.41	0.16	0.03
NGC5205	0.03	0.04	0.01	4.21	5.02	1.05	-0.01	0.01	0.00	0.000	0.002	-0.034	0.007	-0.24	0.18	0.04	0.275	0.038	-0.369	0.026	-0.01	0.01	0.00	-0.25	0.19	0.04	-0.05	0.02	0.01	-0.47	0.27	0.06
NGC5320	0.06	0.05	0.02	0.50	0.51	0.10	-0.05	0.02	0.01	-0.025	0.003	-0.139	0.018	-0.16	0.06	0.01	-0.027	0.014	-0.131	0.013	-0.05	0.02	0.01	-0.18	0.07	0.01	-0.10	0.02	0.01	-0.40	0.21	0.04
NGC5378	0.02	0.02	0.01	0.15	0.11	0.02	0.00	0.00	0.00	-0.005	0.001	0.005	0.003	-0.05	0.03	0.01	0.038	0.003	-0.081	0.003	0.00	0.00	0.00	-0.05	0.03	0.01	0.00	0.00	0.00	-0.08	0.06	0.01
NGC5406	0.02	0.01	0.01	0.15	0.07	0.01	-0.01	0.00	0.00	-0.006	0.001	0.004	0.007	-0.07	0.03	0.01	-0.001	0.009	-0.065	0.008	-0.01	0.00	0.00	-0.08	0.04	0.01	-0.03	0.02	0.01	-0.16	0.09	0.02
NGC5480	0.75	0.38	0.14	2.49	1.43	0.28	-0.37	0.09	0.03	-0.396	0.064	0.156	0.330	-0.37	0.07	0.01	-0.307	0.021	-0.057	0.018	-0.39	0.10	0.04	-0.40	0.08	0.02	-0.64	0.09	0.04	-0.73	0.13	0.02
NGC5614	0.04	0.02	0.00	0.07	0.09	0.04	-0.02	0.00	0.00	-0.019	0.001	-0.002	0.001	-0.02	0.03	0.02	0.017	0.000	-0.020	0.000	-0.03	0.00	0.00	-0.03	0.04	0.02	-0.09	0.04	0.01	-0.09	0.11	0.06

Table 4.2 Continued.

NGC5656	0.17	0.14	0.04	0.86	0.65	0.14	-0.11	0.09	0.03	0.023	0.009	-0.308	0.017	-0.21	0.08	0.02	-0.294	0.030	0.047	0.016	-0.11	0.09	0.03	-0.23	0.08	-2.00	-0.23	0.09	0.03	-0.46	0.08	0.02
NGC5735	0.07	0.06	0.03	0.38	0.26	0.05	-0.04	0.01	0.01	-0.051	0.003	0.134	0.025	-0.10	0.05	0.01	-0.006	0.004	-0.107	0.004	-0.01	0.01	0.01	-0.12	0.06	0.01	-0.10	0.01	0.01	-0.33	0.18	0.04
NGC5772	0.04	0.03	0.01	0.21	0.13	0.03	-0.02	0.02	0.01	0.004	0.009	-0.066	0.021	-0.09	0.04	0.01	-0.035	0.010	-0.037	0.006	-0.02	0.03	0.01	-0.11	0.04	0.01	-0.04	0.03	0.01	-0.18	0.07	0.02
NGC5829	0.17	0.11	0.07	6.72	4.51	0.88	-0.15	0.07	0.04	-0.080	0.005	-1.051	0.067	-0.35	0.19	0.04	-0.564	0.066	0.219	0.061	-0.16	0.06	0.03	-0.36	0.19	0.04	-0.36	0.03	0.02	-0.55	0.22	0.04
NGC6004	0.13	0.08	0.02	0.29	0.21	0.04	-0.08	0.03	0.01	-0.062	0.017	-0.062	0.055	-0.11	0.04	0.01	-0.064	0.014	-0.045	0.013	-0.09	0.04	0.01	-0.13	0.05	0.01	-0.21	0.07	0.02	-0.29	0.07	0.02
NGC6032	0.12	0.13	0.06	5.65	6.08	1.24	-0.11	0.08	0.04	-0.217	0.009	0.724	0.052	-0.19	0.17	0.04	-0.004	0.075	-0.160	0.059	-0.11	0.08	0.04	-0.20	0.17	0.04	-0.12	0.08	0.04	-0.24	0.19	0.04
NGC6154	0.04	0.02	0.01	0.14	0.10	0.02	-0.01	0.01	0.00	-0.011	0.002	0.019	0.006	-0.06	0.04	0.01	0.062	0.005	-0.081	0.003	-0.01	0.01	0.00	-0.07	0.05	0.01	-0.02	0.02	0.01	-0.13	0.10	0.02
NGC6186	0.20	0.13	0.08	0.23	0.22	0.04	-0.17	0.02	0.01	-0.154	0.001	-0.206	0.007	-0.08	0.04	0.01	-0.087	0.015	0.008	0.010	-0.19	0.02	0.01	-0.08	0.05	0.01	-0.24	0.04	0.02	-0.18	0.06	0.01
NGC6278	0.01	0.03	0.01	0.10	0.17	0.04	0.00	0.00	0.00	-0.005	0.002	0.003	0.002	-0.02	0.04	0.01	0.094	0.023	-0.045	0.009	0.00	0.00	0.00	-0.03	0.04	0.01	-0.01	0.01	0.00	-0.03	0.04	0.01
NGC6941	0.06	0.06	0.03	0.58	1.09	0.20	-0.02	0.02	0.01	-0.042	0.002	0.150	0.013	-0.10	0.12	0.02	0.122	0.037	-0.184	0.028	-0.03	0.03	0.01	-0.12	0.12	0.02	-0.04	0.02	0.01	-0.21	0.20	0.04
NGC7321	0.05	0.06	0.03	0.42	0.46	0.10	-0.02	0.01	0.00	-0.031	0.001	0.059	0.004	-0.12	0.06	0.01	-0.034	0.021	-0.067	0.015	-0.03	0.02	0.01	-0.14	0.07	0.01	-0.08	0.02	0.01	-0.27	0.11	0.02
NGC7489	0.54	0.23	0.13	13.71	10.51	1.89	-0.28	0.04	0.02	-0.326	0.006	0.610	0.064	-0.56	0.26	0.05	-0.250	0.081	-0.254	0.059	-0.31	0.05	0.03	-0.60	0.27	0.05	-0.45	0.06	0.03	-0.74	0.30	0.05
NGC7625	0.44	0.17	0.07	0.53	0.48	0.09	-0.27	0.08	0.03	-0.160	0.007	-0.536	0.029	-0.20	0.14	0.03	-0.346	0.058	0.089	0.034	-0.28	0.08	0.03	-0.22	0.15	0.03	-0.62	0.03	0.01	-0.40	0.16	0.03
NGC7653	0.13	0.09	0.03	1.43	0.88	0.17	-0.07	0.04	0.02	-0.025	0.023	-0.168	0.079	-0.27	0.10	0.02	-0.085	0.031	-0.116	0.018	-0.07	0.05	0.02	-0.30	0.11	0.02	-0.13	0.07	0.03	-0.56	0.26	0.05
NGC7691	0.24	0.11	0.06	6.60	4.62	0.91	-0.13	0.01	0.00	-0.120	0.005	-0.096	0.054	-0.62	0.23	0.05	-0.367	0.096	-0.319	0.111	-0.13	0.00	0.00	-0.63	0.23	0.04	-0.16	0.01	0.00	-0.68	0.23	0.05
NGC7716	0.08	0.09	0.03	0.67	0.50	0.11	-0.03	0.03	0.01	0.002	0.011	-0.088	0.023	-0.16	0.07	0.01	0.020	0.010	-0.107	0.006	-0.04	0.03	0.01	-0.18	0.07	0.02	-0.06	0.04	0.01	-0.31	0.17	0.04
NGC7738	0.37	0.26	0.13	0.42	0.73	0.14	-0.28	0.14	0.07	-0.444	0.005	1.058	0.026	-0.07	0.09	0.02	0.031	0.010	-0.063	0.005	-0.31	0.15	0.08	-0.08	0.09	0.02	-0.39	0.16	0.08	-0.13	0.10	0.02
NGC7819	0.49	0.26	0.09	2.58	1.68	0.40	-0.33	0.12	0.04	-0.478	0.037	0.612	0.124	-0.25	0.15	0.04	0.081	0.059	-0.284	0.048	-0.36	0.13	0.05	-0.27	0.17	0.04	-0.42	0.12	0.04	-0.52	0.25	0.06
UGC07012	0.33	0.14	0.06	5.42	4.52	1.07	-0.21	0.07	0.03	-0.121	0.028	-0.324	0.084	-0.51	0.13	0.03	-0.247	0.040	-0.167	0.024	-0.22	0.07	0.03	-0.57	0.13	0.03	-0.55	0.02	0.01	-1.04	0.34	0.08
UGC08234	0.02	0.05	0.02	1.61	1.91	0.40	0.00	0.01	0.00	0.000	0.008	-0.009	0.017	-0.06	0.08	0.02	0.105	0.025	-0.056	0.008	0.00	0.01	0.00	-0.06	0.09	0.02	-0.29	0.08	0.03	-0.21	0.09	0.02
UGC08733	0.37	0.14	0.06	2.32	2.23	0.49	-0.18	0.01	0.00	-0.193	0.007	0.069	0.040	-0.26	0.09	0.02	-0.075	0.030	-0.203	0.031	-0.19	0.02	0.01	-0.28	0.11	0.02	-0.50	0.06	0.02	-0.80	0.25	0.05
UGC09067	0.18	0.14	0.08	6.29	6.95	1.52	-0.09	0.03	0.02	-0.062	0.000	-0.276	0.001	-0.30	0.10	0.02	-0.111	0.015	-0.121	0.009	-0.13	0.03	0.01	0.32	0.10	0.02	-0.22	0.01	0.01	-0.47	0.13	0.03
UGC09291	0.17	0.10	0.05	0.95	1.01	0.20	-0.09	0.01	0.01	-0.071	0.003	-0.167	0.021	-0.18	0.09	0.02	-0.015	0.022	-0.173	0.021	-0.10	0.01	0.01	-0.19	0.10	0.02	-0.20	0.03	0.02	-0.46	0.19	0.04
UGC09476	0.22	0.08	0.04	0.52	0.22	0.04	-0.12	0.01	0.00	-0.125	0.003	0.049	0.023	-0.18	0.04	0.01	-0.220	0.017	0.036	0.015	-0.14	0.01	0.01	-0.21	0.04	0.01	-0.21	0.01	0.00	-0.45	0.08	0.02
UGC10796	2.98	1.67	0.83	3.05	3.42	0.81	-0.34	0.02	0.01	-0.324	0.019	-0.093	0.114	-0.28	0.09	0.02	-0.202	0.046	-0.070	0.038	-0.47	0.09	0.05	-0.32	0.11	0.03	-1.09	0.36	0.18	-0.85	0.21	0.05
UGC12224	0.15	0.09	0.04	4.53	6.14	1.10	-0.09	0.03	0.01	-0.123	0.005	0.361	0.048	-0.34	0.26	0.05	0.169	0.053	-0.567	0.054	-0.10	0.03	0.01	-0.37	0.28	0.05	-0.13	0.02	0.01	-0.57	0.35	0.06

Chapter 5.

Structural Analysis of the Galaxy Sample

By applying the surface photometry methodology detailed in Chapter 3, the $surface\ brightness\ profile$ (SBP) decomposition was obtained for the 66 analyzed galaxies of the sample, and a series of structural parameters were derived. In this Chapter, examples of the profile fitting and decomposition are presented for four sample galaxies, with the left-hand and right-hand side plots illustrating, respectively, the decomposition results prior to and after the subtraction of stars younger than 30 Myr (dmr30M) – by applying $RemoveYoung$ (RY) – on the SDSS r-band data – in Appendix B the reader will find the profile decompositions for the rest of the sample. Additionally, some of the estimated structural quantities obtained both before (D_1) and after (D_2) the application of RY are listed: Table 5.1 presents the estimated photometric parameters for the total SBP, disk and bar, and Table 5.2 presents the parameters for the bulge. Finally, this Chapter includes a brief study on relations between some of these quantities (Figs. 5.5 to 5.8) – in the left hand-side it is displayed the original obtained quantity and in the right hand-side the obtained quantity after applying RY – and the histograms of some of the more relevant structural quantities (Figs. 5.9 and 5.10).

SBP Decomposition

IC1256

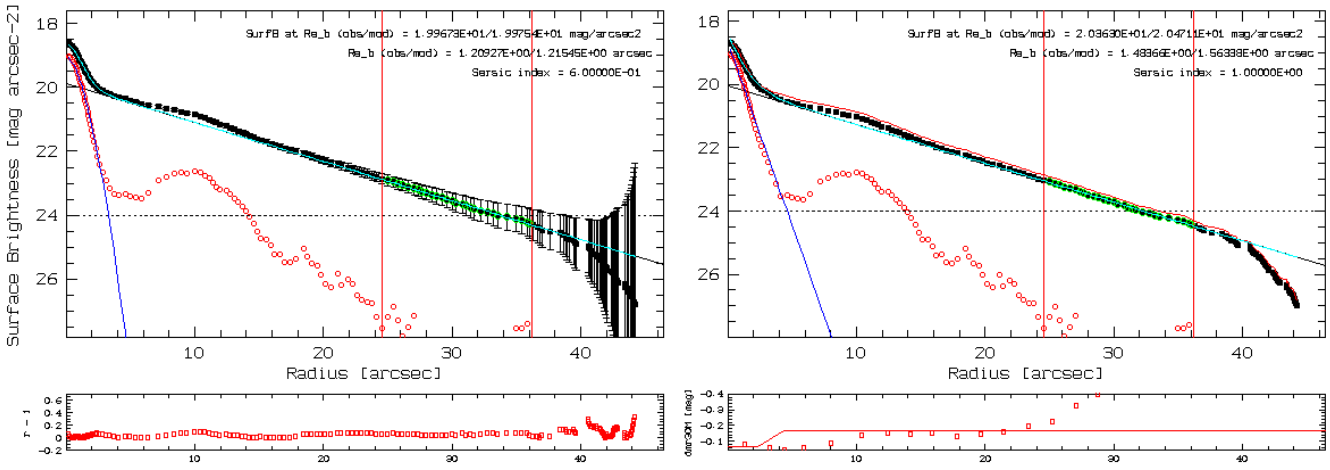

Figure 5.1: Photometric decomposition of IC1256.

NGC0023

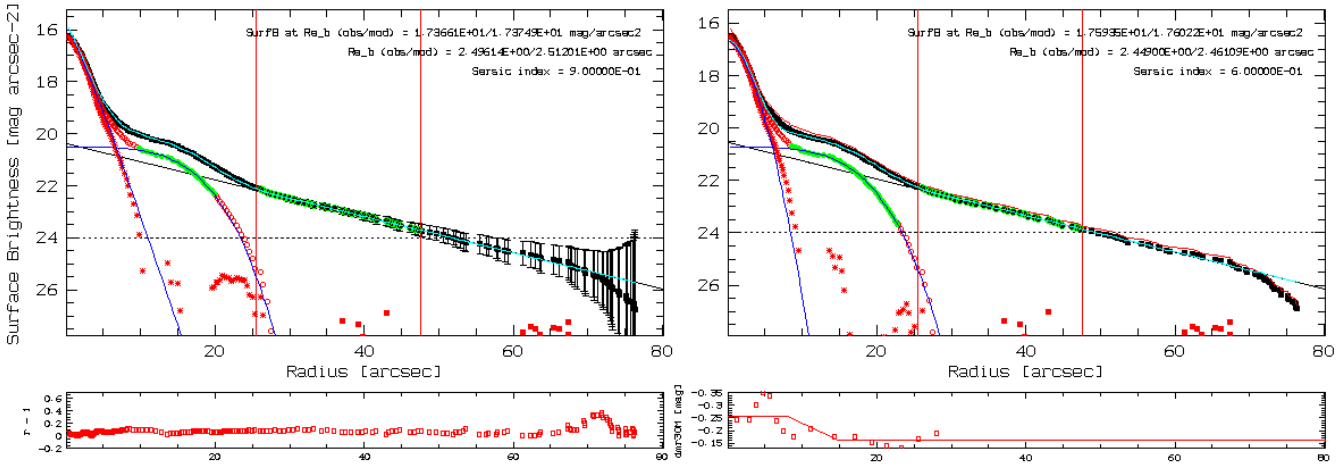

Figure 5.2: Photometric decomposition of NGC0023.

NGC3057

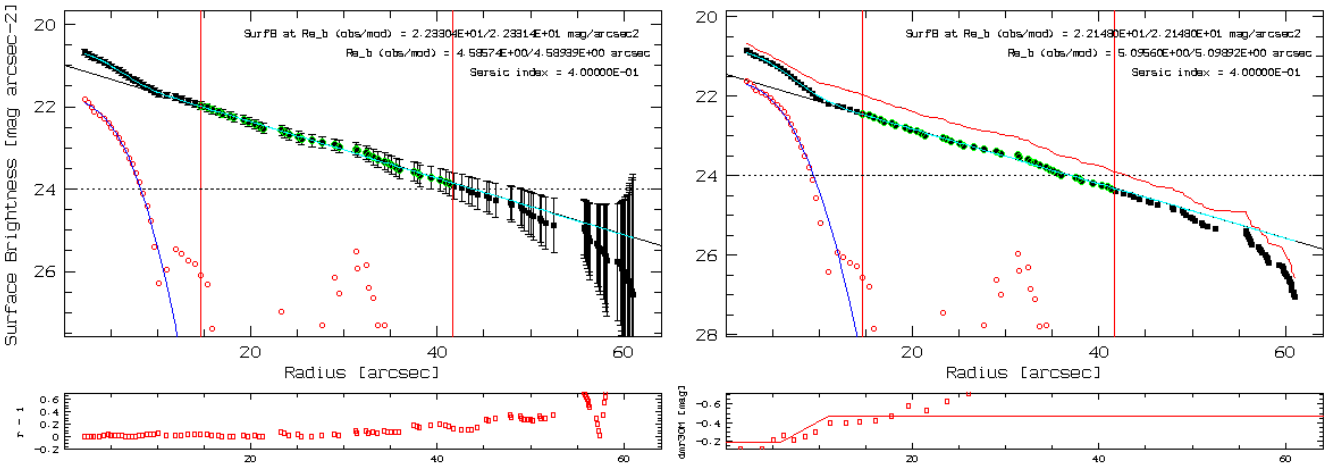

Figure 5.3: Photometric decomposition of NGC3057.

NGC6154

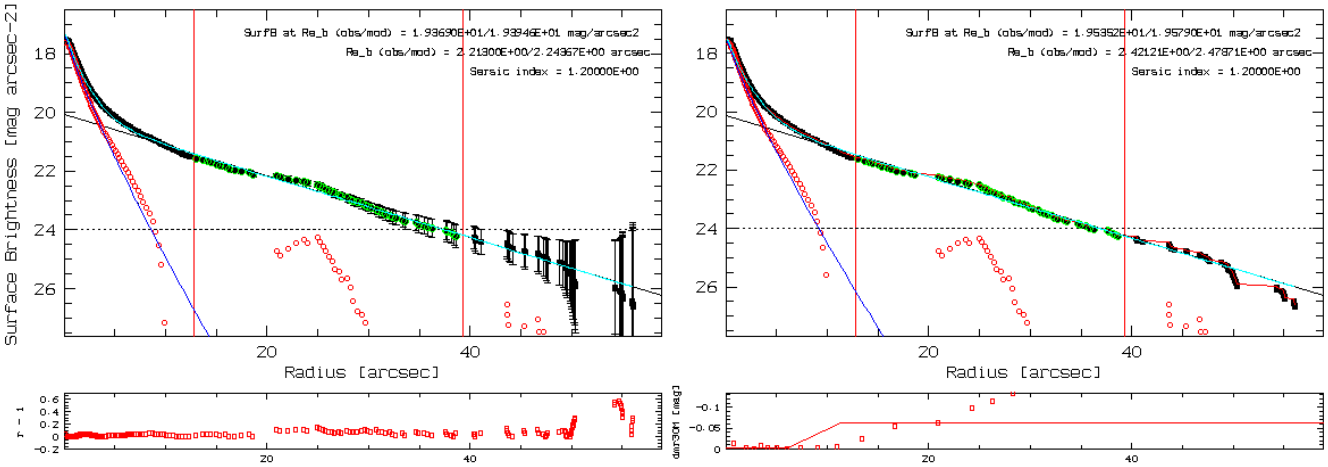

Figure 5.4: Photometric decomposition of NGC6154.

It follows a brief description of the decomposed SBP (Figs. 5.1 to 5.4 presented in this Chapter and the Figs. of Appendix B):

• the values displayed in the right-upper part of each diagram are relative to the bulge component and correspond to, respectively: the surface brightness ($SurfB\ at\ Re_b$) at the effective radius R_{50} obtained by integrating the observed bulge SBP (obs) and at the effective radius R_{mod} obtained by integrating the bulge SBP to infinity (mod), followed by the effective radius R_{50} (obs) and R_{mod} (mod) and Sérsic index.

• the filled black dots correspond, on the right-hand side, to the measured total SBP (in units of mag/arcsec^2) with respective error-bars, on the left-hand side to the total SBP obtained after application of RY;

• the two red vertical lines correspond to the radius range that were used to fit the exponential profile of the disk which is represented by a black solid line;

• the open red dots correspond to the excess emission after the subtraction of the disk exponential fit;

• the filled red starry symbols correspond to the excess emission after the subtraction of both disk and bar fits;

• the blue solid line corresponds to the bulge Sérsic fit and, when a bar is present, its Sérsic fit is also represented by a blue solid line;

• the blue cyan line corresponds to the summation of the different components that were fitted to the total SBP ($disk + bulge$ or $disk + bar + bulge$);

• the green points are the ones that were chosen to be the parameters for the fitting of both disk and bar;

• the bottom diagram below the SBP decomposition (left-hand side) shows the SDSS r - i radial profile and the one below the SBP decomposition after RY (right-hand side) shows the correction that was applied – the dots are the dmr30M [mag] and the solid red line the approximation that will be subtracted from the original SBP.

• in the right-hand side, the red solid line that appears above the SBP represents the original SBP pior to the correction with RY;

Briefly discussing the more prominent features of the SBP decompositions displayed above: in the case of IC1256 (Fig. 5.1) the disk presents a small bump that after subtracting the exponential fit becomes more prominent, appearing below the SBP next to the fitted bulge, marked with unfilled red dots. This emission cannot be quantified by the exponential disk fit nor by a bar Sérsic profile, and is thought to be the consequence of local episodes of stellar formation activity in HII regions. For some of the cases (e.g., IC4566 - Fig. B.2) it is evident that, some of these local star forming regions do not allow to derive a proper exponential fit for the disk – it is clear that the exponential fit is artificially elevated. By subtracting the overestimated disk as is common practice, one would be systematically underestimating the bulge contribution. The method for applying RY that was adopted as a first experiment is not sensitive enough to be able to remove from the SBP this local emission. However, in the small diagram bellow the SBP decomposition on the right-hand side, it is possible to visually identify the bump between ~ 6 and ~ 10.8 arcsec. This suggests that, by adopting a higher resolution method to fit the dmr30M data – for instance, through spline interpolation – and also define a higher cutoff for RY in order to estimate and remove the light contribution of relatively older stars (for instance, 100 Myr), one will be able to remove or attenuate this local extra emission. This will permit to derive a more realistic exponential fit to the disk continuum, and consequently to obtain a more realistic bulge.

Fig. 5.2 displays a classic example of a barred galaxy (see a) of Fig. 4.2 for true color). The bar is also evident in the total SBP before the subtraction of the disk component. By disregarding this contribution one would overestimate the bulge (by assuming the summed emission of the two components), leading this $\eta \sim 0.9$ Sérsic profile to escalate to $3 \leq \eta \leq 4$.

NGC3057 (see Fig. 5.3; a), Fig. 4.3 for true color) seems to be what is called a $bulgeless$ galaxy. As central surface brightness of the bulge this galaxy presents ~ 22 mag/arcsec^2 (left-hand side), but after RY application (right-hand side) the same value is increased by 0.2 mag.

As for NGC6154 (Fig. 5.4), one can also identify the extra emission aforementioned, forcing a lower α for the disk exponential fit, overestimating the disk contribution. By inspection of the true color image (a), Fig. 4.4) it is possible to identify a ring of star formation, that may be the cause of this extra emission.

Table 5.1: Photometric parameters obtained by applying the photometric methodology explained in Chapter 3 both for the original SBP (D_1) and after apllying RY (D_2). It is listed – from left to right – galaxy name, and the estimated quantities for: total absolute magnitude (M), effective radius (R_{eff}) (arcsec and kpc), disk absolute magnitude, disk effective radius (arcsec and kpc), disk central surface brightness (μ_0), disk scale-length (α), bar absolute magnitude, bar central surface brightness, bar scale-length, bar Sérsic index, bar-to-total (BA/T) (light fraction). All the absolute magnitudes where obtained by integrating the SBP to the photometric limit of 24 mag/arcsec^2.

Galaxy	Total						Disk										Bar								BA/T	
	M		R_{eff} [arsec]		R_{eff} [kpc]		M		R_{eff} [arsec]		R_{eff} [kpc]		μ_0		α		M		μ_0		α		η			
	D_1	D_2	D_1	D_2	D_1	D_2	D_1	D_2	D_1	D_2	D_1	D_2	D_1	D_2	D_1	D_2	D_1	D_2	D_1	D_2	D_1	D_2	D_1	D_2	D_1	D_2
IC0776	-18.96	-18.42	16.32	14.23	3.18	2.77	-18.88	-18.22	19.19	16.30	3.74	3.18	21.79	22.21	17.47	17.47	-16.18	-15.65	22.54	22.95	9.17	9.17	0.45	0.45	0.08	0.08
IC1256	-21.15	-20.97	12.56	12.31	4.39	4.30	-21.03	-20.84	13.38	13.20	4.68	4.61	19.87	20.04	8.86	8.86	-	-	-	-	-	-	-		-	-
IC4566	-21.71	-21.63	12.16	11.85	5.09	4.96	-21.56	-21.47	15.02	15.02	6.28	6.28	19.99	20.08	10.12	10.12	-18.86	-18.86	20.77	20.70	5.90	5.71	0.25	0.25	0.07	0.08
NGC0001	-21.43	-21.23	8.58	7.81	2.56	2.33	-20.81	-20.47	15.27	14.73	4.56	4.40	20.04	20.34	10.26	10.17	-	-	-	-	-	-	-		-	-
NGC0023	-22.28	-22.06	10.34	10.80	3.09	3.23	-21.33	-21.14	22.33	21.87	6.68	6.54	20.39	20.55	15.58	15.58	-20.74	-20.55	20.52	20.73	17.44	17.65	0.25	0.25	0.24	0.25
NGC0160	-21.96	-21.68	14.61	10.23	4.99	3.49	-21.49	-20.95	19.07	15.29	6.52	5.23	20.15	20.21	12.93	10.43	-	-	-	-	-	-	-		-	-
NGC0165	-21.35	-21.23	14.86	14.98	5.68	5.73	-21.28	-21.15	17.35	16.96	6.64	6.49	20.43	20.53	12.16	12.16	-	-	-	-	-	-	-		-	-
NGC0171	-21.67	-21.54	20.58	19.33	5.27	4.95	-21.56	-21.41	22.48	21.87	5.76	5.60	19.79	19.88	14.82	14.49	-	-	-	-	-	-	-		-	-
NGC0180	-22.11	-22.04	22.58	22.71	7.73	7.77	-22.11	-22.04	26.11	25.92	8.94	8.87	20.23	20.28	17.85	17.85	-18.78	-18.72	20.89	20.96	7.39	7.40	0.25	0.25	0.05	0.05
NGC0214	-22.04	-21.64	15.03	13.57	4.45	4.01	-21.89	-21.40	17.68	17.27	5.23	5.11	19.21	19.67	11.26	11.26	-19.49	-18.53	20.31	21.68	8.96	11.07	0.35	0.25	0.10	0.06
NGC0237	-20.88	-20.59	10.26	9.71	2.78	2.63	-20.61	-20.28	11.71	11.49	3.17	3.11	19.42	19.72	7.53	7.53	-18.78	-18.48	21.37	21.64	11.65	11.56	0.35	0.35	0.15	0.14
NGC0257	-22.00	-21.55	16.24	14.33	5.54	4.89	-21.94	-21.37	18.12	17.36	6.18	5.93	19.54	20.06	11.74	11.68	-	-	-	-	-	-	-		-	-
NGC0477	-21.47	-21.27	16.11	15.75	6.18	6.04	-21.46	-21.23	16.78	16.40	6.44	6.29	20.15	20.36	11.37	11.37	-	-	-	-	-	-	-		-	-
NGC0776	-21.81	-21.70	15.34	15.17	4.87	4.82	-21.67	-21.55	18.61	18.47	5.91	5.86	19.73	19.84	12.18	12.18	-18.44	-18.24	21.42	21.72	8.76	9.17	0.25	0.25	0.04	0.04
NGC1093	-21.40	-21.28	9.72	9.08	3.34	3.12	-21.09	-20.91	13.75	13.58	4.72	4.66	19.83	19.99	9.09	9.09	-19.35	-19.37	20.56	20.48	8.18	7.95	0.25	0.25	0.15	0.17
NGC1645	-21.67	-21.53	9.71	7.96	3.10	2.54	-21.11	-20.80	17.94	17.37	5.73	5.55	20.26	20.52	12.28	12.28	-19.34	-19.21	21.32	21.41	12.50	12.32	0.25	0.25	0.12	0.12
NGC2253	-21.44	-21.21	13.85	13.20	3.44	3.28	-21.28	-20.98	14.12	13.07	3.51	3.25	18.94	19.08	8.87	8.26	-	-	-	-	-	-	-		-	-
NGC2347	-21.89	-21.57	11.16	9.73	3.41	2.97	-21.60	-21.16	14.32	13.93	4.37	4.25	19.11	19.51	9.06	9.06	-19.80	-19.92	19.38	18.91	6.52	5.51	0.25	0.35	0.15	0.22
NGC2639	-22.09	-22.05	11.59	11.52	2.79	2.77	-21.65	-21.60	16.71	16.59	4.02	3.99	18.86	18.90	10.45	10.41	-	-	-	-	-	-	-		-	-
NGC2730	-20.66	-20.22	18.49	17.50	5.08	4.81	-20.71	-20.21	19.85	18.64	5.46	5.12	20.59	21.01	14.15	14.15	-	-	-	-	-	-	-		-	-
NGC2906	-20.71	-20.63	14.60	14.35	2.37	2.33	-20.69	-20.58	15.38	15.32	2.50	2.49	18.79	18.89	9.60	9.60	-	-	-	-	-	-	-		-	-
NGC2916	-21.91	-21.73	19.49	18.83	5.29	5.11	-21.91	-21.70	22.04	21.77	5.98	5.91	19.50	19.69	14.23	14.22	-	-	-	-	-	-	-		-	-
NGC3057	-18.81	-18.28	19.89	17.14	2.50	2.15	-18.77	-18.15	20.93	18.73	2.63	2.35	20.99	21.46	15.81	15.81	-	-	-	-	-	-	-		-	-
NGC3300	-21.27	-21.22	10.98	10.78	2.55	2.51	-21.02	-20.96	13.52	13.52	3.15	3.15	18.97	19.03	8.51	8.51	-18.89	-18.95	19.30	19.05	5.14	4.61	0.50	0.55	0.11	0.12
NGC3381	-19.83	-19.55	18.78	18.59	2.62	2.60	-19.75	-19.48	20.22	19.73	2.82	2.75	20.06	20.30	13.60	13.60	-16.02	-15.67	22.61	22.95	11.83	12.08	0.25	0.25	0.03	0.03
NGC3614	-20.79	-20.66	28.72	28.32	5.35	5.27	-20.75	-20.59	30.00	29.12	5.58	5.42	20.60	20.73	21.42	21.42	-16.72	-16.54	22.44	22.56	11.14	11.14	0.25	0.25	0.02	0.02
NGC3687	-20.66	-20.56	15.34	14.69	3.06	2.93	-20.41	-20.28	18.17	18.08	3.62	3.60	19.94	20.06	12.17	12.17	-17.49	-17.42	23.17	23.00	22.51	20.57	0.25	0.35	0.05	0.06
NGC4003	-21.77	-21.72	8.60	8.60	4.03	4.03	-21.47	-21.42	11.35	11.30	5.31	5.29	19.70	19.74	7.42	7.42	-18.70	-18.58	22.07	22.25	9.16	9.49	0.25	0.25	0.06	0.06
NGC4047	-21.67	-21.45	13.73	13.41	3.55	3.47	-21.52	-21.29	15.56	15.42	4.02	3.99	19.00	19.22	9.80	9.80	-19.03	-18.90	19.93	19.95	6.99	6.58	0.30	0.35	0.09	0.09
NGC4185	-21.67	-21.59	23.58	23.22	6.97	6.87	-21.68	-21.60	24.90	24.90	7.36	7.36	20.25	20.32	17.18	17.18	-	-	-	-	-	-	-		-	-
NGC4210	-20.83	-20.71	18.88	18.63	3.96	3.90	-20.49	-20.26	16.91	15.39	3.54	3.22	19.80	19.83	11.13	10.16	-	-	-	-	-	-	-		-	-
NGC4961	-19.99	-19.51	10.52	9.56	2.17	1.97	-19.66	-19.10	13.78	13.03	2.84	2.69	20.17	20.67	9.37	9.37	-18.32	-18.00	20.69	20.67	8.97	7.46	0.30	0.45	0.22	0.25
NGC5000	-21.45	-21.27	12.70	12.38	5.23	5.10	-21.29	-21.10	14.86	14.63	6.12	6.02	20.23	20.40	10.17	10.17	-19.01	-18.84	20.15	20.23	4.18	3.93	0.70	0.75	0.11	0.11
NGC5016	-20.86	-20.61	14.81	14.47	3.12	3.05	-20.82	-20.56	15.35	15.10	3.24	3.19	19.24	19.48	9.76	9.76	-16.94	-16.66	21.98	22.24	8.62	8.66	0.25	0.25	0.03	0.03

Table 5.1 Continued.

NGC5205	-19.89	-19.70	14.44	13.06	2.16	1.96	-19.76	-19.49	15.96	15.73	2.39	2.36	19.67	19.92	10.46	10.46	-	-	-	-	-	-	-		-	-
NGC5320	-20.85	-20.66	18.72	17.94	3.96	3.79	-20.81	-20.62	18.99	18.81	4.01	3.98	19.75	19.93	12.51	12.51	-	-	-	-	-	-	-		-	-
NGC5378	-21.10	-21.06	18.65	18.17	4.48	4.37	-20.82	-20.76	25.85	25.68	6.22	6.18	20.79	20.83	18.91	18.91	-18.55	-18.62	21.43	21.18	12.16	11.08	0.25	0.35	0.10	0.11
NGC5406	-22.32	-22.27	16.19	15.95	6.20	6.11	-22.18	-22.10	19.24	19.05	7.37	7.30	19.70	19.76	12.57	12.57	-19.04	-18.98	20.81	20.34	7.14	6.21	0.25	0.35	0.05	0.05
NGC5480	-20.54	-20.12	18.54	17.93	2.96	2.86	-20.42	-19.97	19.07	17.98	3.04	2.87	19.51	19.87	12.31	11.95	-	-	-	-	-	-	-		-	-
NGC5614	-22.41	-22.39	13.21	13.19	3.93	3.93	-22.02	-21.99	19.28	19.14	5.74	5.70	19.29	19.30	12.28	12.24	-	-	-	-	-	-	-		-	-
NGC5656	-21.45	-21.29	12.05	11.35	3.00	2.83	-21.30	-21.08	13.27	13.15	3.31	3.28	18.78	19.00	8.28	8.28	-	-	-	-	-	-	-		-	-
NGC5735	-22.00	-21.93	18.71	18.40	5.41	5.32	-21.78	-21.68	21.41	21.41	6.19	6.19	20.37	20.47	15.10	15.10	-	-	21.65	21.54	7.87	7.34	0.30	0.35	-	-
NGC5772	-21.35	-20.97	13.37	12.76	4.85	4.63	-21.26	-20.86	16.10	16.00	5.84	5.80	19.58	19.68	10.44	10.44	-18.65	-18.28	-	-	-	-	-		0.08	0.08
NGC5829	-21.68	-21.57	15.85	15.11	6.59	6.28	-21.77	-21.65	17.35	16.53	7.22	6.88	20.65	20.99	12.48	12.48	-	-	20.26	20.61	3.80	3.81	0.65	0.65	-	-
NGC6004	-21.13	-20.94	21.15	20.74	6.23	6.11	-20.99	-20.80	26.30	26.30	7.75	7.75	20.27	20.40	18.34	18.34	-	-	-	-	-	-	-		-	-
NGC6032	-21.79	-21.74	14.05	13.66	4.56	4.44	-21.57	-21.51	14.63	14.49	4.75	4.71	19.95	20.14	9.81	9.81	-	-	-	-	-	-	-		-	-
NGC6154	-21.11	-21.02	12.49	12.08	5.37	5.19	-20.94	-20.85	15.27	15.27	6.56	6.56	20.09	20.15	10.41	10.41	-18.66	-18.55	-	-	-	-	-		0.10	0.10
NGC6186	-21.45	-21.44	11.90	12.02	2.77	2.80	-21.02	-21.00	13.66	13.56	3.19	3.16	19.08	19.16	8.62	8.62	-	-	18.91	19.03	4.02	4.06	0.35	0.35	-	-
NGC6278	-22.22	-22.10	8.91	8.73	1.98	1.94	-22.09	-21.95	16.37	16.22	3.64	3.60	19.29	19.30	10.45	10.35	-19.13	-19.04	-	-	-	-	-		0.06	0.06
NGC6941	-22.32	-22.21	16.47	15.94	7.08	6.85	-22.24	-22.12	19.76	19.54	8.49	8.40	20.12	20.25	13.37	13.37	-18.21	-18.49	20.62	20.72	6.07	6.09	0.25	0.25	0.02	0.03
NGC7321	-22.27	-21.74	12.09	11.79	5.74	5.60	-22.26	-21.71	13.17	13.08	6.25	6.21	19.25	19.37	8.38	8.38	-	-	21.34	20.94	5.04	4.76	0.25	0.25	-	-
NGC7489	-20.14	-19.89	14.69	14.20	6.06	5.86	-19.92	-19.68	15.20	14.79	6.27	6.10	19.24	19.76	9.71	9.71	-17.96	-17.56	-	-	-	-	-		0.13	0.12
NGC7625	-21.50	-21.28	12.52	12.65	1.44	1.45	-21.21	-20.90	15.84	15.70	1.82	1.80	18.88	19.11	9.92	9.92	-19.07	-18.92	19.43	20.09	7.57	8.60	0.35	0.25	0.11	0.11
NGC7653	-21.01	-20.40	12.18	11.00	3.44	3.11	-21.01	-20.33	17.17	16.82	4.85	4.75	19.76	20.05	11.29	11.29	-17.31	-16.59	20.79	20.87	9.71	9.44	0.25	0.25	0.03	0.03
NGC7691	-20.79	-20.68	20.92	19.30	5.60	5.16	-20.51	-20.32	22.57	20.82	6.04	5.57	20.51	21.08	16.00	16.00	-	-	21.48	22.26	6.37	6.74	0.30	0.25	-	-
NGC7716	-21.86	-21.76	13.42	12.30	2.32	2.12	-21.59	-21.51	19.81	19.53	3.42	3.37	19.69	19.86	12.94	12.91	-19.62	-19.34	-	-	-	-	-		0.13	0.11
NGC7738	-20.83	-20.53	9.90	10.20	4.39	4.52	-20.70	-20.37	12.47	12.42	5.53	5.50	19.66	19.73	8.13	8.13	-	-	19.43	20.15	3.85	5.05	0.60	0.45	-	-
NGC7819	-19.62	-19.14	14.16	14.03	4.61	4.57	-19.18	-18.56	17.44	16.70	5.68	5.44	20.70	20.98	12.61	12.67	-18.13	-17.72	-	-	-	-	-		0.25	0.27
UGC07012	-22.60	-22.57	9.17	7.96	2.20	1.91	-21.96	-21.91	12.13	11.08	2.91	2.65	20.78	21.28	8.87	8.87	-20.88	-20.72	21.20	21.41	8.97	8.14	0.40	0.45	0.21	0.18
UGC08234	-19.33	-19.02	5.61	5.41	3.16	3.05	-19.29	-18.97	13.11	13.08	7.38	7.36	19.93	19.98	8.73	8.73	-	-	19.67	19.91	6.66	6.91	0.25	0.25	-	-
UGC08733	-21.69	-21.40	17.87	16.98	3.44	3.27	-21.61	-21.31	18.30	17.55	3.52	3.38	21.14	21.40	14.39	14.39	-17.99	-17.57	-	-	-	-	-		0.03	0.03
UGC09067	-20.29	-20.06	8.50	8.20	4.79	4.62	-20.31	-20.09	9.05	8.89	5.10	5.01	19.44	19.73	5.83	5.83	-	-	21.30	21.87	3.73	4.11	0.40	0.35	-	-
UGC09291	-20.75	-20.56	18.64	18.06	4.30	4.17	-20.92	-20.74	19.46	18.96	4.49	4.38	20.57	20.76	13.92	13.92	-16.87	-16.71	-	-	-	-	-		0.03	0.03
UGC09476	-19.28	-18.93	17.65	17.41	4.48	4.42	-19.13	-18.77	21.77	21.77	5.52	5.52	20.41	20.59	15.69	15.69	-16.75	-16.38	22.22	22.26	7.84	7.50	0.25	0.25	0.10	0.10
UGC10796	-20.63	-20.20	10.98	10.41	2.55	2.42	-20.72	-20.24	12.56	11.89	2.92	2.77	20.84	21.13	9.26	9.26	-15.94	-15.27	20.60	21.07	3.42	3.71	0.60	0.55	0.01	0.01
UGC12224	-20.69	-20.31	22.18	20.97	5.24	4.95	-20.77	-20.37	24.85	23.53	5.87	5.56	20.77	21.17	18.37	18.37	-16.28	-15.88	23.24	23.65	9.87	9.89	0.25	0.25	0.02	0.02

Table 5.2: Photometric parameters regarding the bulge, as in the previous table. It is listed – from left to right – galaxy name, bulge absolute magnitude, bulge radius (R_{iso}, assumed to be the radius where the surface brightness of the bulge is 24 mag/arcsec^2), bulge effective radius, bulge R_{80}, surface brightness at bulge effective radius, bulge Sérsic index, bulge CI8020 concentration index (R_{80}/R_{20}), CIP96 concentration index (Papaderos et al., 1996a), B/T, bulge-to-disk (B/D) and bulge to bar (B/BA) (light fraction).

Galaxy	Bulge																									
	M		R_{iso}				R_{eff}				R_{80}				μ_{iso}		η		CI8020		CIP96		B/T		B/D		B/BA	
			[arsec]		[kpc]		[arsec]		[kpc]		[arsec]		[kpc]															
	D_1	D_2	D_1	D_2	D_1	D_2	D_1	D_2	D_1	D_2	D_1	D_2	D_1	D_2	D_1	D_2	D_1	D_2	D_1	D_2	D_1	D_2	D_1	D_2	D_1	D_2	D_1	D_2
IC0776	-14.87	-14.96	4.76	5.06	0.93	0.99	2.69	2.89	0.52	0.56	4.17	4.31	0.81	0.84	22.53	22.52	0.50	0.45	2.10	2.00	0.98	0.97	0.02	0.04	0.02	0.05	0.30	0.53
IC1256	-17.19	-17.44	3.38	5.00	1.18	1.75	1.22	1.32	0.42	0.46	1.95	2.28	0.68	0.80	19.98	20.11	0.60	1.00	4.20	4.39	0.82	0.81	0.03	0.04	0.03	0.04	-	-
IC4566	-19.08	-19.07	4.66	4.66	1.95	1.95	1.47	1.50	0.62	0.63	2.36	2.37	0.99	0.99	18.91	18.96	0.60	0.60	2.42	2.42	0.98	0.98	0.09	0.09	0.10	0.11	1.22	1.21
NGC0001	-20.34	-20.32	16.02	16.83	4.78	5.03	3.79	3.85	1.13	1.15	7.70	7.46	2.30	2.23	19.36	19.46	1.50	1.70	3.77	3.85	0.80	0.76	0.36	0.43	0.64	0.87	-	-
NGC0023	-21.22	-20.78	11.47	8.61	3.43	2.57	2.51	2.50	0.75	0.75	4.39	3.94	1.31	1.18	17.37	17.63	0.90	0.60	2.49	2.45	0.96	0.97	0.38	0.31	0.90	0.71	1.56	1.23
NGC0160	-20.40	-20.42	12.50	13.21	4.27	4.52	3.15	3.35	1.08	1.14	5.82	5.96	1.99	2.04	19.05	19.17	1.10	1.10	3.12	3.21	0.93	0.92	0.24	0.31	0.37	0.61	-	-
NGC0165	-19.20	-19.03	7.76	7.47	2.97	2.86	2.16	2.09	0.83	0.80	3.98	3.74	1.52	1.43	19.67	19.76	1.10	1.10	2.59	2.52	0.96	0.96	0.14	0.13	0.15	0.14	-	-
NGC0171	-19.30	-19.32	12.56	13.11	3.21	3.36	3.31	3.34	0.85	0.85	6.42	5.91	1.64	1.51	19.69	19.68	1.30	1.20	2.90	2.96	0.96	0.96	0.11	0.13	0.13	0.15	-	-
NGC0180	-18.85	-18.64	5.24	5.02	1.79	1.72	1.74	1.71	0.60	0.59	2.79	2.70	0.96	0.92	19.06	19.23	0.60	0.60	2.36	2.31	0.99	0.99	0.05	0.04	0.05	0.04	1.07	0.93
NGC0214	-18.63	-19.51	5.66	10.17	1.67	3.01	1.83	2.95	0.54	0.87	2.92	5.03	0.86	1.49	19.07	19.40	0.60	0.90	2.38	2.64	0.99	0.96	0.04	0.14	0.05	0.18	0.45	2.46
NGC0237	-17.80	-17.96	5.98	7.24	1.62	1.96	2.01	2.42	0.55	0.65	3.42	4.00	0.93	1.08	20.02	20.26	0.80	0.80	2.59	2.64	0.97	0.96	0.06	0.09	0.08	0.12	0.41	0.62
NGC0257	-19.39	-19.70	7.22	11.03	2.46	3.77	2.12	2.50	0.72	0.85	3.61	4.52	1.23	1.54	19.07	19.33	0.80	1.30	2.87	3.00	0.97	0.96	0.09	0.18	0.09	0.21	-	-
NGC0477	-18.14	-18.29	4.71	5.44	1.81	2.09	1.70	1.85	0.65	0.71	2.72	3.02	1.04	1.16	19.95	20.05	0.60	0.70	2.34	2.37	0.99	0.98	0.05	0.06	0.05	0.07	-	-
NGC0776	-19.43	-19.37	5.63	5.86	1.79	1.86	1.74	1.81	0.55	0.57	2.78	2.85	0.88	0.91	18.32	18.46	0.60	0.60	2.39	2.43	0.98	0.98	0.11	0.12	0.13	0.13	2.49	2.83
NGC1093	-18.94	-18.90	6.99	6.74	2.40	2.31	2.07	2.10	0.71	0.72	3.61	3.47	1.24	1.19	19.51	19.54	0.90	0.80	2.61	2.62	0.97	0.97	0.10	0.11	0.14	0.16	0.68	0.65
NGC1645	-20.25	-20.39	9.90	11.79	3.16	3.77	2.67	2.88	0.85	0.92	4.54	5.06	1.45	1.62	18.57	18.68	0.80	1.00	2.76	2.82	0.95	0.94	0.27	0.35	0.45	0.68	2.31	2.97
NGC2253	-18.76	-18.68	6.34	6.66	1.58	1.66	1.48	1.63	0.37	0.41	2.66	2.87	0.66	0.71	18.34	18.62	1.00	1.00	2.78	2.95	0.98	0.97	0.08	0.10	0.10	0.12	-	-
NGC2347	-18.98	-18.37	5.77	3.57	1.76	1.09	1.38	1.18	0.42	0.36	2.48	1.80	0.76	0.55	18.40	18.38	1.00	0.50	2.54	2.38	0.99	0.99	0.07	0.05	0.09	0.08	0.47	0.24
NGC2639	-20.75	-20.79	20.84	22.62	5.01	5.44	5.01	5.18	1.20	1.24	9.48	9.77	2.28	2.35	18.98	19.08	1.20	1.40	3.41	3.41	0.85	0.85	0.29	0.32	0.44	0.48	-	-
NGC2730	-16.88	-17.03	5.50	6.51	1.51	1.79	2.10	2.64	0.58	0.73	3.66	4.52	1.01	1.24	21.06	21.38	0.90	0.90	2.69	2.60	0.98	0.97	0.03	0.05	0.03	0.05	-	-
NGC2906	-17.73	-17.84	6.29	7.20	1.02	1.17	1.54	1.72	0.25	0.28	2.76	3.09	0.45	0.50	18.51	18.69	1.00	1.10	2.53	2.71	0.99	0.98	0.06	0.08	0.07	0.08	-	-
NGC2916	-18.99	-19.10	7.44	8.99	2.02	2.44	1.90	2.22	0.52	0.60	3.41	3.98	0.93	1.08	18.82	19.10	1.00	1.10	2.84	3.03	0.98	0.97	0.07	0.09	0.07	0.09	-	-
NGC3057	-15.27	-15.70	8.47	9.70	1.06	1.22	4.59	5.23	0.58	0.66	6.91	7.67	0.87	0.96	22.33	22.18	0.40	0.40	2.20	2.05	0.96	0.94	0.04	0.09	0.04	0.10	-	-
NGC3300	-18.51	-18.44	5.13	5.13	1.19	1.19	1.45	1.44	0.34	0.34	2.39	2.34	0.56	0.55	18.23	18.29	0.70	0.70	2.48	2.49	0.99	0.99	0.08	0.08	0.10	0.10	0.70	0.63
NGC3381	-16.39	-15.97	6.32	5.57	0.88	0.78	2.42	2.24	0.34	0.31	3.68	3.47	0.51	0.48	20.21	20.51	0.45	0.50	1.91	1.78	0.99	0.99	0.04	0.04	0.05	0.04	1.42	1.32
NGC3614	-16.55	-16.67	6.30	6.90	1.17	1.28	2.38	2.69	0.44	0.50	3.93	4.37	0.73	0.81	20.74	20.88	0.70	0.70	2.49	2.54	0.99	0.99	0.02	0.03	0.02	0.03	0.86	1.12
NGC3687	-18.54	-18.46	9.21	8.64	1.84	1.72	2.19	2.35	0.44	0.47	4.14	4.04	0.83	0.81	18.99	19.10	1.20	0.90	2.85	2.91	0.97	0.97	0.14	0.14	0.18	0.19	2.62	2.60
NGC4003	-19.87	-19.79	7.04	6.61	3.30	3.09	2.06	2.13	0.97	1.00	3.50	3.46	1.64	1.62	19.21	19.29	0.80	0.70	2.58	2.59	0.96	0.95	0.17	0.17	0.23	0.22	2.94	3.04
NGC4047	-17.35	-17.35	4.11	4.42	1.06	1.14	1.32	1.48	0.34	0.38	2.11	2.33	0.54	0.60	19.35	19.60	0.60	0.60	2.45	2.58	0.99	0.99	0.02	0.02	0.02	0.03	0.21	0.24
NGC4185	-18.22	-18.36	8.14	9.33	2.41	2.76	2.63	2.55	0.78	0.75	4.98	4.76	1.47	1.41	20.51	20.43	1.20	1.50	2.91	3.01	0.97	0.97	0.04	0.05	0.04	0.05	-	-
NGC4210	-17.36	-17.55	5.67	6.57	1.19	1.38	1.96	2.05	0.41	0.43	3.14	3.53	0.66	0.74	19.73	19.80	0.60	0.90	2.47	2.50	0.98	0.98	0.04	0.05	0.06	0.08	-	-
NGC4961	-16.17	-16.13	5.13	5.77	1.06	1.19	2.03	2.30	0.42	0.47	3.34	3.79	0.69	0.78	20.99	21.35	0.70	0.80	2.52	2.49	0.98	0.97	0.03	0.04	0.04	0.06	0.14	0.18
NGC5000	-17.83	-17.74	2.99	2.99	1.23	1.23	0.95	1.00	0.39	0.41	1.52	1.59	0.63	0.65	19.20	19.38	0.60	0.60	2.32	2.38	0.99	0.99	0.04	0.04	0.04	0.05	0.34	0.36
NGC5016	-15.83	-16.17	3.17	4.10	0.67	0.86	1.20	1.46	0.25	0.31	1.83	2.37	0.39	0.50	20.11	20.33	0.45	0.70	2.24	2.39	1.00	0.99	0.01	0.02	0.01	0.02	0.36	0.64

Table 5.2 Continued.

NGC5205	-17.43	-17.76	8.64	12.21	1.29	1.83	2.33	3.08	0.35	0.46	4.41	5.75	0.66	0.86	19.60	19.97	1.20	1.50	3.25	3.14	0.94	0.93	0.10	0.17	0.12	0.20	-	-
NGC5320	-16.91	-17.28	6.34	7.96	1.34	1.68	2.13	2.49	0.45	0.53	3.73	4.43	0.79	0.94	20.53	20.62	0.90	1.20	2.51	2.63	0.99	0.98	0.03	0.04	0.03	0.05	-	-
NGC5378	-18.87	-18.88	8.84	8.84	2.12	2.12	2.30	2.23	0.55	0.54	4.23	4.10	1.02	0.99	19.13	19.09	1.10	1.20	3.16	3.15	0.98	0.98	0.13	0.13	0.17	0.18	1.34	1.27
NGC5406	-19.81	-19.84	5.85	6.15	2.24	2.35	1.53	1.49	0.59	0.57	2.60	2.49	1.00	0.95	18.19	18.18	0.80	0.80	2.58	2.53	0.99	0.99	0.10	0.11	0.11	0.12	2.03	2.20
NGC5480	-17.56	-17.05	6.86	5.70	1.09	0.91	1.79	1.81	0.29	0.29	3.21	2.94	0.51	0.47	18.96	19.34	1.00	0.70	2.50	2.51	0.99	0.98	0.06	0.06	0.07	0.07	-	-
NGC5614	-21.35	-21.27	25.99	23.95	7.74	7.13	3.62	3.27	1.08	0.97	10.73	6.46	3.19	1.92	18.67	18.48	3.80	3.30	3.67	3.67	0.92	0.92	0.37	0.35	0.54	0.51	-	-
NGC5656	-18.99	-19.10	10.54	13.55	2.63	3.38	1.69	2.19	0.42	0.54	4.79	4.48	1.19	1.12	18.79	19.33	2.90	3.80	5.02	4.50	0.86	0.86	0.10	0.13	0.12	0.16	-	-
NGC5735	-20.25	-20.25	4.85	4.85	1.40	1.40	1.64	1.70	0.47	0.49	2.71	2.77	0.78	0.80	20.17	20.25	0.70	0.70	2.49	2.51	0.99	0.99	0.20	0.21	0.24	0.27	-	-
NGC5772	-16.32	-16.60	10.46	10.46	3.79	3.79	1.73	2.17	0.63	0.79	3.68	4.19	1.34	1.52	18.25	18.70	1.70	1.70	2.93	3.01	0.98	0.97	0.01	0.02	0.01	0.02	0.12	0.21
NGC5829	-18.95	-18.86	2.18	2.72	0.91	1.13	0.89	1.07	0.37	0.44	1.37	1.68	0.57	0.70	20.47	20.64	0.50	0.60	2.20	2.25	1.00	0.99	0.08	0.08	0.07	0.08	-	-
NGC6004	-18.06	-18.00	11.47	11.97	3.38	3.53	2.69	3.38	0.79	1.00	7.51	6.57	2.21	1.94	20.24	20.72	3.20	2.50	3.86	3.95	0.95	0.94	0.06	0.07	0.07	0.08	-	-
NGC6032	-19.85	-19.88	4.34	4.83	1.41	1.57	1.22	1.40	0.40	0.46	2.13	2.41	0.69	0.78	19.12	19.49	0.90	0.90	2.80	2.89	0.98	0.98	0.17	0.18	0.21	0.22	-	-
NGC6154	-17.00	-16.62	8.73	9.28	3.75	3.99	2.24	2.54	0.96	1.09	4.25	4.68	1.83	2.01	19.39	19.63	1.20	1.20	3.14	3.18	0.94	0.93	0.02	0.02	0.03	0.02	0.22	0.17
NGC6186	-20.30	-20.30	2.73	2.59	0.64	0.60	1.02	0.96	0.24	0.22	1.54	1.40	0.36	0.33	18.78	19.00	0.40	0.40	2.15	2.10	1.00	1.00	0.35	0.35	0.51	0.52	-	-
NGC6278	-19.54	-19.54	14.02	14.02	3.11	3.11	2.54	2.46	0.56	0.55	5.16	4.66	1.15	1.04	17.90	17.84	1.50	1.50	3.31	3.32	0.93	0.93	0.09	0.09	0.10	0.11	1.46	1.58
NGC6941	-19.02	-19.01	5.44	5.44	2.34	2.34	1.53	1.65	0.66	0.71	2.60	2.68	1.12	1.15	18.71	18.81	0.80	0.70	2.60	2.67	0.99	0.99	0.05	0.05	0.05	0.06	2.11	1.62
NGC7321	-17.65	-17.75	4.42	4.42	2.10	2.10	1.34	1.36	0.63	0.65	2.20	2.21	1.05	1.05	19.09	19.13	0.70	0.70	2.47	2.47	0.99	0.99	0.01	0.03	0.01	0.03	-	-
NGC7489	-16.87	-16.78	2.42	3.08	1.00	1.27	1.04	1.18	0.43	0.49	1.50	1.77	0.62	0.73	19.47	19.66	0.30	0.40	2.61	2.41	1.00	0.99	0.05	0.06	0.06	0.07	0.37	0.49
NGC7625	-19.32	-19.34	5.71	6.01	0.66	0.69	2.39	2.63	0.27	0.30	3.53	3.71	0.41	0.43	19.16	19.41	0.30	0.30	2.32	2.30	0.99	0.98	0.13	0.17	0.18	0.24	1.26	1.47
NGC7653	-16.04	-16.91	6.81	7.22	1.93	2.04	1.82	1.99	0.51	0.56	3.09	3.34	0.87	0.94	18.39	18.57	0.80	0.80	2.70	2.79	0.98	0.97	0.01	0.04	0.01	0.04	0.31	1.34
NGC7691	-19.28	-19.28	3.84	5.36	1.03	1.43	1.57	2.23	0.42	0.60	2.51	3.39	0.67	0.91	21.07	20.90	0.60	0.50	2.39	2.22	0.99	0.99	0.25	0.28	0.32	0.38	-	-
NGC7716	-19.08	-18.96	11.20	11.70	1.93	2.02	2.34	2.46	0.40	0.42	4.43	4.46	0.76	0.77	18.09	18.20	1.20	1.20	3.26	3.40	0.91	0.91	0.08	0.08	0.10	0.10	0.61	0.71
NGC7738	-18.88	-18.53	3.81	3.81	1.69	1.69	1.17	1.19	0.52	0.53	1.87	1.88	0.83	0.83	18.55	18.71	0.60	0.60	2.29	2.27	0.99	0.99	0.17	0.16	0.19	0.18	-	-
NGC7819	-16.82	-16.80	7.43	6.77	2.42	2.21	2.16	2.13	0.70	0.69	3.78	3.64	1.23	1.19	19.56	19.86	0.90	0.90	2.60	2.58	0.96	0.96	0.08	0.12	0.11	0.20	0.30	0.43
UGC07012	-21.23	-21.27	5.79	6.02	1.39	1.44	2.18	2.50	0.52	0.60	3.70	4.03	0.89	0.96	20.89	21.13	0.80	0.70	2.38	2.41	0.96	0.93	0.29	0.30	0.51	0.56	1.39	1.66
UGC08234	-15.49	-15.46	4.97	5.19	2.80	2.92	1.39	1.47	0.78	0.83	2.23	2.31	1.25	1.30	17.28	17.35	0.60	0.60	2.27	2.32	0.98	0.98	0.03	0.04	0.03	0.04	-	-
UGC08733	-17.45	-17.95	5.66	5.66	1.09	1.09	2.73	2.76	0.52	0.53	4.49	4.38	0.86	0.84	22.09	22.15	0.70	0.70	2.37	2.34	0.98	0.97	0.02	0.04	0.02	0.05	0.61	1.42
UGC09067	-15.62	-15.84	2.65	3.33	1.50	1.88	0.96	1.29	0.54	0.73	1.54	2.04	0.87	1.15	20.24	20.37	0.60	0.60	2.11	2.28	0.99	0.98	0.01	0.02	0.01	0.02	-	-
UGC09291	-16.75	-16.68	4.49	4.96	1.04	1.14	2.17	2.35	0.50	0.54	3.48	3.68	0.80	0.85	21.81	21.75	0.60	0.60	2.30	2.23	0.99	0.99	0.03	0.03	0.02	0.02	0.89	0.97
UGC09476	-15.56	-15.28	4.34	4.34	1.10	1.10	1.62	1.67	0.41	0.42	2.59	2.61	0.66	0.66	20.34	20.47	0.60	0.60	2.33	2.34	0.99	0.99	0.03	0.03	0.04	0.04	0.34	0.36
UGC10796	-16.39	-16.74	3.24	3.10	0.75	0.72	1.32	1.26	0.31	0.29	2.10	2.04	0.49	0.48	20.91	21.14	0.60	0.70	2.15	2.14	0.99	0.99	0.02	0.04	0.02	0.04	1.51	3.88
UGC12224	-16.43	-16.80	4.83	5.95	1.14	1.41	1.73	2.13	0.41	0.50	2.85	3.53	0.67	0.83	20.73	20.88	0.70	0.80	2.51	2.55	0.99	0.98	0.02	0.04	0.02	0.04	1.14	2.35

Investigated Relations

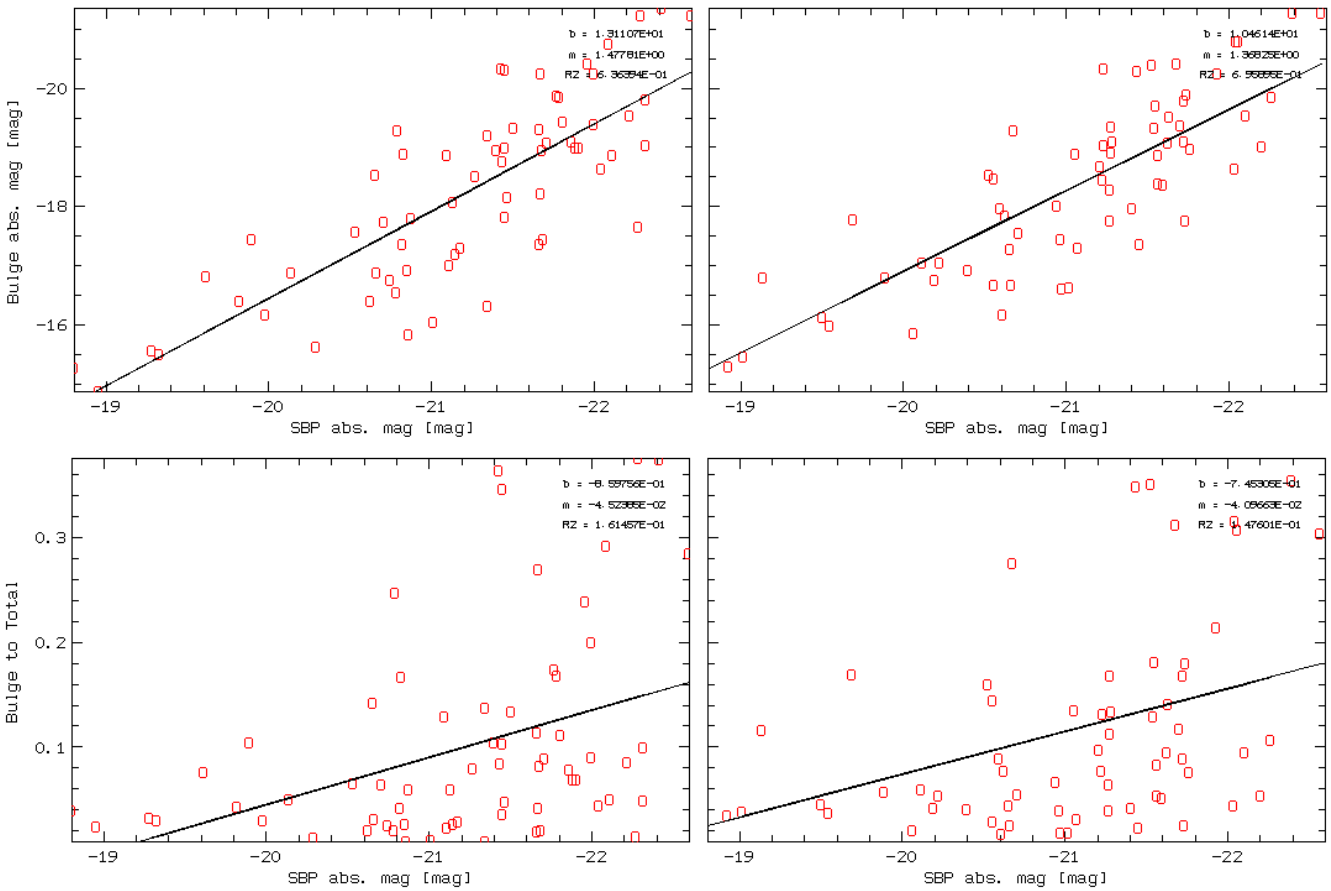

Figure 5.5: Top: SBP absolute magnitude versus bulge absolute magnitude; Bottom: SBP absolute magnitude versus bulge-to-total.

Analyzing the upper part of Fig. 5.5, one may identify a correlation between the bulge absolute magnitude and the total absolute magnitude of the galaxy (coefficient of determination (R^2) $\sim$ 0.64; 0.70, for before and after applying RY, respectively): the more luminous is the galaxy, the more luminous is its bulge component. By comparing both relations before and after application of RY, one can perceive that in the second case the correlation is slightly tighter. However, from the lower diagrams it is obvious that there is no clear correlation between the prominence of the bulge and the total luminosity of the galaxy ($R^2 \sim 0.16; 0.15$). Since the absolute magnitude of an Hubble-type galaxy is also a proxy to its total stellar mass – due to the tight correlation between stellar mass and luminosity – the observed trend suggests that more massive galaxies tend to present more massive bulges, but the prominence of the bulge component does not correlate with the total luminosity of the galaxy.

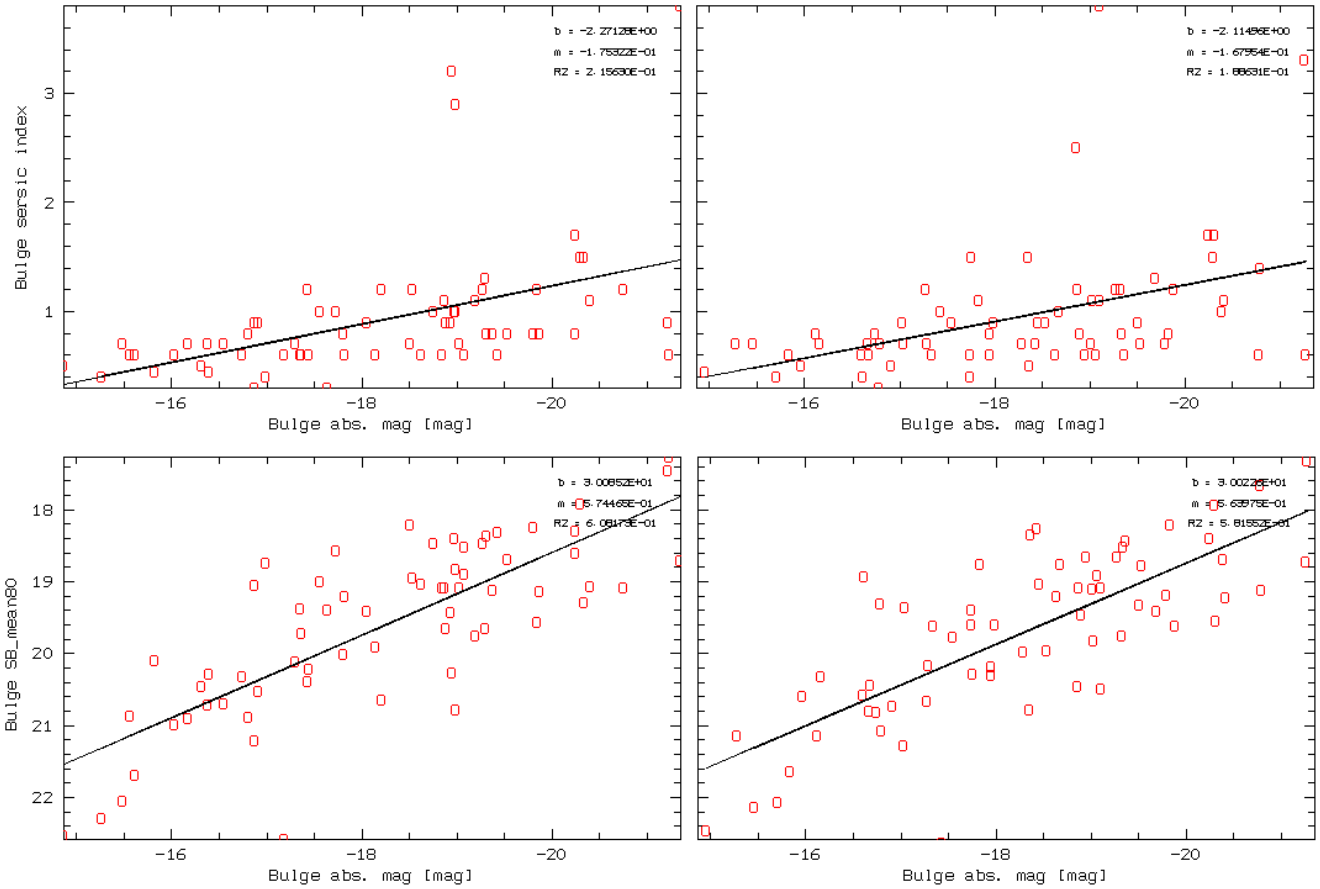

Figure 5.6: Top: Bulge absolute magnitude versus bulge Sérsic index; Bottom: Bulge absolute magnitude versus μ_{80} [mag/arcsec$_2$].

The previous Fig. (5.6) correlates the compactness of the bulge with the bulge absolute magnitude (i.e., bulge stellar mass). The upper part of the diagram shows the relation between the bulge Sérsic index and the bulge absolute magnitude: the correlation between the two parameters is minimal in the left-hand side and almost non-existent in the right-hand side diagram ($R^2 \sim 0.22$; 0.19). The lower part of Fig. 5.6 shows how the bulge mean surface brightness within R_{80} ($\mu 80$) is related to the bulge absolute magnitude ($R^2 \sim 0.61$; 0.58). This parameter is computed by dividing the apparent magnitude of the observed bulge by the area within R_{80}, indirectly measuring the mean stellar mass surface density. It can be perceived as a measure of the compactness of the bulge component – higher values indicate a denser, highly concentrated bulge, probably associated with a steeper potential well – whereas lower values indicate a bulge with lower mean stellar surface density. There is a clear correlation between these two parameters, indicating that more luminous galaxies – in principle more massive – present denser bulges. Once again, the application of RY leads to a more tight tendency (right-hand side). These results suggests that

μ_{80} is a more reliable/sensitive indicator of the compactness of the bulge than the Sérsic index.

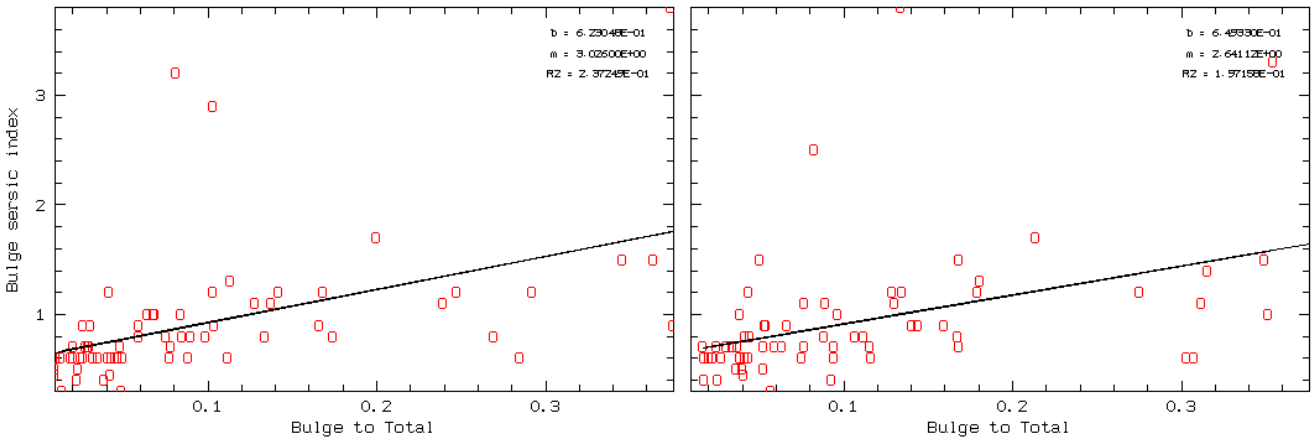

Figure 5.7: Bulge-to-total versus bulge Sérsic index

Analyzing the previous Fig. 5.7 one can conclude that there is no clear correlation between the Sérsic index of the bulge and B/T ratio ($R^2 \sim 0.24$; 0.20), indicating that the Sérsic index is not a sensitive indicator of the prominence of the bulge in a spiral galaxy.

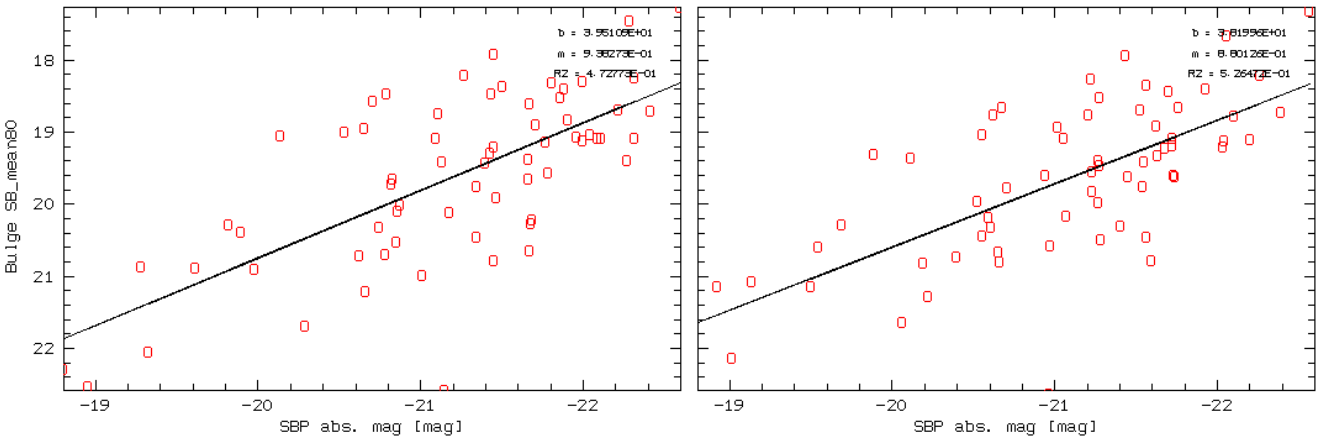

Figure 5.8: Total absolute magnitude versus μ_{80}.

Fig. 5.5 it was shown that there is no clear correlation between the prominence of the bulge relatively to the host galaxy (B/T) and the total absolute magnitude – a proxy to the total stellar mass of the galaxy. On the other hand, Fig. 5.8 shows that the more luminous/massive the galaxy, the higher the probability of having a compact bulge, with a steeper potential well ($R^2 \sim 0.47$; 0.53).

Histograms

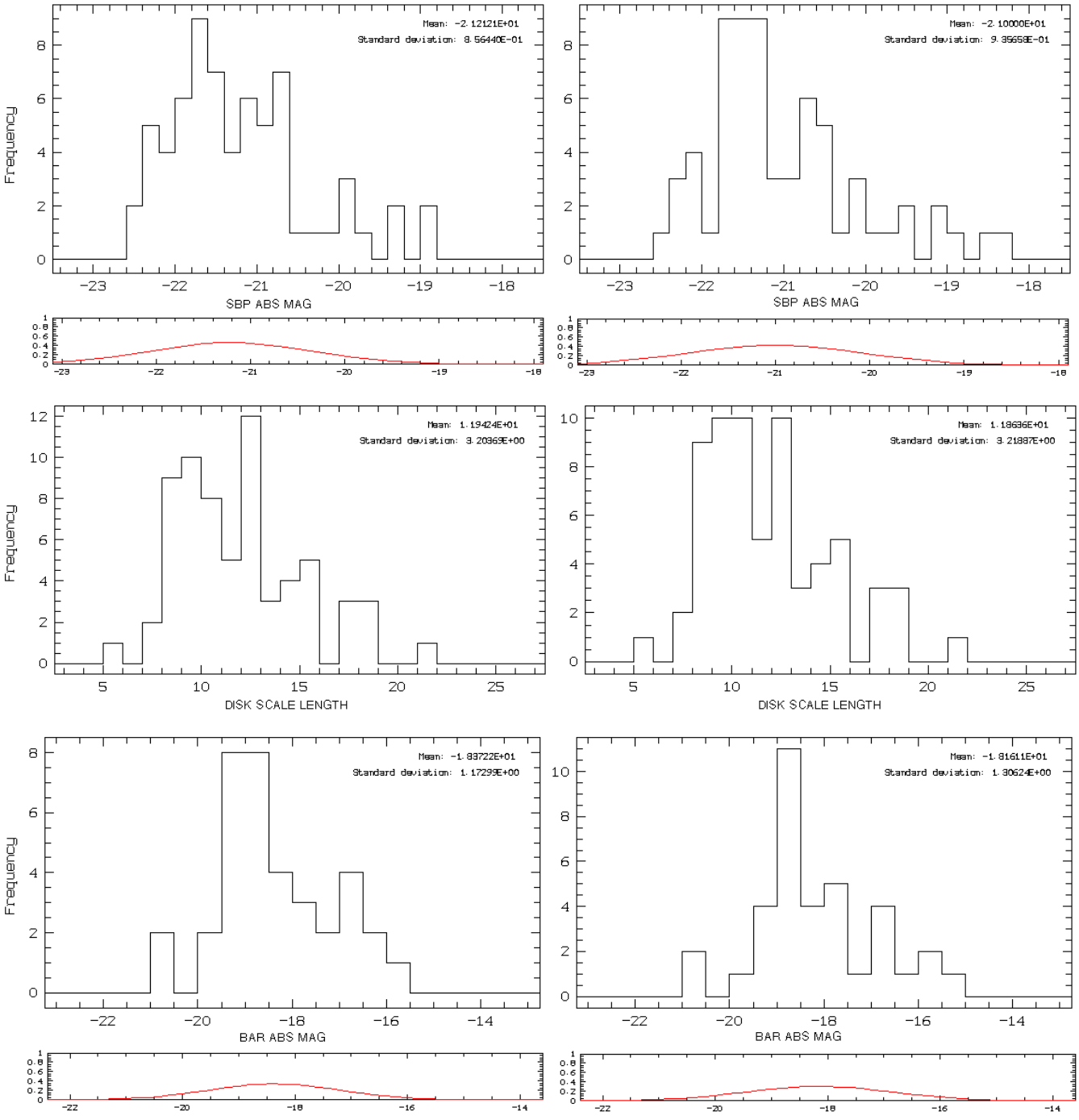

Figure 5.9: Histograms for the most relevant photometric quantities that where estimated (part1): From top to bottom: total absolute magnitude, disk scale-length, bar absolute magnitude.

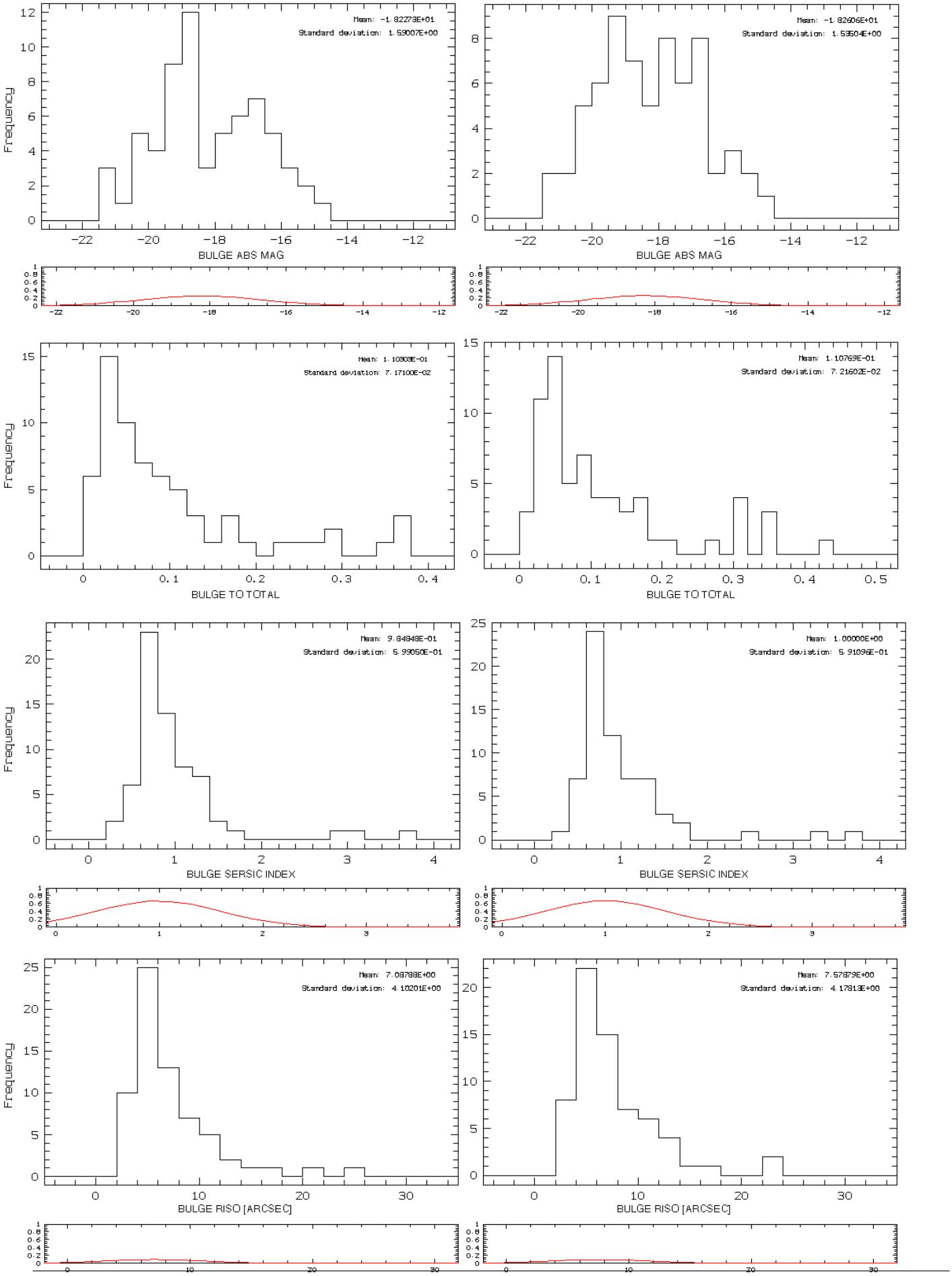

Iris Pereira Breda

Figure 5.10: Histograms for the most relevant photometric quantities that where estimated (part2): From top to bottom: bar absolute magnitude, bulge absolute magnitude, bulge to total, bulge Sérsic index and bulge radius.

The histograms of Fig.s 5.9 and 5.10 (from left to right, before and after applying RY, respectively) translate the shape of the distribution of the more relevant estimated quantities within the analyzed sample. In Fig. 5.9, from top to bottom: total SBP absolute magnitude [mag] ($< D1 >= -21.21, < D2 >= -21.00$); disk scale lenght [arcsec] ($< D1 >= 11.94, < D2 >= 11.86$); bar absolute magnitude [mag] ($< D1 >= -18.37, < D2 >= 18.16$). In Fig. 5.9, from top to bottom: bulge absolute magnitude [mag] ($< D1 >= -18.23, < D2 >= -18.26$); bulge-to-total ($< D1 >= 0.110, < D2 >= 0.111$); bulge Sérsic index ($< D1 >= 0.98, < D2 >= 1.00$); bulge R_{iso} ($< D1 >= 0.709, < D2 >= 0.758$). By visual inspection one can perceive that, for most of the displayed photometric quantities, the sample is relatively heterogeneous.

For the B/T ratio (Hist. 2 of 5.10) most of the galaxies present values bellow 0.2 with average in 0.1, indicating that in average, the bulges of the analysed sample are $\sim 90\%$ fainter than sum of the other galactic components. The Sérsic index distribution of the sample (Hist. 3 of 5.10) shows that, adopting the Kormendy & Kennicutt (2004) classification scheme, $\sim 95\%$ $(63/66)$ of the analyzed galaxies host a PB in its cores. The ones that are classified as CB are NGC5614, NGC5656 and NGC6004.

Chapter 6.

Mean Metallicity and Metallicity Gradient in the Bulge

This chapter provides a summary and discussion of the mean metallicity and its gradients in bulges, as derived by applying the methodology detailed in Chapter 3. The metallicity maps and radial profiles, normalized to R_{eff}, are shown for the four representative examples from the analyzed sample – the profiles for the bulk sample can be found in Appendix C. Sequently, are listed some of the spectroscopic quantities that were derived: Table 6.1 lists the parameters for the stellar luminosity- and mass-weighted metallicity for bulge and disk, and Table 6.2 lists those for the gas-phase metallicity in the bulge and disk, followed by the derived quantities for stellar and nebular extinction. Additionally it is displayed the obtained results for some relations between spectroscopic quantities (Figs. 6.5 to 6.8), and the histograms for the more relevant quantities (Figs. 6.9 and 6.10).

Metallicity Maps and Radial Profiles

IC1256

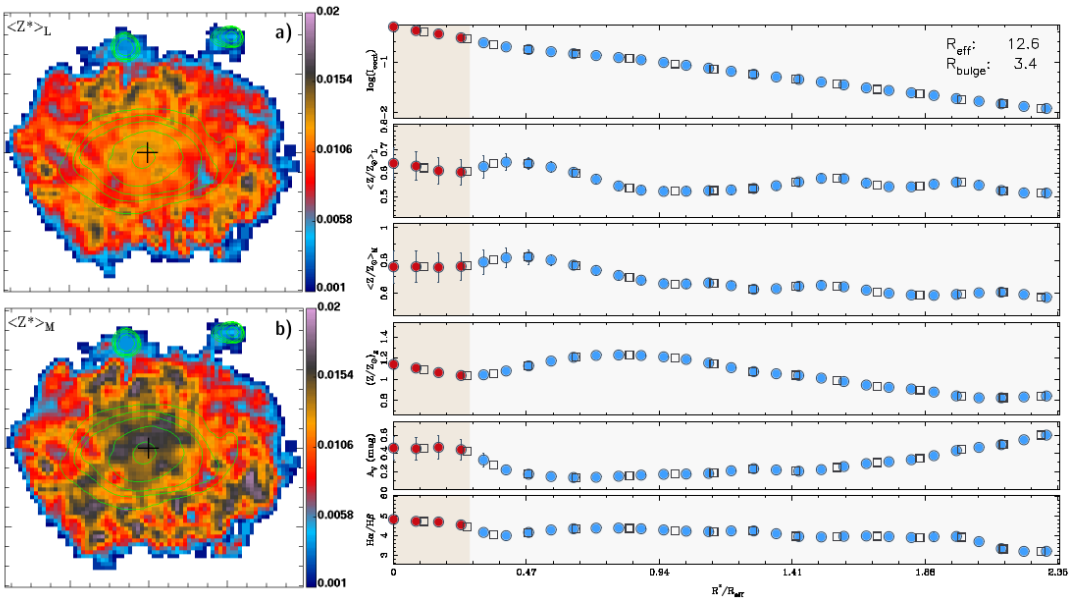

Figure 6.1: Metallicity maps and radial profiles* of IC1256.

NGC0023

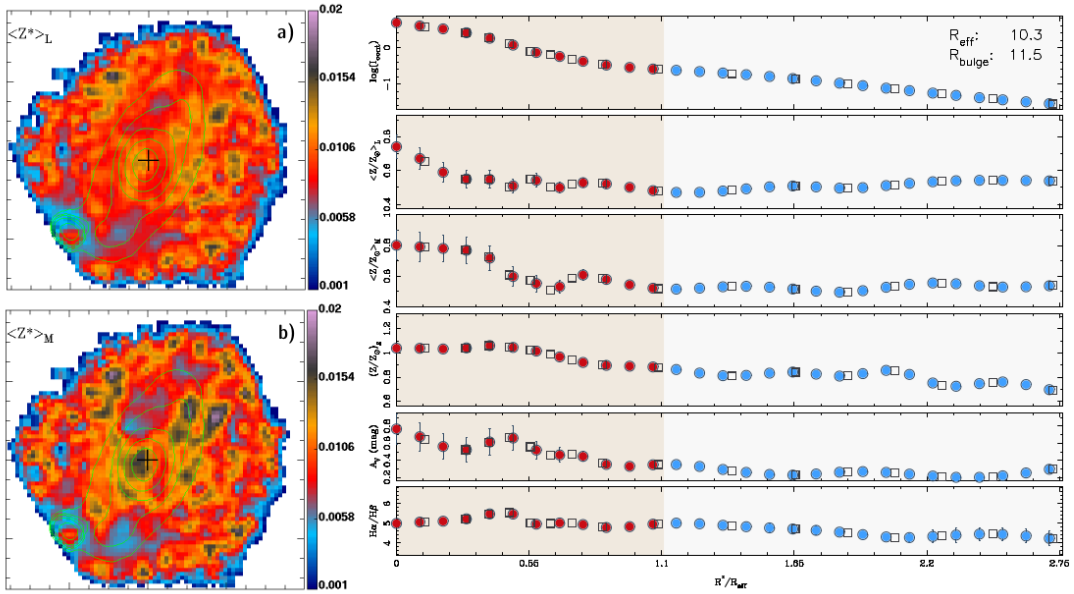

Figure 6.2: Metallicity maps and radial profiles* of NGC0023.

NGC3057

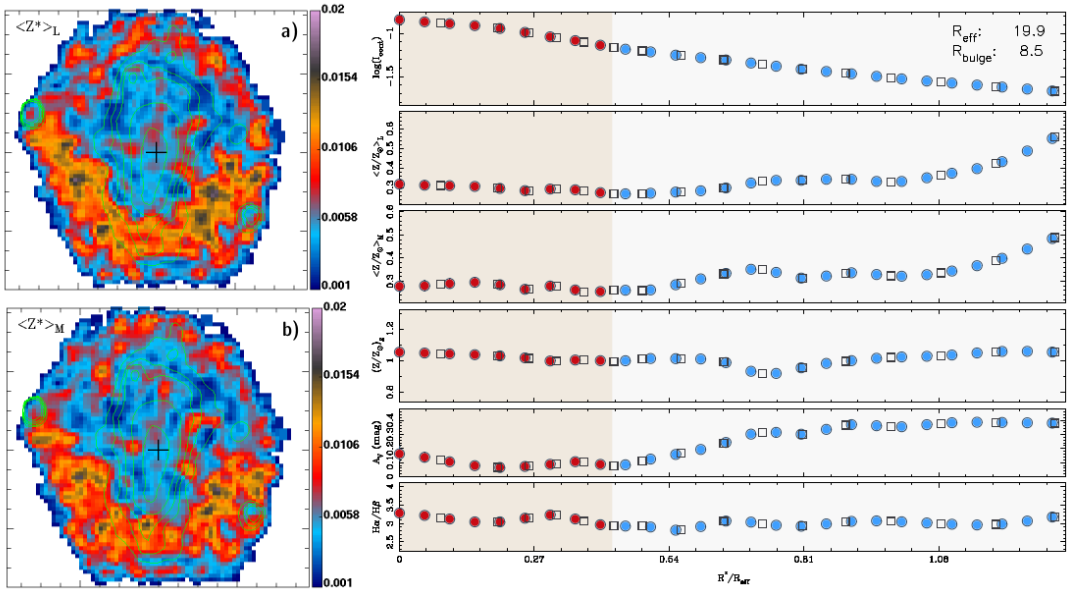

Figure 6.3: Metallicity maps and radial profiles* of NGC3057.

NGC6154

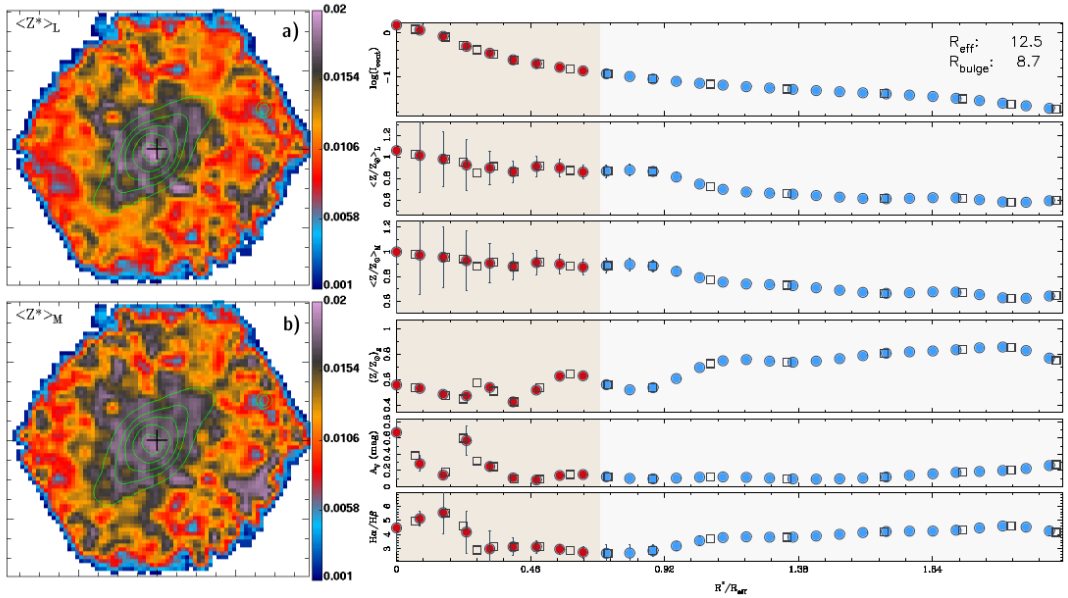

Figure 6.4: Metallicity maps and radial profiles* of NGC6154.

* - Left-hand side: a) luminosity-weighted stellar metallicity map; b) mass-weighted stellar metallicity map. Right-hand side (from top to bottom), radial profiles of: logarithm of the emission-line free continuum; luminosity-weighted stellar metallicity [$Z_{\odot}$]; mass-weighted stellar metallicity [$Z_{\odot}$]; gas-phase metallicity [$Z_{\odot}$]; stellar extinction [mag] and gas-phase extinction, in the form of $H\alpha/H\beta$ ratio [mag]. In the maps, the cross corresponds to the maximum of the stellar continuum, the contours to the emission-line free continuum with a spacing of 0.5 dex, and in the radial profiles, the error bars correspond to the $\sigma/\sqrt{n}$, the squares to the minimum values within the irregular annulli, the circles to the splined values. All radial profiles are normalized to the R_{eff} of the galaxy.

It follows a brief discussion on the most relevant features of radial profiles presented above:

• in the right upper part of the radial profiles the reader will find the effective radius of the galaxy (R_{eff}), which is the normalizing factor, and the radius of the bulge $R_{bulge} \equiv R_{iso}$.

• the red, left-handed part corresponds to where the bulge is the main contributor, and the blue right-handed side to where the disk is the main contributor (the limit, R_{iso}, is the angular radius of the bulge estimated by integrating the modeled bulge till the photometric limit of 24 mag/arcsec^2);

• the R_{iso} of IC1256 is very small when compared to the total galactic extent. For the quantities that are shown in the radial profiles of the Fig. 6.1, the gradients are also very shallow or even zero. Not the case of the disk, which presents, for almost every displayed quantity a significant variance. This may indicate that the contribution of the disk can be very significant, and that is necessary to remove it from the bulge emission, if one pursuits a deeper understanding of the pure bulge component. A detailed discussion of the different radial profiles will be given in Breda et al., (2014, in prep).

Table 6.1: The table lists – from left to right – galaxy name, and the estimated quantities for: mean ($<>$), standard deviation (σ), mean standard deviation ($\bar{\sigma}$), intercept of the gradient (b), intercept error (b_{err}), slope of the gradient (m in arcsec and m_k in kpc) and slope error (m_{err}) for luminosity weighted stellar metallicity in the bulge and disk, mass weighted stellar metallicity in the bulge and disk in units of $Z_\odot = 0.019$. The values presented in arcsec are normalized to the effective radius of the galaxy.

Galaxy	$< Z/Z_0 >$ L Bulge								$< Z/Z_0 >$ L Disk								$< Z/Z_0 >$ M Bulge								$< Z/Z_0 >$ M Disk							
	$<>$	σ	$\bar{\sigma}$	b	b_{err}	m	m_k	m_{err}	$<>$	σ	$\bar{\sigma}$	b	b_{err}	m	m_k	m_{err}	$<>$	σ	$\bar{\sigma}$	b	b_{err}	m	m_k	m_{err}	$<>$	σ	$\bar{\sigma}$	b	b_{err}	m	m_k	m_{err}
IC0776	0.25	0.15	0.07	0.247	0.018	0.058	0.02	0.121	0.32	0.09	0.02	0.206	0.014	0.116	0.04	0.013	0.28	0.17	0.08	0.331	0.014	-0.451	-0.14	0.097	0.32	0.10	0.02	0.220	0.015	0.103	0.03	0.015
IC1256	0.62	0.26	0.13	0.641	0.003	-0.165	-0.04	0.023	0.56	0.08	0.02	0.613	0.015	-0.041	-0.01	0.010	0.76	0.33	0.16	0.761	0.002	0.007	0.00	0.016	0.67	0.14	0.03	0.819	0.015	-0.117	-0.03	0.010
IC4566	0.76	0.34	0.15	0.822	0.018	-0.407	-0.08	0.088	0.62	0.09	0.02	0.647	0.021	-0.020	0.00	0.015	0.80	0.35	0.16	0.837	0.023	-0.223	-0.04	0.115	0.70	0.13	0.03	0.800	0.014	-0.073	-0.01	0.010
NGC0001	0.55	0.16	0.04	0.685	0.029	-0.150	-0.06	0.026	0.50	0.09	0.02	0.495	0.031	0.003	0.00	0.011	0.67	0.18	0.04	0.816	0.026	-0.159	-0.06	0.024	0.56	0.12	0.03	0.652	0.041	-0.034	-0.01	0.015
NGC0023	0.56	0.16	0.00	0.654	0.024	-0.184	-0.06	0.038	0.51	0.08	0.02	0.416	0.008	0.049	0.02	0.004	0.65	0.20	0.06	0.806	0.027	-0.295	-0.10	0.043	0.53	0.11	0.03	0.499	0.016	0.015	0.00	0.008
NGC0160	0.85	0.28	0.08	0.974	0.039	-0.309	-0.06	0.080	0.75	0.09	0.02	0.790	0.018	-0.025	-0.01	0.012	0.87	0.26	0.07	0.949	0.023	-0.181	-0.04	0.047	0.84	0.13	0.03	0.753	0.021	0.057	0.01	0.014
NGC0165	0.56	0.20	0.07	0.531	0.023	0.139	0.02	0.083	0.45	0.09	0.02	0.498	0.026	-0.040	-0.01	0.023	0.69	0.22	0.08	0.696	0.031	-0.025	0.00	0.111	0.52	0.13	0.03	0.647	0.025	-0.111	-0.02	0.021
NGC0171	0.72	0.23	0.06	0.722	0.034	-0.008	0.00	0.098	0.55	0.09	0.02	0.610	0.036	-0.057	-0.01	0.034	0.74	0.23	0.06	0.735	0.031	0.032	0.01	0.090	0.59	0.12	0.03	0.651	0.028	-0.055	-0.01	0.026
NGC0180	0.72	0.32	0.13	0.612	0.054	1.016	0.13	0.405	0.63	0.15	0.03	0.935	0.016	-0.406	-0.05	0.020	0.83	0.32	0.13	0.817	0.033	0.149	0.02	0.248	0.71	0.18	0.04	1.025	0.018	-0.424	-0.05	0.023
NGC0214	0.73	0.27	0.11	0.787	0.005	-0.314	-0.07	0.025	0.62	0.09	0.02	0.522	0.017	0.083	0.02	0.013	0.79	0.30	0.12	0.785	0.013	0.047	0.01	0.066	0.67	0.13	0.03	0.568	0.026	0.087	0.02	0.020
NGC0237	0.52	0.21	0.08	0.554	0.003	-0.149	-0.05	0.009	0.38	0.09	0.02	0.300	0.026	0.049	0.02	0.015	0.53	0.21	0.08	0.533	0.013	-0.007	0.00	0.046	0.42	0.10	0.02	0.416	0.019	0.003	0.00	0.011
NGC0257	0.67	0.27	0.10	0.882	0.022	-0.980	-0.18	0.087	0.57	0.08	0.02	0.480	0.010	0.079	0.01	0.008	0.81	0.31	0.11	1.012	0.022	-0.940	-0.17	0.085	0.62	0.13	0.03	0.589	0.034	0.028	0.01	0.027
NGC0477	0.59	0.24	0.11	0.631	0.002	-0.333	-0.05	0.014	0.44	0.08	0.02	0.502	0.020	-0.056	-0.01	0.018	0.74	0.28	0.13	0.779	0.008	-0.331	-0.05	0.052	0.50	0.14	0.03	0.651	0.028	-0.148	-0.02	0.026
NGC0776	0.80	0.29	0.12	0.924	0.017	-0.784	-0.16	0.088	0.56	0.09	0.02	0.656	0.016	-0.078	-0.02	0.013	0.89	0.33	0.14	0.986	0.004	-0.563	-0.12	0.022	0.66	0.13	0.03	0.792	0.018	-0.116	-0.02	0.014
NGC1093	0.77	0.25	0.09	0.850	0.009	-0.273	-0.08	0.024	0.49	0.09	0.02	0.582	0.023	-0.052	-0.02	0.012	0.87	0.27	0.10	0.918	0.004	-0.157	-0.05	0.010	0.59	0.14	0.03	0.785	0.030	-0.111	-0.03	0.016
NGC1645	0.88	0.31	0.10	1.013	0.017	-0.288	-0.09	0.031	0.62	0.09	0.02	0.627	0.027	-0.006	0.00	0.013	0.89	0.30	0.09	0.964	0.015	-0.167	-0.05	0.028	0.62	0.14	0.03	0.597	0.041	0.013	0.00	0.020
NGC2253	0.57	0.18	0.07	0.590	0.008	-0.095	-0.03	0.032	0.39	0.07	0.01	0.450	0.019	-0.041	-0.01	0.013	0.65	0.21	0.08	0.621	0.011	0.149	0.04	0.042	0.48	0.12	0.02	0.645	0.027	-0.121	-0.04	0.019
NGC2347	0.75	0.28	0.12	0.887	0.007	-0.606	-0.18	0.027	0.45	0.09	0.02	0.577	0.017	-0.079	-0.02	0.010	0.85	0.31	0.13	0.923	0.007	-0.316	-0.09	0.026	0.51	0.15	0.03	0.732	0.027	-0.139	-0.04	0.016
NGC2639	0.73	0.23	0.05	0.919	0.022	-0.221	-0.08	0.022	0.63	0.12	0.04	0.761	0.093	-0.059	-0.02	0.040	0.77	0.23	0.05	0.954	0.021	-0.212	-0.08	0.020	0.64	0.15	0.04	0.682	0.086	-0.020	-0.01	0.037
NGC2730	0.48	0.18	0.08	0.588	0.014	-0.772	-0.15	0.086	0.40	0.07	0.01	0.349	0.014	0.048	0.01	0.013	0.61	0.24	0.10	0.754	0.015	-1.074	-0.21	0.094	0.42	0.10	0.02	0.431	0.011	-0.015	0.00	0.010
NGC2906	0.81	0.29	0.11	0.951	0.014	-0.694	-0.29	0.058	0.55	0.09	0.02	0.513	0.031	0.028	0.01	0.022	0.87	0.30	0.11	0.959	0.009	-0.458	-0.19	0.037	0.61	0.13	0.03	0.663	0.037	-0.037	-0.02	0.026
NGC2916	0.80	0.28	0.10	0.768	0.030	0.168	0.03	0.140	0.55	0.12	0.02	0.731	0.035	-0.189	-0.04	0.034	0.80	0.30	0.11	0.728	0.046	0.381	0.07	0.213	0.55	0.16	0.03	0.770	0.044	-0.224	-0.04	0.043
NGC3057	0.30	0.10	0.03	0.317	0.003	-0.099	-0.04	0.012	0.35	0.11	0.03	0.133	0.029	0.248	0.10	0.032	0.28	0.11	0.04	0.290	0.006	-0.065	-0.03	0.026	0.34	0.10	0.02	0.188	0.026	0.173	0.07	0.028
NGC3300	0.94	0.37	0.15	1.003	0.008	-0.288	-0.11	0.031	0.74	0.11	0.02	0.937	0.013	-0.117	-0.05	0.007	0.92	0.38	0.15	0.960	0.006	-0.162	-0.06	0.023	0.75	0.15	0.03	0.925	0.017	-0.104	-0.04	0.010
NGC3381	0.33	0.15	0.06	0.291	0.016	0.234	0.09	0.086	0.33	0.06	0.01	0.295	0.008	0.038	0.01	0.007	0.42	0.17	0.07	0.397	0.018	0.162	0.06	0.094	0.41	0.09	0.02	0.371	0.009	0.033	0.01	0.008
NGC3614	0.55	0.17	0.07	0.486	0.011	0.572	0.11	0.087	0.48	0.07	0.01	0.554	0.012	-0.104	-0.02	0.017	0.58	0.19	0.07	0.513	0.022	0.608	0.11	0.178	0.51	0.10	0.02	0.600	0.014	-0.130	-0.02	0.020
NGC3687	0.68	0.19	0.06	0.754	0.015	-0.263	-0.09	0.044	0.48	0.07	0.02	0.491	0.020	-0.005	0.00	0.014	0.75	0.19	0.06	0.794	0.013	-0.159	-0.05	0.036	0.57	0.11	0.02	0.678	0.030	-0.080	-0.03	0.021
NGC4003	1.46	0.30	0.10	1.516	0.014	-0.144	-0.04	0.028	1.29	0.13	0.03	1.552	0.021	-0.130	-0.03	0.010	1.41	0.32	0.11	1.523	0.016	-0.267	-0.07	0.033	1.21	0.15	0.03	1.380	0.015	-0.084	-0.02	0.007
NGC4047	0.66	0.23	0.10	0.684	0.007	-0.176	-0.05	0.038	0.48	0.07	0.01	0.475	0.021	0.002	0.00	0.014	0.77	0.29	0.13	0.718	0.010	0.325	0.09	0.054	0.57	0.13	0.02	0.679	0.032	-0.081	-0.02	0.021
NGC4185	0.69	0.21	0.07	0.670	0.010	0.142	0.02	0.048	0.62	0.08	0.02	0.745	0.009	-0.150	-0.02	0.010	0.80	0.23	0.08	0.780	0.012	0.113	0.02	0.057	0.70	0.12	0.03	0.907	0.009	-0.238	-0.03	0.010
NGC4210	0.70	0.24	0.10	0.677	0.017	0.142	0.04	0.103	0.51	0.11	0.02	0.691	0.012	-0.198	-0.05	0.012	0.75	0.25	0.10	0.728	0.009	0.201	0.05	0.057	0.58	0.14	0.03	0.798	0.009	-0.245	-0.06	0.009
NGC4961	0.45	0.18	0.07	0.541	0.011	-0.375	-0.17	0.037	0.31	0.10	0.02	0.180	0.032	0.080	0.04	0.019	0.38	0.17	0.07	0.417	0.006	-0.173	-0.08	0.020	0.30	0.11	0.02	0.226	0.035	0.046	0.02	0.020
NGC5000	0.56	0.35	0.20	0.538	0.009	0.295	0.06	0.091	0.60	0.09	0.02	0.652	0.023	-0.044	-0.01	0.017	0.69	0.41	0.24	0.664	0.008	0.288	0.06	0.078	0.65	0.16	0.03	0.768	0.037	-0.095	-0.02	0.027
NGC5016	0.49	0.25	0.12	0.476	0.001	0.110	0.04	0.011	0.46	0.07	0.01	0.445	0.018	0.010	0.00	0.013	0.65	0.31	0.16	0.626	0.001	0.207	0.07	0.010	0.52	0.12	0.02	0.598	0.021	-0.063	-0.02	0.016
NGC5205	0.63	0.20	0.07	0.664	0.017	-0.116	-0.05	0.050	0.45	0.10	0.02	0.371	0.041	0.054	0.02	0.028	0.64	0.19	0.06	0.679	0.006	-0.134	-0.06	0.019	0.45	0.11	0.02	0.440	0.034	0.007	0.00	0.024
NGC5320	0.57	0.19	0.07	0.570	0.006	-0.033	-0.01	0.033	0.44	0.08	0.02	0.558	0.012	-0.119	-0.03	0.011	0.66	0.22	0.08	0.676	0.016	-0.085	-0.02	0.081	0.50	0.12	0.02	0.665	0.027	-0.165	-0.04	0.025
NGC5378	0.73	0.25	0.08	0.773	0.023	-0.180	-0.04	0.091	0.65	0.08	0.02	0.748	0.017	-0.092	-0.02	0.015	0.79	0.26	0.09	0.823	0.019	-0.159	-0.04	0.073	0.70	0.12	0.00	0.830	0.013	-0.122	-0.03	0.012
NGC5406	1.00	0.44	0.18	1.097	0.010	-0.612	-0.10	0.054	0.63	0.13	0.03	0.823	0.037	-0.181	-0.03	0.033	0.97	0.42	0.17	1.010	0.007	-0.249	-0.04	0.036	0.73	0.16	0.03	0.927	0.018	-0.189	-0.03	0.016
NGC5480	0.40	0.23	0.09	0.412	0.055	-0.055	-0.02	0.280	0.40	0.11	0.02	0.224	0.020	0.172	0.06	0.018	0.49	0.24	0.09	0.480	0.048	0.060	0.02	0.244	0.44	0.11	0.02	0.350	0.025	0.083	0.03	0.023

Table 6.1 Continued.

NGC5614	0.73	0.24	0.05	0.950	0.029	-0.229	-0.06	0.027	0.65	0.31	0.15	0.341	0.031	0.150	0.04	0.015	0.82	0.20	0.04	0.967	0.011	-0.158	-0.04	0.010	0.71	0.26	0.13	0.575	0.026	-0.065	0.02	0.012
NGC5656	0.55	0.20	0.06	0.752	0.011	-0.485	-0.16	0.022	0.39	0.09	0.02	0.201	0.011	0.107	0.04	0.006	0.61	0.19	0.06	0.769	0.011	-0.393	-0.13	0.022	0.39	0.10	0.02	0.394	0.017	0.000	0.00	0.009
NGC5735	0.46	0.21	0.09	0.401	0.018	0.547	0.10	0.141	0.48	0.07	0.01	0.464	0.017	0.014	0.00	0.017	0.48	0.23	0.10	0.385	0.031	0.840	0.16	0.236	0.50	0.11	0.02	0.569	0.017	-0.070	-0.01	0.017
NGC5772	0.85	0.35	0.10	1.104	0.021	-0.692	-0.14	0.046	0.54	0.10	0.02	0.679	0.004	-0.091	-0.02	0.003	0.87	0.31	0.09	1.011	0.011	-0.371	-0.08	0.025	0.63	0.16	0.04	0.928	0.016	-0.202	-0.04	0.010
NGC5829	0.47	0.29	0.17	0.504	0.002	-0.487	-0.07	0.026	0.35	0.09	0.02	0.343	0.028	0.003	0.00	0.026	0.72	0.41	0.24	0.759	0.007	-0.640	-0.10	0.086	0.48	0.17	0.03	0.659	0.028	-0.179	-0.03	0.026
NGC6004	0.60	0.17	0.05	0.726	0.018	-0.479	-0.08	0.058	0.49	0.07	0.01	0.442	0.012	0.047	0.01	0.011	0.69	0.18	0.05	0.738	0.029	-0.171	-0.03	0.096	0.54	0.10	0.02	0.674	0.019	-0.128	-0.02	0.017
NGC6032	0.49	0.24	0.11	0.432	0.025	0.391	0.09	0.142	0.62	0.09	0.02	0.619	0.026	0.003	0.00	0.021	0.61	0.27	0.12	0.522	0.032	0.602	0.13	0.183	0.69	0.11	0.02	0.654	0.011	0.032	0.01	0.009
NGC6154	0.93	0.35	0.12	1.022	0.020	-0.279	-0.05	0.053	0.68	0.14	0.03	0.958	0.034	-0.189	-0.04	0.022	0.93	0.34	0.11	0.982	0.011	-0.177	-0.03	0.029	0.73	0.16	0.04	0.986	0.024	-0.175	-0.03	0.015
NGC6186	0.53	0.29	0.17	0.563	0.002	-0.401	-0.14	0.018	0.54	0.08	0.01	0.575	0.014	-0.028	-0.01	0.010	0.63	0.37	0.21	0.677	0.004	-0.542	-0.20	0.040	0.62	0.14	0.03	0.720	0.017	-0.077	-0.03	0.011
NGC6278	0.92	0.29	0.08	1.050	0.021	-0.163	-0.08	0.023	0.81	0.13	0.03	1.140	0.036	-0.126	-0.06	0.013	0.91	0.27	0.07	0.976	0.013	-0.088	-0.04	0.014	0.83	0.15	0.03	1.144	0.035	-0.121	-0.06	0.013
NGC6941	0.91	0.38	0.15	0.992	0.021	-0.561	-0.08	0.115	0.66	0.13	0.02	0.897	0.015	-0.199	-0.03	0.012	0.91	0.39	0.16	0.977	0.012	-0.435	-0.06	0.063	0.71	0.17	0.03	0.977	0.018	-0.218	-0.03	0.014
NGC7321	0.81	0.31	0.14	0.842	0.003	-0.177	-0.03	0.017	0.53	0.13	0.03	0.716	0.032	-0.141	-0.02	0.023	0.88	0.35	0.15	0.885	0.007	-0.048	-0.01	0.036	0.62	0.18	0.04	0.915	0.029	-0.221	-0.04	0.020
NGC7489	0.60	0.29	0.17	0.658	0.003	-0.780	-0.13	0.031	0.43	0.10	0.02	0.359	0.029	0.057	0.01	0.021	0.54	0.36	0.21	0.520	0.003	0.275	0.05	0.033	0.45	0.13	0.02	0.455	0.026	-0.004	0.00	0.019
NGC7625	0.50	0.19	0.08	0.555	0.007	-0.299	-0.21	0.030	0.45	0.07	0.01	0.389	0.013	0.036	0.03	0.008	0.56	0.23	0.09	0.704	0.012	-0.703	-0.49	0.049	0.49	0.10	0.02	0.488	0.019	0.002	0.00	0.011
NGC7653	0.64	0.28	0.10	0.764	0.044	-0.492	-0.14	0.150	0.41	0.07	0.01	0.351	0.010	0.038	0.01	0.006	0.67	0.28	0.11	0.777	0.056	-0.436	-0.13	0.191	0.47	0.11	0.02	0.470	0.010	-0.003	0.00	0.006
NGC7691	0.48	0.26	0.13	0.398	0.013	1.180	0.21	0.143	0.59	0.11	0.02	0.636	0.036	-0.059	-0.01	0.042	0.56	0.32	0.16	0.403	0.014	2.249	0.40	0.162	0.69	0.12	0.02	0.650	0.014	0.045	0.01	0.016
NGC7716	0.71	0.28	0.08	0.972	0.011	-0.630	-0.27	0.023	0.48	0.08	0.02	0.447	0.007	0.017	0.01	0.004	0.71	0.27	0.08	0.936	0.011	-0.541	-0.23	0.024	0.49	0.12	0.02	0.424	0.018	0.038	0.02	0.010
NGC7738	0.59	0.28	0.14	0.551	0.026	0.231	0.05	0.135	0.69	0.10	0.02	0.828	0.010	-0.082	-0.02	0.006	0.62	0.34	0.17	0.531	0.005	0.573	0.13	0.026	0.72	0.14	0.03	0.904	0.012	-0.108	-0.02	0.006
NGC7819	0.40	0.13	0.05	0.402	0.031	-0.024	-0.01	0.103	0.35	0.08	0.02	0.370	0.018	-0.019	0.00	0.015	0.53	0.18	0.06	0.550	0.063	-0.077	-0.02	0.214	0.41	0.11	0.03	0.473	0.027	-0.051	-0.01	0.022
UGC07012	0.35	0.16	0.06	0.441	0.015	-0.320	-0.15	0.047	0.29	0.10	0.02	0.168	0.021	0.080	0.04	0.013	0.38	0.17	0.07	0.428	0.018	-0.170	-0.08	0.054	0.34	0.12	0.03	0.183	0.019	0.100	0.05	0.011
UGC08234	0.80	0.29	0.13	0.860	0.009	-0.157	-0.05	0.020	0.56	0.13	0.03	0.797	0.011	-0.084	-0.03	0.004	0.90	0.34	0.15	0.913	0.008	-0.050	-0.02	0.019	0.64	0.17	0.04	0.905	0.021	-0.094	-0.03	0.007
UGC08733	0.24	0.16	0.06	0.172	0.022	0.454	0.13	0.128	0.31	0.08	0.02	0.268	0.018	0.044	0.01	0.018	0.25	0.16	0.07	0.213	0.020	0.297	0.09	0.116	0.34	0.10	0.02	0.292	0.019	0.051	0.01	0.020
UGC09067	0.60	0.31	0.18	0.656	0.001	-0.443	-0.09	0.006	0.40	0.10	0.02	0.451	0.028	-0.032	-0.01	0.017	0.67	0.37	0.21	0.692	0.001	-0.198	-0.04	0.005	0.48	0.15	0.03	0.586	0.023	-0.072	-0.02	0.013
UGC09291	0.40	0.20	0.09	0.332	0.022	0.660	0.15	0.170	0.40	0.07	0.01	0.375	0.019	0.029	0.01	0.019	0.42	0.22	0.10	0.314	0.021	0.953	0.22	0.158	0.41	0.11	0.02	0.419	0.025	-0.010	0.00	0.024
UGC09476	0.50	0.18	0.08	0.486	0.006	0.158	0.04	0.040	0.45	0.07	0.01	0.411	0.014	0.040	0.01	0.013	0.53	0.20	0.09	0.488	0.003	0.398	0.09	0.025	0.52	0.09	0.02	0.520	0.013	0.002	0.00	0.012
UGC10796	0.31	0.19	0.09	0.346	0.029	-0.240	-0.09	0.173	0.28	0.10	0.02	0.203	0.022	0.071	0.03	0.018	0.43	0.27	0.13	0.588	0.019	-1.180	-0.46	0.111	0.32	0.14	0.03	0.255	0.032	0.058	0.02	0.026
UGC12224	0.46	0.20	0.09	0.438	0.004	0.269	0.05	0.033	0.43	0.08	0.01	0.384	0.021	0.053	0.01	0.021	0.55	0.23	0.10	0.476	0.014	0.838	0.16	0.126	0.48	0.10	0.02	0.494	0.023	-0.016	0.00	0.023

Table 6.2: The table lists – from left to right – galaxy name, and the estimated quantities for: $<>$, σ, $<\sigma>$, b, b_{err}, m, m_{kpc} and m_{err} for gas-phase metallicity within the bulge and disk in units of $Z_{\odot} = 8.63$ and $<\mu>$, σ, $<\sigma>$ for stellar extinction in the bulge, stellar extinction in the disk, gas-phase extinction in the bulge and gas-phase extinction in the disk. The values presented in arcsec are normalized to the effective radius of the galaxy.

Galaxy	$<Z/Z_0>$ G Bulge								$<Z/Z_0>$ G Disk								$Av\ Bulge$			$Av\ Disk$			$H\alpha/H\beta\ Bulge$			$H\alpha/H\beta\ Disk$		
	$<>$	σ	$<\sigma>$	b	b_{err}	m	m_{kpc}	m_{err}	$<>$	σ	$<\sigma>$	b	b_{err}	m	m_{kpc}	m_{err}	$<>$	σ	$<\sigma>$	$<>$	σ	$<\sigma>$	$<>$	σ	$<\sigma>$	$<>$	σ	$<\sigma>$
IC0776	0.98	0.01	0.01	0.960	0.002	0.151	0.05	0.011	1.03	0.04	0.01	1.033	0.013	-0.006	0.00	0.013	0.06	0.22	0.10	0.34	0.19	0.04	3.21	0.26	0.12	3.13	0.17	0.04
IC1256	1.09	0.05	0.02	1.142	0.004	-0.448	-0.10	0.024	1.04	0.15	0.03	1.305	0.035	-0.203	-0.05	0.024	0.45	0.37	0.19	0.27	0.18	0.04	4.69	0.32	0.16	4.01	0.35	0.07
IC4566	0.52	0.06	0.03	0.524	0.057	0.002	0.00	0.283	0.71	0.14	0.03	0.824	0.064	-0.083	-0.02	0.044	0.37	0.32	0.14	0.27	0.15	0.03	3.77	1.02	0.46	3.77	0.81	0.16
NGC0001	1.19	0.04	0.01	1.195	0.020	-0.008	0.00	0.018	0.92	0.09	0.02	1.251	0.037	-0.119	-0.05	0.013	0.51	0.23	0.06	0.63	0.27	0.07	5.32	0.32	0.08	4.57	0.41	0.10
NGC0023	0.99	0.07	0.02	1.082	0.018	-0.178	-0.06	0.029	0.80	0.08	0.02	0.961	0.031	-0.084	-0.03	0.015	0.52	0.26	0.07	0.25	0.13	0.03	5.07	0.25	0.07	4.57	0.28	0.07
NGC0160	0.61	0.10	0.03	0.603	0.055	0.012	0.00	0.114	0.67	0.10	0.02	0.646	0.064	0.018	0.00	0.042	0.18	0.17	0.05	0.70	0.12	0.03	2.32	0.71	0.20	2.58	0.50	0.12
NGC0165	1.05	0.30	0.11	1.458	0.053	-1.744	-0.31	0.188	0.92	0.15	0.04	0.913	0.059	0.007	0.00	0.051	0.44	0.37	0.13	0.18	0.16	0.04	4.93	0.41	0.14	4.41	0.32	0.07
NGC0171	0.65	0.05	0.01	0.615	0.024	0.119	0.02	0.069	0.85	0.07	0.02	0.901	0.048	-0.050	-0.01	0.045	0.23	0.31	0.08	0.31	0.20	0.05	3.12	0.31	0.09	3.43	0.30	0.07
NGC0180	1.31	0.12	0.05	1.312	0.099	-0.057	-0.01	0.740	0.92	0.16	0.03	0.658	0.053	0.342	0.04	0.065	0.42	0.41	0.17	0.14	0.15	0.03	4.73	1.15	0.47	3.89	0.37	0.08
NGC0214	0.62	0.18	0.07	0.383	0.030	1.410	0.32	0.147	1.01	0.18	0.04	1.376	0.036	-0.306	-0.07	0.028	0.46	0.39	0.16	0.44	0.16	0.03	4.47	0.64	0.26	4.30	0.69	0.14
NGC0237	1.20	0.01	0.00	1.214	0.005	-0.050	-0.02	0.016	1.08	0.11	0.02	1.336	0.013	-0.159	-0.06	0.008	0.33	0.34	0.14	0.40	0.15	0.03	4.24	0.19	0.08	3.81	0.39	0.08
NGC0257	1.27	0.08	0.03	1.191	0.045	0.353	0.06	0.174	1.02	0.14	0.03	1.350	0.028	-0.285	-0.05	0.023	0.49	0.28	0.10	0.52	0.12	0.02	5.04	0.27	0.10	4.66	0.52	0.11
NGC0477	1.19	0.04	0.02	1.243	0.010	-0.426	-0.07	0.064	0.98	0.10	0.02	1.129	0.033	-0.141	-0.02	0.030	0.39	0.31	0.14	0.26	0.16	0.03	4.78	0.45	0.20	4.57	0.41	0.08
NGC0776	1.02	0.05	0.02	1.007	0.036	0.072	0.01	0.181	0.97	0.09	0.02	1.078	0.035	-0.094	-0.02	0.028	0.44	0.34	0.14	0.22	0.12	0.02	4.37	0.20	0.08	4.22	0.21	0.04
NGC1093	0.62	0.21	0.08	0.336	0.042	0.914	0.27	0.115	0.92	0.14	0.03	1.149	0.036	-1.129	-0.34	0.019	0.07	0.10	0.04	0.20	0.19	0.04	5.15	1.23	0.46	3.94	0.41	0.09
NGC1645	0.64	0.08	0.03	0.543	0.030	0.205	0.07	0.055	0.78	0.11	0.02	0.904	0.063	-0.065	-0.02	0.031	0.17	0.15	0.05	0.58	0.23	0.05	3.20	0.44	0.14	3.42	0.40	0.09
NGC2253	1.04	0.15	0.06	1.219	0.058	-0.832	-0.24	0.221	1.09	0.14	0.03	1.356	0.033	-0.193	-0.06	0.023	0.49	0.39	0.15	0.30	0.15	0.03	5.58	0.41	0.16	4.62	0.24	0.05
NGC2347	0.95	0.26	0.10	0.612	0.027	1.511	0.44	0.099	1.07	0.16	0.03	1.349	0.018	-0.178	-0.05	0.011	0.18	0.21	0.08	0.36	0.20	0.04	4.17	0.29	0.12	4.08	0.27	0.05
NGC2639	0.75	0.19	0.04	0.494	0.042	0.297	0.11	0.042	0.61	0.16	0.05	1.222	0.061	-0.268	-0.10	0.026	0.09	0.05	0.01	0.38	0.22	0.06	6.33	1.77	0.39	3.04	0.91	0.26
NGC2730	1.18	0.03	0.01	1.164	0.019	0.106	0.02	0.113	1.05	0.06	0.01	1.143	0.016	-0.093	-0.02	0.015	0.39	0.29	0.12	0.43	0.12	0.02	4.02	0.29	0.12	3.70	0.17	0.03
NGC2906	0.71	0.14	0.05	0.525	0.026	0.883	0.37	0.104	0.95	0.20	0.04	1.373	0.047	-0.317	-0.13	0.033	0.28	0.25	0.09	0.14	0.11	0.02	5.38	0.91	0.34	3.80	0.71	0.14
NGC2916	0.55	0.04	0.01	0.539	0.026	0.047	0.01	0.122	0.95	0.15	0.03	0.724	0.079	0.229	0.04	0.077	-	-	-	-	-	-	3.19	1.11	0.39	3.93	0.32	0.07
NGC3057	1.03	0.02	0.01	1.056	0.004	-0.152	-0.06	0.015	1.01	0.05	0.01	0.927	0.028	0.091	0.04	0.030	0.10	0.10	0.03	0.30	0.12	0.03	3.13	0.17	0.06	2.99	0.13	0.03
NGC3300	0.76	0.11	0.04	0.705	0.081	0.233	0.09	0.295	0.51	0.08	0.02	0.499	0.025	0.007	0.00	0.014	0.13	0.30	0.12	-	-	-	-	-	-	1.97	1.76	0.34
NGC3381	1.24	0.05	0.02	1.310	0.006	-0.413	-0.16	0.034	1.12	0.06	0.01	1.206	0.007	-0.080	-0.03	0.007	0.13	0.13	0.05	0.17	0.10	0.02	3.28	0.18	0.07	3.21	0.12	0.02
NGC3614	0.83	0.06	0.02	0.906	0.018	-0.728	-0.14	0.142	1.03	0.07	0.01	0.960	0.028	0.098	0.02	0.038	0.22	0.25	0.10	0.14	0.11	0.02	4.41	0.51	0.19	4.17	0.32	0.06
NGC3687	0.71	0.10	0.03	0.587	0.040	0.420	0.14	0.115	1.01	0.11	0.02	1.220	0.032	-0.152	-0.05	0.022	0.07	0.12	0.04	0.11	0.09	0.02	3.73	0.44	0.14	3.45	0.19	0.04
NGC4003	0.78	0.10	0.04	0.862	0.058	-0.209	-0.05	0.119	0.63	0.09	0.02	0.577	0.031	0.025	0.01	0.015	0.21	0.24	0.09	0.19	0.17	0.04	4.90	1.07	0.38	2.92	0.61	0.14
NGC4047	1.14	0.07	0.03	1.054	0.013	0.564	0.16	0.072	1.06	0.21	0.04	1.509	0.012	-0.323	-0.09	0.008	0.27	0.25	0.11	0.21	0.14	0.03	4.89	0.26	0.12	4.31	0.44	0.08
NGC4185	0.83	0.15	0.05	0.642	0.051	1.119	0.16	0.252	0.95	0.11	0.02	1.086	0.036	-0.159	-0.02	0.040	0.04	0.08	0.03	0.05	0.07	0.01	5.01	0.94	0.31	4.77	0.37	0.08
NGC4210	0.59	0.09	0.04	0.525	0.062	0.476	0.12	0.386	1.02	0.10	0.02	0.933	0.039	0.102	0.03	0.410	0.13	0.18	0.07	0.10	0.10	0.02	3.81	0.97	0.29	3.97	0.31	0.06
NGC4961	1.14	0.01	0.00	1.128	0.002	0.054	0.02	0.007	1.05	0.05	0.01	1.126	0.017	-0.044	-0.02	0.010	0.24	0.12	0.05	0.57	0.21	0.04	3.47	0.22	0.09	3.20	0.28	0.06
NGC5000	1.09	0.06	0.04	1.155	0.012	-0.775	-0.15	0.115	0.84	0.11	0.02	0.797	0.042	0.034	0.01	0.031	0.67	0.55	0.32	0.31	0.22	0.04	6.42	0.45	0.26	4.62	0.57	0.11
NGC5016	0.91	0.15	0.07	0.733	0.002	1.708	0.55	0.012	1.05	0.16	0.03	1.341	0.025	-0.237	-0.08	0.018	0.27	0.22	0.11	0.38	0.29	0.05	4.03	0.27	0.14	3.90	0.34	0.06
NGC5205	0.69	0.13	0.04	0.547	0.054	0.535	0.25	0.165	0.90	0.09	0.02	0.908	0.026	-0.006	0.00	0.018	0.11	0.16	0.05	0.40	0.26	0.05	4.71	1.76	0.59	3.69	0.55	0.11
NGC5320	0.91	0.12	0.04	0.756	0.020	0.992	0.25	0.103	1.09	0.10	0.02	1.229	0.024	-0.140	-0.04	0.022	0.26	0.21	0.08	0.27	0.17	0.03	3.96	0.33	0.13	3.78	0.22	0.04
NGC5378	0.59	0.01	0.00	0.595	0.007	-0.003	0.00	0.029	0.68	0.05	0.01	0.602	0.029	0.076	0.02	0.027	0.05	0.07	0.02	0.21	0.09	0.02	2.96	0.33	0.11	3.59	0.46	0.10
NGC5406	0.52	0.04	0.02	0.478	0.026	0.267	0.04	0.137	0.87	0.16	0.03	0.573	0.059	0.287	0.05	0.052	0.16	0.18	0.07	0.10	0.09	0.02	4.51	1.36	0.55	4.28	0.51	0.11
NGC5480	1.31	0.02	0.01	1.337	0.008	-0.173	-0.06	0.041	1.11	0.18	0.03	1.500	0.048	-0.372	-0.13	0.042	0.48	0.41	0.15	0.43	0.17	0.03	4.59	0.44	0.17	4.11	0.29	0.06

Table 6.2 Continued.

NGC5614	0.61	0.07	0.01	0.522	0.016	0.094	0.02	0.014	0.69	0.15	0.08	1.075	0.057	-0.184	-0.05	0.027	0.20	0.12	0.02	0.16	0.20	0.10	5.19	0.89	0.17	4.11	0.57	0.28
NGC5656	1.08	0.22	0.07	0.774	0.050	0.742	0.25	0.101	1.00	0.16	0.03	1.409	0.020	-0.231	-0.08	0.011	0.20	0.15	0.04	0.23	0.11	0.02	4.68	0.53	0.16	3.59	0.42	0.09
NGC5735	0.70	0.11	0.05	0.563	0.019	1.242	0.23	0.147	0.98	0.08	0.02	0.933	0.023	0.052	0.01	0.024	0.39	0.36	0.16	0.13	0.13	0.03	5.82	1.48	0.66	3.80	0.34	0.07
NGC5772	0.75	0.21	0.06	0.472	0.061	0.740	0.15	0.138	0.96	0.14	0.03	1.256	0.024	-0.200	-0.04	0.015	0.13	0.16	0.05	0.11	0.11	0.02	3.96	0.91	0.27	4.38	0.35	0.08
NGC5829	1.20	0.05	0.03	1.256	0.008	-0.837	-0.13	0.096	1.03	0.14	0.03	1.249	0.035	-0.223	-0.03	0.032	0.49	0.47	0.27	0.66	0.20	0.04	4.52	0.58	0.33	3.66	0.22	0.04
NGC6004	0.99	0.10	0.03	0.938	0.053	0.204	0.03	0.174	1.05	0.14	0.03	1.454	0.035	-0.380	-0.06	0.032	0.27	0.29	0.08	0.15	0.12	0.03	4.55	0.42	0.12	3.98	0.20	0.04
NGC6032	0.91	0.19	0.08	1.149	0.014	-1.664	-0.36	0.082	0.70	0.11	0.02	0.666	0.028	0.030	0.01	0.022	0.54	0.50	0.22	0.37	0.26	0.05	4.66	0.56	0.25	3.59	0.48	0.10
NGC6154	0.53	0.07	0.02	0.491	0.041	0.124	0.02	0.107	0.74	0.12	0.03	0.457	0.040	0.191	0.04	0.026	0.27	0.26	0.09	0.14	0.13	0.03	3.81	1.34	0.45	3.86	0.64	0.14
NGC6186	1.32	0.03	0.01	1.292	0.002	0.298	0.11	0.022	0.88	0.15	0.03	1.068	0.054	-0.142	-0.05	0.037	0.61	0.59	0.34	0.31	0.19	0.04	5.24	0.36	0.21	4.21	1.00	0.20
NGC6278	0.56	0.08	0.02	0.463	0.026	0.128	0.06	0.028	0.63	0.08	0.02	0.518	0.033	0.041	0.02	0.012	-	-	-	-	-	-	2.82	1.25	0.32	2.05	0.29	0.07
NGC6941	0.88	0.16	0.07	1.074	0.056	-1.310	-0.19	0.306	0.89	0.15	0.03	0.844	0.061	0.039	0.01	0.046	0.23	0.26	0.11	0.22	0.22	0.04	4.40	0.62	0.25	4.34	0.65	0.10
NGC7321	0.63	0.05	0.02	0.562	0.008	0.396	0.07	0.041	0.97	0.16	0.03	0.976	0.083	-0.008	0.00	0.058	0.32	0.29	0.13	0.19	0.13	0.03	5.25	0.67	0.30	4.32	0.45	0.09
NGC7489	1.07	0.03	0.02	1.039	0.003	0.434	0.07	0.039	1.00	0.13	0.02	1.226	0.024	-0.188	-0.03	0.017	1.05	0.58	0.34	0.68	0.21	0.04	5.47	0.40	0.23	4.06	0.62	0.11
NGC7625	1.27	0.01	0.00	1.260	0.007	0.048	0.03	0.029	0.88	0.18	0.03	1.252	0.042	-0.233	-0.16	0.024	0.79	0.39	0.16	0.54	0.19	0.03	5.08	0.19	0.08	4.26	0.86	0.16
NGC7653	0.81	0.23	0.09	0.501	0.044	1.249	0.36	0.149	1.06	0.13	0.03	1.283	0.010	-0.137	-0.04	0.006	0.41	0.30	0.11	0.35	0.16	0.03	4.28	0.41	0.16	3.98	0.16	0.03
NGC7691	1.10	0.03	0.01	1.092	0.028	0.097	0.02	0.312	1.02	0.13	0.03	1.228	0.036	-0.268	-0.05	0.042	0.38	0.38	0.19	0.54	0.13	0.03	3.82	0.57	0.28	3.66	0.40	0.08
NGC7716	0.69	0.18	0.05	0.455	0.053	0.585	0.25	0.109	0.91	0.10	0.02	0.883	0.038	0.014	0.01	0.022	0.25	0.24	0.07	0.22	0.12	0.03	3.39	1.40	0.40	3.89	0.27	0.06
NGC7738	0.76	0.03	0.02	0.731	0.011	0.215	0.05	0.058	0.67	0.07	0.01	0.574	0.016	0.060	0.01	0.009	1.70	0.87	0.44	0.22	0.23	0.05	9.80	1.54	0.77	4.26	1.24	0.24
NGC7819	1.25	0.13	0.05	1.422	0.026	-0.713	-0.15	0.088	0.94	0.11	0.02	1.010	0.045	-0.058	-0.01	0.037	0.35	0.27	0.10	0.33	0.19	0.04	4.14	0.31	0.11	4.09	0.23	0.05
UGC07012	1.12	0.02	0.01	1.148	0.010	-0.089	-0.04	0.029	1.01	0.05	0.01	1.112	0.011	-0.062	-0.03	0.006	0.24	0.25	0.10	0.48	0.24	0.06	3.67	0.17	0.07	3.28	0.20	0.05
UGC08234	0.48	0.06	0.03	0.546	0.024	-0.181	-0.06	0.054	0.56	0.09	0.02	0.525	0.044	0.013	0.00	0.014	0.22	0.38	0.17	0.33	0.24	0.05	-	-	-	2.25	1.93	0.40
UGC08733	1.08	0.04	0.02	1.119	0.020	-0.288	-0.08	0.117	0.99	0.07	0.02	1.087	0.030	-0.108	-0.03	0.031	0.15	0.17	0.07	0.34	0.17	0.04	3.40	0.36	0.15	3.40	0.19	0.04
UGC09067	1.23	0.01	0.01	1.225	0.000	0.074	0.02	0.000	1.05	0.14	0.03	1.337	0.010	-0.186	-0.04	0.006	0.60	0.55	0.32	0.58	0.29	0.06	4.99	0.36	0.21	4.02	0.53	0.12
UGC09291	1.13	0.02	0.01	1.104	0.010	0.264	0.06	0.073	1.04	0.09	0.02	1.207	0.019	-0.180	-0.04	0.018	0.18	0.22	0.10	0.19	0.14	0.03	3.48	0.39	0.17	3.65	0.18	0.03
UGC09476	1.28	0.08	0.04	1.379	0.018	-0.883	-0.20	0.126	1.06	0.12	0.02	1.302	0.009	-0.235	-0.05	0.008	0.24	0.25	0.11	0.18	0.11	0.02	4.17	0.26	0.12	4.15	0.26	0.05
UGC10796	0.98	0.01	0.00	0.969	0.004	0.072	0.03	0.026	0.92	0.10	0.02	1.099	0.035	-0.155	-0.06	0.028	0.19	0.11	0.06	0.42	0.19	0.04	3.38	0.19	0.09	3.03	0.23	0.05
UGC12224	1.20	0.11	0.05	1.347	0.009	-1.586	-0.30	0.082	1.02	0.10	0.02	1.158	0.017	-0.153	-0.03	0.017	0.23	0.26	0.12	0.38	0.24	0.04	4.11	0.79	0.35	3.68	0.29	0.05

Investigated Relations

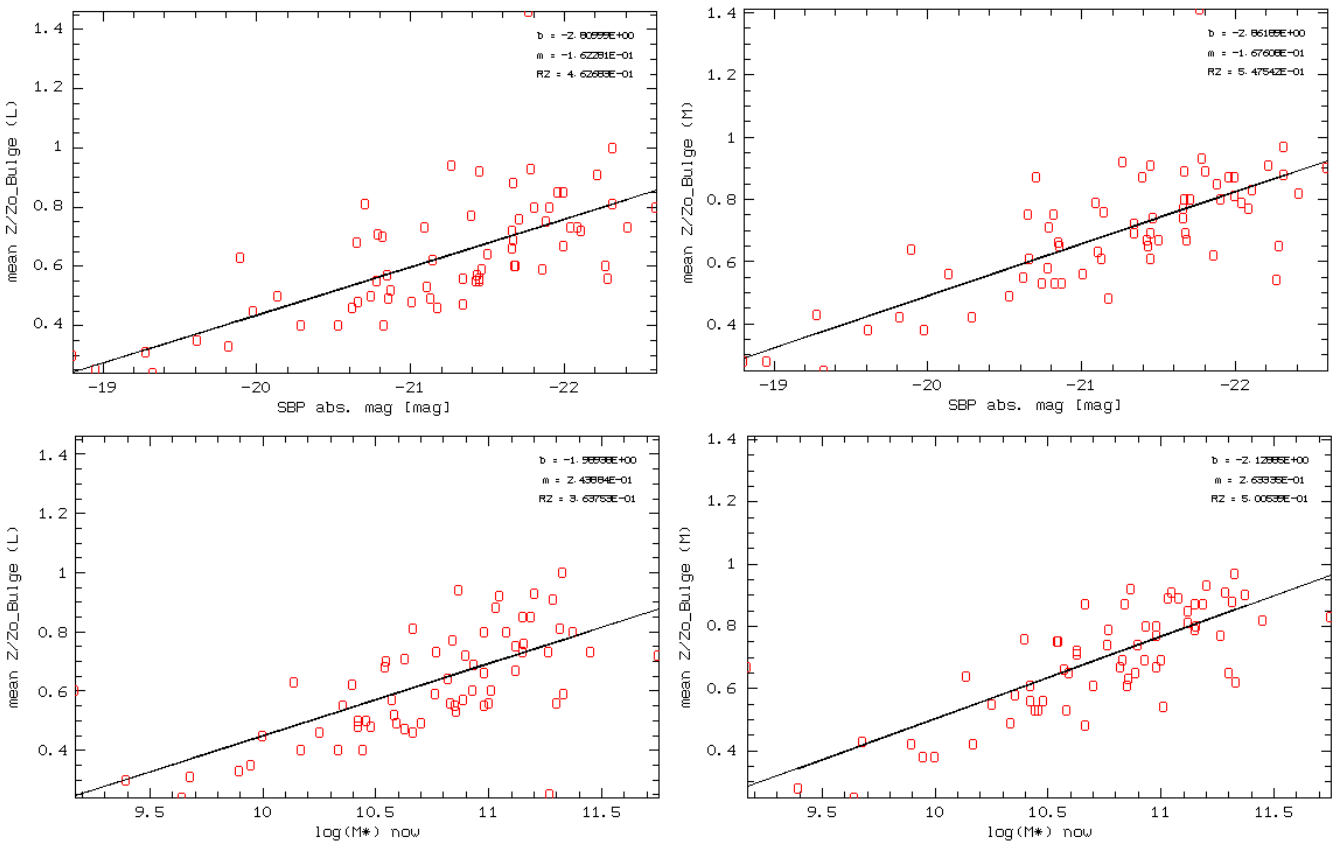

Figure 6.5: Top: Mean stellar metallicity in the Bulge [$Z_{\odot}$] versus total SBP absolute magnitude [mag]; Bottom: Mean metallicity in the Bulge [$Z_{\odot}$] versus the logarithm of the stellar mass that the galaxy contains (Left: luminosity weighted metallicity; Right: mass weighted metallicity).

Fig. 6.5 shows how the mean stellar metallicity of the bulge relates with the total absolute magnitude of the galaxy (top) and the total stellar mass (bottom). There is an obvious correlation ($R^2 \sim 0.46$; 0.55 luminosity- and mass-weighted quantities, respectively, for the total absolute magnitude and $R^2 \sim 0.36$; 0.50 for the total mass): the more luminous/massive the galaxy, the higher is its metal content in the bulge. This fact may be attributed to the galactic gravitational potential: since a more massive galaxy has a deeper gravitational potential well, it is expected that it will be able to retain a larger fraction of metal enriched gas which can be reprocessed into a subsequent generation of stars. From Table 6.2 the reader can confirm that, in average, the more luminous/massive galaxies are the ones showing a higher mean stellar age in the bulge. Since the time-scale for incorporating the metals into the stars is relatively long (up to 1Gyr, depending on gas density and metallicities – Papaderos; lectures on Advanced Topics in Extragalactic Astronomy – P/L)), one possible explanation is that the stars already had enough time to incorporate

the metals formed trough previous SF activity. This correlation can be perceived both in luminosity and mass weighted metallicity.

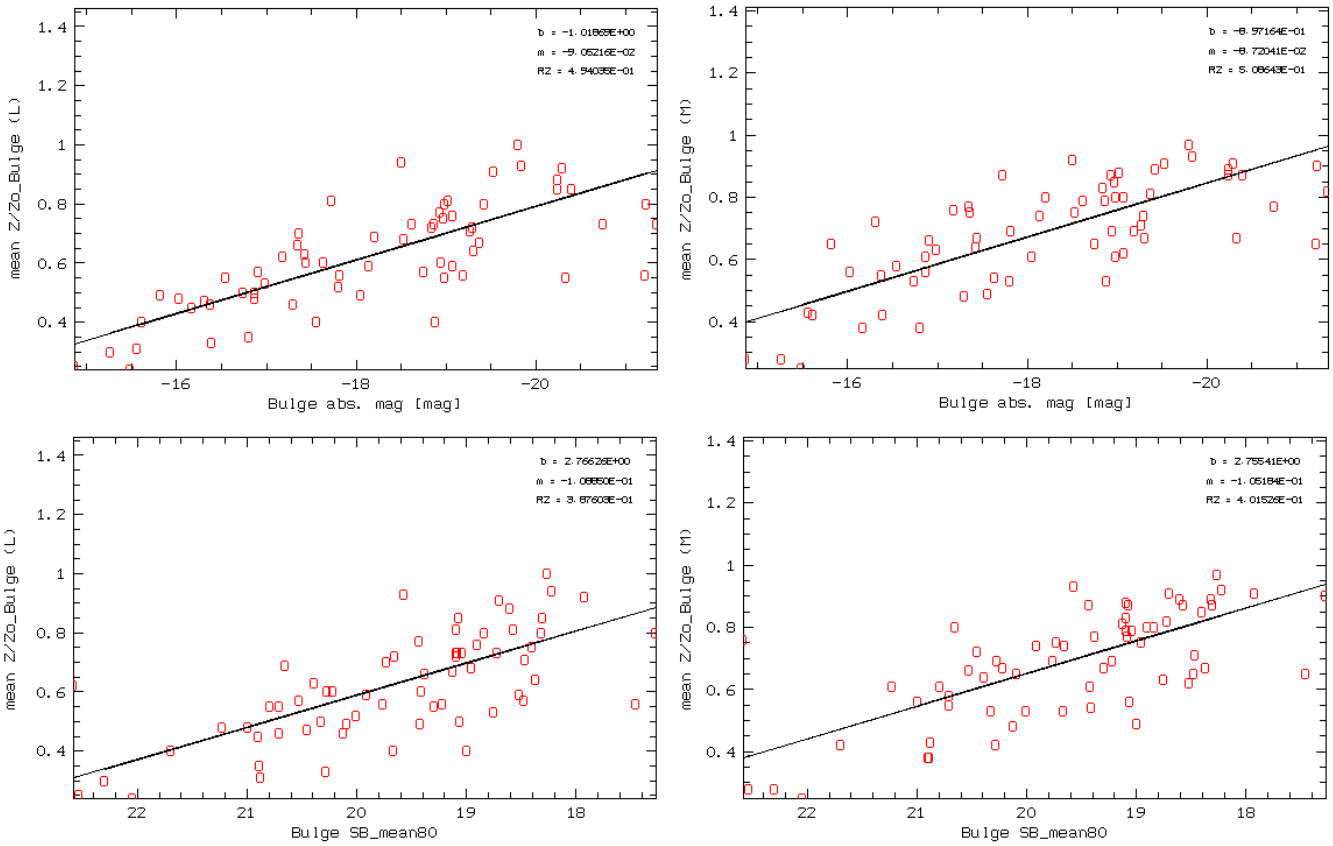

Figure 6.6: Top: Mean stellar metallicity in the Bulge [$Z_{\odot}$] versus bulge absolute magnitude [mag]; Bottom: Mean stellar metallicity in the Bulge [$Z_{\odot}$] versus bulge mean surface brightness at R_{80} [mag/arcsec^2] (left: luminosity weighted metallicity; right: mass weighted metallicity).

By relating the mean stellar metallicity with the absolute magnitude of the bulge, one can visualize the same trend as before: more luminous/massive bulges present a higher metal content ($R^2 \sim 0.49$; 0.51). From the lower panels it is apparent that this trend is preserved when the Z_* is related to the μ_{80} ($R^2 \sim 0.39$; 0.40): more compact/denser bulges also present higher mean contents of metals weighted both in light and in mass. One explanation for these trends is the same as the one proposed before: more massive/compact bulges present deeper and steeper gravitational potential wells, retaining a larger fraction of the metals, likely efficient collapse of gas into stars.

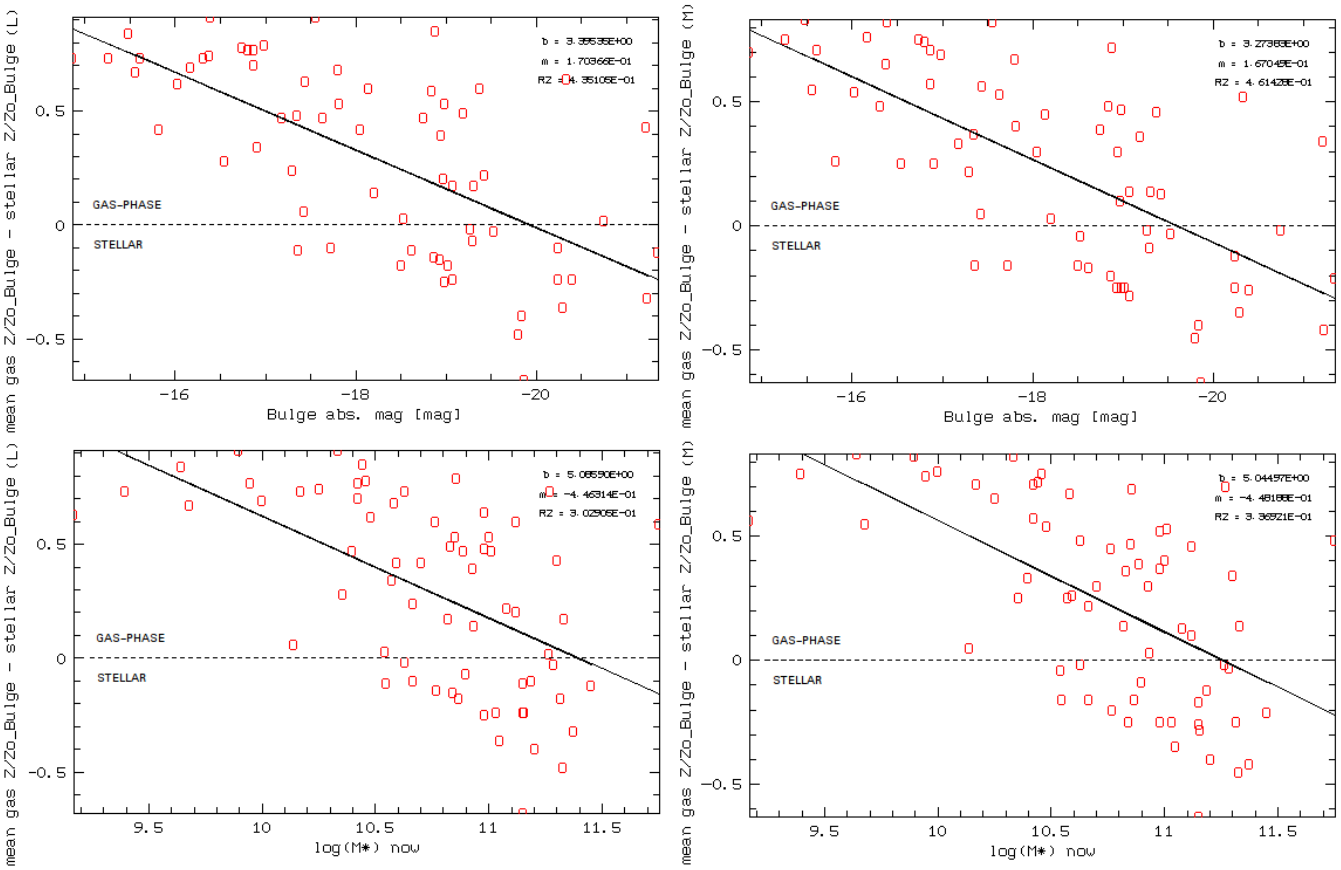

Figure 6.7: Top left: Difference between the mean gas-phase metallicity and luminosity weighted stellar metallicity in the bulge [$Z_{\odot}$] versus bulge absolute magnitude [mag]; Top right: Difference between the mean gas-phase metallicity and mass weighted stellar metallicity in the bulge [$Z_{\odot}$] versus bulge absolute magnitude [mag]; Bottom left: Difference between the mean gas-phase metallicity and luminosity weighted stellar metallicity in the bulge [$Z_{\odot}$] versus the logarithm of the stellar mass of the galaxy; Bottom right: Difference between the mean gas-phase metallicity and mass weighted stellar metallicity in the bulge [$Z_{\odot}$] versus the logarithm of the stellar mass presently available.

From Fig. 6.7 it can be seen that the difference between the gas-phase metallicity and both luminosity- and mass-weighted stellar metallicity correlates with the bulge absolute magnitude (top) ($R^2 \sim 0.44$; 0.46) and with the total stellar mass of the galaxy (bottom) ($R^2 \sim 0.30$; 0.34): for less luminous bulges and less massive galaxies, the gas contained within the bulge tends to have a higher metallicity than the stellar component. For more luminous bulges and more massive galaxies, the metals tend to be incorporated within the stellar component, whereas the ionized gas has comparable or lower metallicity. This trend might again be connected to the scenario where low-mass galaxies present a shallow potential well, not being able to effectively retain metals in SF episodes, whereas in high mass galaxies part of the gas might be virialized to X-Ray temperatures, being invisible in the optical. Analyzing more carefully the sample ($H\alpha$ and $EW(H\alpha)$ radial profiles, App. A), one can perceive that the less massive galaxies are the ones that are

actively forming stars, gathering the necessary conditions for ionizing the gas. Since the gas is enriched in much shorter time-scales than the stars (P/L), one would expect this type of galaxies to have higher content in metals in the gas-phase than incorporated into the stars. On the other hand, massive galaxies do not present intensive ongoing star formation, which may explain why no significant metal production took place in the recent past. Alternatively or additionally, effective inflow of comparatively metal-poor gas from the disk onto the massive bulge component of those galaxies may lead to a dilution of the gas-phase metallicity.

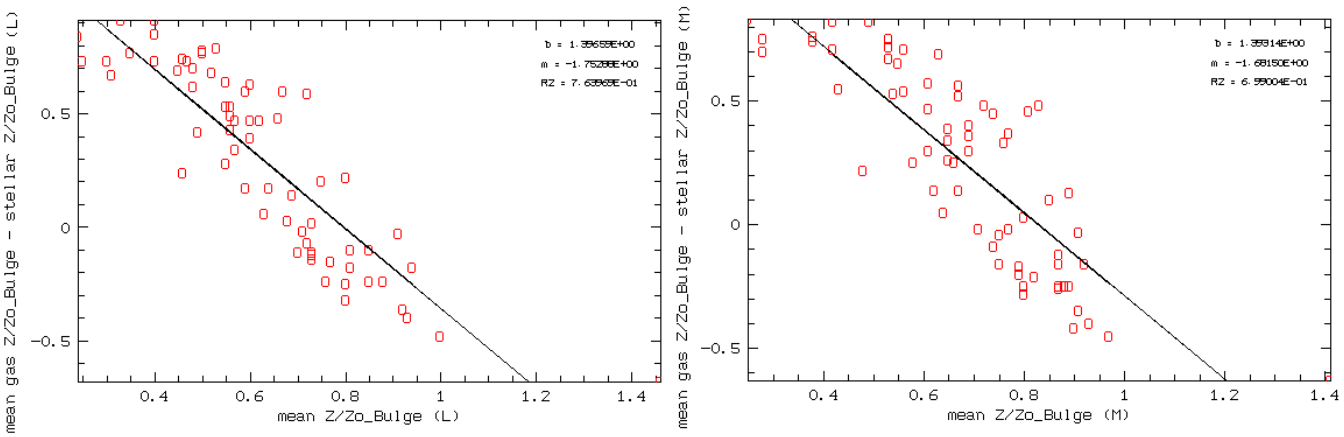

Figure 6.8: Left: Difference between the mean gas-phase metallicity and luminosity-weighted stellar metallicity in the bulge [$Z_{\odot}$] versus mean luminosity-weighted stellar metallicity [$Z_{\odot}$]; Right: Difference between the mean gas-phase metallicity and mass-weighted stellar metallicity in the bulge [$Z_{\odot}$] versus mean mass-weighted stellar metallicity [$Z_{\odot}$].

Fig. 6.8 shows a tight correlation ($R^2 \sim 0.76$; 0.70) between the difference of the mean gas-phase metallicity and stellar metallicity in the bulge, and the mean stellar metallicity (both luminosity- and mass-weighted): galactic bulges with higher stellar metallicity usually present a low gas-phase metallicity, whereas the opposite is the case for systems with a low stellar metallicity. One may interpret this result by considering that systems with higher stellar metallicity have depleted their metal-enriched gas, converting it into stars and/or contains a hot (several 10^7 K) halo of metal-rich gas that remains invisible in the optical wavelengths. Inflow of relatively metal-poor gas from the halo offers a second hypothesis.

Histograms

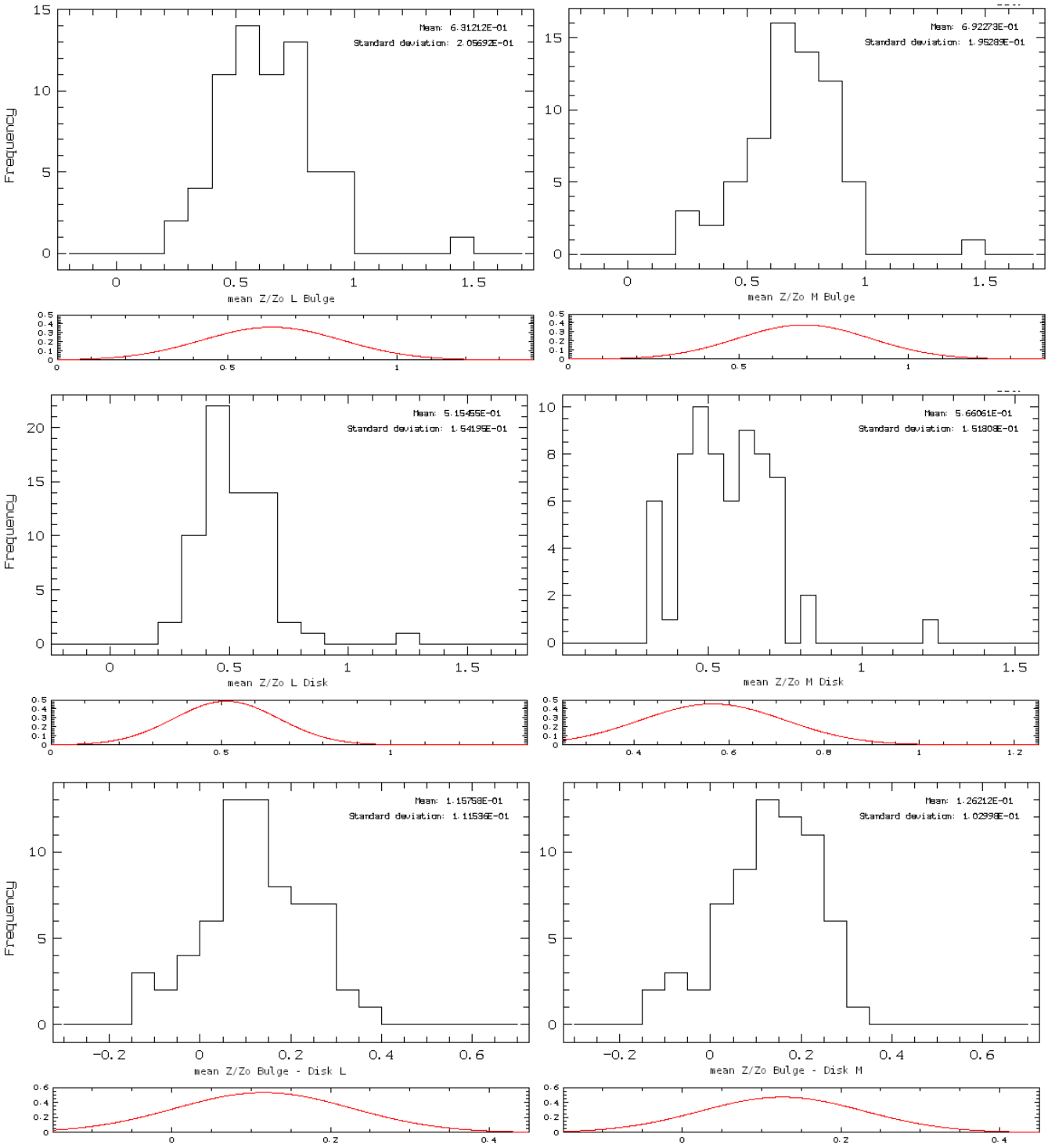

Figure 6.9: Histograms for some of the estimated spectroscopic quantities (part1): From top to bottom: mean stellar metallicity in the bulge, mean stellar metallicity in the disk, difference between the mean stellar metallicity of the bulge and the disk (left: luminosity weighted; right: mass weighted).

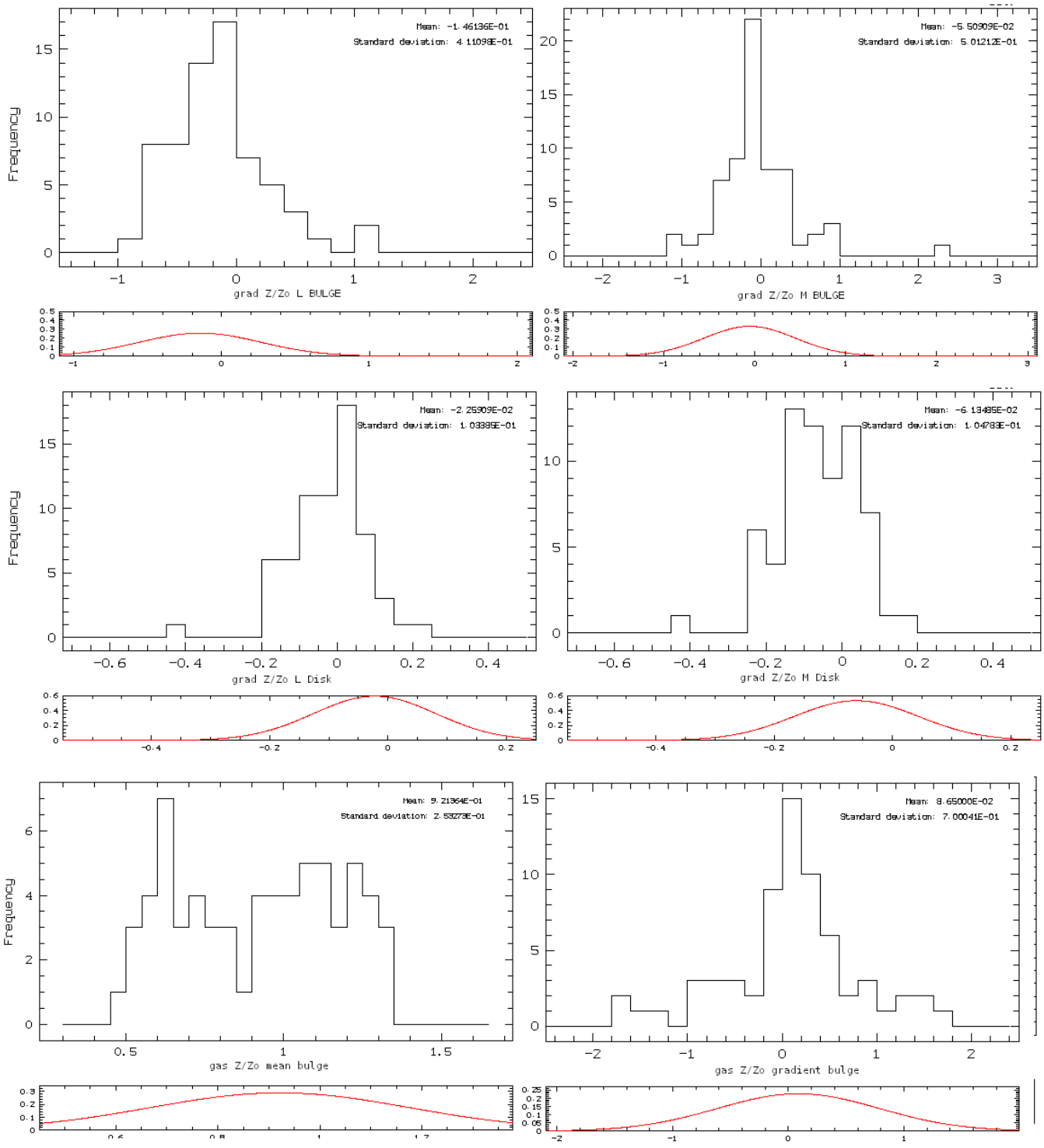

Figure 6.10: Histograms for some of the estimated spectroscopic quantities (part2): From top to bottom: gradient of the stellar metallicity within the disk, gradient of the stellar metallicity within the bulge, gas-phase metallicity mean values (left) and gas-phase metallicity gradient (right).

The histograms of Fig.s 6.9 and 6.10 (from left to right, luminosity- and mass-weighted quantities, respectively, excluding the last row of diagrams) show how the more relevant estimated quantities are distributed throughout the analyzed sample. In Fig. 6.9, from top to bottom: mean stellar metallicity of the bulge ($< Z_L >= 0.631$, $< Z_M >= 0.692$); mean stellar metallicity of the disk ($< Z_L >= 0.515$, $< Z_M >= 0.566$); difference between mean stellar metallicity of the bulge and the same of the disk ($< Z_L >= 0.116$, $< Z_M >= 0.126$). In Fig. 6.10, from top to bottom: stellar metallicity gradient of the bulge ($< Z_L >= -0.146$, $< Z_M >= -0.055$); stellar metallicity gradient of the disk ($< Z_L >= -0.023$, $< Z_M >= -0.061$); mean gas-phase metallicity of the bulge ($< Z_g >= 0.921$); gas-phase metallicity gradient of the bulge ($< Z_g >= 0.087$). All the quantities for the stellar metallicity show approximately a Gaussian distribution, revealing a homogeneous sample. The exception is the mean gas-phase metallicity of the bulge which visual inspection may suggest two different populations.

Besides the fact that no obvious correlation exists between the stellar (luminosity- and mass-weighted) gradient for the bulge and the disk with other photometric and evolutionary properties, the histograms suggest the presence of possibly two distinct types of galaxy bulges in the analyzed sample: one with positive metallicity gradients - implying that the content in metals is increasing from the center to the periphery of the bulge - and another that presents negative metallicity gradients, implying the opposite. One can see this behavior both in the disk and in the bulge. The disk gradients will not be discussed in detail in this work, since its main aim regards the nature of the galactic bulge.

An interesting question to be discussed next is how the stellar metallicity gradients are related with those in stellar age. Since the Master Thesis of Sandra Reis concerns the stellar age gradients in the same analyzed sample, she kindly provided her determinations of the age gradients, which will be correlated with metallicity gradients. The following image shows the distribution of the galaxies in a scheme where, for luminosity-weighted quantities, the red dots show bulges where both gradients are positive, the blue dots, the bulges presenting both negative gradients, the cyan the ones, with negative age gradient and positive metallicity gradient and the green ones showing positive age gradient and negative metallicity gradient:

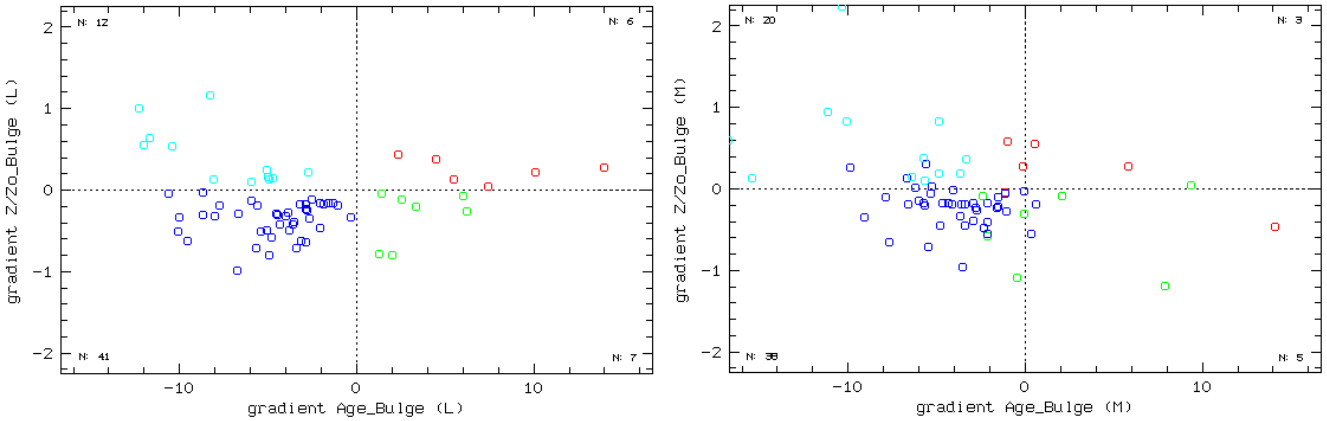

Figure 6.11: Distribution of the nature of the stellar gradients (both metallicity and age) in the analyzed sample [dex/R_{eff}].

The analyzed sample was then divided into 4 distinct classes according to the nature of the luminosity-weighted stellar metallicity and age gradients. The mean values of each class for the stellar metallicity ($< Z_{B*} >$), stellar age ($< A_{B*} >$), gas-phase metallicity gradient ($< Z_{BNm} >$), gas-phase metallicity ($< Z_{BN} >$), total absolute magnitude ($< AbsMag >$), mean $H\alpha$ equivalent width ($< EW(H\alpha)_B >$), mean mass fraction of stars younger than 100 Myr ($< M_{100\%} >$) and light fraction of the disk plus bar contribution ($< fr_{BA+D} >$) were also estimated – values for the bulge component excepting the integral quantity $< AbsMag >$. The result is shown in the next table:

Table 6.3: Signal of the luminosity-weighted metallicity and age gradients in the bulges of the analyzed sample (Z_{B*} and A_{B*}, respectively) presenting the mean values for the stellar metallicity ($< Z_{B*} >$), stellar age ($< A_{B*} >$), gas-phase metallicity gradient ($< Z_{BNm} >$) and gas-phase metallicity ($< Z_{BN} >$) for each of the four classes of galaxies within the bulge, followed by the mean total absolute magnitude ($< AbsMag >$), mean $H\alpha$ equivalent width ($< EW(H\alpha)_B >$), mean mass fraction of stars younger than 100 Myr ($< M_{100\%} >$) and light fraction of the disk plus bar contribution ($< fr_{BA+D} >$) – all of this quantities, with exception of $< AbsMag >$, are relative to the bulge component. For each mean value is the mean standard deviation ($< \sigma >$) included within the parenthesis.

Galaxy	$Luminosity\ Weighted$				$Gas-phase\ Z$			$< AbsMag >$	$< EW(H\alpha)_B >$	$< M_{100\%} >$	$< fr_{BA+D} >$
	Z_{B*}	$< Z_{B*} >$	A_{B*}	$< A_{B*} >$	Z_{BN}	$< Z_{BNm} >$	$< Z_{BN} >$				
IC0776	+		+		+						
NGC0165	+		+		-						
NGC5000	+		+		-						
NGC6032	+	0.448	+	6.908	-	-0.684	0.978	-20.680	26.923	0.303	0.647
NGC7738	+	(0.066)	+	(1.096)	+	(0.354)	(0.052)	(0.498)	(5.798)	(0.052)	(0.034)
UGC08733	+		+		-						
IC1256	-		-		-						
IC4566	-		-		+						
NGC0001	-		-		-						
NGC0160	-		-		+						
NGC0171	-		-		+						
NGC0214	-		-		+						
NGC0237	-		-		-						
NGC0257	-		-		+						
NGC0477	-		-		-						
NGC1093	-		-		+						
NGC1645	-		-		+						
NGC2253	-		-		-						
NGC2347	-		-		+						
NGC2639	-		-		+						
NGC2906	-		-		+						
NGC3300	-		-		+						
NGC3687	-		-		+						
NGC4003	-		-		-						
NGC4047	-		-		+						
NGC4961	-		-		+						
NGC5205	-	0.712	-	9.121	+	0.232	0.866	-21.449	7.958	0.130	0.622
NGC5320	-	(0.030)	-	(0.373)	+	(0.089)	(0.041)	(0.109)	(1.373)	(0.020)	(0.020)
NGC5378	-		-		-						
NGC5406	-		-		+						
NGC5614	-		-		+						
NGC5656	-		-		+						
NGC5772	-		-		+						
NGC5829	-		-		-						
NGC6004	-		-		+						
NGC6154	-		-		+						
NGC6186	-		-		+						
NGC6278	-		-		+						
NGC6941	-		-		-						
NGC7321	-		-		+						
NGC7489	-		-		+						
NGC7625	-		-		+						
NGC7653	-		-		+						
NGC7716	-		-		+						
UGC07012	-		-		-						
UGC08234	-		-		-						
UGC09067	-		-		+						

NGC0180	+		-		-						
NGC2916	+		-		+						
NGC3381	+		-		-						
NGC3614	+		-		-						
NGC4185	+		-		+						
NGC4210	+	0.548	-	7.762	+	0.107	0.972	-20.987	14.101	0.184	0.684
NGC5016	+	(0.042)	-	(0.601)	+	(0.274)	(0.079)	(0.189)	(5.655)	(0.046)	(0.024)
NGC5735	+		-		+						
NGC7691	+		-		+						
UGC09291	+		-		+						
UGC09476	+		-		-						
UGC12224	+		-		-						
NGC0023	-		+		-						
NGC0776	-		+		+						
NGC2730	-		+		+						
NGC3057	-	0.464	+	5.004	-	-0.138	1.108 (0.051)	-20.602	28.763	0.820	0.586
NGC5480	-	(0.066)	+	(1.039)	-	(0.107)	(0.051)	(0.471)	(3.595)	(0.370)	(0.063)
NGC7819	-		+		-						
UGC10796	-		+		+						

From inspection of the above table one can identify four classes of bulges:

◦ Class 1 (both gradients positive for Z_* and A_*): bar dominated $(4/6)$, with intermediate-to-low luminosity values ($< AbsMag >= -20.680$) and were morphologically classified as flocculent/diffuse ($\sim$ III in the Extension of the Hubble Scheme by Van den Berg scale (EHSVB)(1960), later included in the Revised Shapley Ames Catalog). From the $EW(H\alpha)$ and $H\alpha$ flux (Table 4.1, Chapter 4) one can perceive that these bulges are actively forming stars.

◦ Class 2 (both gradients negative for Z_* and A_*): faint to strong bars $(25/41)$, with high luminosity values ($< AbsMag >= -21.449$) and were morphologically classified, in most classes as grand design spiral arms (from I to II in the EHSVB scale). All the three CBs belong to this class.

◦ Class 3 (positive gradient for Z_* and negative gradient for A_*): faint bars $(7/12)$, with intermediate to high luminosity values ($< AbsMag >= -20.987$) and the low prominence of the spiral arms are their main morphological features ($\sim$ II in the EHSVB scale).

◦ Class 4 (negative gradient for Z_* and positive gradient for A_*): strong $(3/7)$ or no bar, with low-to-intermediate luminosity values ($< AbsMag >= -20.602$) and were morphologically classified

as diffuse ($\sim$ III in the EHSVB scale), being actively forming stars.

Several mean quantities were estimated for these four classes and listed in the Table 6.3, in order to facilitate a comparison of their main properties. By analyzing the tabulated mean values one can recognize a segregation with regard to the considered bulge and integral properties. For instance, the $fourth\ class$ shows the highest values for $< Z_{BN} >$, $< EW(H\alpha)_B >$ and $< M_{100\%} >$ and the lowest values for $< Z_{B*} >$, $< A_{B*} >$ and $< AbsMag >$. On the other hand, the $second\ class$ shows the highest values for $< Z_{B*} >$, $< A_{B*} >$ and $< AbsMag >$ and the lowest values for $< Z_{BN} >$, $< EW(H\alpha)_B >$ and $< M_{100\%} >$. This fact seems to indicate that these two classes of galactic bulges may be dominated by different physical processes, and/or have undergone a different formation history. As for Class 1 and 3, they lie in the intermediate range: the $first\ class$ presents the second higher values for $< Z_{BN} >$, $< EW(H\alpha)_B >$ and $< M_{100\%} >$ and the second lower values for $< Z_{B*} >$ and $< \mu_{A_{B*}} >$; the $third\ class$ presents the second higher values for $< Z_{B*} >$, $< A_{B*} >$ and $< AbsMag >$ and the second lower values for $< Z_{BN} >$, $< EW(H\alpha)_B >$ and $< M_{100\%} >$. In addition, Class 1 and 4 present negative mean gas-phase metallicity gradient whereas Class 2 and 3 present positive mean gas-phase metallicity gradient. The four classes always follow the same trends, indicating a well defined sequence: classes 4, 1, 3 and finally 2, in order of increasing mass, age and Z_* luminosity, and decreasing gas-phase metallicity and ongoing star formation activity. Although, one must carefully interpret these results due to the fact that the the derived quantities for stellar and gas-phase metallicity and age don't refer to the pure bulge but $bulge + disk + bar$ (for barred galaxies) or $bulge + disk$. The last column of Table 6.3 shows the mean values for the $disk + bar$ contribution (in light fraction): for all the cases the light contribution of these external components is highly significant, being higher than 50 $\%$. In the future it is intended to remove the $disk + bar$ contribution within the bulge radius and compare with the present obtained results.

Chapter 7.

Conclusions and Discussion

This Chapter summarizes and provides a brief discussion of the most significant results obtained in this work, by order of appearance in the document.

Photometric Analysis

The surface photometry technique devised here has permitted, thanks to an elaborated $bulge + bar + disk$ decomposition technique, to estimate structural parameters that were correlated with the output from spectral synthesis models. Out of a sample of 66 late-type galaxies, with mean total absolute magnitude of -21.205 mag, it was found that 36 of these galaxies contain a bar (being clearly identified after the subtraction of the exponential disk component, sometimes evident from visual inspection of SDSS r band Fig.s), in $16/36$ of the cases being equally or more pronounced than the bulge. This fact indicates that one should not disregard the bar contribution in 1D or 2D galaxy decomposition. In cases where a prominent bar is present, a simple $bulge + disk$ galaxy decomposition would lead to an overestimation of the luminosity of the bulge, as both the combined bar and bulge luminosity would erroneously be ascribed to the bulge only, when fitting a single Sérsic model. On the other hand, in some of the analyzed galaxies, it is possible to visually identify the bar component being marginally traceable on the r band SBPs. In some of the cases this could be because the extent of the bar is only slightly larger than that of the bulge, requiring further exploration, as for instance, the investigation of other photometric bands. The mean ab-

solute magnitude of the bulge of the galaxies of the sample is -18.227 and its mean angular and linear extent is 7.078 arcsec and 2.002 kpc, respectively. The mean bulge η of the sample is 0.92 and the mean bulge-to-total ratio is 0.10. It were found 63 objects with bulge $\eta \leq 2$ that, by adopting the Kormendy & Kennicutt (2004) classification scheme, would qualify as pseudo-bulges. The three CBs in the sample are NGC5614, NGC5656 and NGC6004.

After applying the dmr30M correction computed spaxel-by-spaxel by $RemoveYoung$ (Gomes et al. 2014, in prep.) for the light contribution of stars younger than 30 Myr, the mean values for the galaxies's absolute magnitude, bulge absolute magnitude, isophotal bulge extent, bulge Sérsic η and bulge-to-total luminosity ratio are, -20.993 mag, -18.262 mag, 7.575 arcsec / 2.136 kpc, 0.95 and 0.115, respectively. By comparing these values with those obtained prior to RY, it is clear that even though the total absolute magnitude of the galaxy decreases – as it is expected through the removal of the young ionizing stellar component – the bulge component become more prominent both in terms of luminosity and isophotal extent.

As discussed in Chapter 4 (see Papaderos et al. 2014, in prep.), the standard technique of subtracting an exponential fit to the disk from the SBP in order to determine the residual emission of the bulge (and eventually of the the bar) is only correct when the star formation rate per unit area $\Sigma_{\rm SFR}$ in the disk is proportional to the local stellar surface density $\Sigma_\star$, with an overall constant proportionality factor. For a geometrically thin, face-on disk this implies a radially constant $EW(H\alpha)$, which, was shown in Chapter 4 not to be the case for the analyzed sample: the presented evidence indicates that the disks are forming stars more actively than the bulge and that the $\Sigma_{\rm SFR}$ throughout the disk is not constant. The enhanced surface brightness of the disk due to star formation, together with the virtual absence of star formation in the bulge, will obviously result in an oversubtraction of the disk emission beneath the bulge, as discussed in Papaderos et al. (2014). Consequently, to simply subtract an exponential disk to the SBP will systematically reduce both the luminosity and the isophotal radius of the bulge. The goal of RY is to filter out from an observed spectrum the contribution of stars younger than a user-defined cutoff, taken here to be 30 Myr (see Gomes et al. 2014, in prep. and the three lower panels of the Figs. of App. A for the variation of dmr with increasing age cutoff), placing a conservative limit for the removal

of ionizing stellar populations by stripping of the galaxy disk from regions of active star formation which elevate the disk's surface brightness (by up to 1 mag).

In the sequence of this work there were identified several interesting relations between some of the estimated parameters. The first one is the relation between the bulge absolute magnitude and the total absolute magnitude ($R^2 \sim 0.64$; 0.70), for before and after applying RY, respectively), together with the bulge-to-total ratio versus the total absolute magnitude of the galaxy ($R^2 \sim 0.16$; 0.15). From the first relation one might naively expect that the more massive the galaxy is, the more prominent is its bulge, whereas considering the second relation, one will immediately understand that this statement is false, since there is no clear relation between the bulge-to-total ratio and the total absolute magnitude. The trend that appears in the upper part of Fig. 5.5 might be partly artificial due to the fact that both plotted quantities are distance dependent. This subject also needs to be more deeply explored in the future.

In the upper part of the Fig. 5.6 it is presented the relation between the bulge Sérsic η and the bulge absolute magnitude ($R^2 \sim 0.22$; 0.19). The trend between both quantities is very weak, indicating that the bulge η is not a sensitive indicator of the luminosity/mass or prominence/compactness of the bulge. By carefully analyzing the photometric decompositions for some of the galaxy's SBPs, one can draw the same conclusion. The Sérsic model involves 3 parameters, and so the η by itself is not sufficient for defining an SBP. For instance, by comparing the profile decompositions of NGC0214 with that of NGC4047 (before applying RY) and assuming, for the sake of this exercise, that both profiles have the same bulge central surface brightness, one can realize that, despite presenting equal η, it is clear that the NGC0214 encompasses much more light emission than NGC4047. This is because the R_{eff} of the bulge of NGC0214 is significantly higher than that of NGC4047, which will "open" the Sersic profile, enclosing a higher fraction of light, yet maintaining the same η.

In the lower part of the same Fig. it is presented the relation between the mean surface brightness of the bulge μ_{80} (i.e. the apparent magnitude of the bulge divided by the area encircled within R_{80}), and the bulge absolute magnitude ($R^2 \sim 0.61$; 0.58). This parameter is a proxy to the stellar

mass surface density within R_{80} so it is expected that compact bulges present higher values for this quantity whereas more tenuous bulges should present lower values. By inspection of the Fig. 5.6 it is possible to identify a clear trend between μ_{80} and the absolute magnitude of the bulge. The interpretation is that high-luminosity bulges tend to be more dense, with their stellar surface density (and presumably also their volume density) steeply increasing at their centers, whereas low luminosity galaxies tend to present the opposite. The tightness of both relations of Fig. 5.6 suggests that the parameter μ_{80} is a more sensitive indicator of the compactness of the bulge than the bulge η, which, as it was pointed out above, suffers from a degeneracy.

In the following Fig. (5.7) it is presented the relation between the bulge η and the bulge-to-total ratio ($R^2 \sim 0.24$; 0.20). As is was already discussed above, there is no clear correlation between the bulge η and the prominence of the bulge in the galaxy.

Fig. 5.8 relates the bulge μ_{80} with the total absolute magnitude of the galaxy ($R^2 \sim 0.47$; 0.53), revealing a trend which becomes tighter after the application of RY. One of the possible interpretations for this correlation is that for more luminous/massive galaxies, the bulge tend to be more dense, preserving its stellar component more compacted and closer to the center. This is probably a consequence of the deeper potential well of these massive galaxies: it is expected that more massive galaxies have a deeper gravitational potential that effects a higher central stellar mass density, promoting the assembly of the bulge stars in a more compressed form.

Spectroscopic Analysis

The second part of this work is devoted to the determination of radial metallicity profiles (both in the stellar component and in the ionized gas) for each of the galaxies of the sample, based on auxilliary codes that computes the radial distribution of various quantities from the output data-cubes of PORTO3D pipeline. As discussed in Chapter 3, the spaxel-by-spaxel modeling of IFS data from the CALIFA Survey employs STARLIGHT (Cid Fernandes et al., 2005), a stellar spectral synthesis code, that decomposes a spectrum into SSP spectral templates, providing information about metallicity, age, SFH, kinematics, stellar extinction and others. As for the gas-phase metal-

licities, they were computed with a MIDAS code developed in this project based in the Marino et al. (2013) calibration, that estimates the $12 + log(O/H)$ based in strong line methods, specifically on the $[OIII]\lambda5007/H\beta$ and $H\alpha/[NII]\lambda6583$ ratios, as it is explained in Chapter 3. For this purpose it was also developed a MIDAS code, inspired in a Fortran code kindly provided by J.M. Gomes, that estimates the gas-phase extinction based on the observed $H\alpha/H\beta$ ratio. The PORTO3D pipeline computes and stores into different layers of an output data-cube several other spectroscopic quantities such as the $H\alpha$ flux, $EW(H\alpha)$ and mass fraction M_{100} of stars younger than 100 million years. In addition, Sandra Reis has kindly provided her results on the nature of the luminosity-weighted age gradients in the bulge and the mean stellar age in the bulge for four classes of galaxies that will be discussed later on in this Chapter.

Considering the entire sample, it was found a mean luminosity-weighted stellar metallicity of $0.631\ Z_{\odot}$ for the bulge and $0.515\ Z_{\odot}$ for the disk, yielding a difference of 0.12 dex, and a mean mass-weighted stellar metallicity of $0.692\ Z_{\odot}$ for the bulge and $0.566\ Z_{\odot}$ for the disk (0.13 dex of difference). On average, the mass-weighted metallicities are higher than the luminosity weighted metallicities. This may be attributed to different SFHs, although, clearly, a quantitative investigation of this issue is needed. For the gas-phase metallicity it was found $0.921\ Z_{\odot}$ for the bulge and $0.923\ Z_{\odot}$ for the disk, yielding a difference of only -0.002 dex, indicating that the ionized gas in both bulge and disk are nearly equally enriched in heavy metals.

By comparing the estimated mean values for the stellar metallicity, one can conclude that for these spiral galaxies, the stars in the bulge are more metal enriched than the ones in the disk, and that the mass fraction of metals in the gas is significantly higher than the same in the stellar component. On the other hand, there is no clear difference between the gas-phase metallicity in the bulge and in the disk. Analyzing the histograms related with the stellar radial metallicity distribution in the bulge, one can infer that there are both positive and negative gradients, which implies, respectively, an increasing and decreasing metallicity with galactocentric radius, which is also seen with regard to the gas-phase metallicity.

In this work all the estimated quantities were corrected for extinction. The average value for the stellar extinction in the bulge is $0.330\ V$ mag and disk $0.313\ V$ mag, implying that the stellar

extinction is higher in the bulge than in the disk. The average $H\alpha/H\beta$ ratio in the bulge is 4.421 and in the disk 3.802. Assuming the theoretical value for $H\alpha/H\beta = 2.86$, the gas-phase extinction is notably higher in the bulge than in the disk.

As in the photometric study, a number of clear trends were found by considering the quantities inferred from modeling the IFS data with PORTO3D. The first regards the mean stellar metallicity in the bulge versus the total absolute magnitude (Fig. 6.5, top) and the mean stellar metallicity in the bulge versus the logarithm of the total stellar mass present in the galaxy now (Fig. 6.5, bottom), both weighted by luminosity and mass (left-side and right-side panel, respectively – $R^2 \sim$ 0.46; 0.55 luminosity- and mass-weighted quantities, respectively, for the total absolute magnitude and $R^2 \sim$ 0.36; 0.50 for the total mass). The trend between these three parameters is clear: more luminous/massive galaxies tend to present higher stellar metallicities in their bulge. In the next Fig., comparing the mean stellar metallicity in the bulge with the bulge luminosity (Fig. 6.6, top – $R^2 \sim$ 0.49; 0.51) or with μ_{80} (Fig. 6.5, bottom – $R^2 \sim$ 0.39; 0.40) one can perceive the same trend as before: more massive (and compact) bulges display a higher metal content in their stars. One of the possible explanations for this trend is that, in high mass galaxies, due to their deep gravitational potential, a large fraction of metal-enriched gas will be prevented from escape and subsequently incorporated in the following stellar generation. Another point that might support the interpretation of this trend may be related with the mean age of the stars that constitute the bulges of high-mass galaxies: as it is shown in Table 6.3, these galaxies (Class 2) are the ones that present higher mean stellar age in their bulge. As the time-scale for a galaxy to be able to convert its metal-enriched gas into stars is of one Gyrs (P/L), one may assume that these more massive galaxies with older bulges, already had time to reprocess metals into multiple stellar populations.

The next relation that is presented (6.7) concerns the difference between the gas-phase metallicity and the – luminosity- (left) and mass- (right) weighted – stellar metallicity in the bulge versus the bulge absolute magnitude (top – $R^2 \sim$ 0.44; 0.46) and the logarithm of the total stellar mass of the galaxy (bottom – $R^2 \sim$ 0.30; 0.34). It can be seen that more luminous bulges or massive

galaxies have their stellar component more metal enriched – a trend consistent with the mass-metallicity relation (Tremonti et al., 2004) – and display lower gas-phase metallicity. The opposite occurs for less luminous bulges or less massive galaxies. From the previous Fig. (6.5) it was already concluded that more massive galaxies tend to present metal enriched stars in the bulge and the opposite for less massive galaxies. This observational evidence suggests that more massive galaxies can efficiently incorporate metals in their stellar component, presenting metal poor gas, while less massive galaxies present mostly all of its metal content not incorporated in stars but in their ionized gas. This puzzling behavior may be due to a combination of several factors, one of them being that most of the gas in massive bulges may be virialized to X-Ray temperatures (P/L) remaining almost invisible in optical wavelengths. By inspecting the mean values for Class 2 bulges listed in Table 6.3, one can verify that these massive bulges are older comparing with the other classes and present almost no star formation over the past 100 Myr, which is consistent with the virtual absence of cold gas in these systems. This is also consistent with a low metal production from young stars and the comparatively low gas-phase metallicity observed, despite an old dominant stellar population which, due to its deep gravitational potential, could retain metals and chemically enrich itself in the course of several Gyr of galactic evolution.

On the other hand, the low mass galaxies which are the ones that belong to Class 4, present the lowest mean stellar age and the highest present star formation. As they are actively forming stars, it is to be expected for them to contain a cold-gas supply to feed star formation which is chemically enriched, given that the time-scale for the ejection of metals from high-mass stars ending their main sequence life as SNe is on the order of $\sim$ 10 Myr (e.g., P/L). The fact that the luminosity-weighted stellar age in Class 4 bulges are comparatively low (mean age of 5Gyrs) is consistent with a lower level of metal enrichment in the stellar component than in the massive and old Class 2 bulges.

Fig. 6.8 shows a clear relation between the difference (ΔZ) between the gas-phase metallicity and the stellar metallicity in the bulge and the stellar metallicity in the bulge (luminosity-weighted and mass-weighted values in the left-side right-side panel, respectively – $R^2 \sim 0.76$; 0.70), attesting the trend found in Fig. 6.8: the higher the metallicity of the stellar component, the lowest the metallicity of the gas component. Interestingly, this trend is reminiscent of the results of

Petropoulou et al. (2011) who found, by studying a statistically complete sample of star-forming galaxies in the Hercules galaxy cluster, a trend for increasing ΔZ with decreasing luminosity-weighted (given the $L - Z$ relation for both cluster and field galaxies) gas-phase metallicity.

Finally, the sample was divided into four classes defined by the nature of the luminosity weighted stellar metallicity and age gradients: The $first\ class$ corresponds to bulges showing both positive stellar metallicity and age gradients (i.e. where both stellar metallicity and stellar age increase from the center to the periphery of the bulges). The $second\ class$ comprises bulges where both gradients are negative: both stellar metallicity and stellar age decrease from the center to the periphery. The bulges that belong to the $third\ class$ present positive stellar metallicity gradients and negative stellar age gradients and in the $fourth\ class$ the stellar metallicity shows a negative gradient, opposite to the gradient derived for the stellar age. For these four classes it were computed the mean values (in the bulge, except for the total absolute magnitude) for the stellar metallicity ($< Z_{B*} >$), stellar age ($< A_{B*} >$), gas-phase metallicity gradient ($< Z_{BNm} >$), gas-phase metallicity ($Z_{BN} >$), total absolute magnitude ($< AbsMag >$), $H\alpha$ equivalent width ($< EW(H\alpha)_B >$) and mass fraction of stars younger than 100 Myr ($< M_{100\%} >$). An intercomparison of these quantities reveals a clear, unexpected sequence in these bulge classes in the order: 4, 1, 3 and 2, from younger metal-poor to old, metal-rich stellar populations – in App. D the sample is divided by these classes, here is displayed the values for these quantities for each galaxy and respective true color. The next table provides a schematic overview of the distribution of the aforementioned quantities among the respective classes, where the first row corresponds to the lowest value and the last to the highest, being the ones in the middle the intermediary values for columns $< Z_{B*} >$, $< A_{B*} >$ and $< AbsMag >$, and the opposite for columns $< Z_{BN} >$, $< EW(H\alpha)_B >$ and $< M_{100\%} >$. In this way the reader will find, for instance in the first row, the Class with lowest total absolute magnitude, lowest stellar metallicity and lowest stellar age but highest gas-phase metallicity, highest equivalent width of $H\alpha$ and highest stellar mass fraction of stars younger than 100 Myr. The last column lists the nature of the determined mean gas-phase metallicity gradient (in the bulge) for the referent Class:

$< AbsMag >$	$< Z_{B*} >$	$< A_{B*} >$	$< Z_{BN} >$	$< EW(H\alpha)_B >$	$< M_{100\%} >$	Z_{BNm}
4	4	4	4	4	4	-
1	1	1	1	1	1	-
3	3	3	3	3	3	+
2	2	2	2	2	2	+

Comparing classes 4 and 2: the Class 4 corresponds to the lowest $< AbsMag >$, $< Z_{B*} >$ and $< A_{B*} >$ and highest $< Z_{BN} >$, $< EW(H\alpha)_B >$ and $< M_{100\%} >$, and presents a mean negative value for the gas-phase metallicity gradient. As for Class 2, it corresponds to the highest $< AbsMag >$, $< Z_{B*} >$ and $< A_{B*} >$ and lowest $< Z_{BN} >$, $< EW(H\alpha)_B >$ and $< M_{100\%} >$, and presents a mean positive value for the gas-phase metallicity gradient. This so clear tendency suggests that, classes 4 and 2 may correspond to different stages in galactic evolution.

◦ Class 4:

From the analyzed sample of 66 galaxies, 7 belong to this Class, which it is not considered a representative sample. Statistically, by visual inspection, the more notable characteristics of the galaxies of this Class are its diffuse/flocculent morphology ($\sim$ III in EHSVB) and intense ongoing star formation, with $\sim 40\%$ being strongly barred systems. These are the faintest objects (mean = -20.602 mag, $\frac{\sigma}{\sqrt{n}} \equiv < \sigma >$ = 0.471), presenting the lowest stellar metallicity (mean = 0.464 $Z_{\odot}$, $< \sigma >$ = 0.066) and the youngest stars (mean = 5.000 Gyrs, $< \sigma >$ = 1.039), with the highest $EW(H\alpha)$ (mean = 28.763 Å, $< \sigma >$ = 3.595) and mass fraction of young stars younger than 100 Myr (mean = 0.820 $\%$, $< \sigma >$ = 0.370). This Class also presents the highest gas-phase metallicity (mean = 1.108 $Z_{\odot}$, $\sigma >$ = 0.051) with a negative gradient, suggesting that the gas is more metal enriched in the central part of the bulge than in the periphery. Summarizing, these faint, low mass galaxies are the ones that hold the youngest, less stellar metal enriched bulges of the sample presenting ongoing star formation. The presence of a positive age gradient and negative stellar metallicity gradient indicates that the bulge central stars are the youngest, with slightly – because the positive metallicity gradient is in most cases very weak – higher metallicity – compared with the stars of the periphery of the bulge – which is also where the gas have highest metallicity. It was also found a negative mean $M_{100\%}$ gradient (mean = -0.194, $< \sigma >$ = 0.419) indicating that

there is a significant – due to the high $< M_{100\%} >$ – ongoing star formation in the central part of the bulge.

◦ Class 1:

For this Class it were found only 6 galaxies out of 66, which, as Class 4, it is not considered representative. The most significant characteristics of this Class that were identified by visual inspection are its diffuse/flocculent morphology ($\sim$ III in the EHSVB scale), star forming and the presence of strong, prominent bars in $\sim 70\%$ of the objects of this Class. These galaxies are the second faintest (mean = -20.680 mag, $< \sigma >$ = 0.498) with the second lowest stellar metallicity (mean = 0.448 $Z_{\odot}$, $< \sigma >$ = 0.066) and stellar ages (mean = 6.908 Gyrs, $< \sigma >$ = 1.096), showing the second highest $EW(H\alpha)$ (mean = 26.923 Å, $< \sigma >$ = 5.798) , $M_{100\%}$ (mean = 0.303 $\%$, $< \sigma >$ = 0.052) and gas-phase metallicity (mean = 0.978 $Z_{\odot}$, $< \sigma >$ = 0.052) with a negative gradient. Comparing these values with the ones obtained for Class 4 one may suggest that these two classes are very similar – both presenting their youngest, metal-poor stars in the central part of the bulge together with highly enriched gas – except for the nature of the stellar metallicity gradient, which in this case is positive whereas in the other is negative, but it's also much stronger then in the previous. The mean gradient of the $M_{100\%}$ is also negative and strong (mean = -0.525, $< \sigma >$ = 0.350) revealing that the star formation is much more significant in the central part of the bulge than in the periphery, since it rapidly decreases outwards the center.

◦ Class 3:

There are 12 objects in this Class, from the 66 of the sample. The morphological attributes that are shared between this galaxies are the low prominence of the spiral arms ($\sim$ II in the EHSVB scale) and the presence of faint bars in $\sim 60\%$ of the cases. These objects are the ones that present the second highest mean luminosity (mean = -20.987 mag, $< \sigma >$ = 0.189), mean stellar metallicity (mean = 0.548 $Z_{\odot}$, $< \sigma >$ = 0.042) and mean age (mean = 7.762 Gyrs, $< \sigma >$ = 0.601) and the second lowest values for $EW(H\alpha)$ (mean = 14.101 Å, $< \sigma >$ = 5.655), $M_{100\%}$ (mean = 0.184 $\%$, $< \sigma >$ = 0.046) and gas-phase metallicity (mean = 0.972 $Z_{\odot}$, $< \sigma >$ = 0.079) with a positive mean gradient but with high standard deviation error, being twice as the value of the mean

gradient itself. The mean gradient of the $M_{100\%}$ is also negative but shows a large spread (mean = -0.134, $< \sigma >$ = 0.131), being positive for half of the sample and negative for the other half. By comparing the mean values of total absolute magnitude, stellar metallicity, age, $EW(H\alpha)$ and $M_{100\%}$ with the ones from Class 2, one will find striking similarities: these are relatively high mass galaxies that present their most old, relatively metal poor stars in the central part of their bulges, where it is also found, on average, the lowest values for the gas-phase metallicity. The exception is the strong (mean = 0.433, $< \sigma >$ = 0.105) positive mean gradient for stellar metallicity, since the Class 2 objects present a high (mean = -0.358, $< \sigma >$ = 0.034) negative mean gradient for this quantity. Half of the galaxies of this Class present positive $M_{100\%}$ gradients, indicating that there is ongoing – but not significant due to the low $M_{100\%}$ and $EW(H\alpha)$ mean values – star formation in the central part of the bulge, while the other half presents the contrary. For $\sim 75\%$ of the galaxies of this Class, the nature of the $M_{100\%}$ gradient is the same as the nature of the gas-phase metallicity gradient – from the center to the periphery of the bulge, whenever the $M_{100\%}$ increases, so does the gas metallicity and vice-versa – which might indicate that the gas-phase metallicity is well correlated with the star formation activity. To note that this is verified for approximately $\sim 75\%$ of the total sample, and approximately $\sim 70\%$ of each individual sample (Class 1: $\sim 66\%$; Class 2: $\sim 70\%$; Class 3: $\sim 75\%$; Class 4: $\sim 71\%$). This question requires further exploration, for instance, to relate the gas-phase metallicity with $EW(H\alpha)$ and $H\alpha$ flux surface brightness gradients.

◦ Class 2:

In the analyzed sample, the Class 2 is the dominant one since it contains 41 of the 66 galaxies. The morphological analyses indicate that these are grand design galaxies (from I to II in the EHSVB scale) and that $\sim 60\%$ of the galaxies of this Class are barred systems, $14/41$ showing prominent bars. These are the most luminous objects (mean = -21.449 mag, $< \sigma >$ = 0.109), with highest stellar metallicity (mean = 0.712 $Z_{\odot}$, $< \sigma >$ = 0.030), holding the oldest stars (mean = 9.121 Gyrs, $< \sigma >$ = 0.373) and showing the lowest values for $EW(H\alpha)$ (mean = 7.958 Å, $< \sigma >$ = 1.373), the lowest mass fraction of young stars (mean = 0.130 $\%$, $< \sigma >$ = 0.020) and the lowest gas-phase metallicity (mean = 0.866 $Z_{\odot}$, $< \sigma >$ = 0.041). By analyzing these values one can conclude that these massive galaxies hold older, stellar enriched bulges, presenting

almost no recent star formation. The stars within the bulge are metal enriched whereas the gas-phase presents low values of metallicity – that could be due to the effective absence of heavy metals or due to the virialization of the gas to high temperatures, as it was aforementioned – and a mean positive gradient. The negative age and stellar metallicity gradients suggests that the oldest, metal-enriched stars are found in the central part of the bulge. Additionally, it was derived a positive mean $M_{100\%}$ gradient (mean = 0.150, $< \sigma >$ = 0.064) allowing to affirm that this Class presents very weak ongoing star formation in the periphery of the bulge but virtually none in the center.

In App. D, the reader will find the galaxy sample divided by classes in the same order as described here. It presents the true color images and tables that list the individual values for the quantities discussed above. Bellow the red lines are the deviant cases, that were selected by intercomparing the values for mean luminosity-weighted stellar metallicity and age within the bulge. This so clear sequence may indicate that metallicity and age gradients within the bulge may provide sensitive indicators of the evolutionary stage and star formation history of a normal late-type galaxy.

Chapter 8.

Outlook

The novel methodological approach taken in this study combines, for the first time, a detailed structural analysis of PB galaxies via surface photometry with spaxel-by-spaxel spectral modeling of IFS data. This allows to determine several physical quantities of the stellar and ionized gas component within radial zones that are adapted to the galaxy morphology, permitting a comparative study of the bulge and disk component, and the determination of various trends as a function of galactocentric radius. Whereas the discussion in Chapter 3 highlights the potential of our methodology, it also reveals different aspects where improvements are both necessary and possible. These refinements will be pursued in the framework of a PhD thesis and address the following issues:

Optimal Structural Characterization of the Disk Component

As already discussed in Chapter 3, some of our sample galaxies do not present a pure exponential profile throughout their disk (see, e.g., profile decomposition of NGC2253, Fig. B.15) but display instead deviations from an exponential distribution either at small and/or at large (typically $R \geq 1.5R_p$) galactocentric radii. SBPs of the first class (Type I) present a central flattening – typically for $R \leq R_{eff}$), with an observed surface brightness being by up to ~ 2 mag lower than the value predicted by inwards extrapolation of the outer exponential slope. Fitting such a disk profile with a pure exponential model will over-predict the disk luminosity beneath the bulge, con-

sequently lead to a systematic underestimation of the luminosity and the structural parameters (e.g., isophotal radius, Sérsic index) of the latter. This type of exponential profiles with a central flat core – also observed in dwarf galaxies – can be approximated by the fitting function proposed by P96a (Eq. 3.8).

The second class of profiles (Type II) is characterized by a double-slope exponential, with a relatively shallow slope at intermediate radii, followed by a steeper exponential decrease for typically $R \leq 1.5R_p$. Whereas an accurate modeling of the inner exponential slope only is sufficient for a proper separation of the bulge emission from the disk, a reasonable understanding of the photometric structure of these systems requires modeling of both exponential regimes of the disk using, e.g., the functional form proposed in Chapter 3, equation 3.7.

One of the future improvements will therefore center on the implementation of both above mentioned fitting functions in our surface photometry code. It is further planned to develop an iterative scheme for fitting multiple structural components (disk, bulge, bar, a central point source) to SBPs taking simultaneously into account PSF convolution effects.

The optimal fitting of such disk profiles is not a purely technical task but also a necessary step towards the exploration of the physical origin of the observed deviations from the exponentiality. This issue will be investigated in depth, under consideration of the output from spatially resolved spectral synthesis of IFS data, by exploring, e.g., possible distinctive characteristics with regard to the SFH and the IMF in the inner and outer of Type I and Type II profiles, respectively.

Sérsic Index Estimation

The new physically motivated method developed in this work to estimate the Sérsic index of the bulge still needs some improvements. The major problem regards the fact that, after the subtraction of the disk – plus bar for barred galaxies – in some cases one may not obtain the pure bulge emission but the bulge plus some additional emission that usually belongs to point-like sources within the disk (e.g., aging stellar clusters that can not be eliminated by RY when setting a conservative age cutoff of 30 Myr) which obviously can not be accounted by a pure exponential profile. Owing to this fact, the surface photometry code was written in a way that the user is prompted to first visually inspect a temporary profile with the emission in excess of the disk and

subsequently to interactively select the radial limit for the bulge component. Since this truncation radius for the bulge differs in some cases from the $2R_p$ encoded in equation 3.13 (as an example, photometric decomposition of IC1256, Fig. 5.1), the decomposition result is mildly dependent on the subjective definition of the size of the bulge.

The procedure that will be adopted to overcome this caveat will be integrated in the iterative profile decomposition scheme mentioned in Sect. 8.0.11: After the subtraction of the disk – or disk plus bar – the code will analyze the residual emission. As the bulge is expected to show a radially monotonously decreasing intensity, the code will integrate the emission in excess to the disk + bar only out to the radius where the intensity eventually starts ascending. It will then compute a Sérsic profile based on the estimated physical quantities for the R_{mod} and μ_{mod}. At this point, the code will integrate the obtained modeled profile and estimate new values for R_{mod} and μ_{mod} and consequently for the η, leading to an improved Sérsic fit for the bulge. This process will be repeated until the relative change in the R_{mod} and μ_{mod} between two consecutive iterations has decreased below a threshold of approximately 5%. This way it can be ensured that the parameters of the best-fitting Sérsic model for the bulge are unbiased and reproducible. It should be noted that resolution effects will be taken into account through convolution of each trial Sérsic model with a Gaussian function approximating the PSF.

Implementation of $RemoveYoung$ into the SBP Decomposition Scheme

Since this approach was never taken before, it is necessary to investigate what would be the best way for applying the radius-dependent scale-down factor dmr30 on SBPs. One problem emerge from the limited field of view (FoV) of CALIFA PMAS/PPAK which maps for most of our sample galaxies represents only approximately 1/2 of their isophotal extent at the Holmberg radius. For this reason, the dmr30 correction (in mag) can be applied to SBPs only out to an intermediate radius of approximately 30 arcsec, i.e. the maximum photometric radius (R_{FOV}) corresponding to the PMAS/PPAK FoV. Even though R_{FOV} is in all cases it at least twice the galaxy's R_{eff} and encircles the disk emission outside the bulge over a radius interval of typically one exponential scale length, it misses in many cases the disk periphery.

Hereupon it was decided to adopt in this study a simple approach: to compute the *mean* dmr30 within the bulge and the disk, and subtract these values from the original SDSS r band SBP, prior to profile decomposition. This is to be regarded merely as proof of concept and it is meant to gauge the principle impact of the application of RY on the photometric properties of the bulge and the disk.

The next step to be undertaken is to apply to all SBPs an accurate correction for dmr30 out to $R \leq R_{FOV}$. This will be done through spline interpolation of the SDSS r band SBPs and dmr30 to equal radius steps and subsequent subtraction of the latter from the former. This is a straightforward task that will be pursued next. To note that the spline interpolated values for dmr30 have already been computed (see lower panels of Figs. of App. B). For radii greater than R_{FOV}, where no spectroscopic information is available, it will be assumed a constant scale-down offset computed from the average of dmr30 within the outermost zone studied spectroscopically through IFS. It is also intended to experiment with time cutoff for RY, allowing it to vary between 30 Myr and 1 Gyr, in order to evaluate the change in the SBPs and the recovered structural properties of the bulge as a function of lookback time.

Repetition of the structural analysis of bulges after application of $RemoveYoung$

In this study various quantities obtained from spectral modeling of the bulge and the disk were compared with photometric properties inferred from SBP decomposition prior to application of RY. However, as discussed in Chapter 4, bulge-disk decomposition in the standard manner can act towards reducing the luminosity of the bulge whenever the disk sustains active star formation, introducing a systematic bias in the recovered photometric properties of bulges.

This is apparent from the following image that displays the difference between the estimated quantities for the isophotal radius of the bulge and the R_{eff} of the total SBP, before and after application of RY:

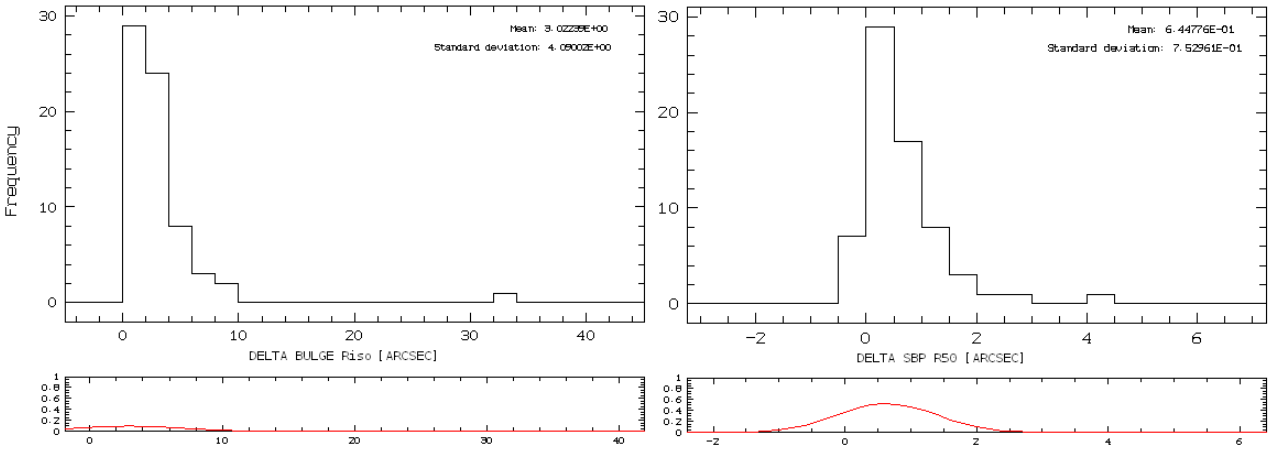

Figure 8.1: Histogram presentation of the diference between the estimated values for the bulge R_{iso} (left) and for R_{eff} of the SBP (right) before and after removing the light contribution of stars younger than 30 Myr.

Figure 8.1 reveals that the effective radius of the galaxy will suffer a minor reduction whereas, on the contrary, the isophotal radius of the bulge for the analyzed galaxies will slightly increase by ~ 4 arcsec. This indicates that by fitting the real continuum of the disk, not taking into account the contribution of star forming regions, in general, one will obtain more extended bulges. In the future, we intend to recompute all the spectroscopic parameters taking into account the new values for the extent of the bulge and SBP effective radius for the whole sample and perform a statistical study in order to understand how these parameters will change.

Removal of the disk contribution from the integral spectrum of the bulge inside $R_{\rm bulge}$

In the photometric study presented here (Chapter 5) the luminosity contribution of the disk – plus bar for barred galaxies – inside the radius of the bulge (fr_{BA+D}) could be subtracted through SBP decomposition, permitting to isolate and study the pure bulge emission. However, an inconsistency in our analysis consists in the fact that the spectroscopic data within R_{iso} that was used for the study of various relations as a function of galactocentric radius (e.g., mean stellar metallicity and metallicity gradient) are still contaminated by the underlying disk emission. As our SBP decomposition indicates, the latter may contribute between $\sim 20\%$ and $\sim 60\%$ of the line-of-sight emission within R_{iso}, depending on the central disk surface brightness and the intrinsic luminosity of the bulge. Quite importantly, since bulges differ from the underlying disk in their age and stellar metallicity (see Chapter 6), the luminosity contamination by the underlying disk can strongly impact the spectrum of intrinsically faint bulges, introducing a bias, or scatter, in several

of the relations (e.g., Z_* vs M_{Riso}) discussed in Chapter 6. For example, the superposition of a relatively young disk on an old bulge will result in a systematic underestimation of the age of the latter via spectral fitting.

To solve this issue, our team has developed and successfully tested a technique for the spectroscopic subtraction of the disk from the integrated spectrum within R_{iso}. This technique, after a few minor refinements, will be applied to our galaxy sample and permit the extraction of the pure spectrum of the bulge which will then be re-modeled with spectral synthesis codes in order to obtain an improved determination of the stellar age and metallicity, and their radial gradients.

It should be noted that the decontamination of the bulge spectrum from the emission of the underlying disk has not been previously attempted in the literature. In fact, our knowledge on the metallicity of bulges relies on Lick indices, uncorrected for the disk' contribution and measured through single-fiber SDSS or longslit spectroscopy within only a tiny portion of the area of bulges (e.g., Bedregal et al., 2011). In this respect, wide-field IFS spectroscopy from CALIFA in conjunction with the methodology developed by our team offers an important opportunity to advance our understanding on bulge formation and evolution.

Comparative analysis of the star formation and chemical enrichment history of pseudobulges of different classes

In Chapter 6 it was identified four sub-classes of PB based on a combination of indicators, such as metallicity and age gradients, and proposed a working hypothesis according to which the observed differences primarily reflecting distinct star formation and chemical enrichment histories. A natural step at this stage is therefore to analyze and compare the SFHs in the four classes of bulges, once their integral spectra have been decontaminated for the contribution of the underlying disk. Besides state-of-the-art spectral fitting codes, such as STARLIGHT and STECKMAP, we will use the conceptually novel spectral population synthesis code FADO (Gomes & Papaderos 2014, in prep.) under development at IA-CAUP.

Connected to this project will be a detailed study of non-thermal activity, with the goal of gaining insight into the role of an AGN on the growth (aka SFH) of CB and PB. This task will be supported

both by spaxel-by-spaxel modeling of CALIFA IFS data with FADO and the evolutionary synthesis code REBETIKO (Gomes et al. 2014, in prep., Papaderos & Gomes 2015, Cardoso et al. 2015) in which provision has been made for the inclusion of an AGN power law component. These spectral synthesis modeling studies will be supplemented through a spatially resolved analysis of emission-line diagnostics (e.g., BPT ratios) within the bulge, aiming to clarify the relative role of star formation and AGN on the excitation of the warm interstellar medium.

Bibliography

Aguerri, J. A. L., Balcells, M., & Peletier, R. F. 2001, AA, 367, 428

Aguerri, J. A. L., Méndez-Abreu. J., & Corsini, E. M. 2009, A&A, 495, 491

Athanassoula, E., & Misiriotis, A. 2002, MNRAS, 330, 35

Athanassoula, E. 1992, MNRAS, 259, 345

Athanassoula, E. 2003, RevMexAA (Serie de Conferencias), 17, 28–29

Athanassoula, E. 2008, MNRAS, 390, L69

Barazza, F. D., Jogee, S., & Marinova, I. 2008, ApJ, 675, 1194

Barbosa, F. K. B., Storchi-Bergmann, T., Cid Fernandes, R., Winge, C., & Schmitt, H. 2006, MNRAS, 371,170

Barrera-Ballesteros, J.K., et al. 2014, A&A, submitted

Bedregal, A., Cardiel, N., Aragón-Salamanca, A. & Merrifield, M. 2011, MNRAS, 415, 2063–2080

Bender, R. & Moellenhoff. C., 1987, A&A, 177,71

Berentzen, I., Shlosman, I., & Jogee, S. 2006, ApJ, 637, 582

Binney, J., & Merrifield, M., 1998, Galactic Astronomy, Princeton University Press, Princeton

Bournaud, F., Jog, C. Combes, F. 2007, A&A, 476, 1179–1190

Brinchmann, J., Charlot, S., White, S. D. M., et al. 2004, MNRAS, 351, 1151

Brooks A. M., Governato F., Booth C. M., Willman B., Gardner J. P., Wadsley G., Stinson G., Quinn T., 2007, ApJ, 655, L17

Bruzual, G. & Charlot, S. 2003, Monthly Notices of the Royal Astronomical Society, 344, 1000–1028

Charlot, S, & Longhetti, M. 2001, MNRAS, 323, 887

Cid Fernandes, R., Mateus, A., Sodré, L., Stasińska, G., Gomes, J.M. 2005, MNRAS, 358, 363

Cid Fernandes, R., Asari, N. V., Sodré, L., Stasińska, G., Mateus, A., Torres-Papaqui, J. P., & Schoenell, W. 2007, MNRAS, 375, L16

Cid Fernandes, R., González Delgado, R.M., Garcáa Benito, R. et al. 2014, A&A, 561A, 130C

Ciotti, L. 1991, A&A, 249, 99

Combes, F., & Sanders, R.H. 1981. A&A 96:164

D{iaz, A. I., & Pérez-Montero, E. 2000, MNRAS, 312, 130

Díaz, A. I., Terlevich, E., Castellanos, M., Hägele, G. F. 2007,MNRAS, 382, 251

De Lucia, G., Fontanot, F., Wilman, D., & Monaco, P. 2011, MNRAS, 414, 1439

de Vaucouleurs, G. 1959, in Hdb. d. Phys. 53 (Berlin: Springer-Verlag), p. 275

Debattista, V. P., & Sellwood, J. A. 1998, ApJ, 493, L5

Dekel A., & Silk, J. 1986, 1986, ApJ, 303, 39

Dors, O. L., Storchi-Bergmann, T., Riffel, R. A., Schimdt, A. A. 2008, A&A, 482, 59

Drory, N. & Fisher, D. 2007, ApJ, 664, 640

Durbala, A., Sulentic, J., Buta, R. & Verdes-Montenegro, L. 2008, MNRAS, 390, 881–905

Edvardsson, B., Andersen, J., Gustafsson, B., et al. 1993, A&A, 275, 101

Eggen OJ, Lynden-Bell D, Sandage AR. 1962. Ap. J. 136:748

Ellis, S. C., Driver, S. P., Allen, P. D., et al. 2005, MNRAS, 363, 1257

Ellison S. L., Patton D. R., Simard L., McConnachie A. W., 2008a, ApJ, 672, L107

Elmegreen, B. G. 1994, ApJ, 425, L73

Erwin, P., Pohlen, M, & Beckman, J.E. 2008, AJ, 135, 20

Eskridge, P. B., Frogel, J. A., Pogge, R. W., et al. 2000, AJ, 119, 536

Faber SM, Jackson RE. 1976. ApJ 204:668

Falcón-Barroso, J. et al. 2014, in prep.

Feltzing, S., Holmberg, J., & Hurley, J. R. 2001, A&A, 377, 911

Fisher, D. & Drory, N. 2008, The Astronomical Journal, 136, 773

Freeman, K. C. 1970, ApJ, 160, 811

Gültekin, K., Cackett, E. Miller, J. et al. 2009, ApJ, 706, 404

Gadotti, D. 2008, arXiv preprint arXiv:0810.1953,

Gallazzi A., Charlot S., Brinchmann J., White S. D. M., Tremonti C. A., 2005, MNRAS, 362, 41

García-Lorenzo, B., Márquez, I., Barrera-Ballesteros, J.K., Masegosa, J.,Husemann, B. et al. 2013, A&A, submitted

Garcia-Rissmann, A., Vega, L. R., Asari, N. V., Cid Fernandes, R., Schmitt, H., González Delgado, R. M., & Storchi-Bergmann, T. 2005, MNRAS 359, 765

Garnett, D. R., & Shields, G. A. 1987, ApJ, 317, 82

Garnett D. R., 2002, ApJ, 581, 1019

Gerssen, J., Wilman, D. J., & Christensen, L. 2012, MNRAS, 420, 197

Giovanelli, R., Haynes, M. P., Salzer, J. J., et al. 1995, AJ, 110, 1059

Giovanelli, R., Haynes, M. P., Herter, T., et al. 1997, AJ, 113, 22

Gomes, J. M., Papaderos, P. et al. 2014 A&A, received

González-Delgado, R.M., Pérez, E., Cid Fernandes, R. et al. 2014, A&A, 562, A47

Graham, A., Driver, S., Petrosian, V., Conselice, C., Bershady, M., Crawford, S. and Goto, T. (2005), AJ, 130(4), pp.1535-1544

Guo, Q., White, S., Boylan-Kolchin, M., et al. 2011, MNRAS, 413, 101

Heller, C. H., & Shlosman, I. 1994, ApJ, 424, 84

Hirashita, H., Inoue, A.K., Kamaya, H. & Shibai, H. 2001, A&A, 366, 83

Hopkins, A. M., Driver, S. P., Brough, S., et al. 2013, MNRAS, 700

Hughes, T., PhD diss., 'A Phenomenological Study of Star Formation and Chemical Evolution in Nearby Galaxies'

Husemann, B., Jahnke, K., Sánchez, S. F. et al. 2013, A&A, 549, A87H

Iglésias-Páramo, J., Vílchez, J. & Galbany, L. et al. 2013, A&A 553,L7

Jønch-Sørensen H. 1995. A&A 298:799-817

Jogee, S., Scoville, N., Kenney, J. D. P. 2005, ApJ, 630, 837

Kehrig, C., Monreal-Ibero, A. & Papaderos, P. et al. 2012, A, 540, 11

Kelz, A., Verheijen, M. A. W., Roth, M. M., et al. 2006, PASP, 118, 129

Kennicutt, R.C., Jr. 1989, ApJ, 344, 685

Kennicutt, R. C. 1998, ARA&A, 36, 189

Kewley, L. J., Jansen, R. A., & Geller, M. J. 2005, PASP, 117, 227

Kewley, L. J., Rupke, D., Zahid, H. J., Geller, M. J., & Barton, E. J. 2010, ApJ,721, L48

Kobulnicky, H. A., Kennicutt, R. C., Pizagno, J. L. 1999, ApJ, 514, 544

Kormendy, J. & Ho L. C., 2012, PIAU, 8, 241–256

Kormendy, J. & Kennicutt Jr, R. 2004, ARAA, 42, 603

Kormendy, J., Bender, R. Cornell, M. 2011, Nature, 469, 374–376

Kormendy, J., 1993, in Galactic Bulges, IAU Symposium 153, ed. H. Dejonghe & H. J. Habing (Dordrecht: Kluwer), 209

Kronberger, T., Kapferer, W., Unterguggenberger, S., Schindler, S., Ziegler, B. L. 2008, A&A, 483, 783

Lang, P., Wuyts, S., Somerville, R., et al. 2014, ArXiv e-prints

Lamareille, F., Mouhcine, M., Contini, T., Lewis, I., & Maddox, S. 2004, MNRAS, 350, 396

Lara-López, M. A., Cepa, J., Bongiovanni, A., et al. 2010, A&A, 521, L53

Larson, R. 1974, MNRAS, 166, 585–616

Le Fèvre, O., Saisse, M., Mancini, D., et al. 2003, Proc. SPIE, 4841, 1670

Lee, H., Grebel, E. K., & Hodge, P. W. 2003, A&A, 401, 141

Leitherer, C., Schaerer, D., Goldader, J.D., González-Delgado, R.M., Robert, C., Kune, D.F., de Mello, D.F., Devost, D. Heckman, T.M. 1999, ApJS, 123, 3 (STARBURST 99)

Lequeux J., Peimbert M., Rayo J. F., Serrano A., Torres-Peimbert S., 1979, A&A, 80, 155L

Lynden-Bell, D. 1992, in Elements and the Cosmos. Proceedings of the 31st. Herstmonceux Conference, held in Cambridge, England July 16-20 1990, Edmunds M. G. & Terlevich R. (eds.), Cambridge University Press. P. 270

Mannucci F., Cresci G., Maiolino R., Marconi A., Gnerucci A., 2010, M.N.R.A.S., 408, 2115

Marino, R., Rosales-Ortega, F. & Sánchez, S. et al. 2013, A&A, 559, A114

Marinova, I., Jogee, S. 2007, ApJ, 659, 1176

Mast, D., Rosales-Ortega, F.F., Sánchez, S.F., Vílchez, J.M., Iglésias-Páramo, J. et al. 2014, A&A, 561, A129

Mast, D., Rosales-Ortega, F. & Sánchez, S. et al. 2013, arXiv preprint arXiv:1311.3941

Melbourne, J., & Salzer, J. J. 2002, AJ, 123, 2302

Melvin, T., Masters, K. Lintott, C. et al. 2014, MNRAS, 2397

Menéndez, K., Sheth, K., Schinnerer, E., et al. 2007, ApJ, 657, 790

Meusinger H, Reimann H-G, and Stecklum B. 1991. A&A 245:57-74

Noeske, K. G., Papaderos, P., Cairós, L. M. & Fricke, K. J. 2003, A&A, 410, 481 (N03)

Pérez, E., Cid Fernandes, R., González Delgado, R.M. et al. 2013, ApJ, 764, L1P

Pagel, B. E. J., Edmunds, M. G., Blackwell, D. E., Chun, M. S., Smith, G. 1979, MNRAS, 189, 95

Papaderos, P. & Östlin, G., 2012, A&A, 537, A126

Papaderos, P., Loose, H.-H., Thuan, T. X., & Fricke, K. J. 1996a, A&A, 120, 207

Papaderos, P., Izotov, Y.I., Fricke, K.J., Thuan, T.X., Guseva, N.G. 1998, A&A, 338, 43

Papaderos, P., Izotov, Y. I., Thuan, T. X. et al. 2002 A&A, 393, 461

Papaderos, P., Gomes, J. & Vílchez, J. et al. 2013, A&A, 555, L1

Peng, Y. & Maiolino, R. 2013, MNRAS, 2175

Petropoulou, V., Vílchez, J., Iglésias-Páramo, J., Papaderos, P., Magrini, L., Cedrés, B., Reverte, D. 2011, ApJ, 734, 32

Pettini, M., & Pagel, B. E. J. 2004, MNRAS, 348, L59

Pfenniger, D., & Norman, C. 1990, ApJ, 363, 391

Pilyugin, L. S. 2001, A&A, 369, 594

Piovan, L., Tantalo, R. & Chiosi, C. 2006, MNRAS, 366, 923

Pohlen, M., & Trujillo, I. 2006, A&A, 454, 759

Reis, S. MSc Thesis, 'Age Gradients in CALIFA Pseudo-Bulges'

Rich, J. A., Torrey, P., Kewley, L. J., Dopita, M. A., & Rupke, D. S. N. 2012,ApJ, 753, 5

Roth, M. M., Kelz, A., Fechner, T., et al. 2005, PASP, 117, 620

Sánchez, S. F., Kennicutt, R. C., Gil de Paz, A., et al. 2012a, A&A, 538, A8

Sánchez, S., Rosales-Ortega, F. & Jungwiert, B. et al. 2013, A&A 554,A58

Sánchez, S., Rosales-Ortega, F. & Iglesias-Páramo, J. et al. 2013, A&A, 553, L7

Sánchez, S.F., Rosales-Ortega, F.F., Iglésias-Páramo, J. et al. 2014b, A&A, in press

Sánchez, S., Advances in Astronomy, Issue: Metals in 3D: A Cosmic View from Integral Field Spectroscopy, 2014a, in press

Sánchez-Blázquez, P. et al. 2014, A&A, submitted

Salim, S., Rich, R. M., Charlot, S., et al. 2007, ApJS, 173, 267

Salzer, J. J., Lee, J. C., Melbourne, J., Hinz, J. L., Alonso-Herrero, A., & Jangren, A. 2005, ApJ,624, 661

Saviane, I., Bresolin, F. & Salzer, J. 2007, ASPC, 374, 99

Saviane, I., Yegorova, I. & Proust, D. et al. 2014, arXiv preprint arXiv:1401.8284

Schlafly, E. & Finkbeiner, D. 2011, ApJ, 737, 103

Schlegel, D., Finkbeiner, D. & Davis, M. 1998, ApJ, 500, 525

Schmidt, M. 1959, ApJ, 129, 243

Sérsic, J.-L. 1963, Boletin de la Asociacion Argentina de Astronomia, vol.6, p.41

Silk, J. 1993, Proceedings of the National Academy of Science, 90, 4835

Singh, R. van de Ven, G., Jahnke, K., Lyubenova, M., Falcón-Barroso, J. et al. 2013, A&A, 558, A43

Skillman, E. D., Kennicutt, R. C., Hodge, P. W. 1989, ApJ, 347, 875

Sreedhar, Y., Odell, A., Rakos, K., Hensler, G. Zeilinger, W. 2012, ApJ, 747, 68

Tinsley, B. M., & Larson, R. B. 1979, MNRAS, 186, 503

Tremonti, C. A. et al. 2004, ApJ, 613, 898

Twarog, B. 1980, ApJ, 242, 242–259

Vílchez, J. M., & Esteban, C. 1996, MNRAS, 280, 720

van Zee, L., & Haynes, M. P. 2006, ApJ, 636, 214

Vega, L. R. 2004, MSc Thesis, Universidade Federal de Santa Catarina

Verheijen, M., Bershady, M., Andersen, D., et al. 2004, Astronomische Nachrichten, 325, 151

Wada, K., & Habe, A. 1992, MNRAS, 258, 82

Walcher, C., Wisotzki, L. Bekeraité, S. et al. 2014, A&A, 569, 1

Weinberg, M. D. 1985, MNRAS, 213, 451

Woosley S. E. & Weaver, T.A. 1995, ApJS, 101, 181

Worthey 1994, ApJS, 95, 107

Yates, R. & Kauffmann, G. 2014, MNRAS, 439, 3817–3834

Yates, R., Kauffmann, G. & Guo, Q. 2012, MNRAS, 422, 215–231

Zahid, H. J., Yates, R. M., Kewley, L. J., & Kudritzki, R. P. 2013, ApJ, 763, 92

Zaritsky, D., Kennicutt, R. C., Jr., & Huchra, J. P. 1994, ApJ, 420, 87

Appendices

Appendix A.

True color, Continuum, $H\alpha$ and dmr30M Maps and Radial Profiles

IC0776

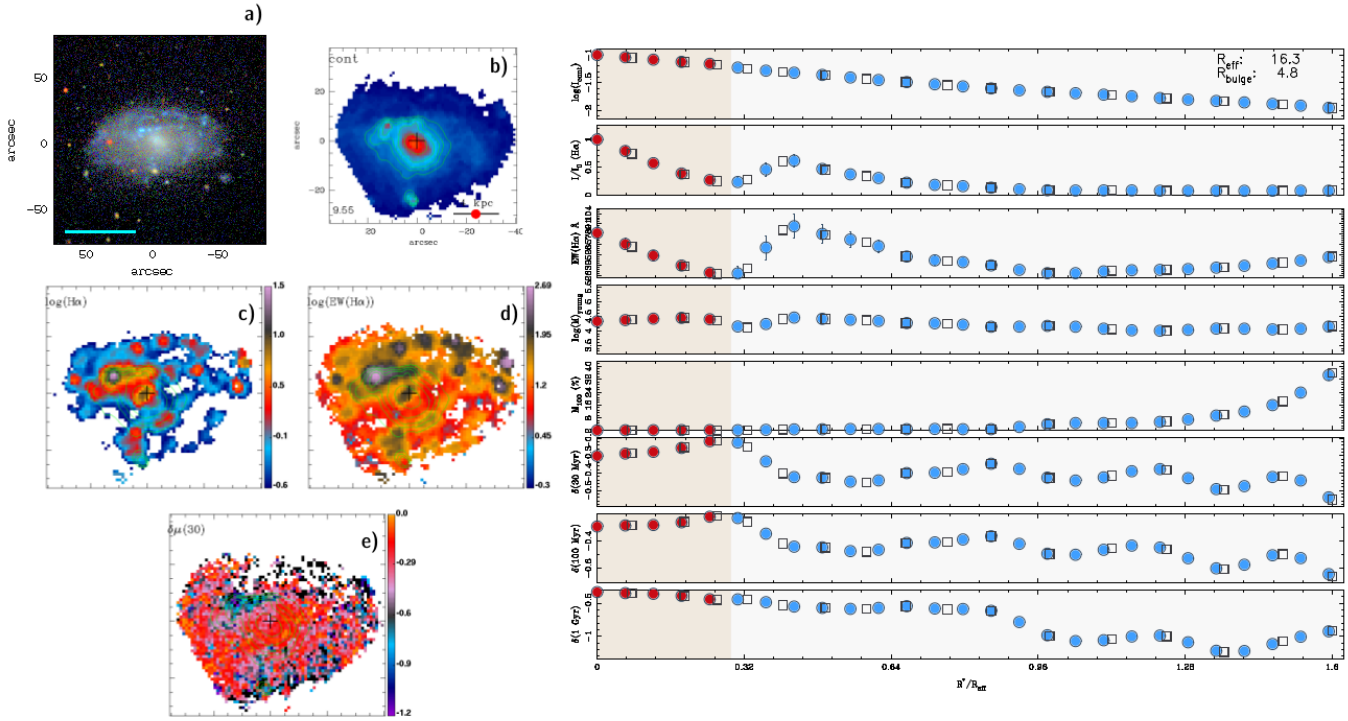

Figure A.1: Maps and radial profiles of IC0776.

IC4566

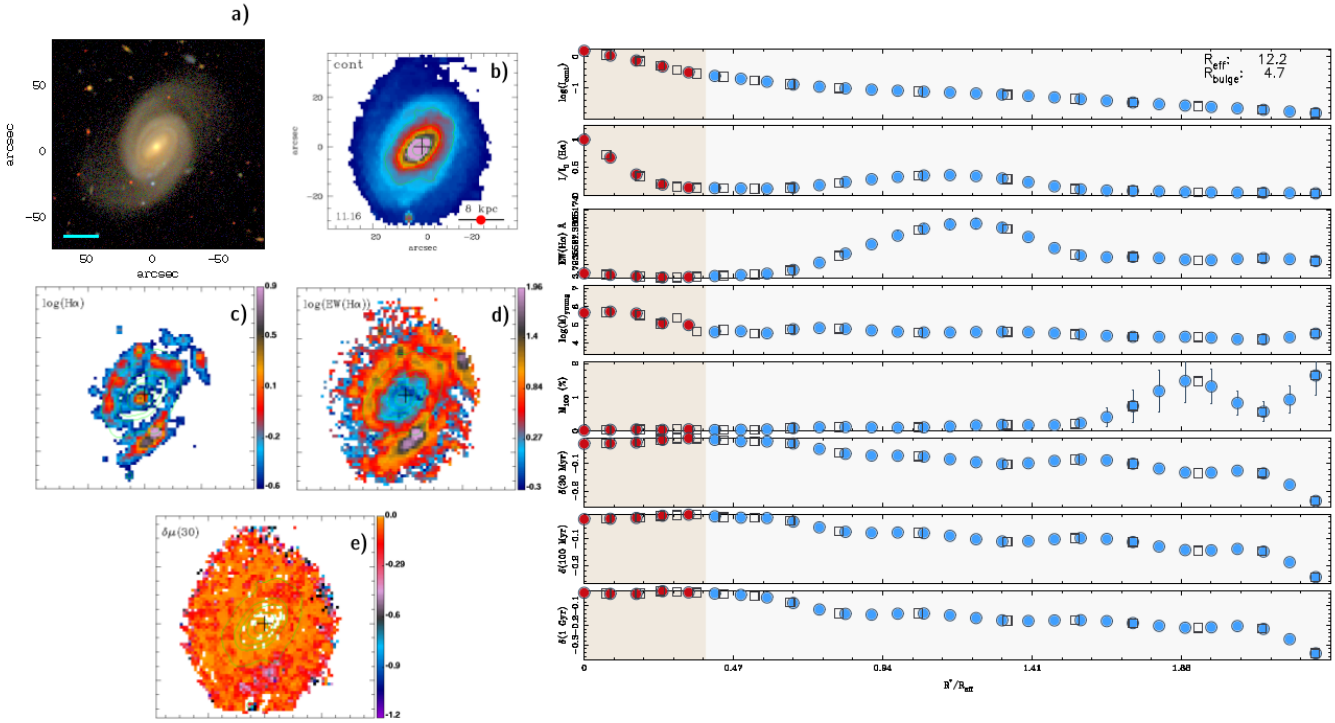

Figure A.2: Maps and radial profiles of IC4566.

NGC0001

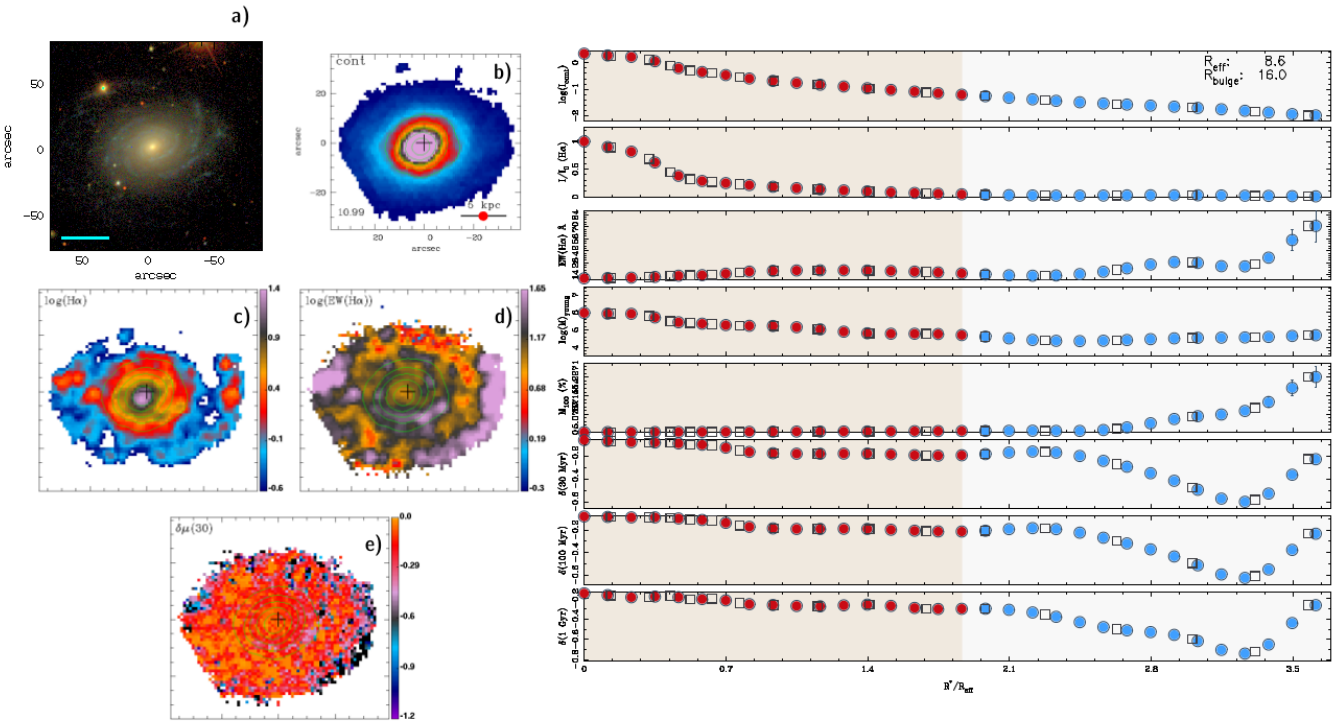

Figure A.3: Maps and radial profiles of NGC0001.

NGC0160

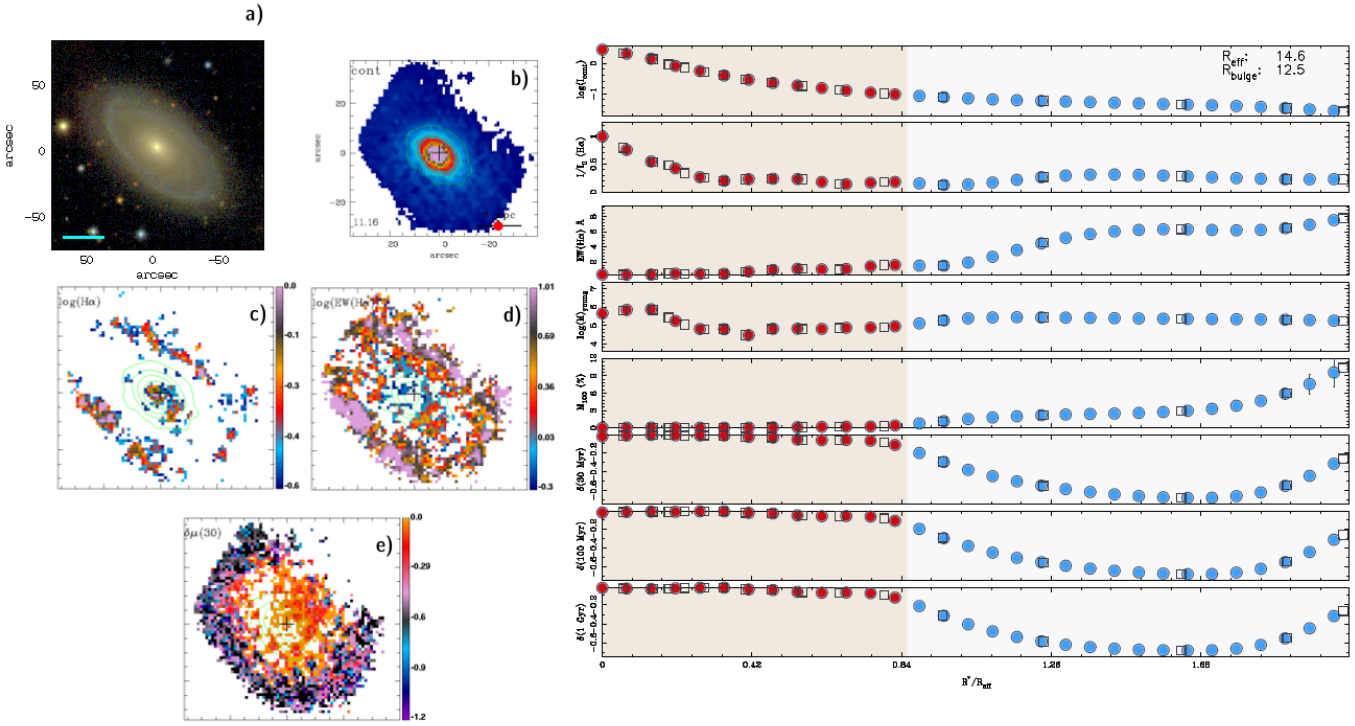

Figure A.4: Maps and radial profiles of NGC0160.

NGC0165

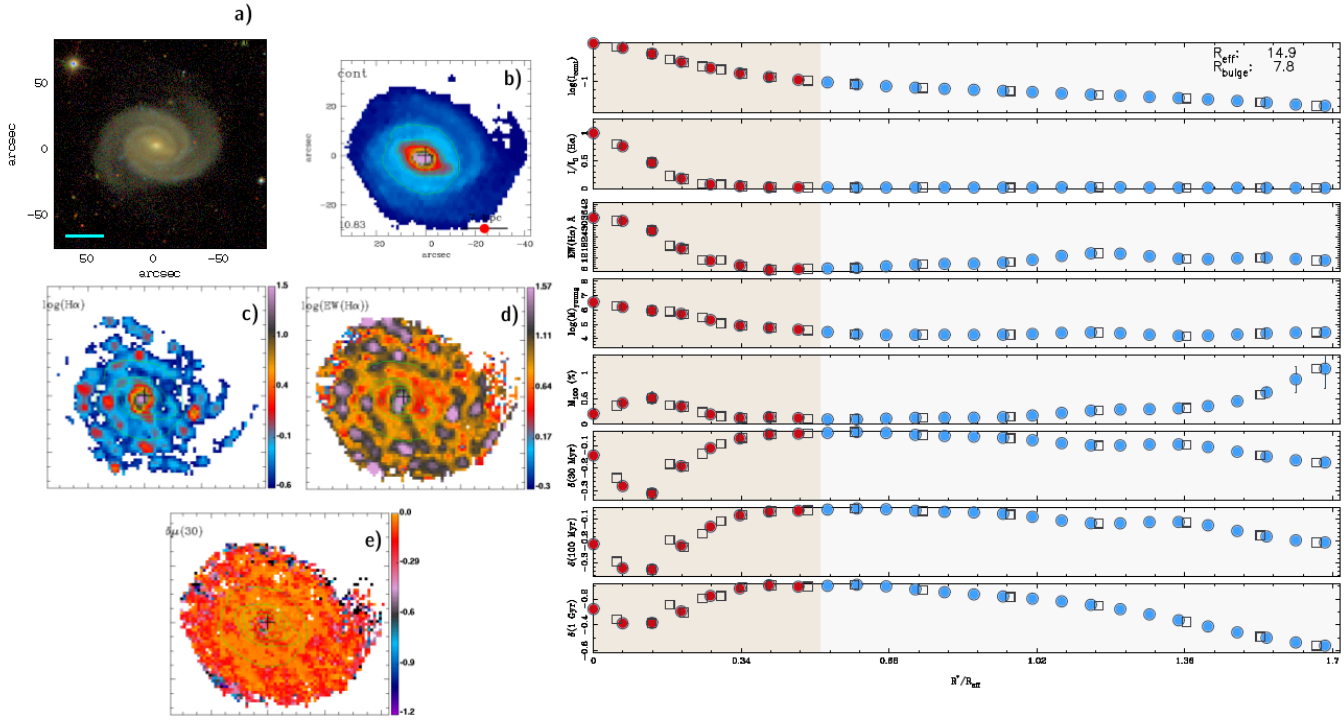

Figure A.5: Maps and radial profiles of NGC0165.

NGC0171

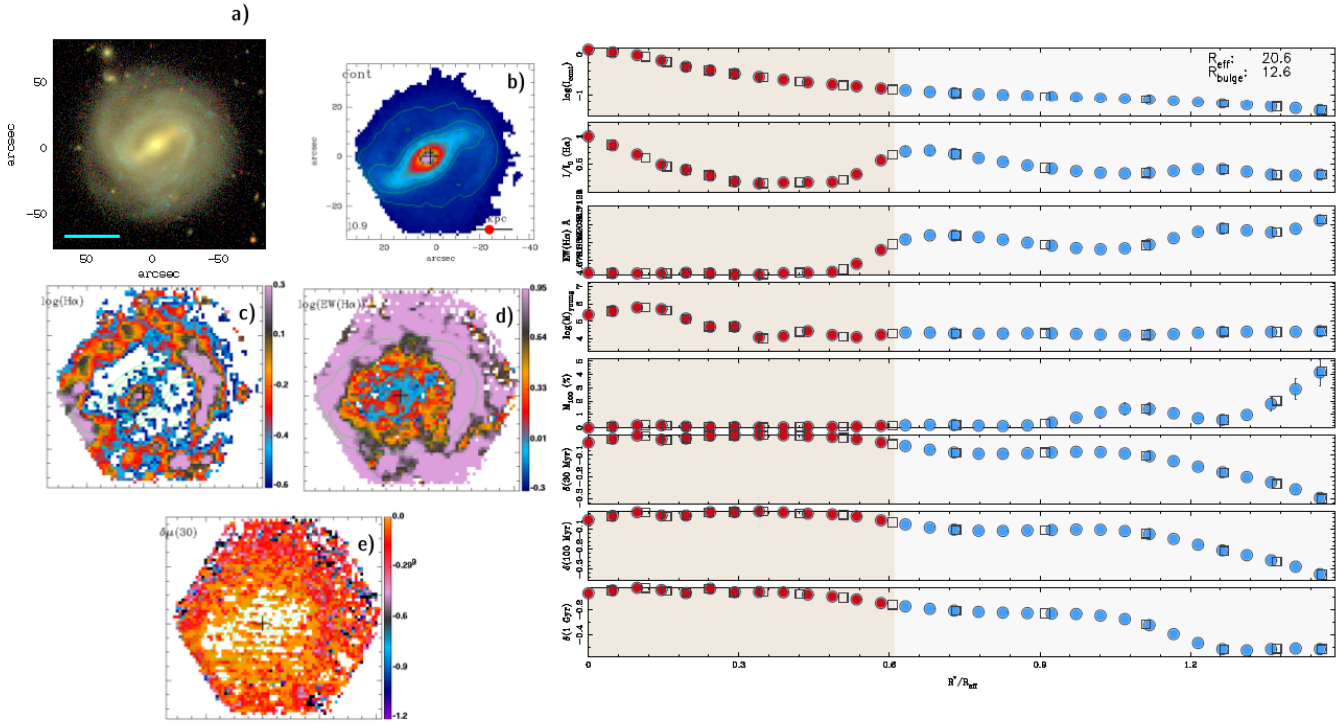

Figure A.6: Maps and radial profiles of NGC0171.

NGC0180

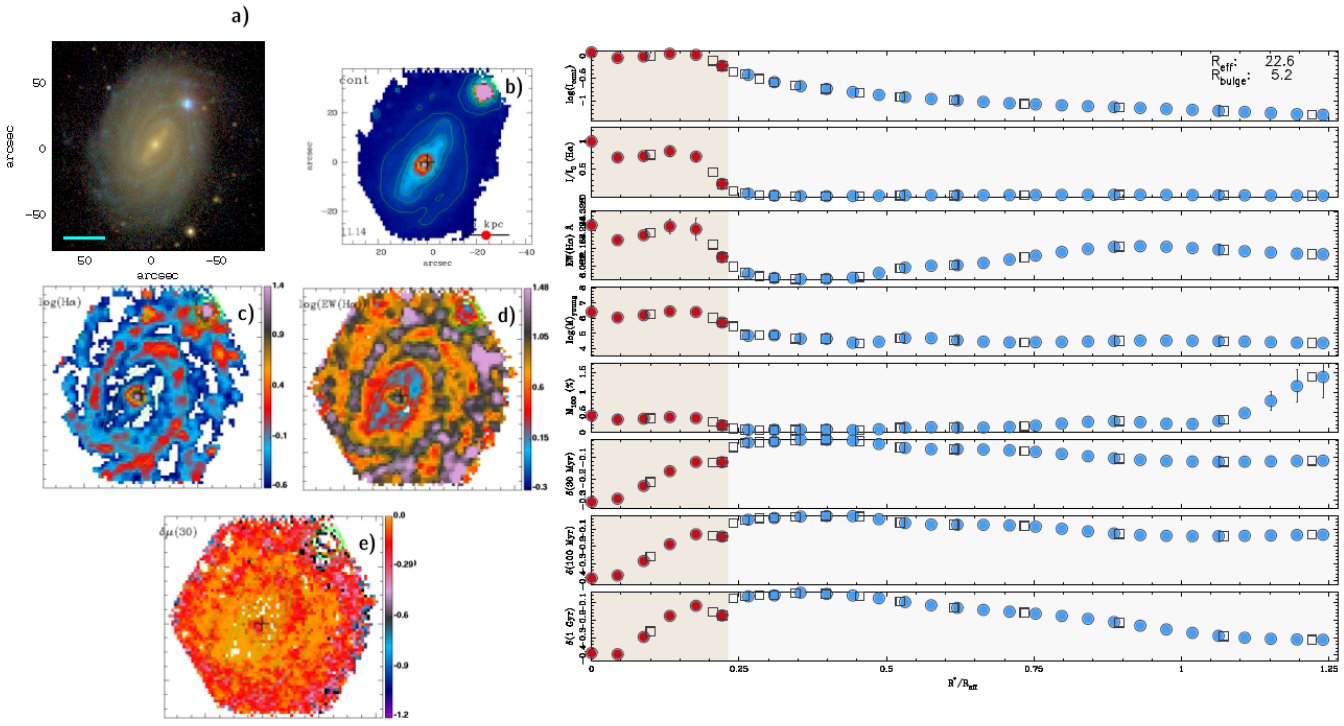

Figure A.7: Maps and radial profiles of NGC0180.

NGC0214

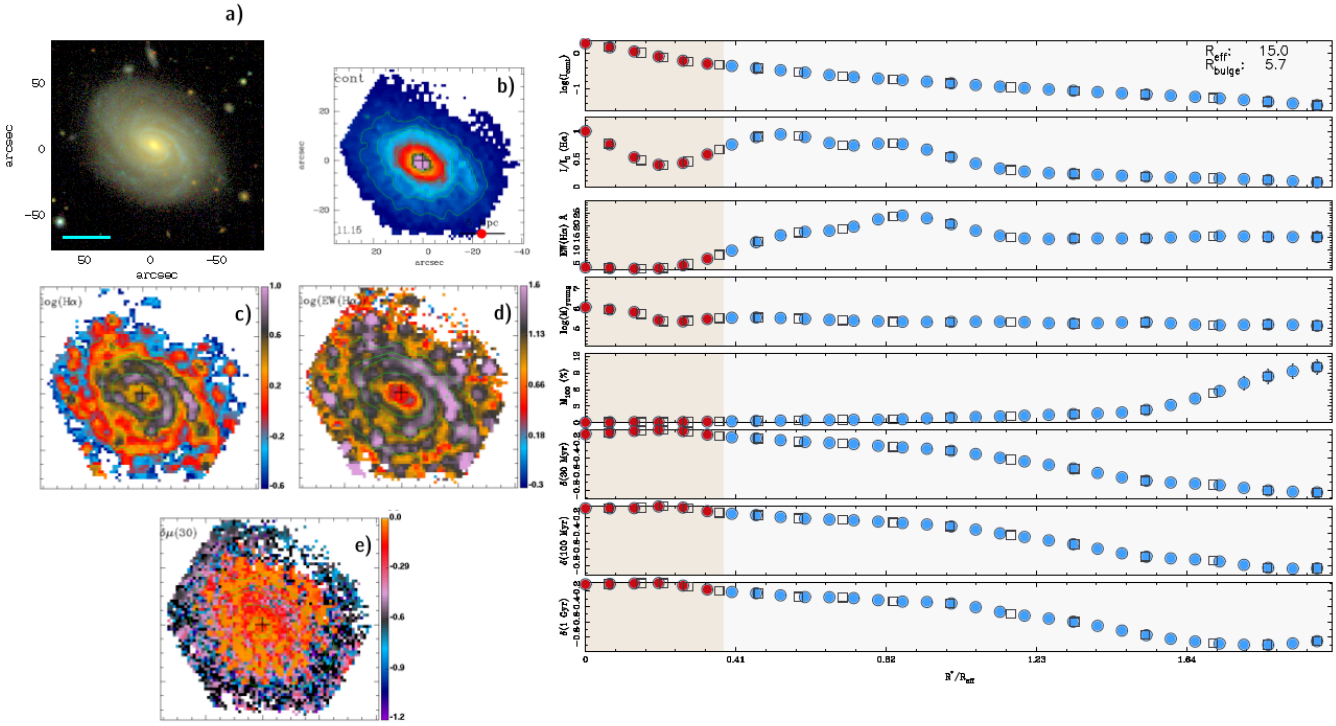

Figure A.8: Maps and radial profiles of NGC0214.

NGC0237

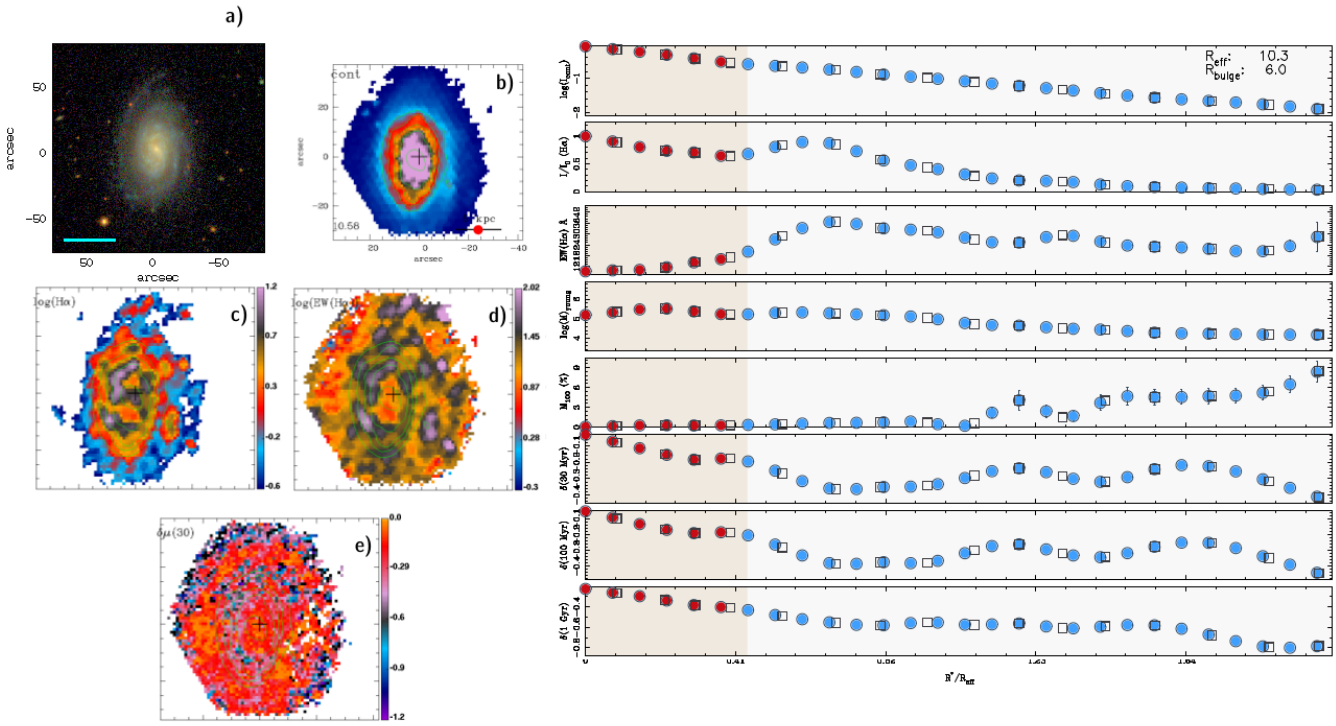

Figure A.9: Maps and radial profiles of NGC0237.

NGC0257

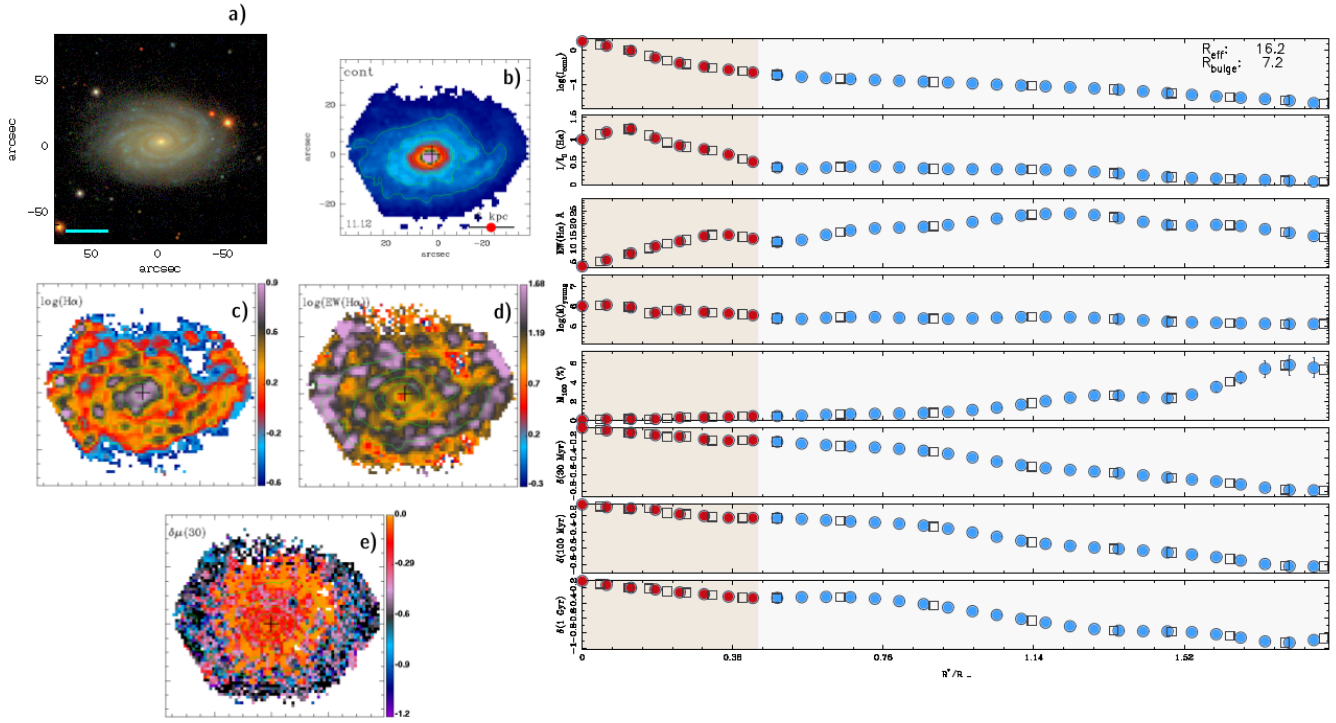

Figure A.10: Maps and radial profiles of NGC0257.

NGC0477

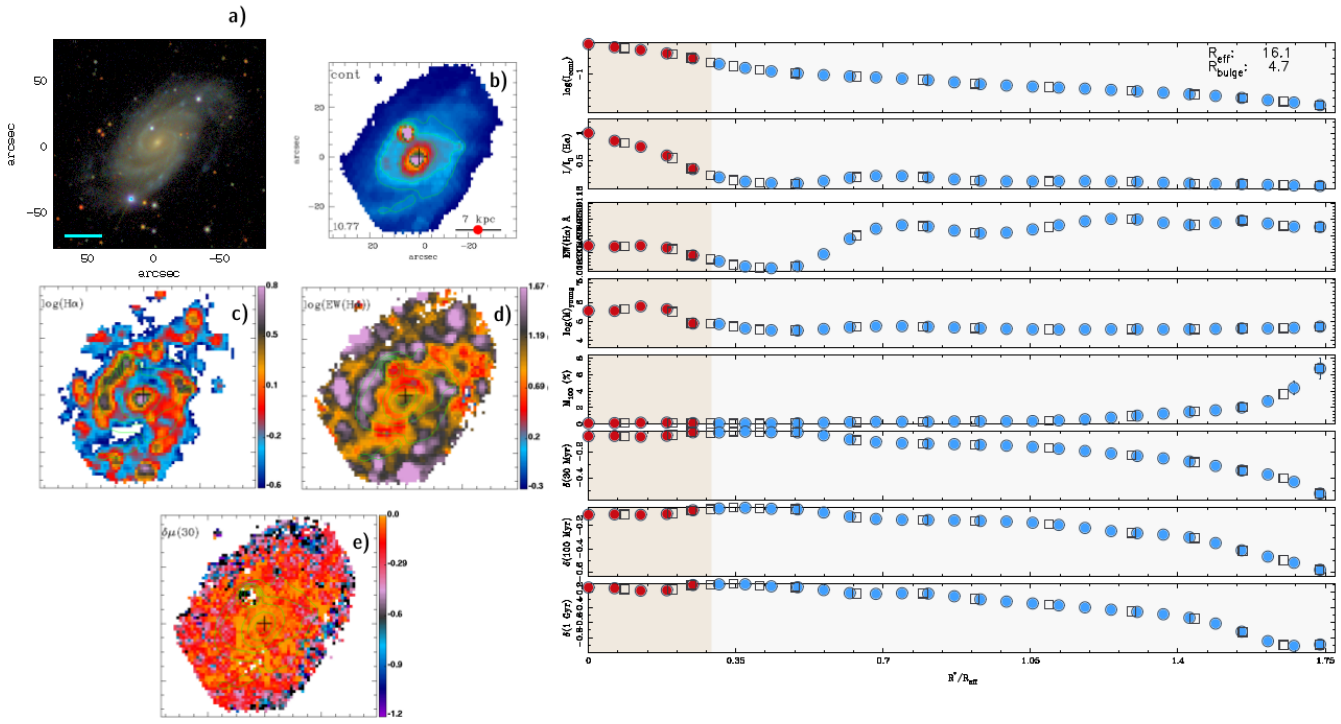

Figure A.11: Maps and radial profiles of NGC0477.

NGC0776

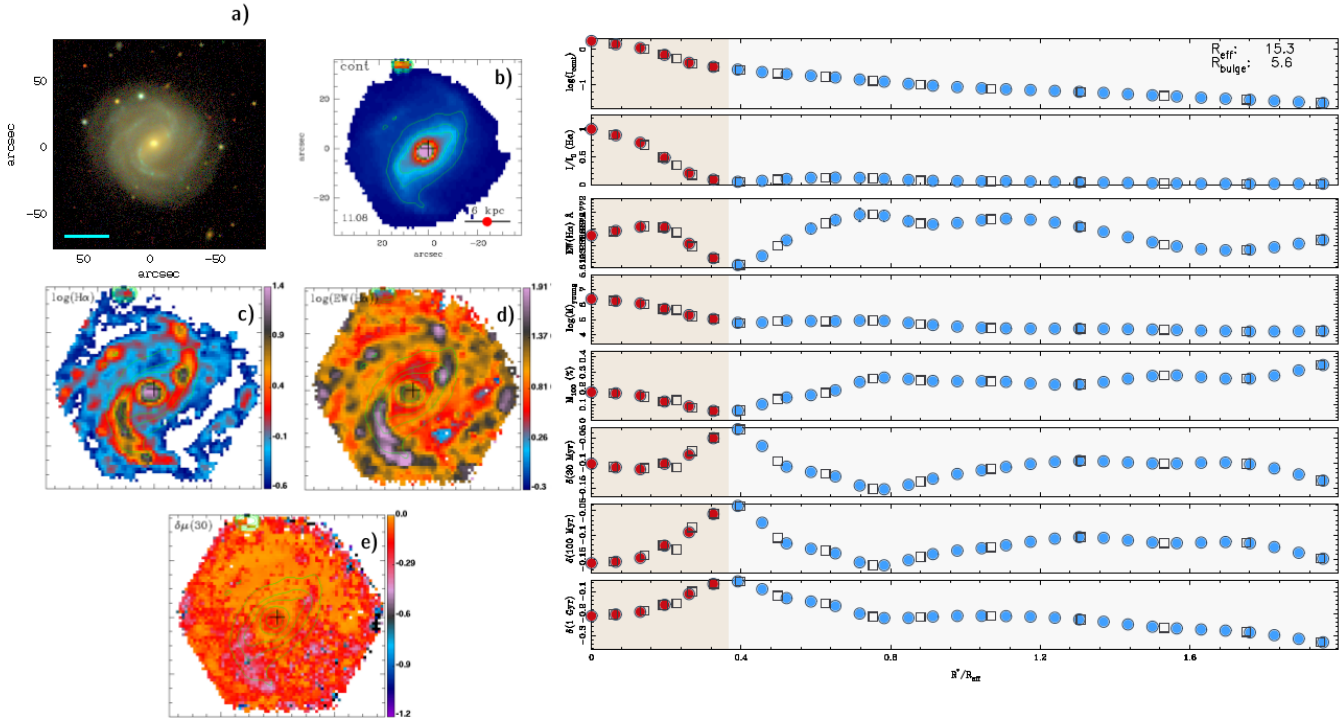

Figure A.12: Maps and radial profiles of NGC0776.

NGC1093

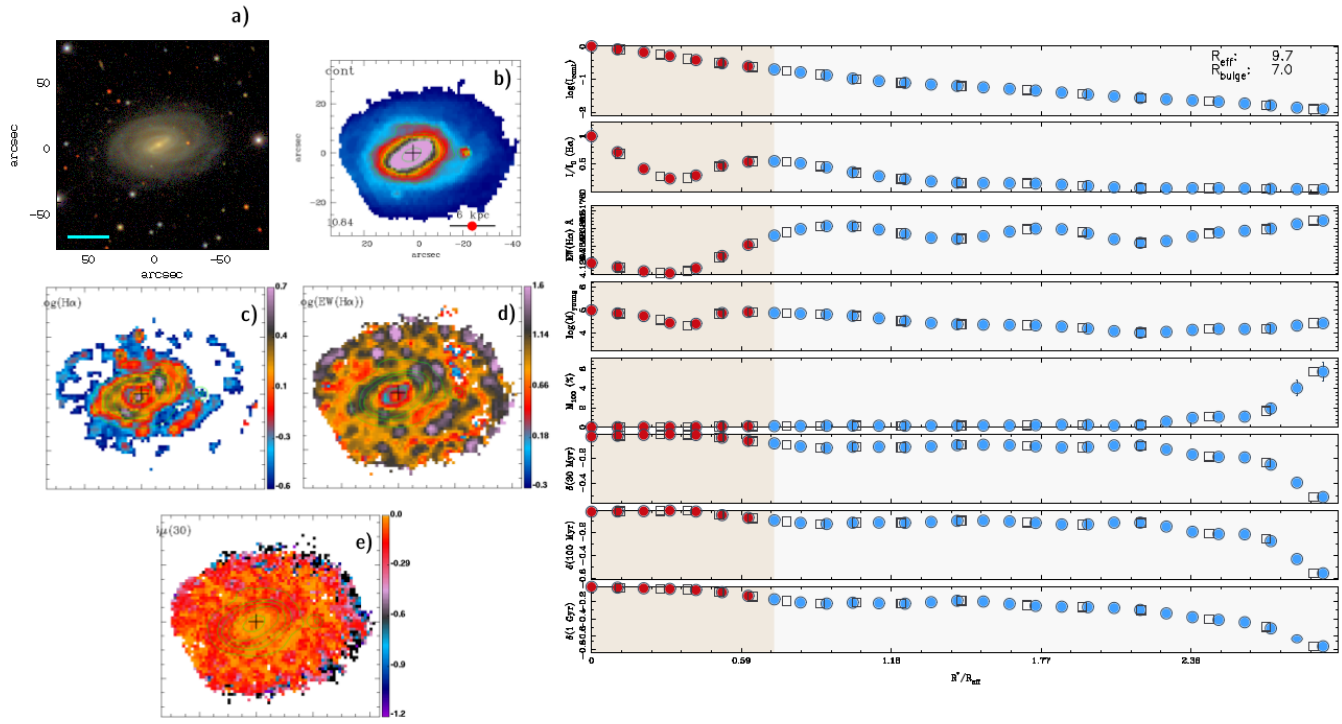

Figure A.13: Maps and radial profiles of NGC1093.

NGC1645

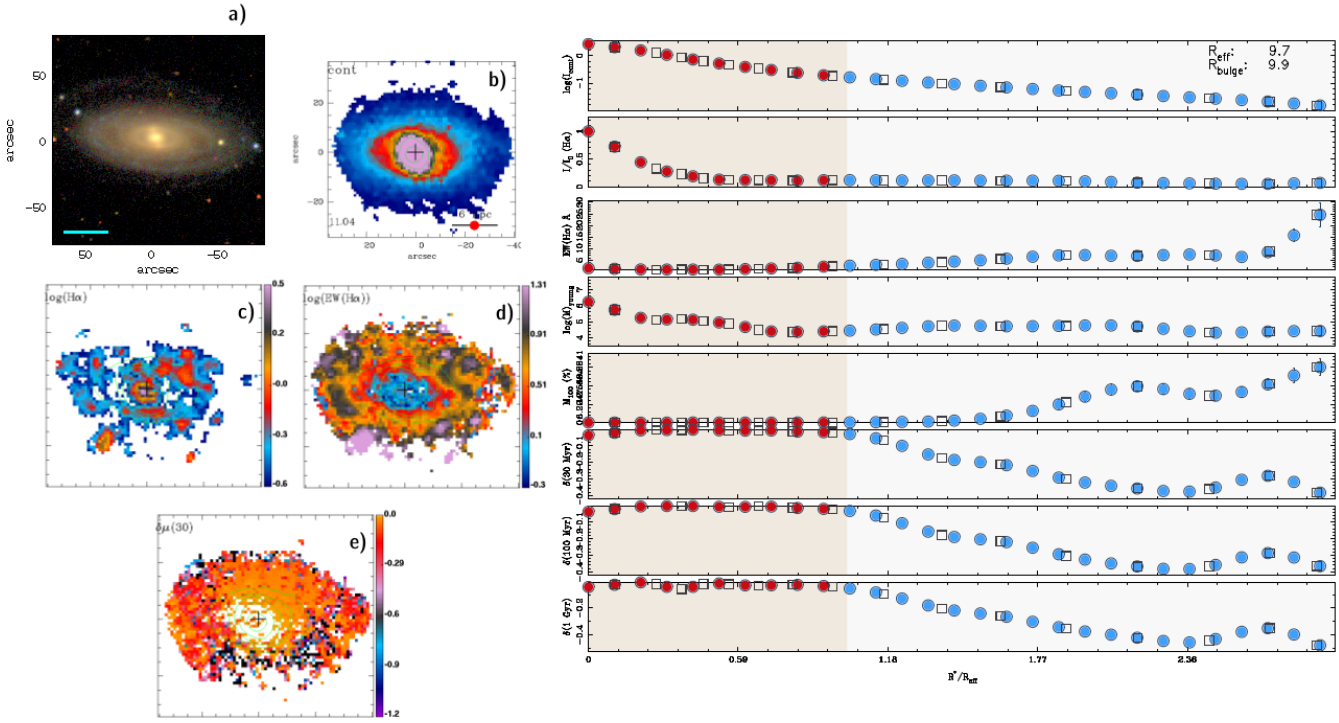

Figure A.14: Maps and radial profiles of NGC1645.

NGC2253

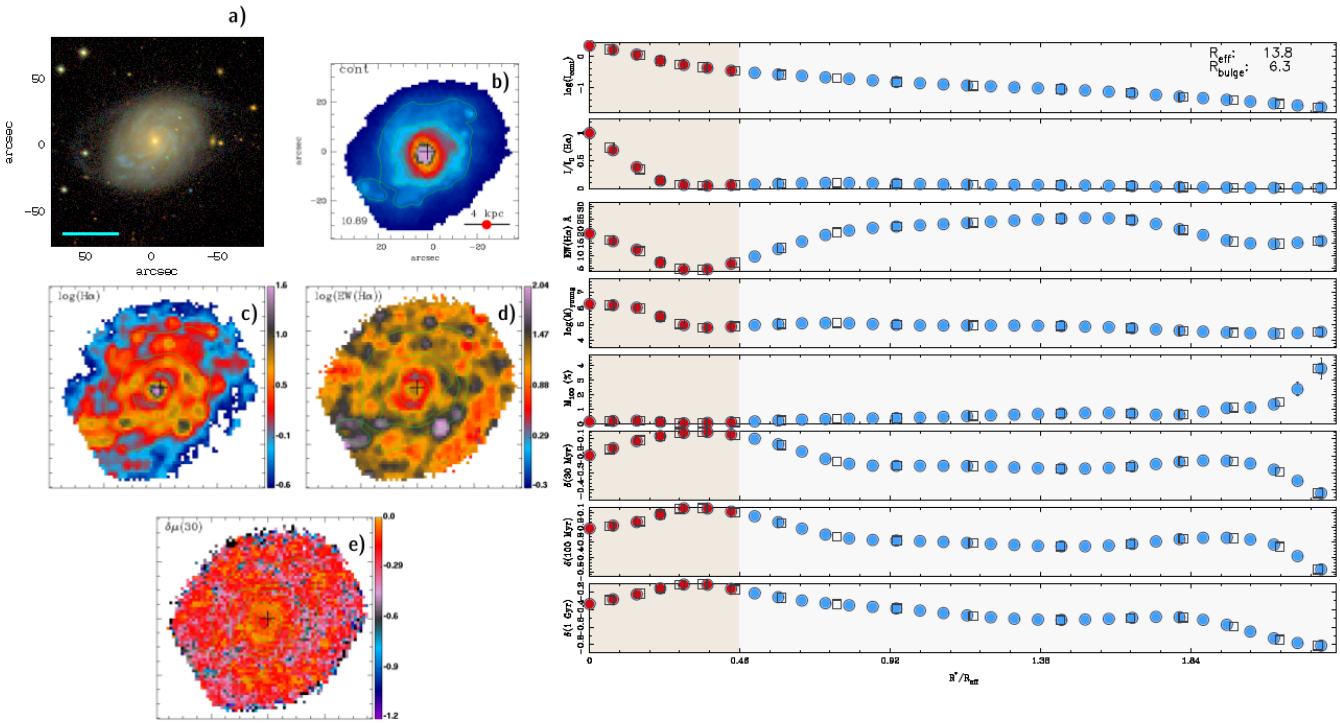

Figure A.15: Maps and radial profiles of NGC2253.

NGC2347

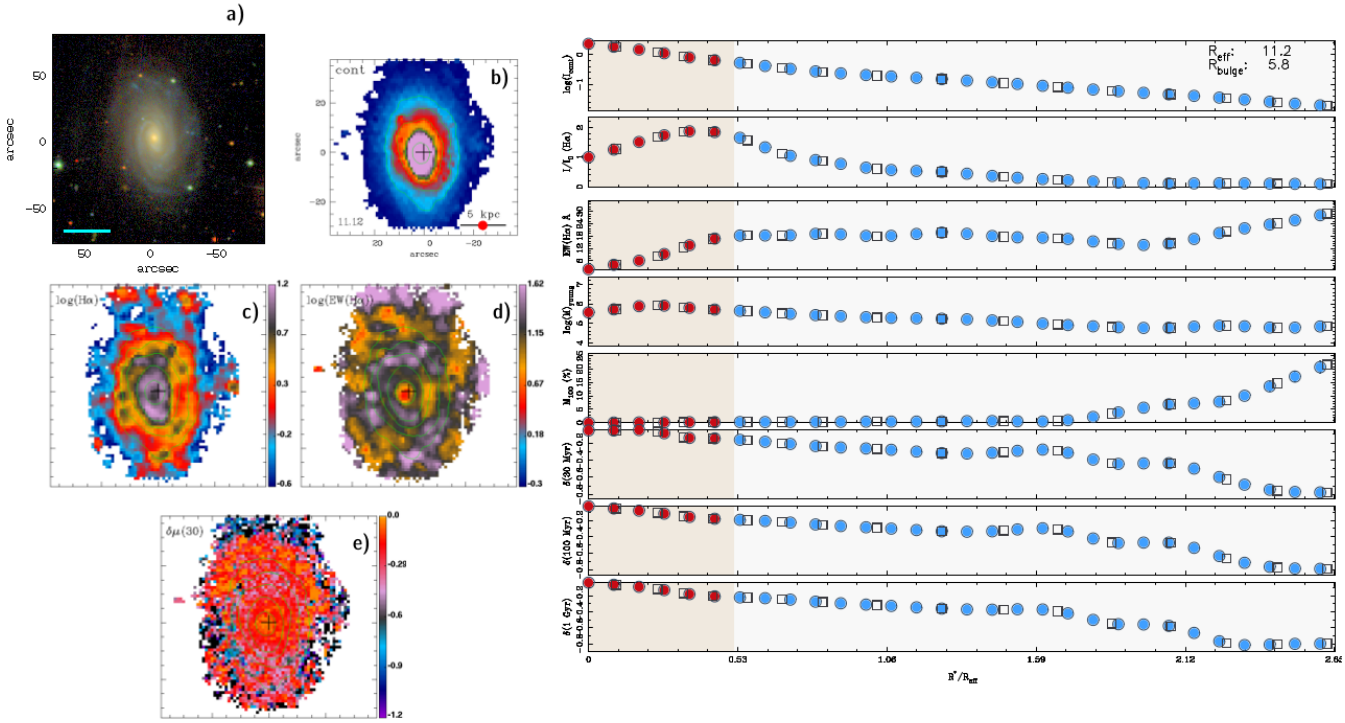

Figure A.16: Maps and radial profiles of NGC2347.

NGC2639

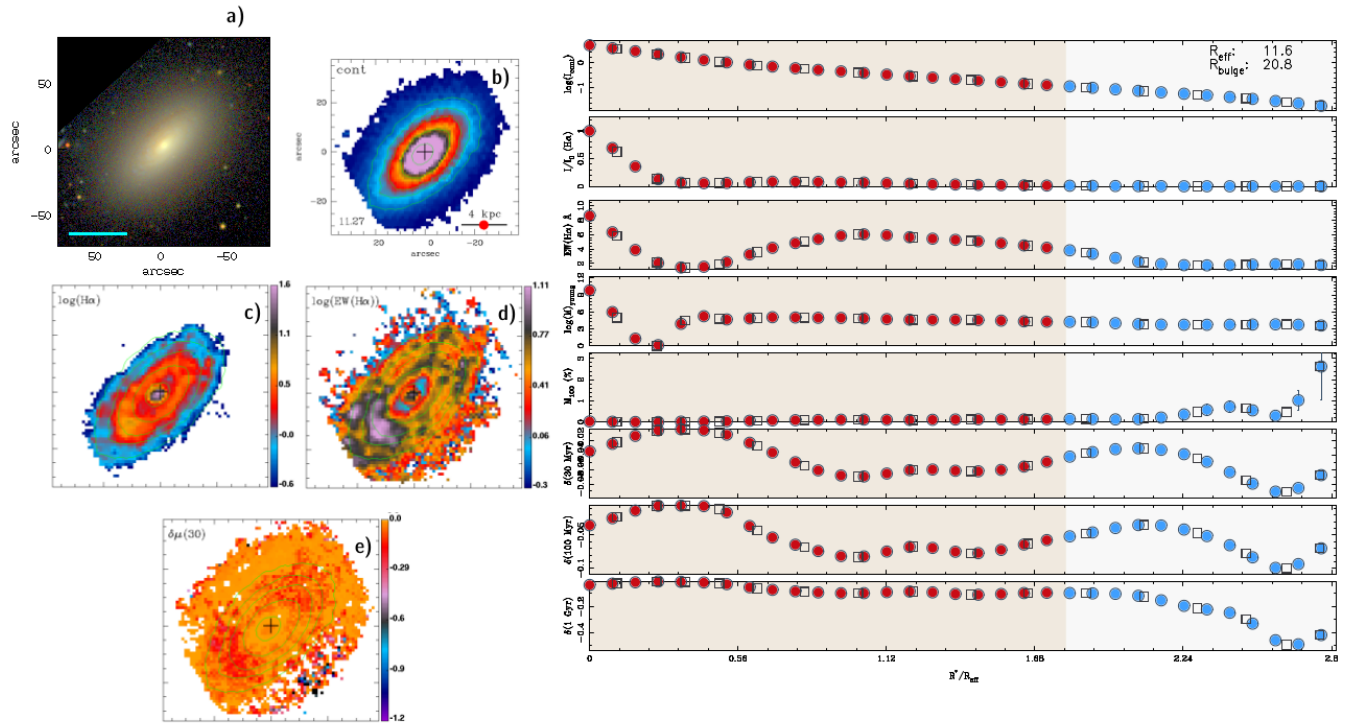

Figure A.17: Maps and radial profiles of NGC2639.

NGC2730

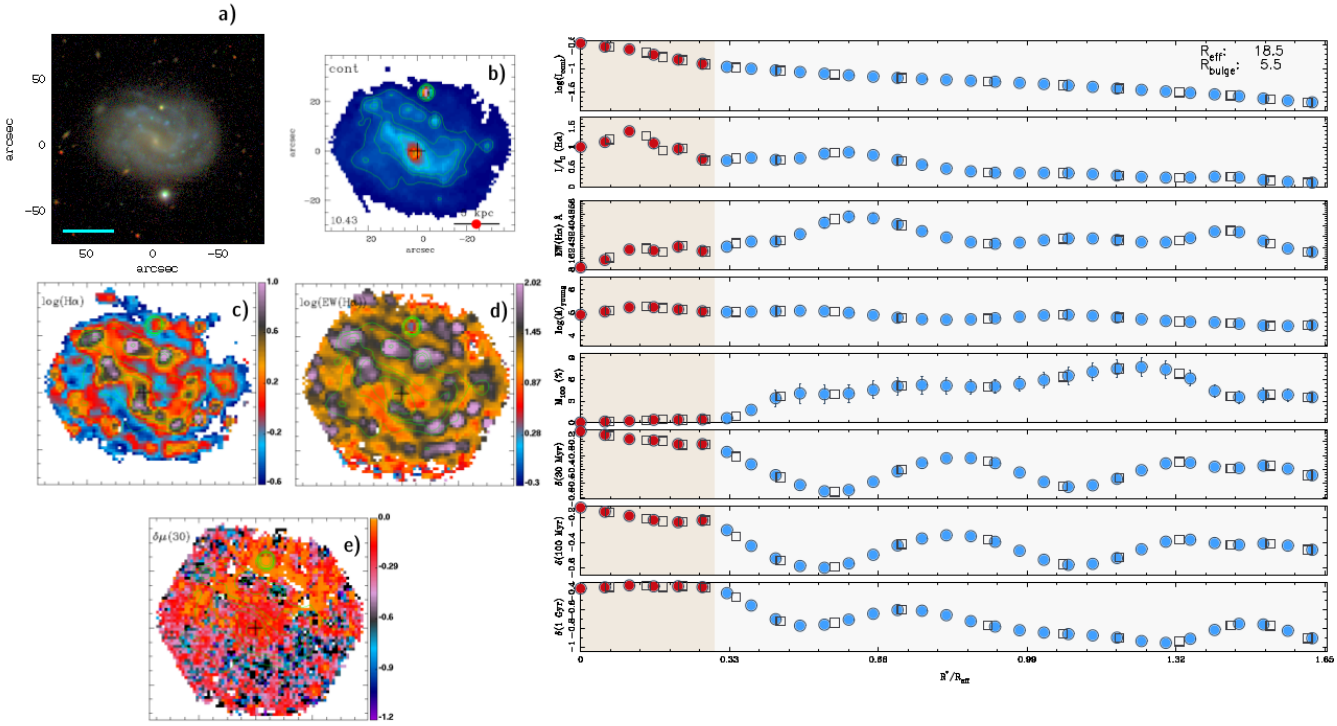

Figure A.18: Maps and radial profiles of NGC2730.

NGC2906

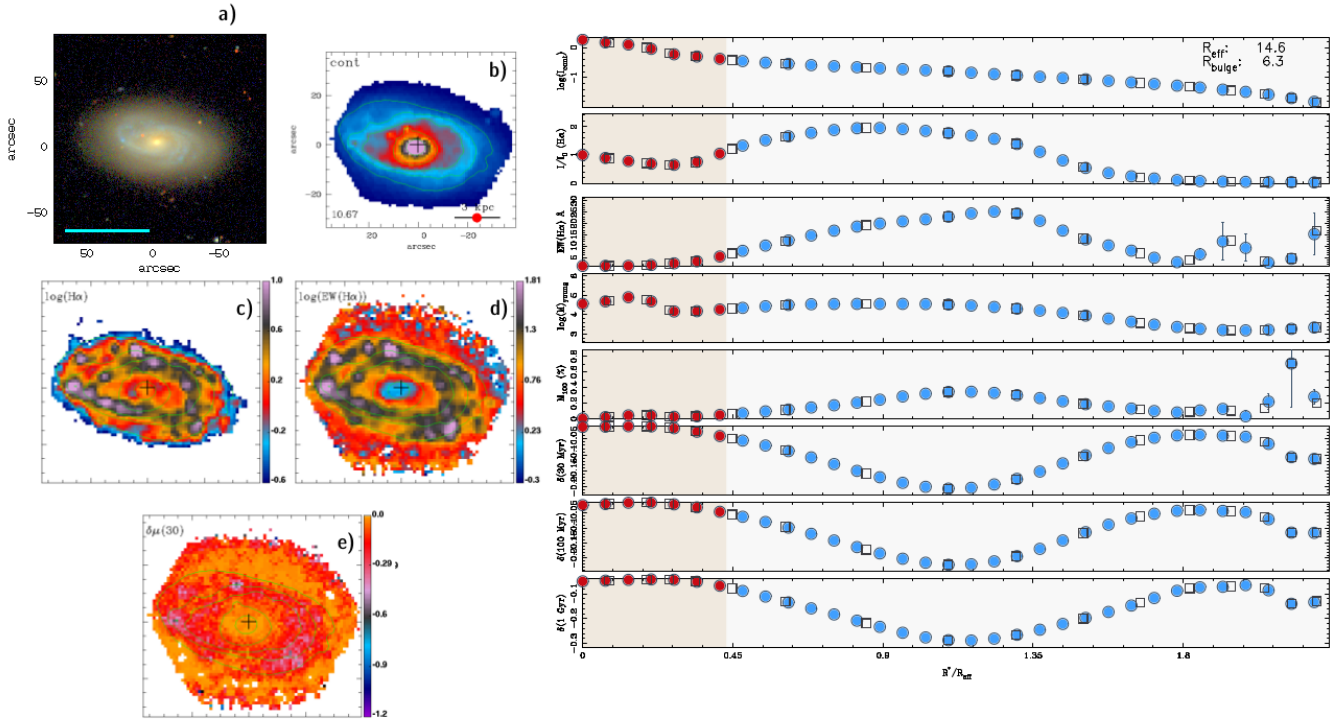

Figure A.19: Maps and radial profiles of NGC2906.

NGC2916

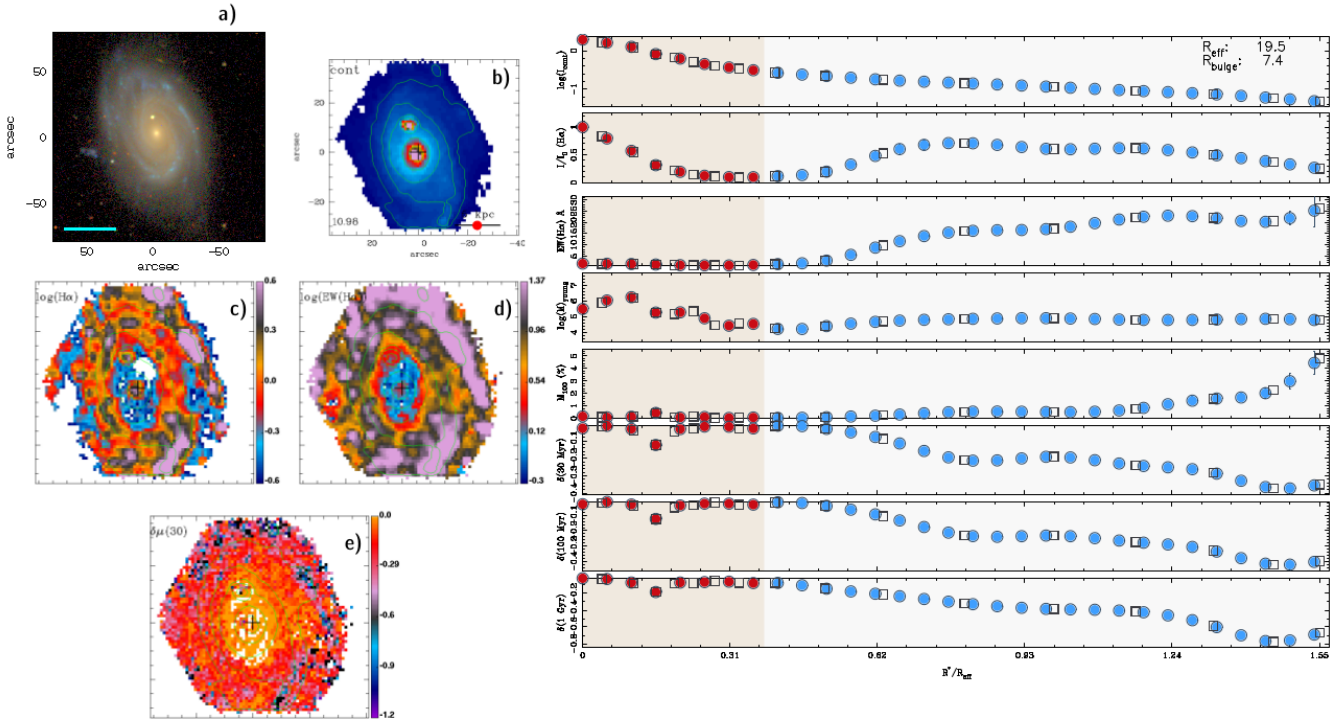

Figure A.20: Maps and radial profiles of NGC2916.

NGC3300

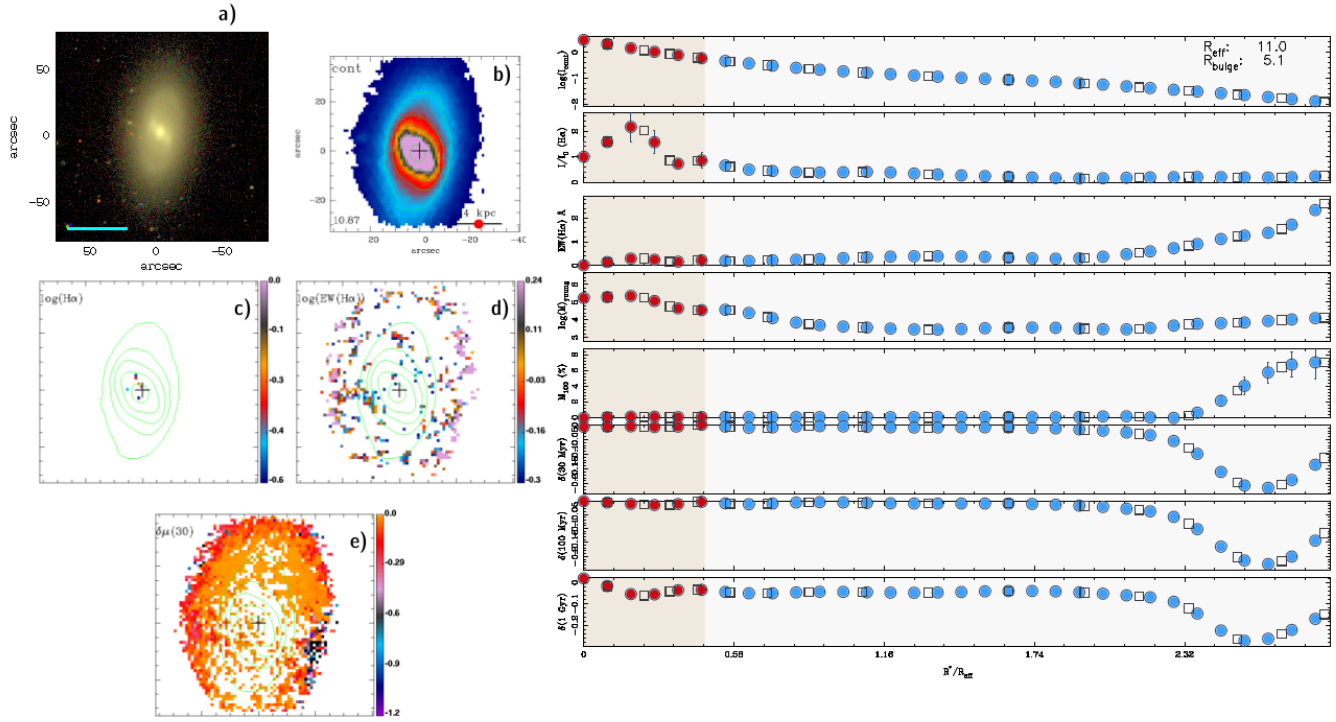

Figure A.21: Maps and radial profiles of NGC3300.

NGC3381

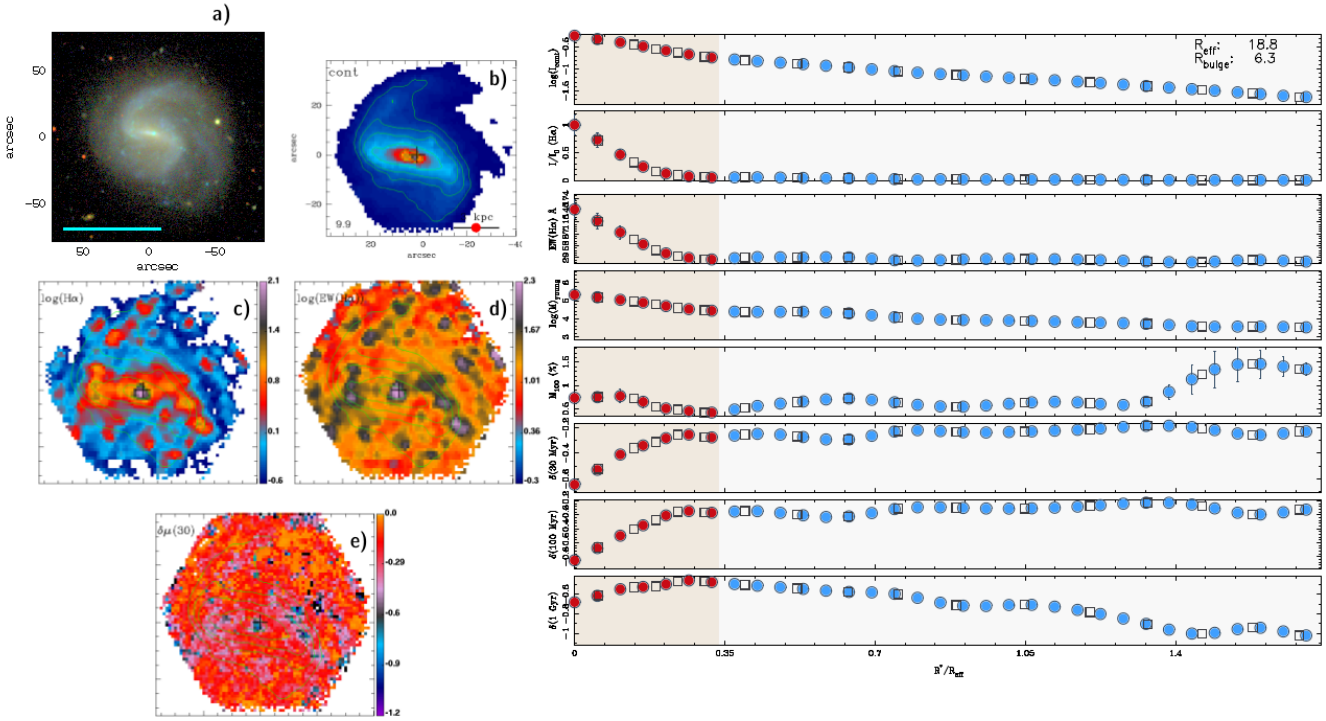

Figure A.22: Maps and radial profiles of NGC3381.

NGC3614

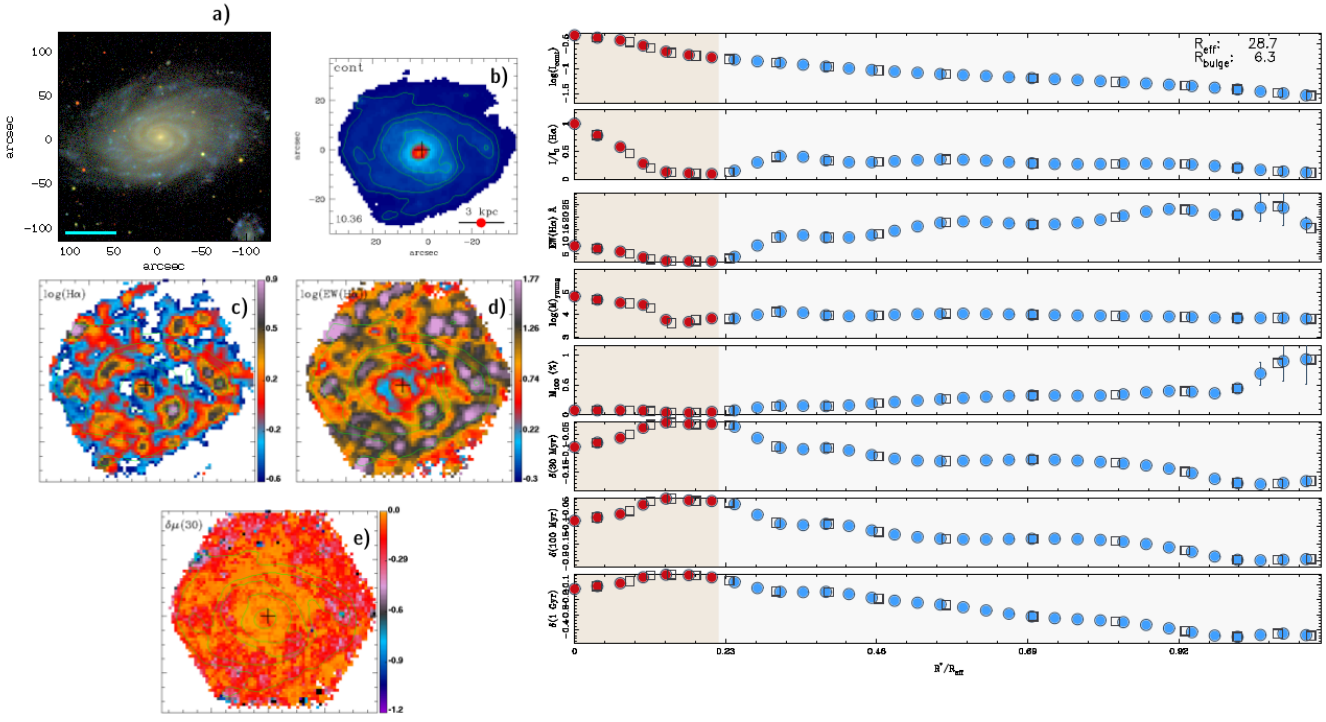

Figure A.23: Maps and radial profiles of NGC3614.

NGC3687

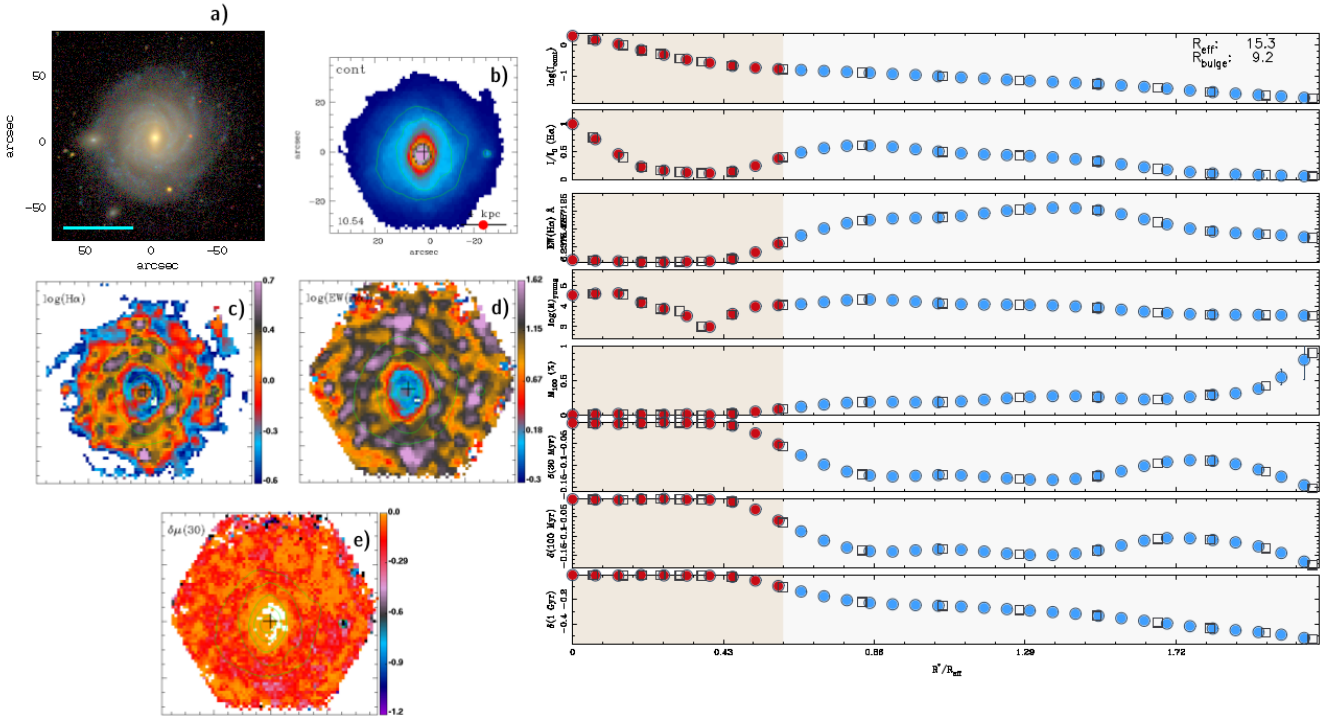

Figure A.24: Maps and radial profiles of NGC3687.

NGC4003

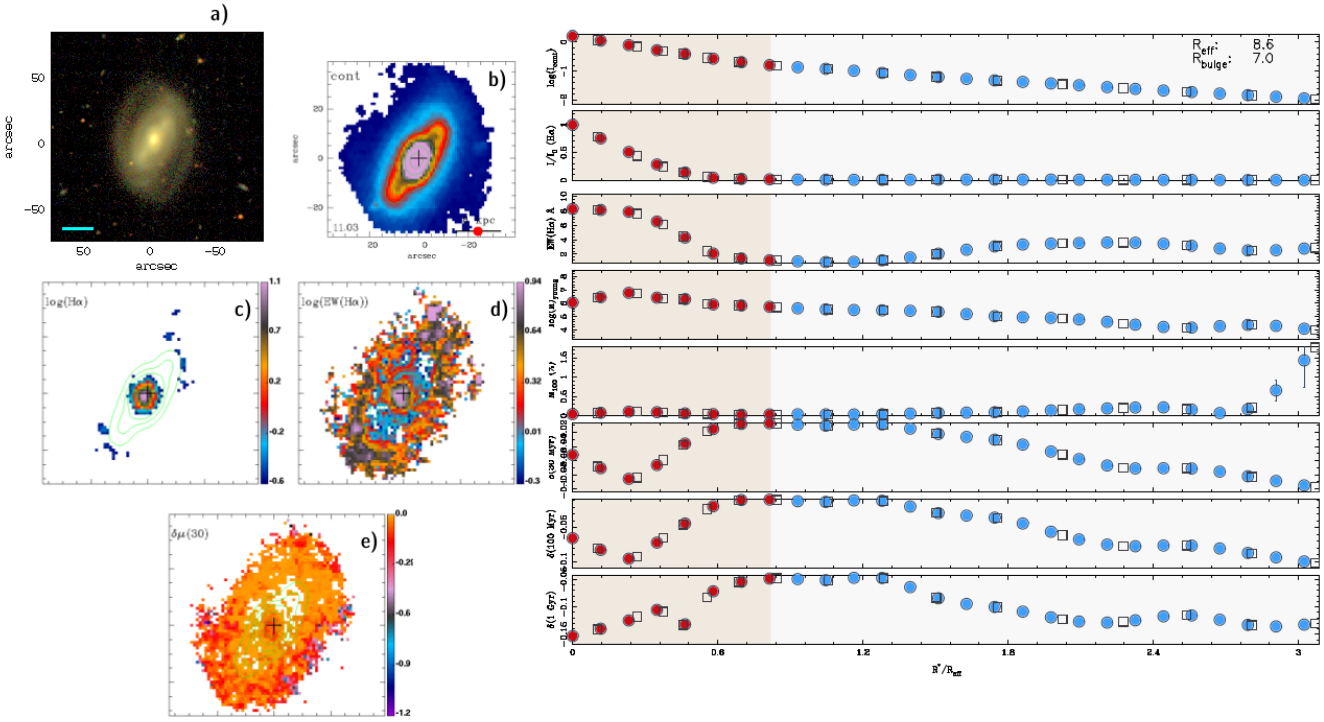

Figure A.25: Maps and radial profiles of NGC4003.

NGC4047

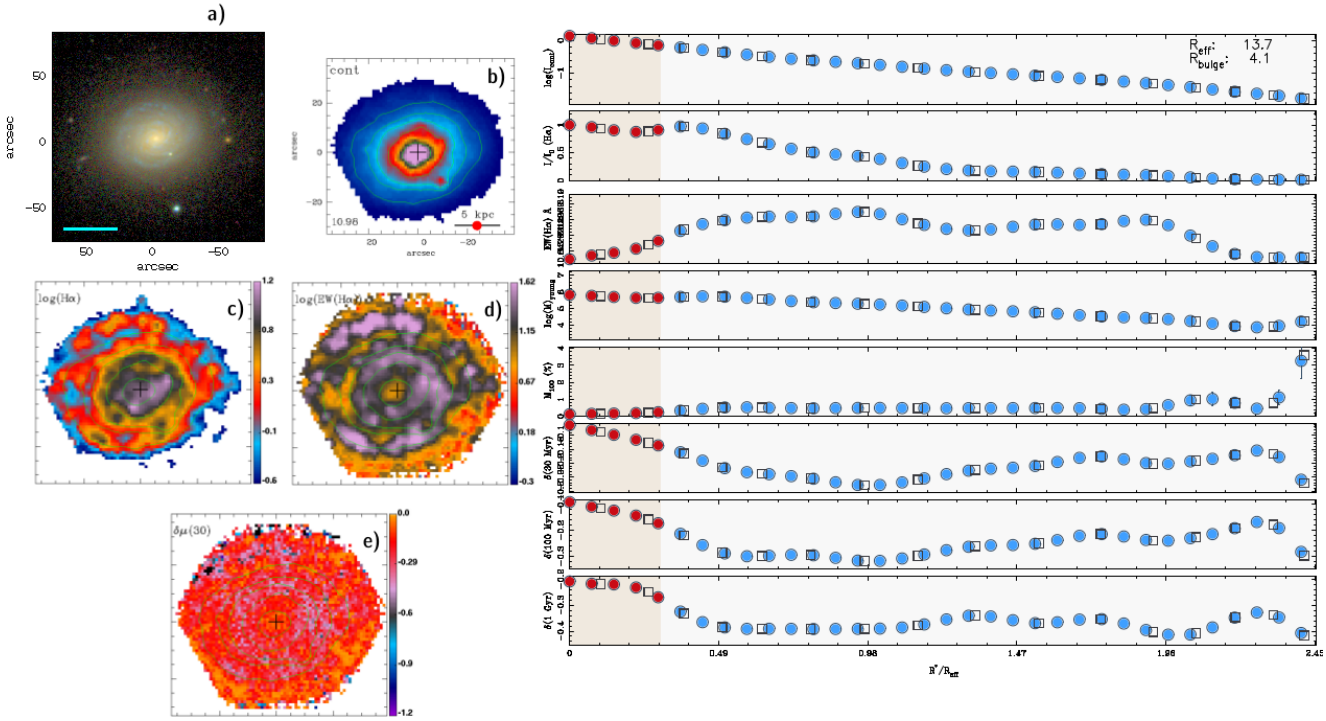

Figure A.26: Maps and radial profiles of NGC4047.

NGC4185

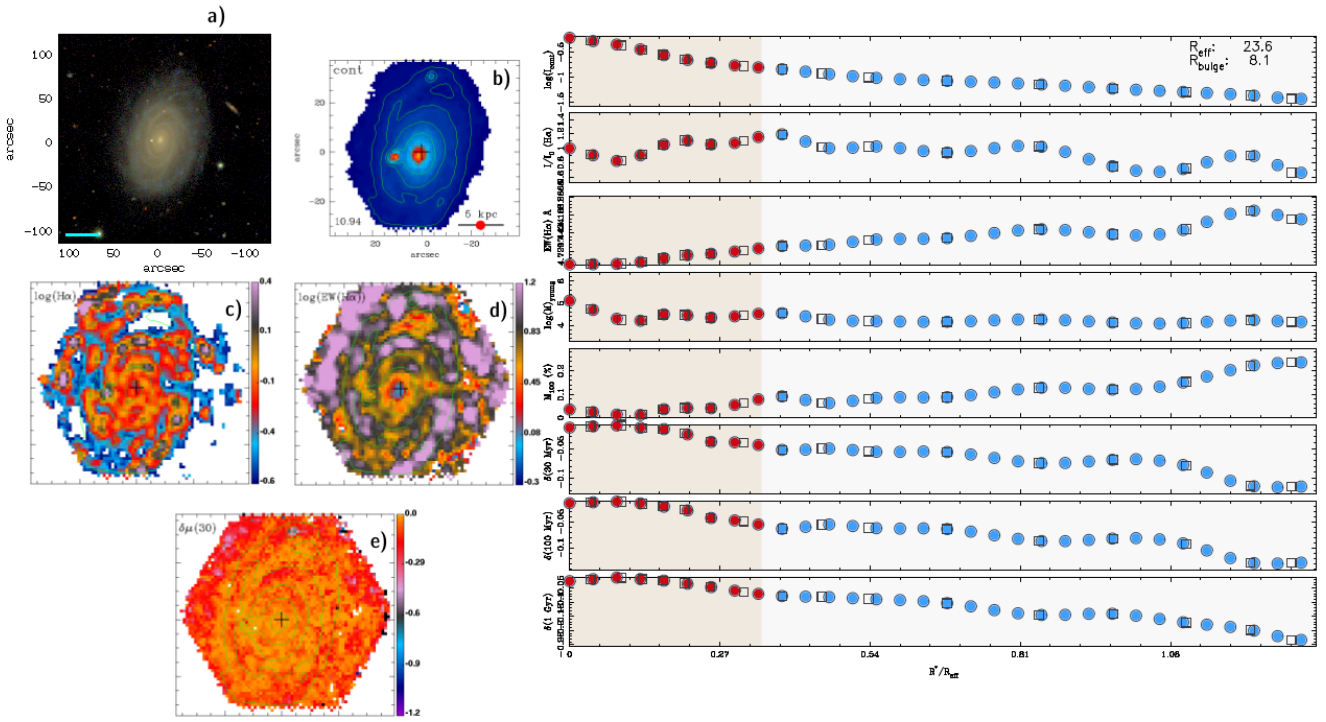

Figure A.27: Maps and radial profiles of NGC4185.

NGC4210

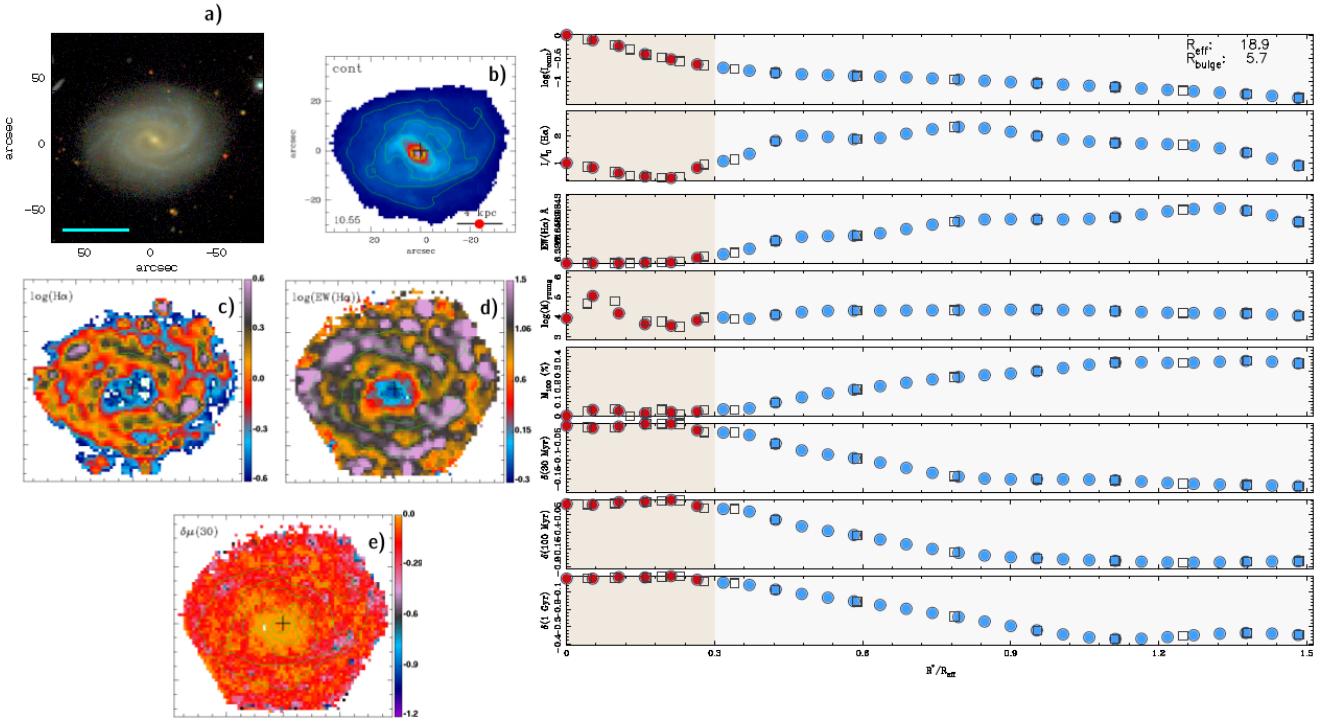

Figure A.28: Maps and radial profiles of NGC4210.

NGC4961

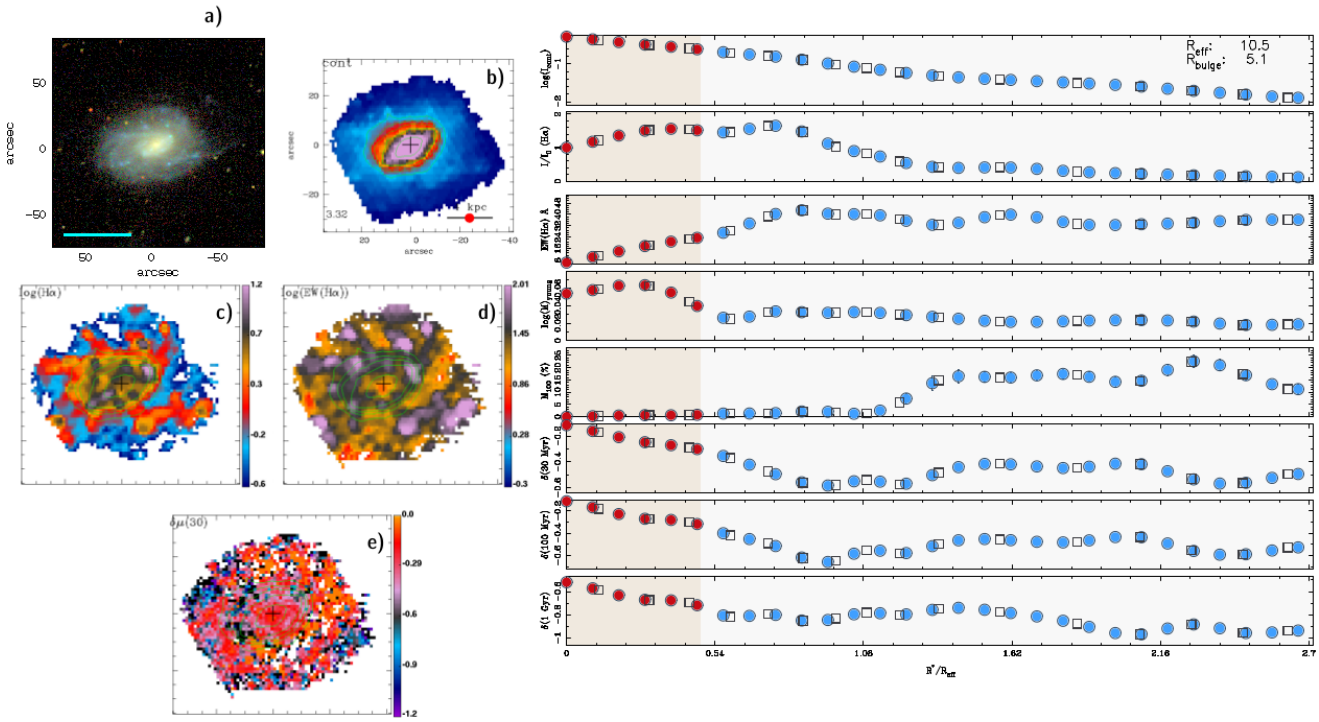

Figure A.29: Maps and radial profiles of NGC4961.

NGC5000

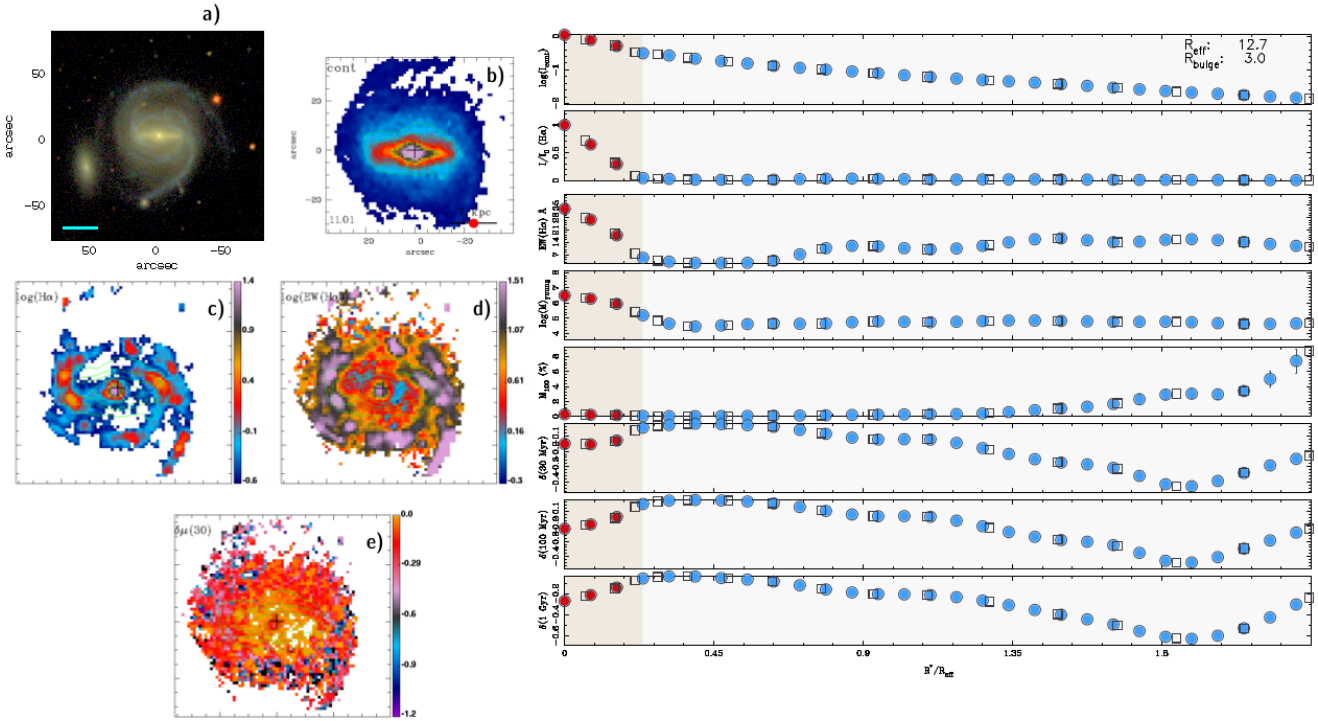

Figure A.30: Maps and radial profiles of NGC5000.

NGC5016

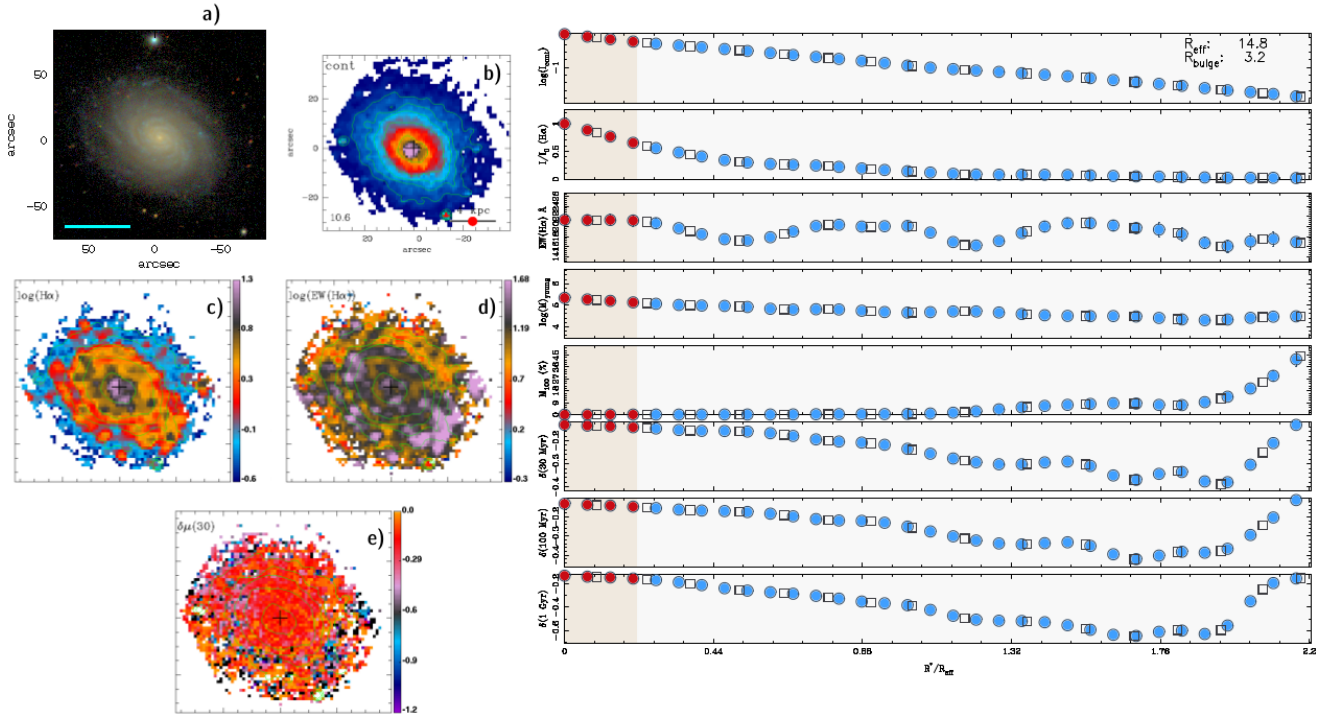

Figure A.31: Maps and radial profiles of NGC5016.

NGC5205

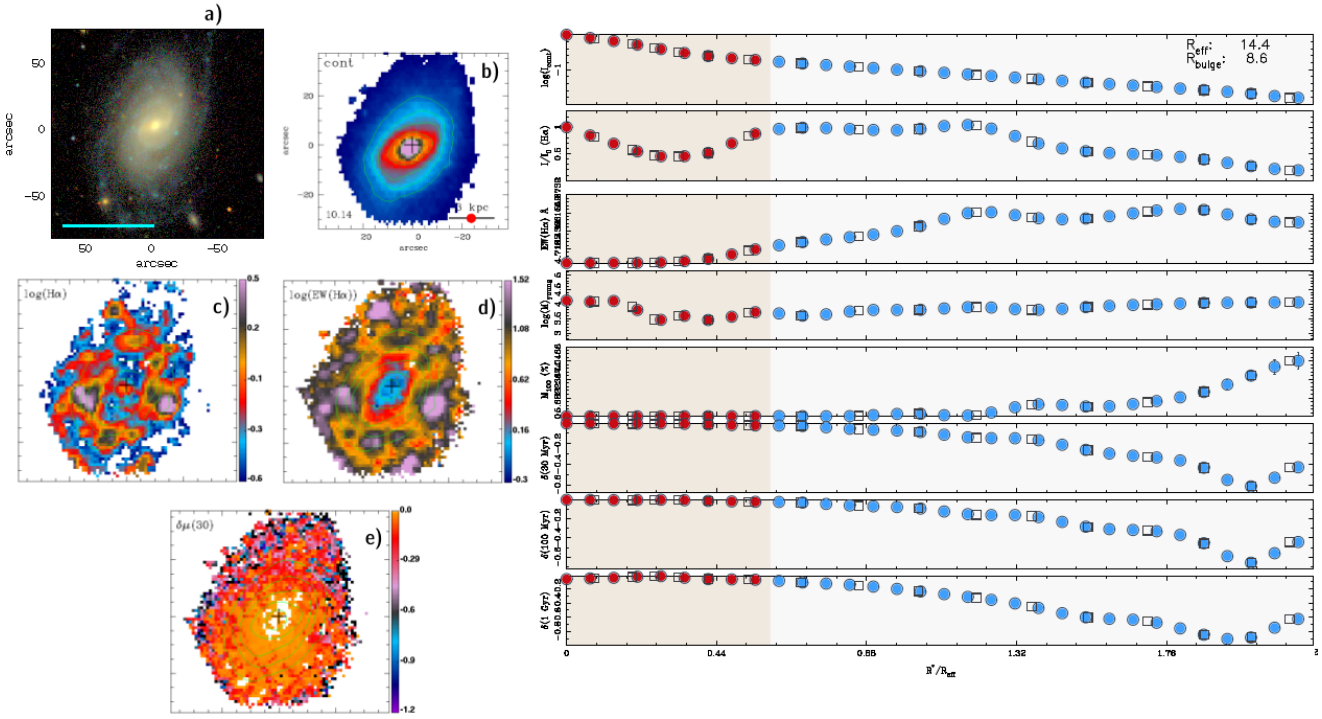

Figure A.32: Maps and radial profiles of NGC5205.

NGC5320

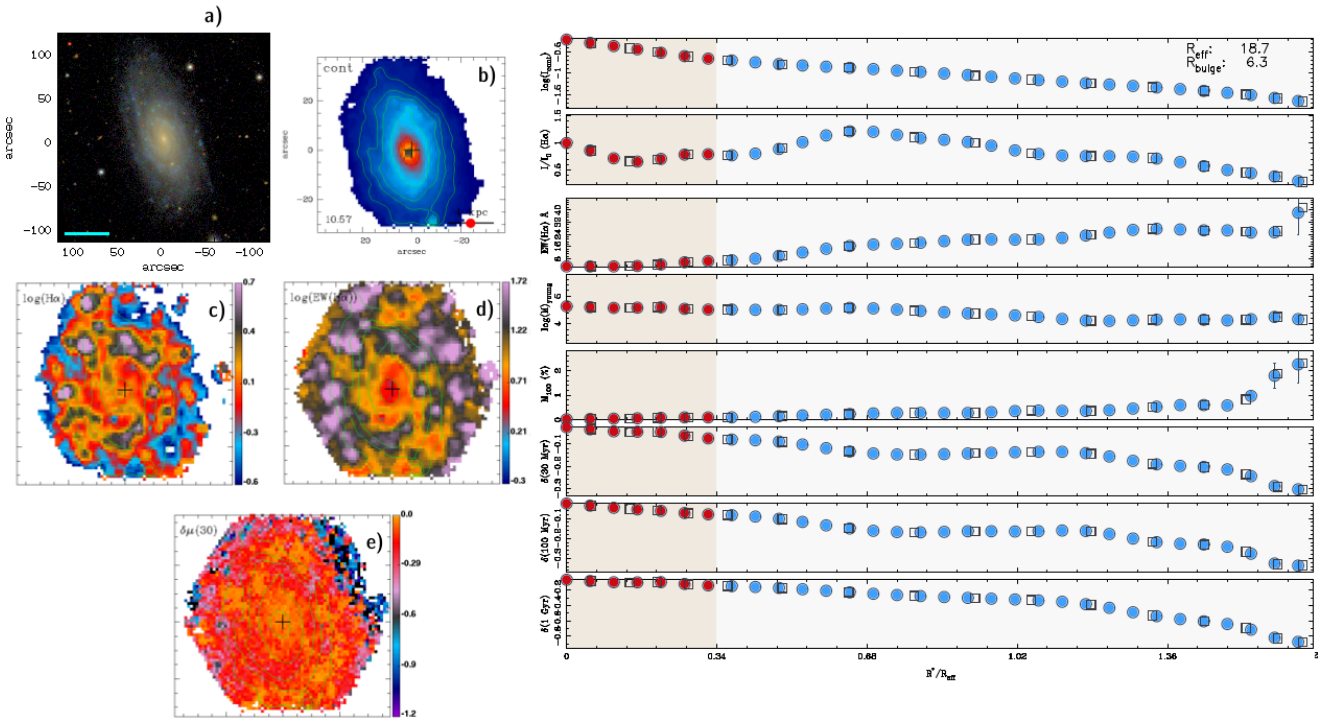

Figure A.33: Maps and radial profiles of NGC5320.

NGC5378

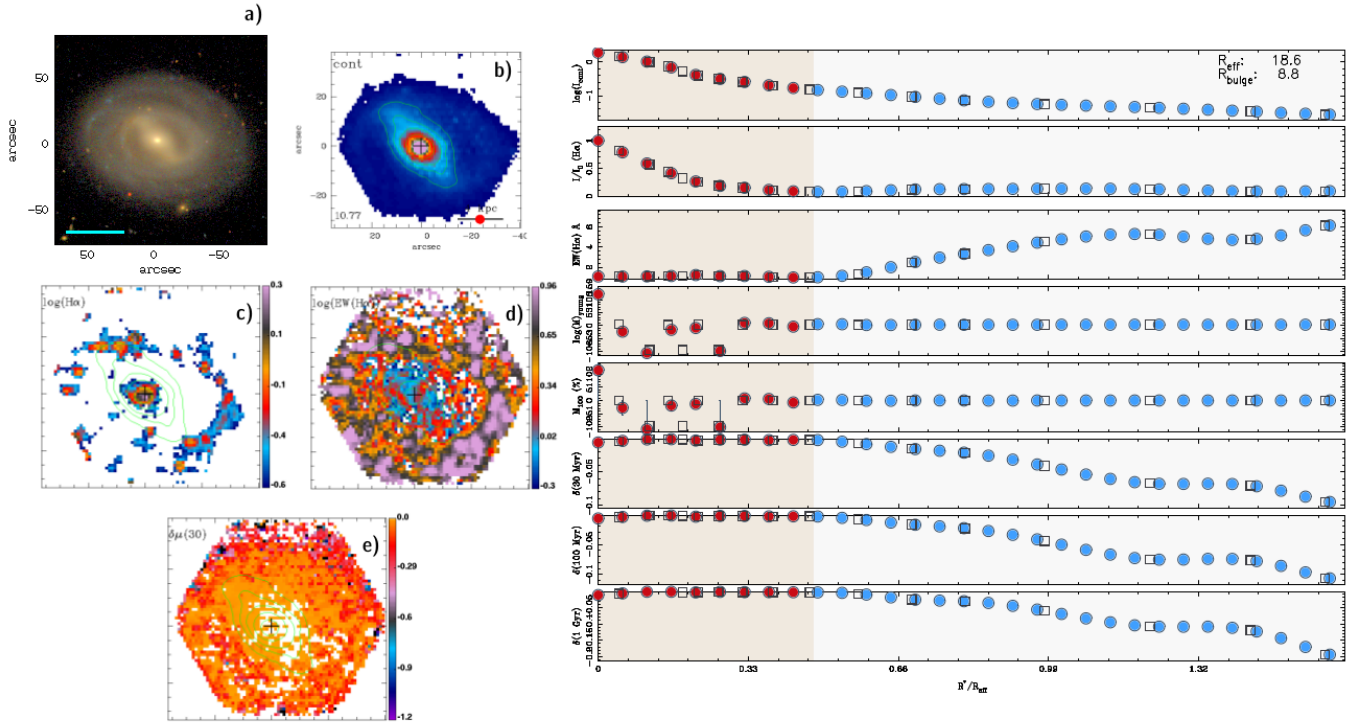

Figure A.34: Maps and radial profiles of NGC5378.

NGC5406

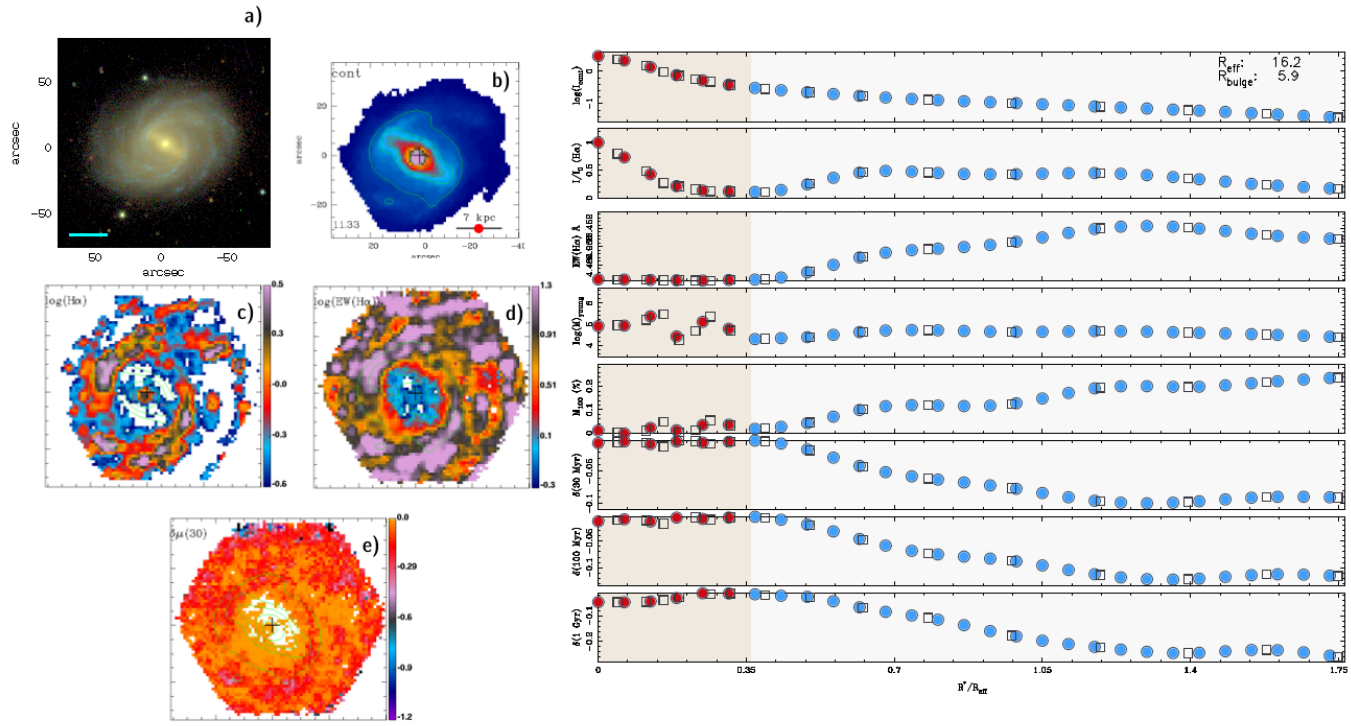

Figure A.35: Maps and radial profiles of NGC5406.

NGC5480

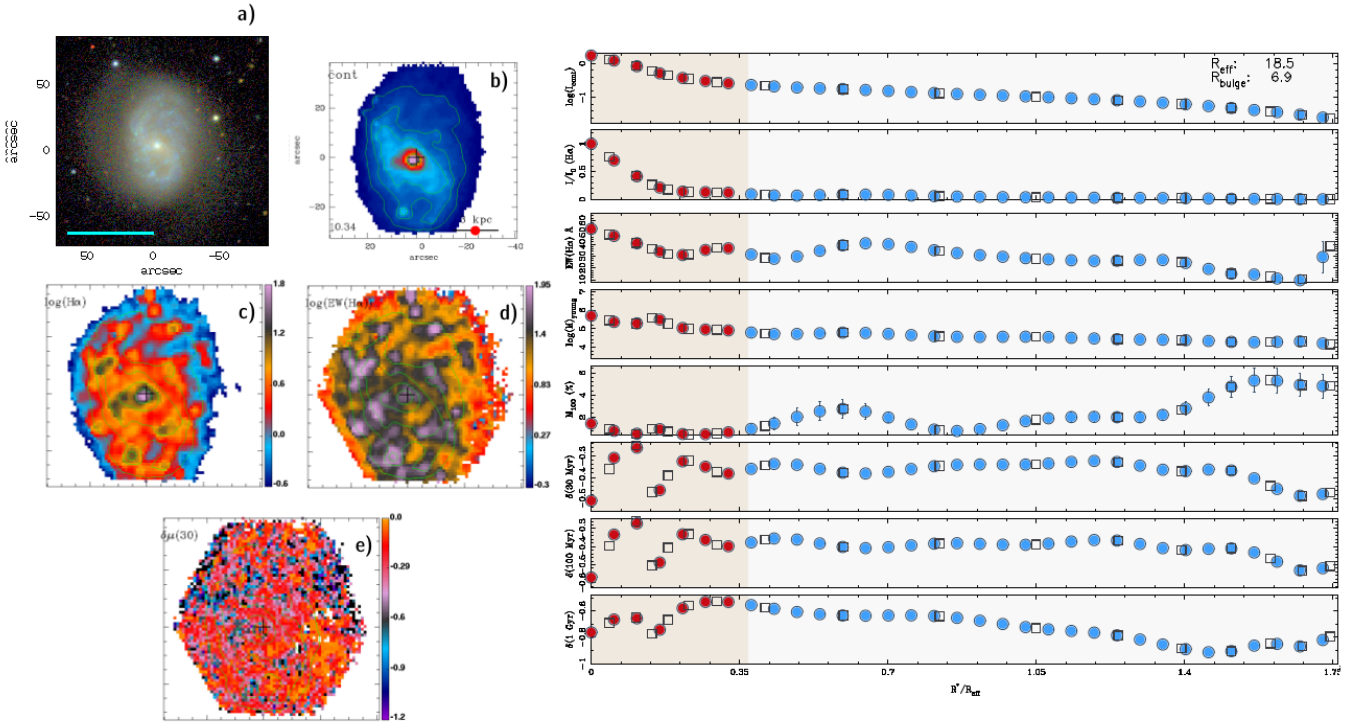

Figure A.36: Maps and radial profiles of NGC5480.

NGC5614

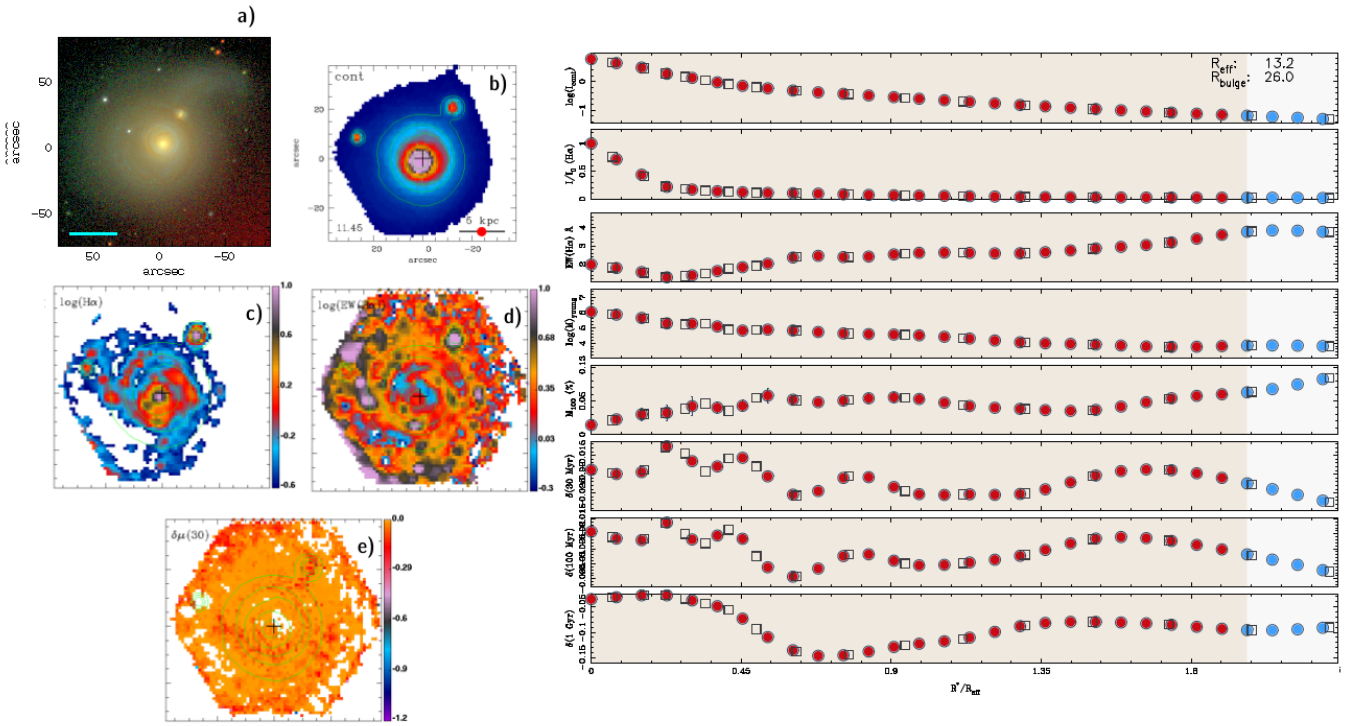

Figure A.37: Maps and radial profiles of NGC5614.

NGC5656

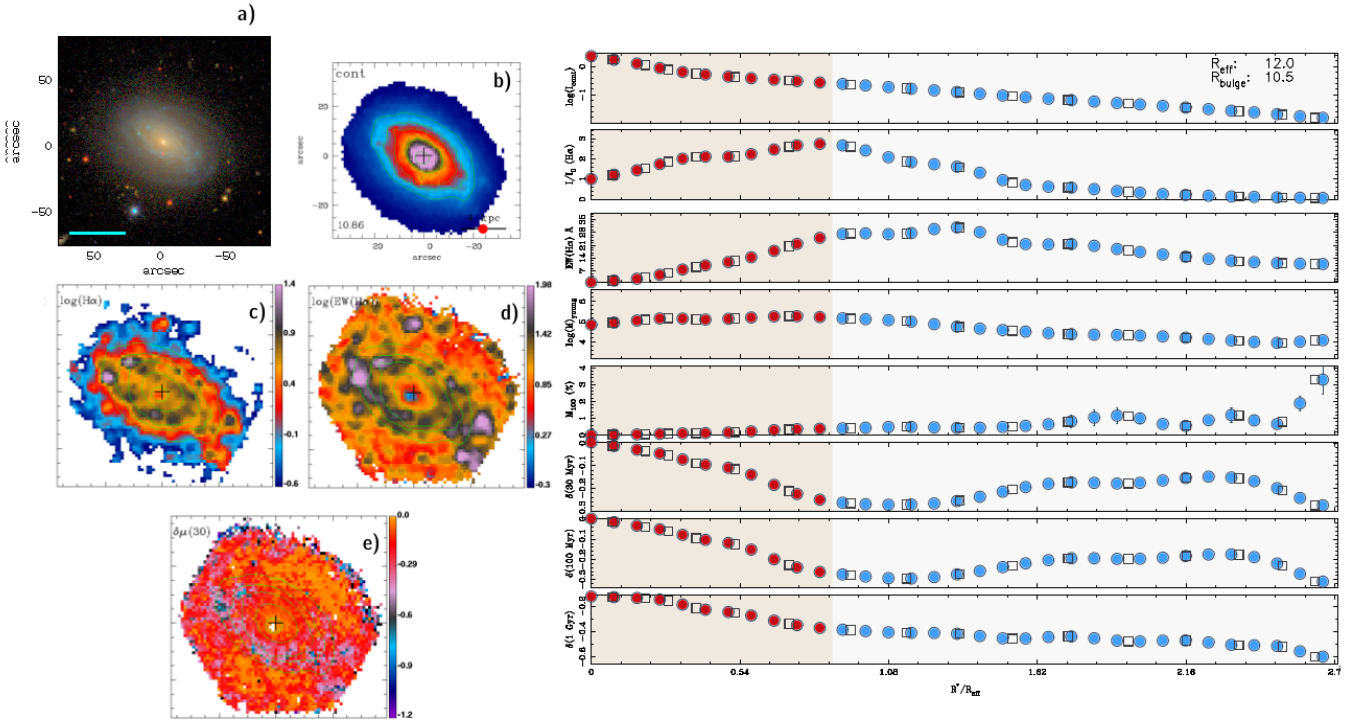

Figure A.38: Maps and radial profiles of NGC5656.

NGC5735

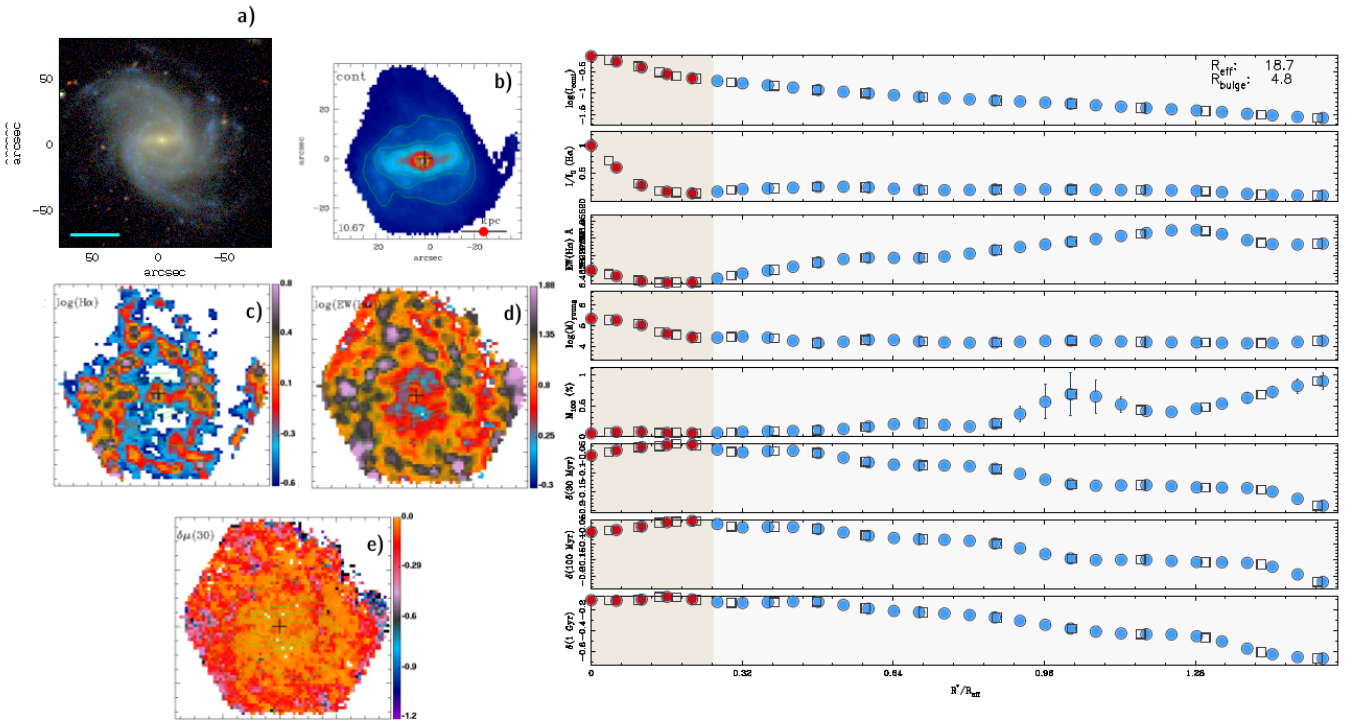

Figure A.39: Maps and radial profiles of NGC5735.

NGC5772

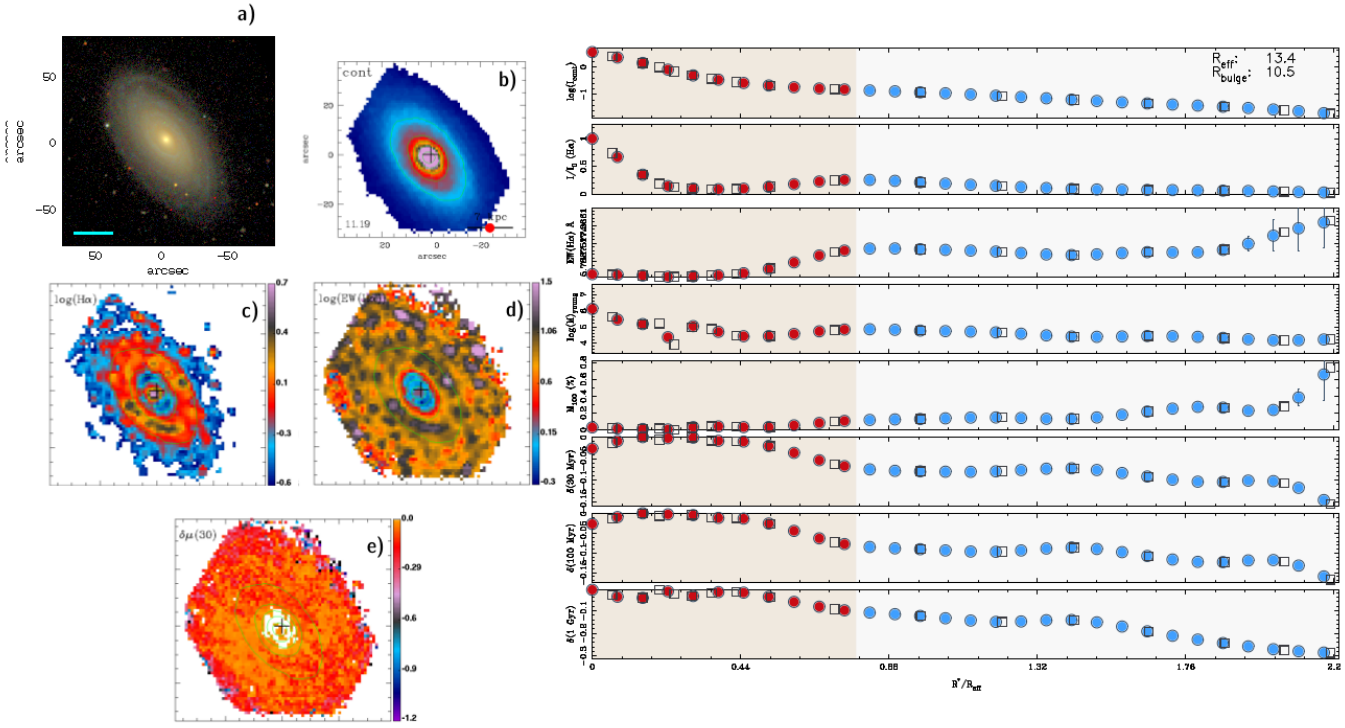

Figure A.40: Maps and radial profiles of NGC5772.

NGC5829

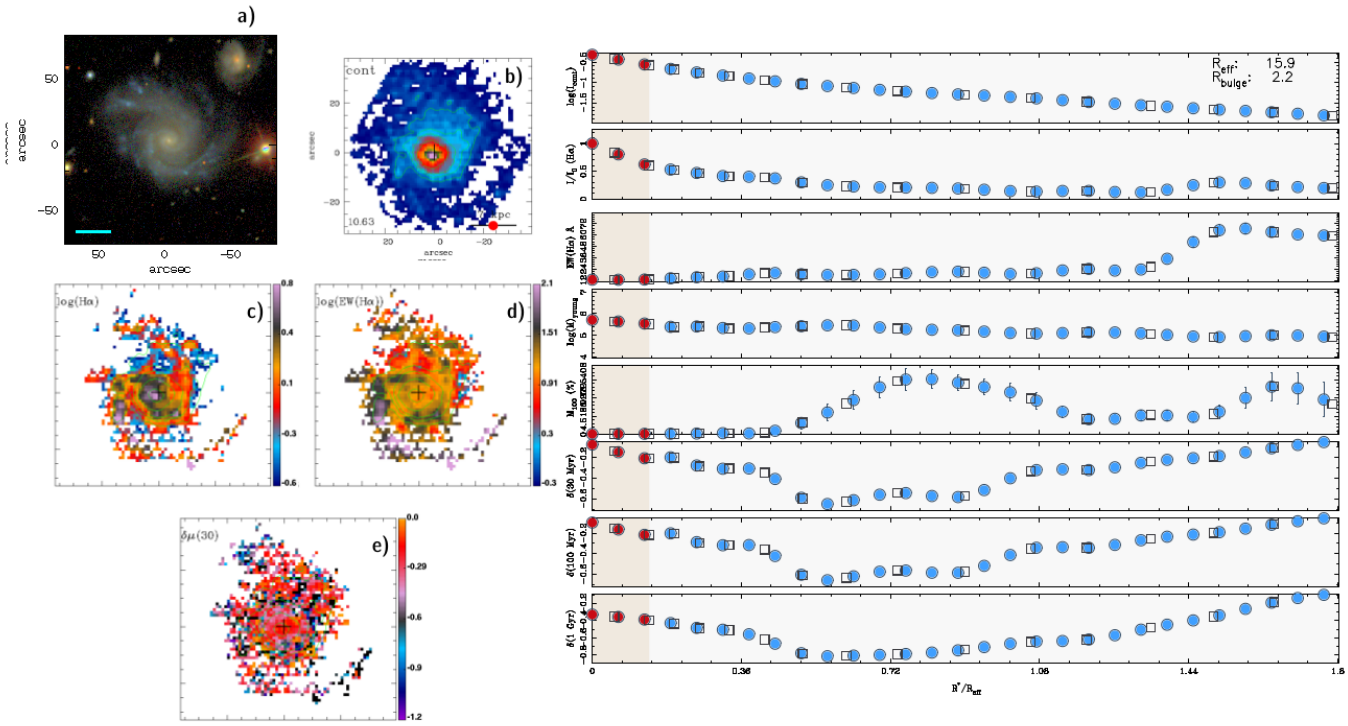

Figure A.41: Maps and radial profiles of NGC5829.

NGC6004

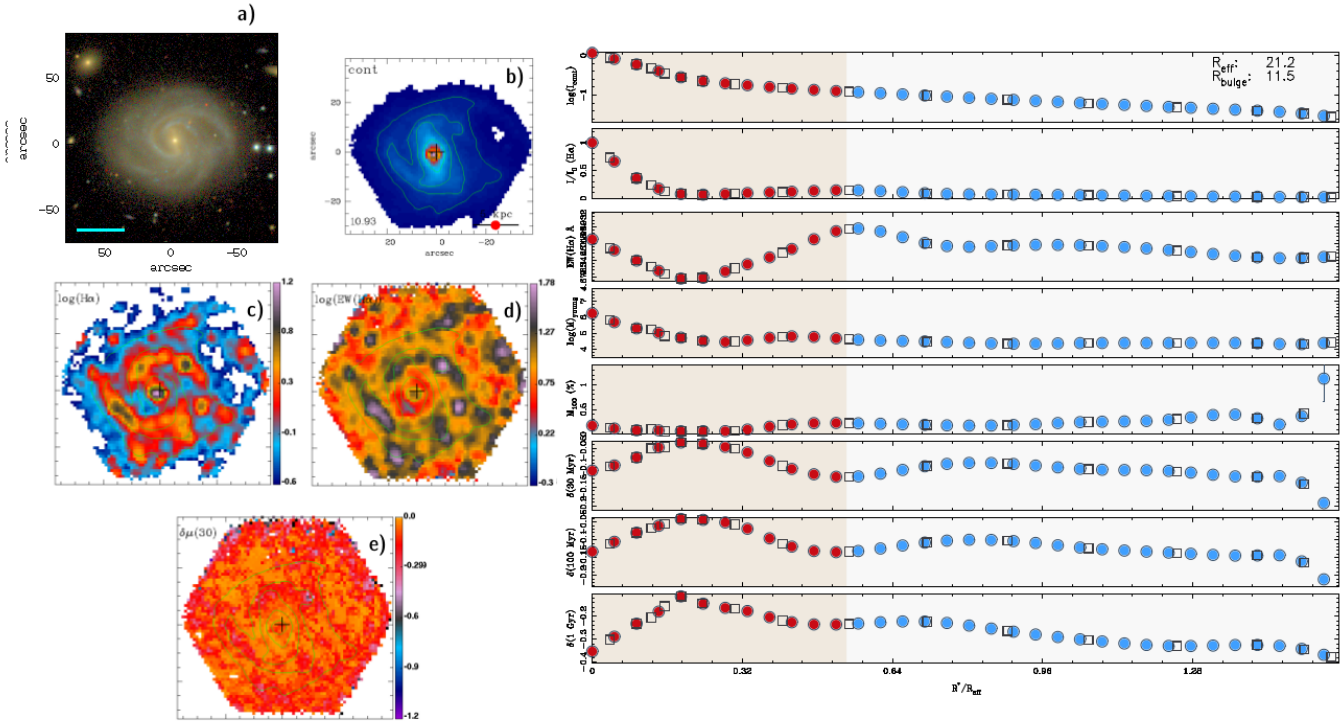

Figure A.42: Maps and radial profiles of NGC6004.

NGC6032

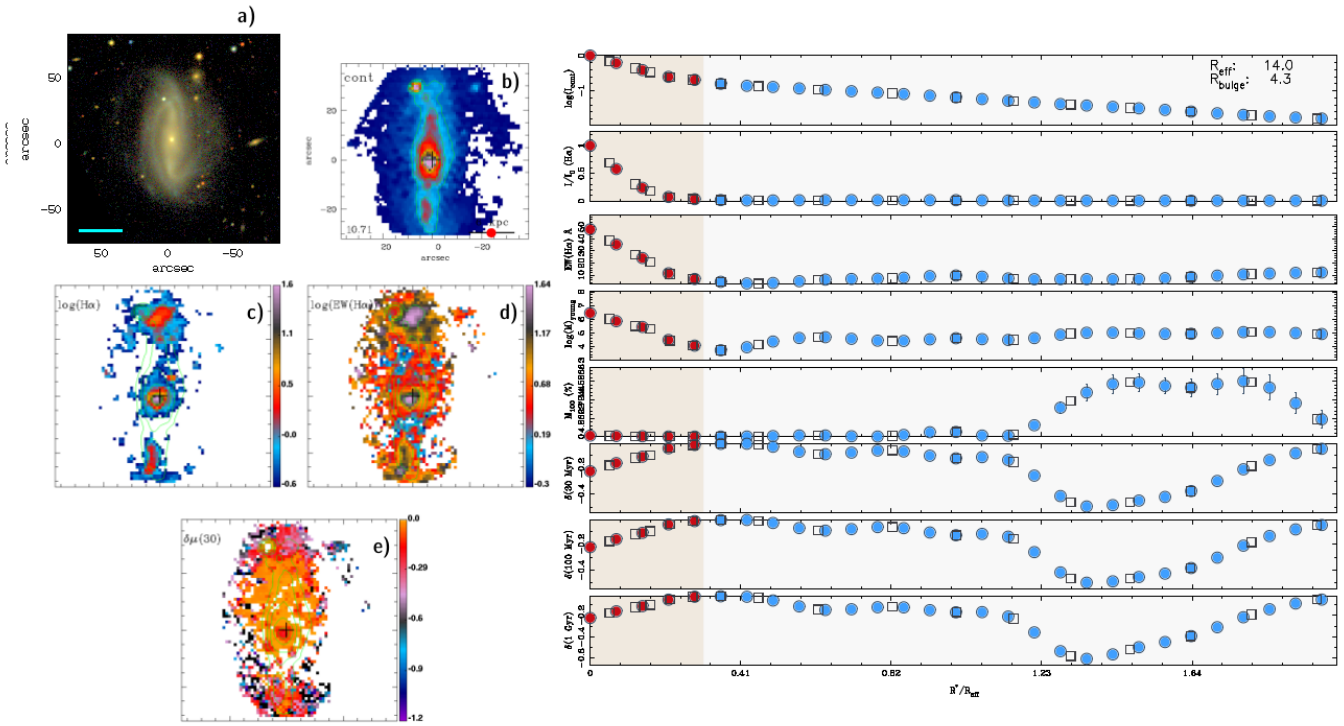

Figure A.43: Maps and radial profiles of NGC6032.

NGC6186

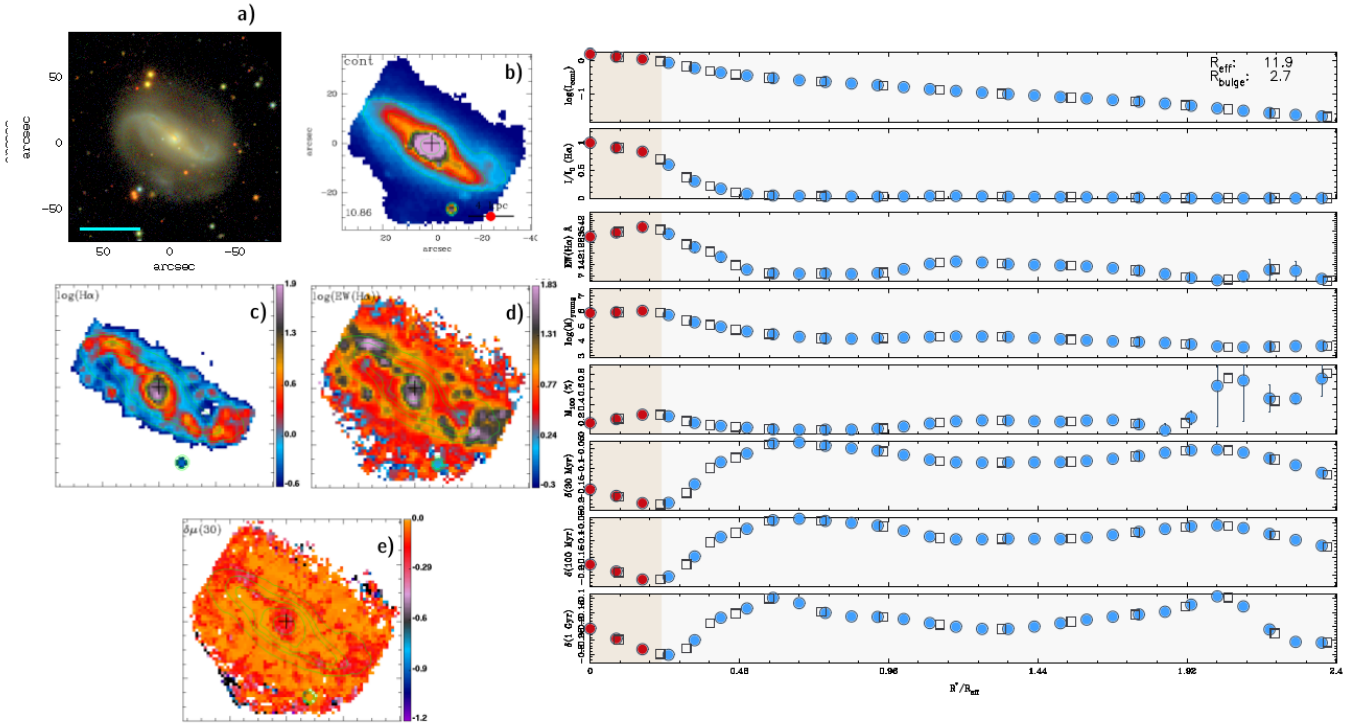

Figure A.44: Maps and radial profiles of NGC6186.

NGC6278

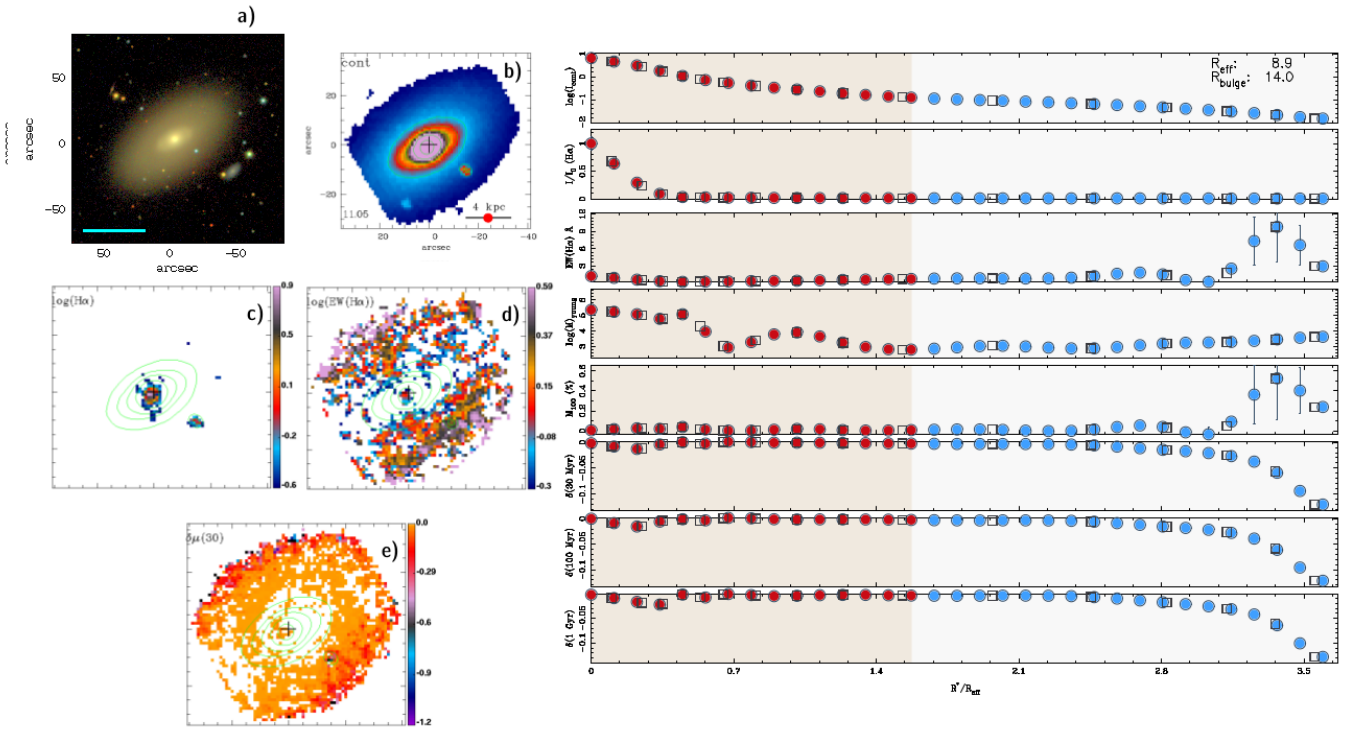

Figure A.45: Maps and radial profiles of NGC6278.

NGC6941

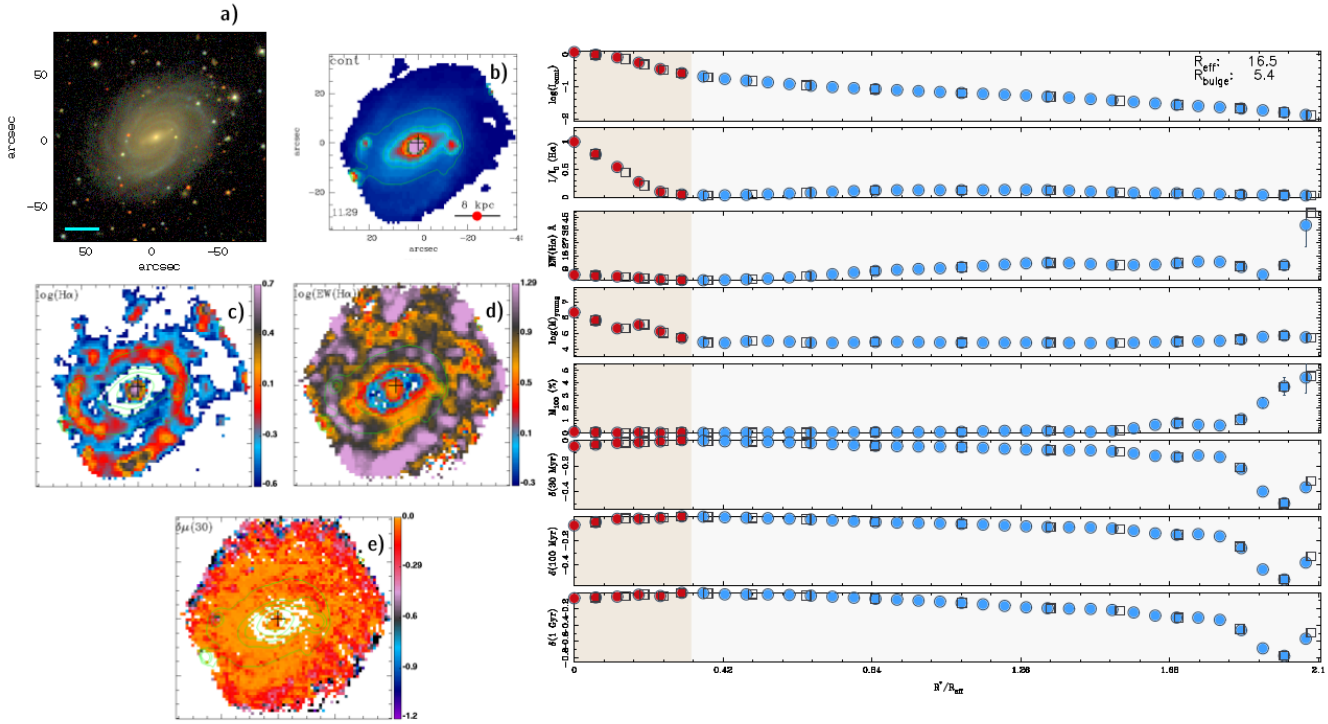

Figure A.46: Maps and radial profiles of NGC6941.

NGC7321

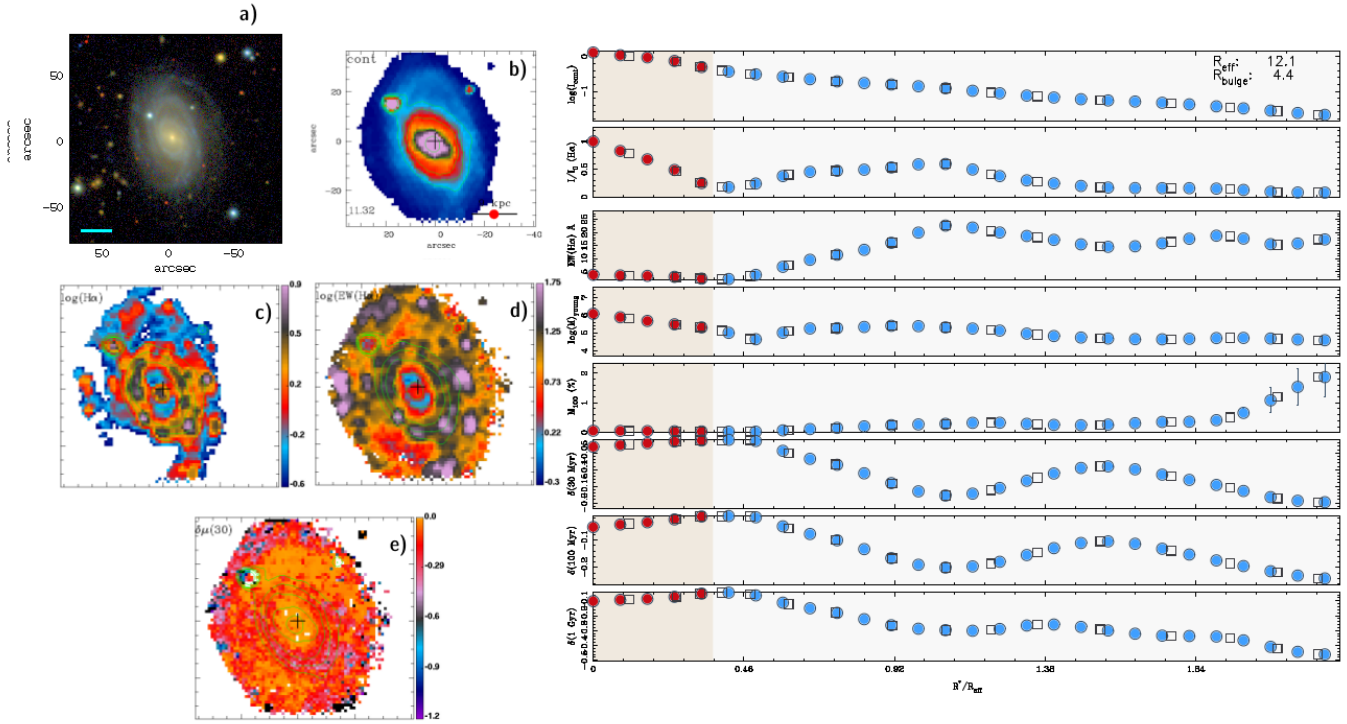

Figure A.47: Maps and radial profiles of NGC7321.

NGC7489

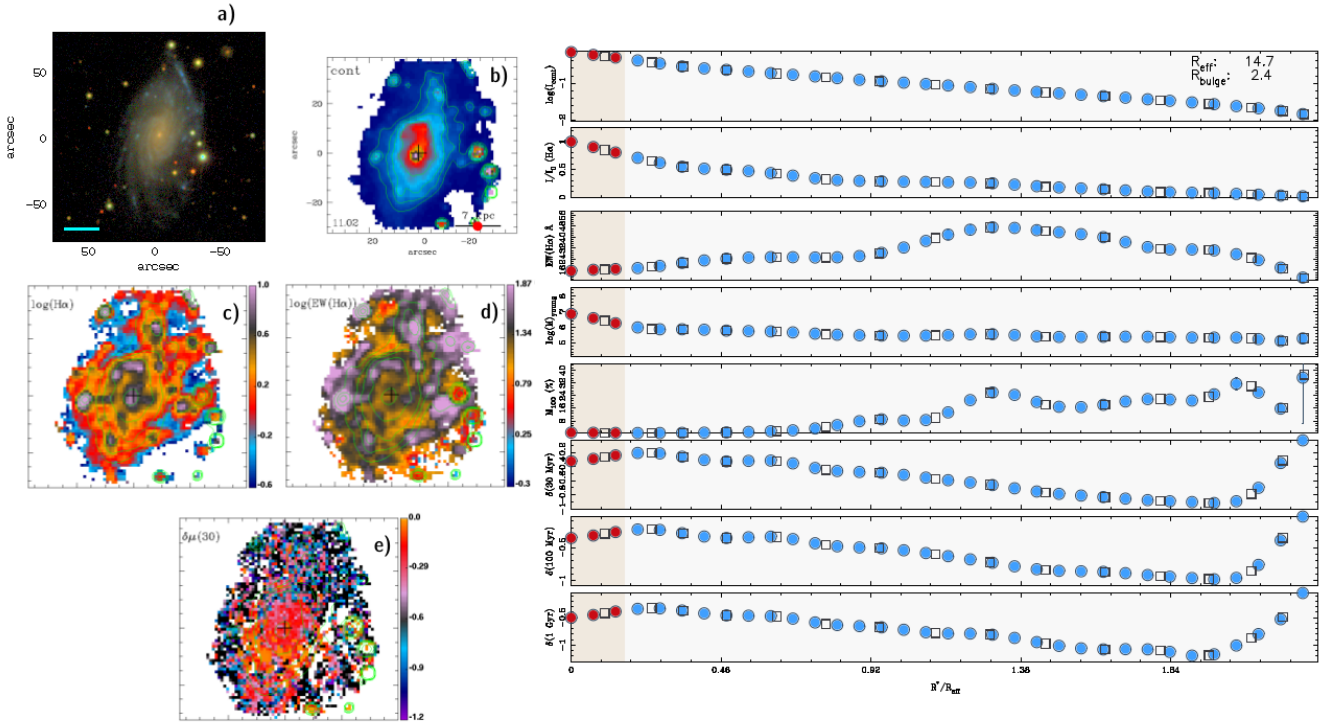

Figure A.48: Maps and radial profiles of NGC7489.

NGC7625

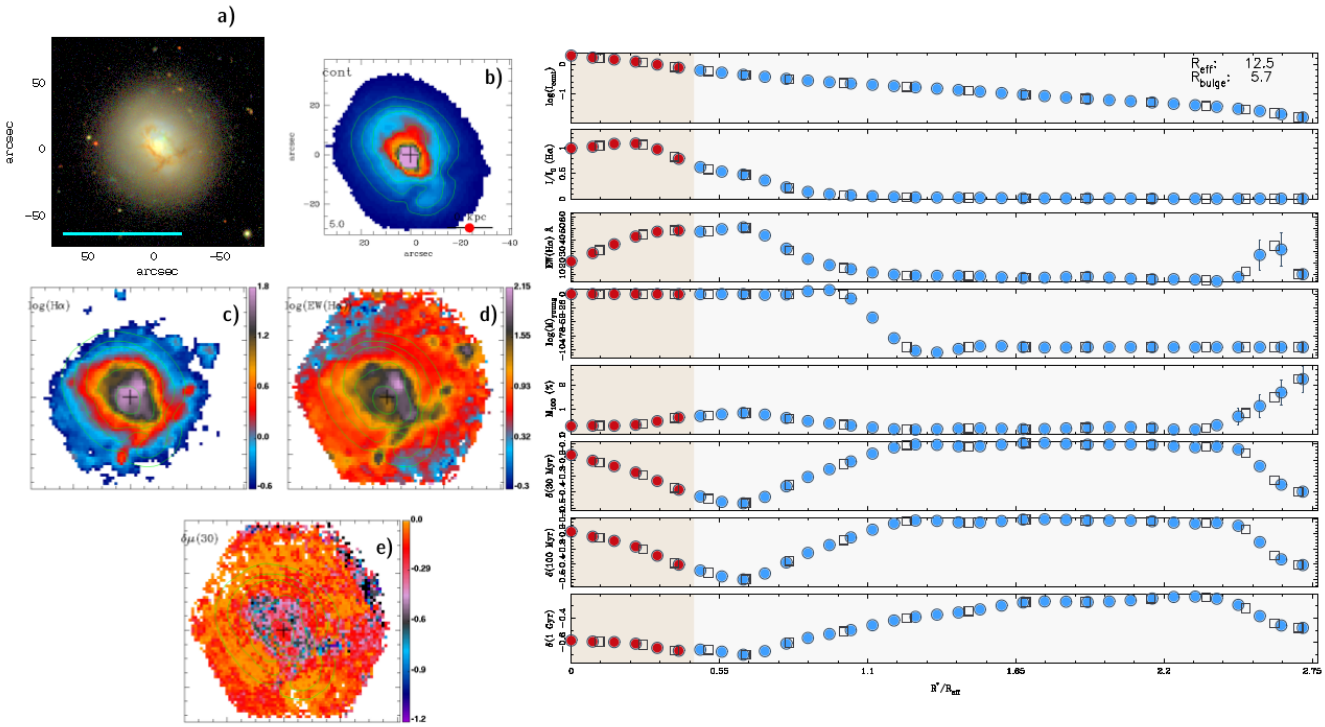

Figure A.49: Maps and radial profiles of NGC7625.

NGC7653

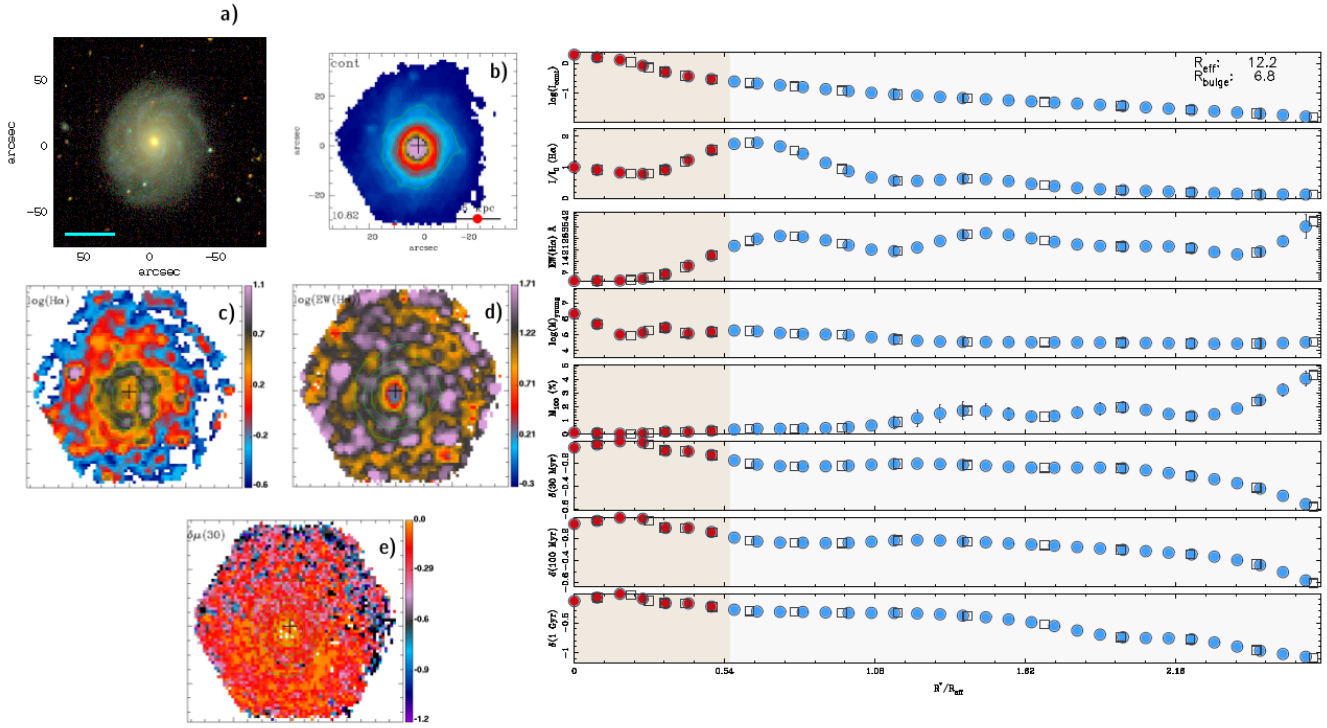

Figure A.50: Maps and radial profiles of NGC7653.

NGC7691

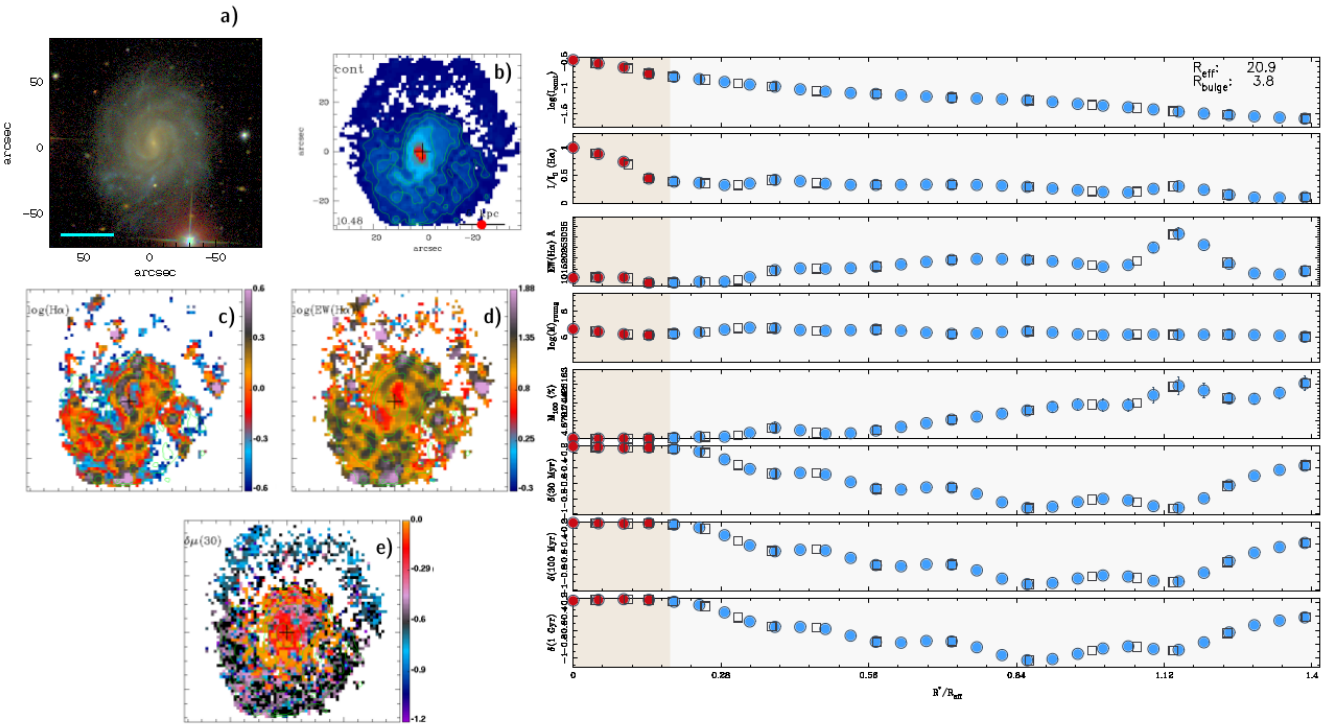

Figure A.51: Maps and radial profiles of NGC7691.

NGC7716

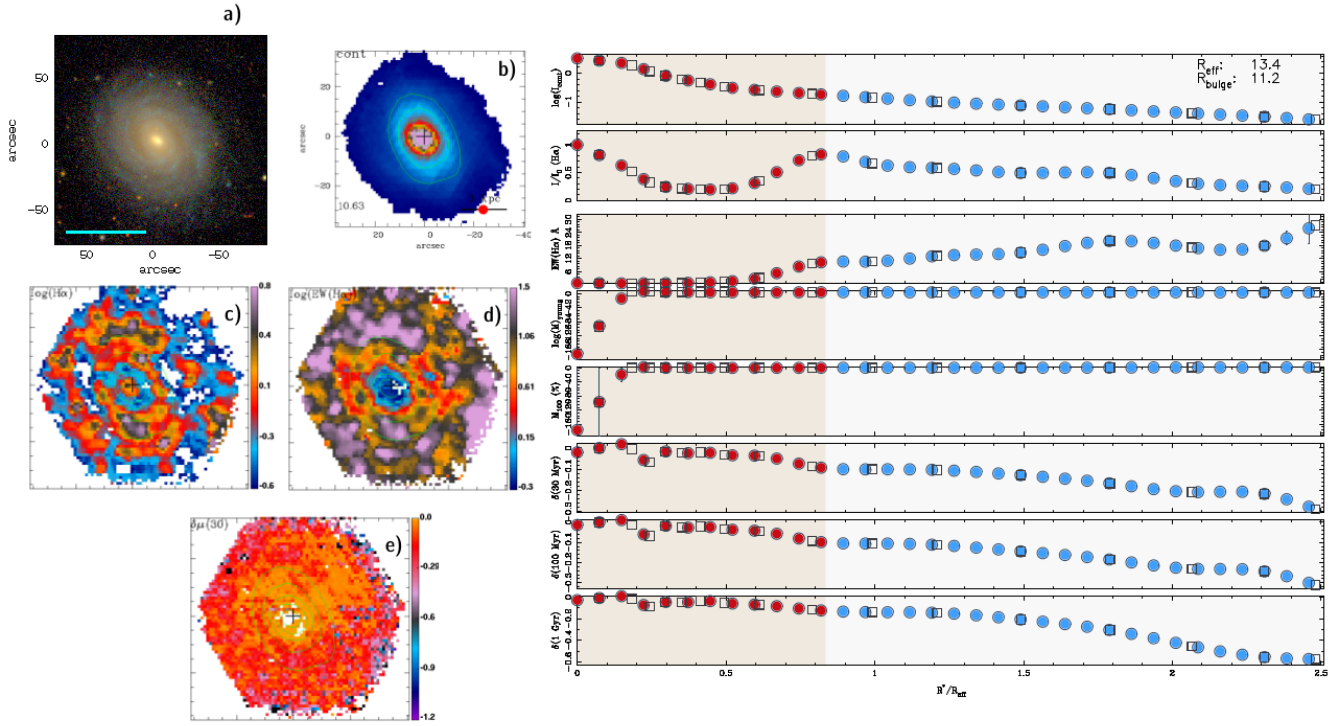

Figure A.52: Maps and radial profiles of NGC7716.

NGC7738

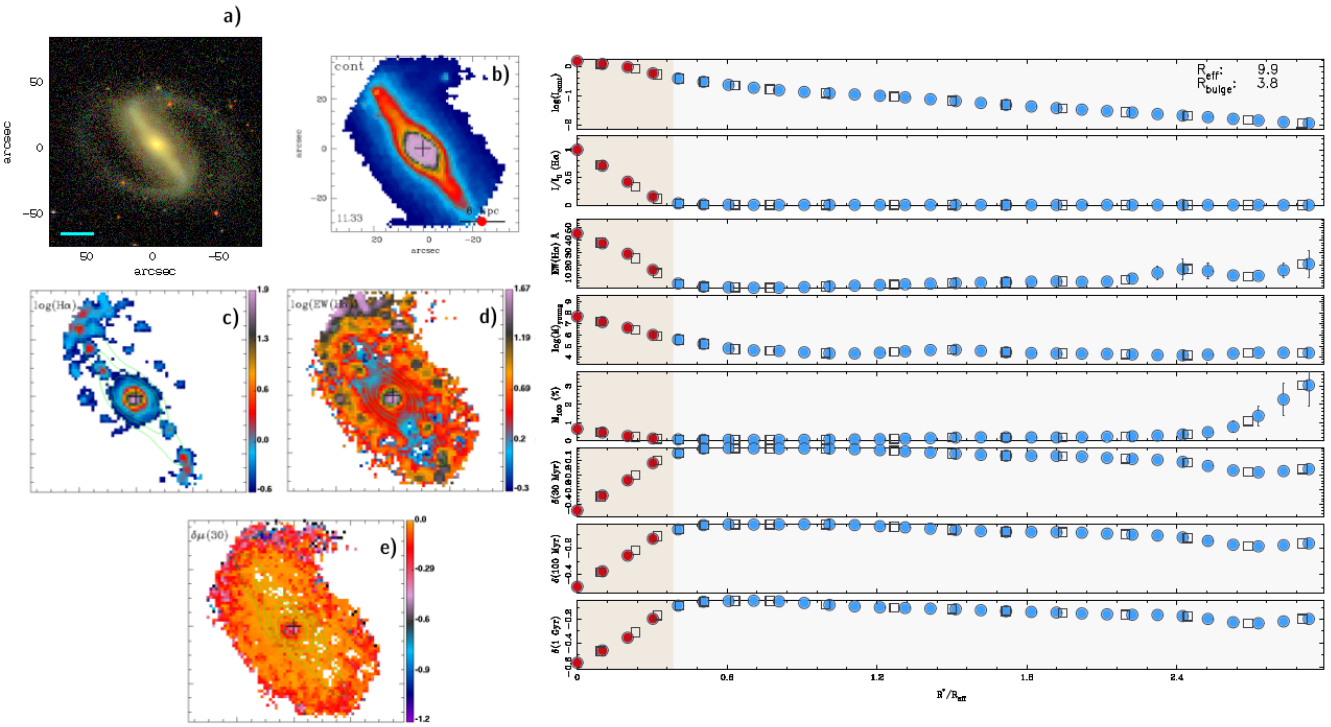

Figure A.53: Maps and radial profiles of NGC7738.

NGC7819

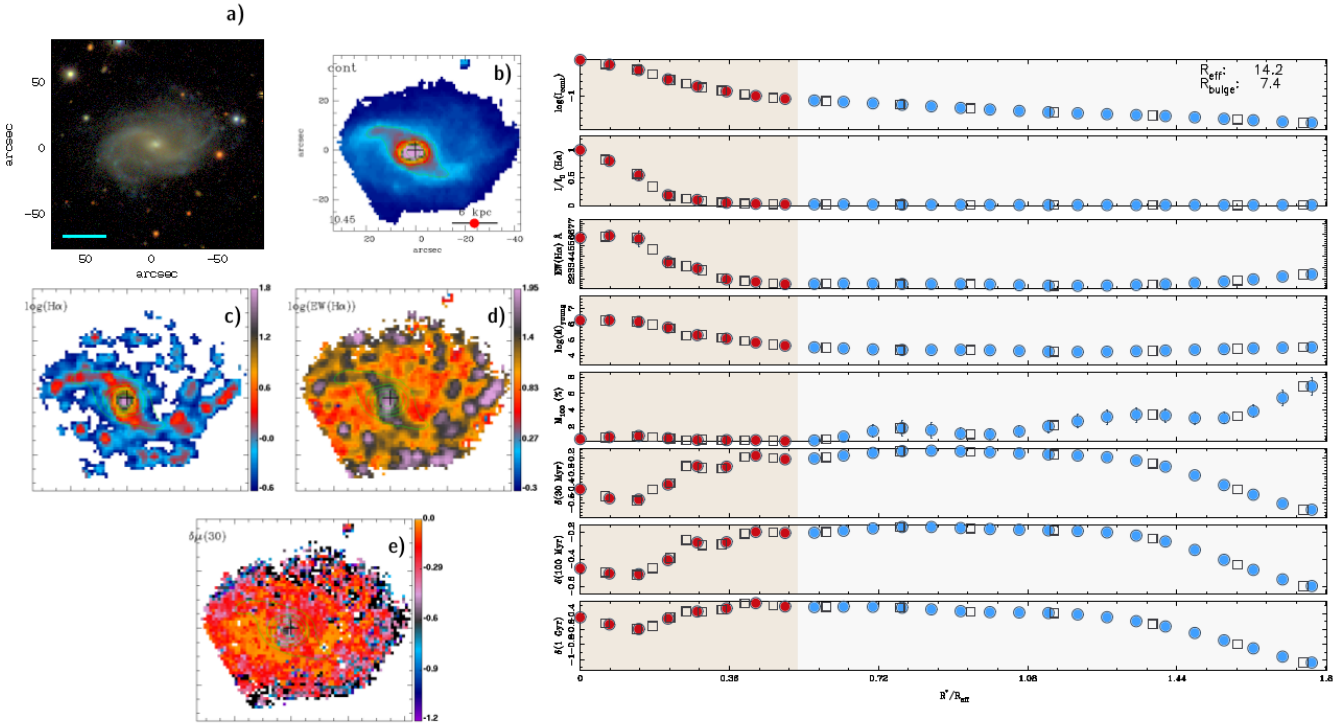

Figure A.54: Maps and radial profiles of NGC7819.

UGC07012

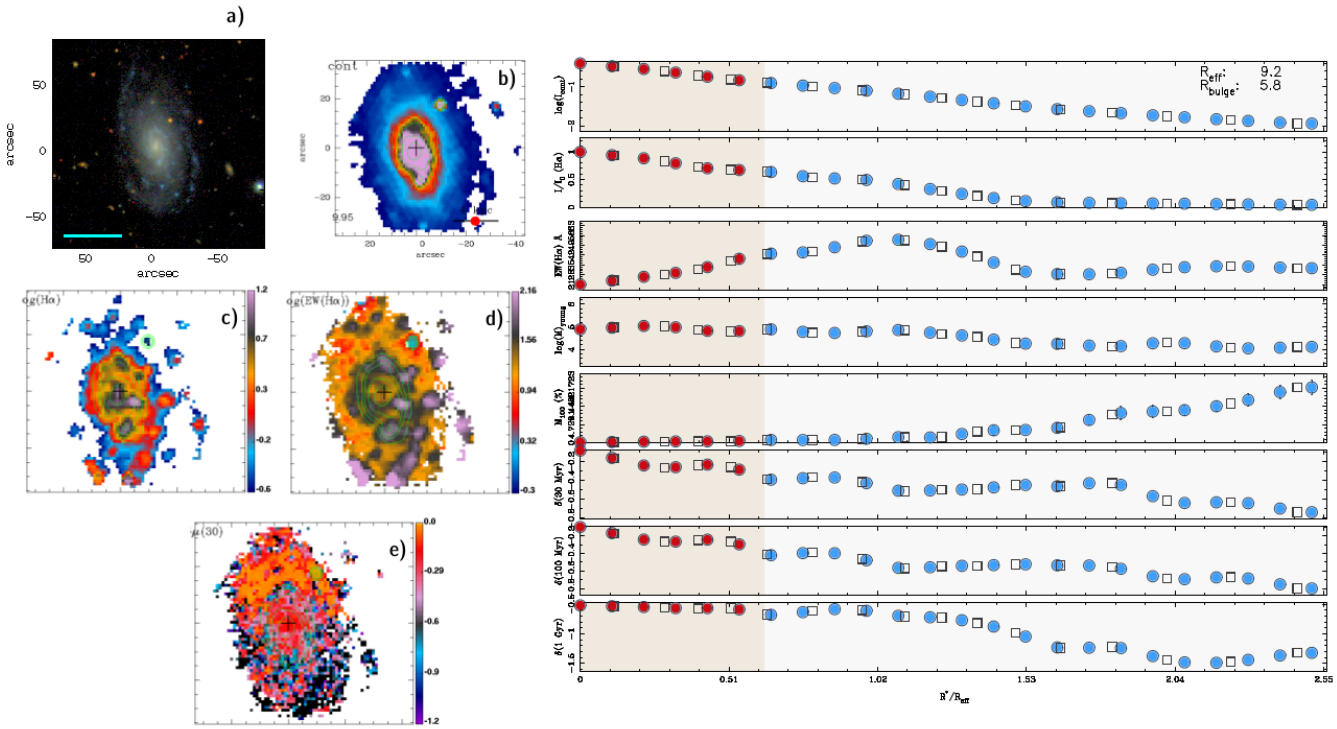

Figure A.55: Maps and radial profiles of UGC07012.

UGC08234

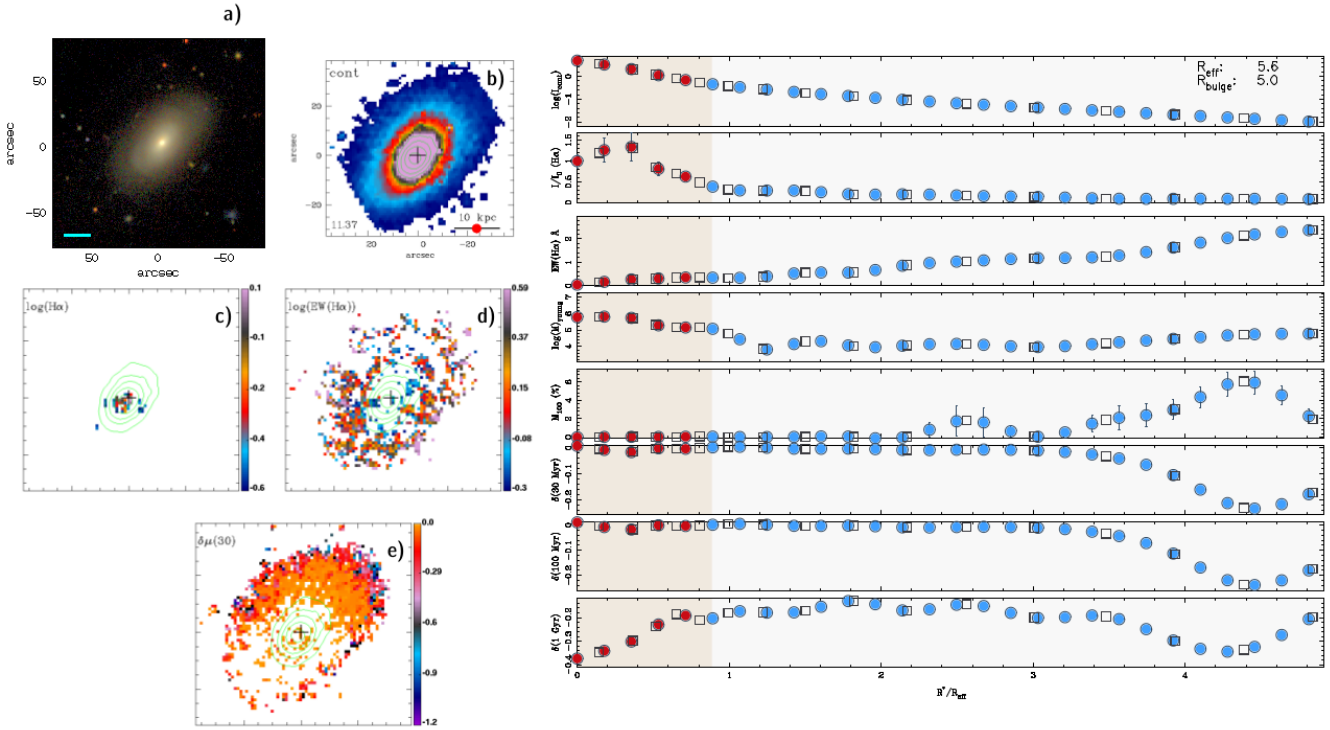

Figure A.56: Maps and radial profiles of UGC08234.

UGC08733

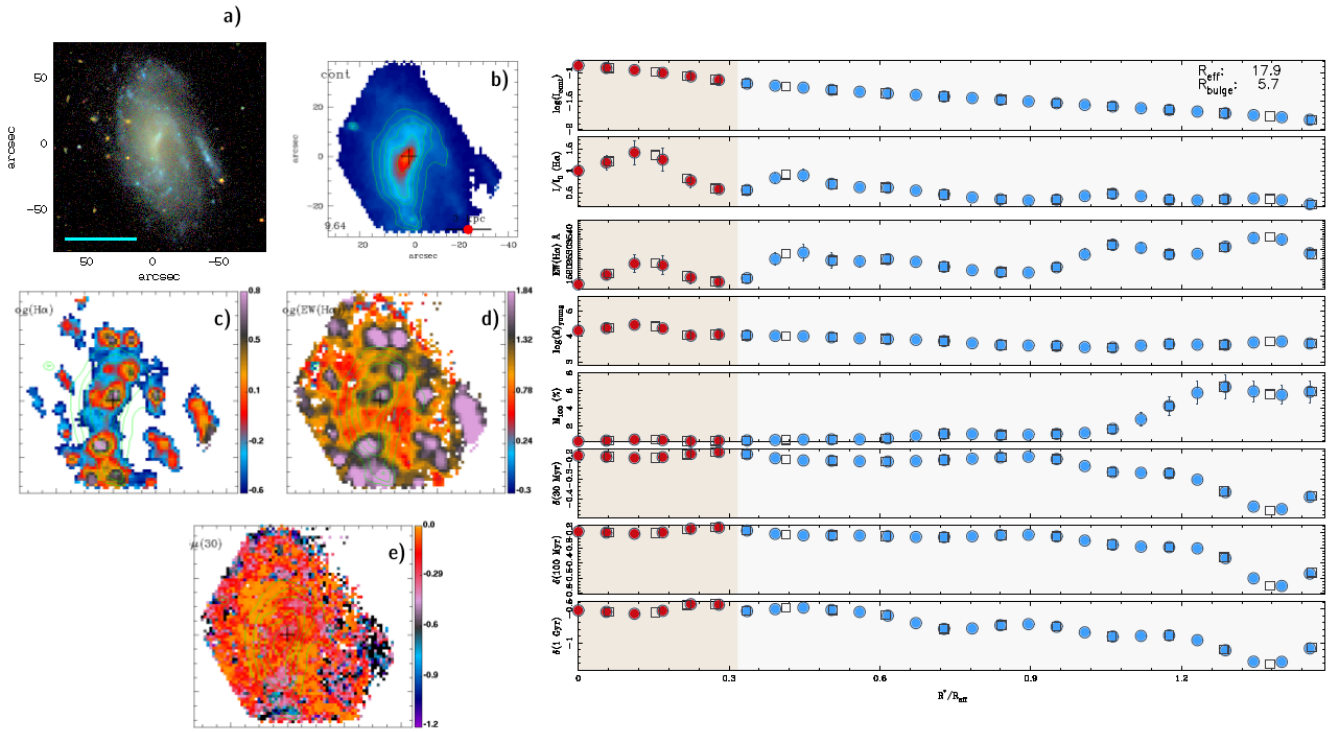

Figure A.57: Maps and radial profiles of UGC08733.

UGC09067

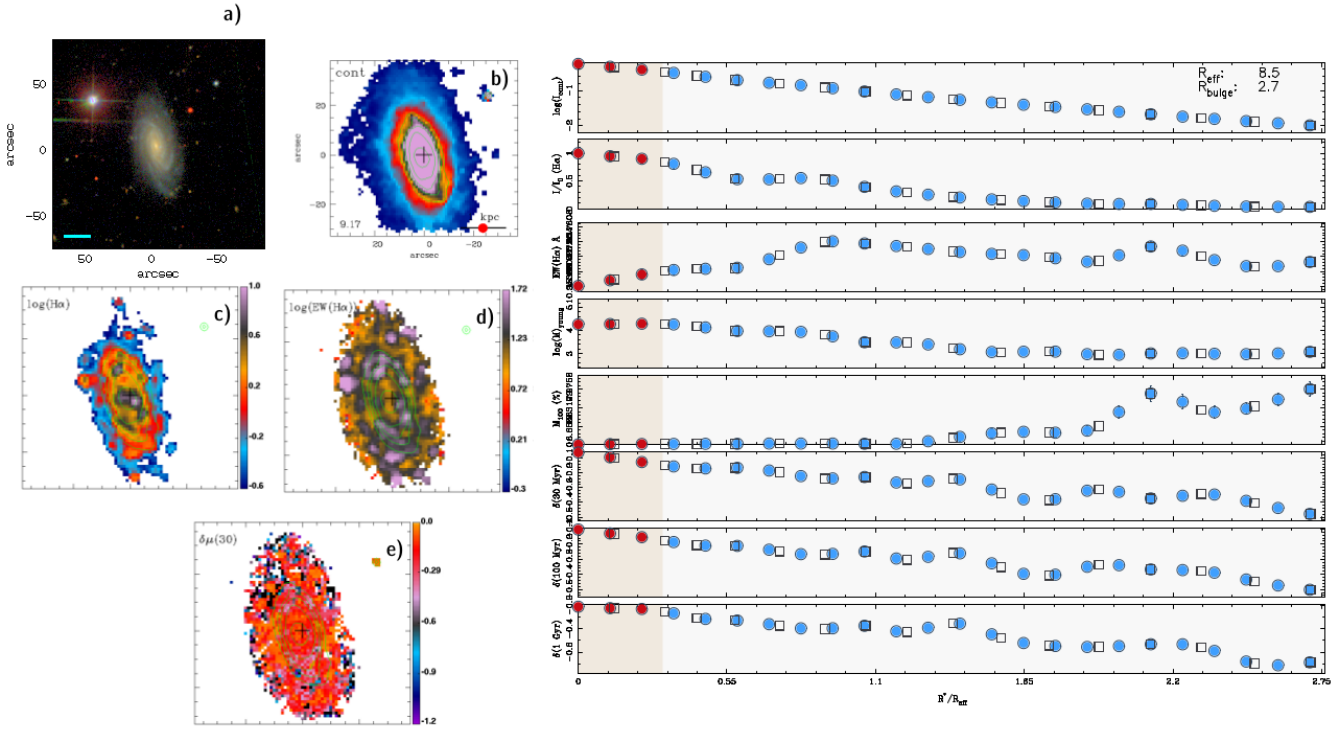

Figure A.58: Maps and radial profiles of UGC09067.

UGC09291

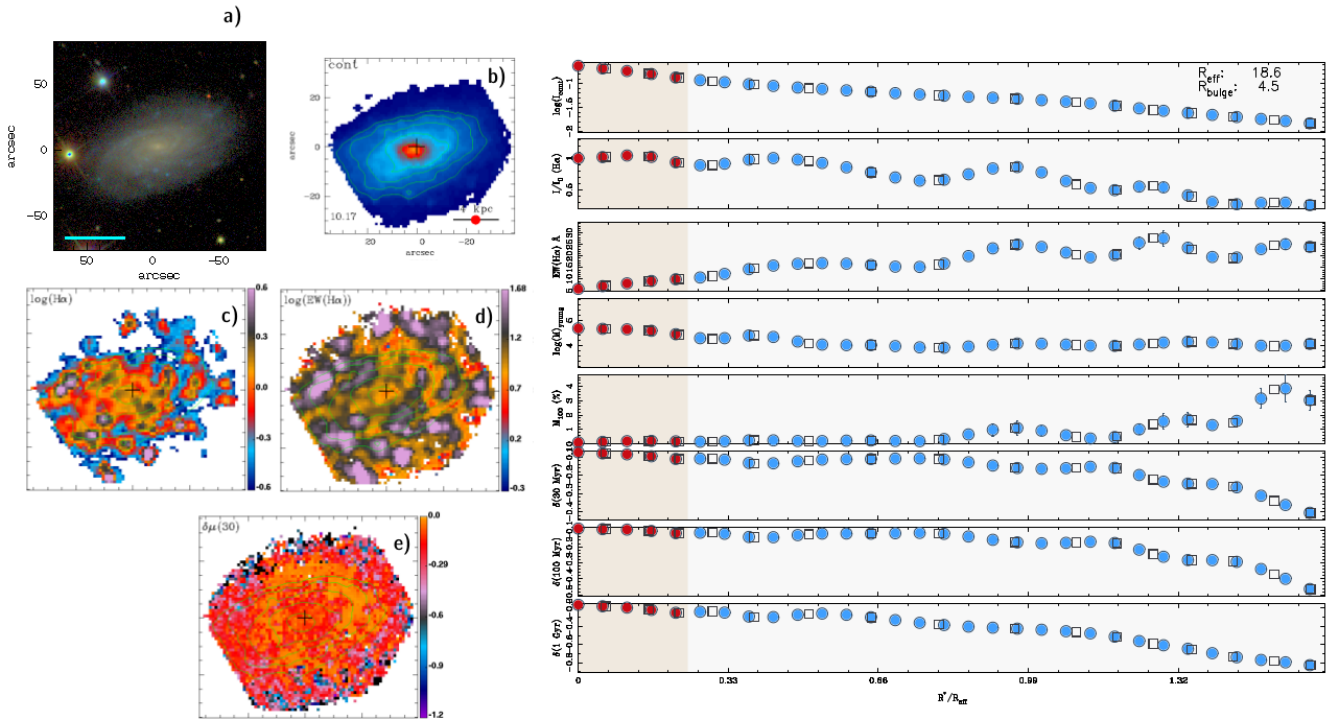

Figure A.59: Maps and radial profiles of UGC09291.

UGC09476

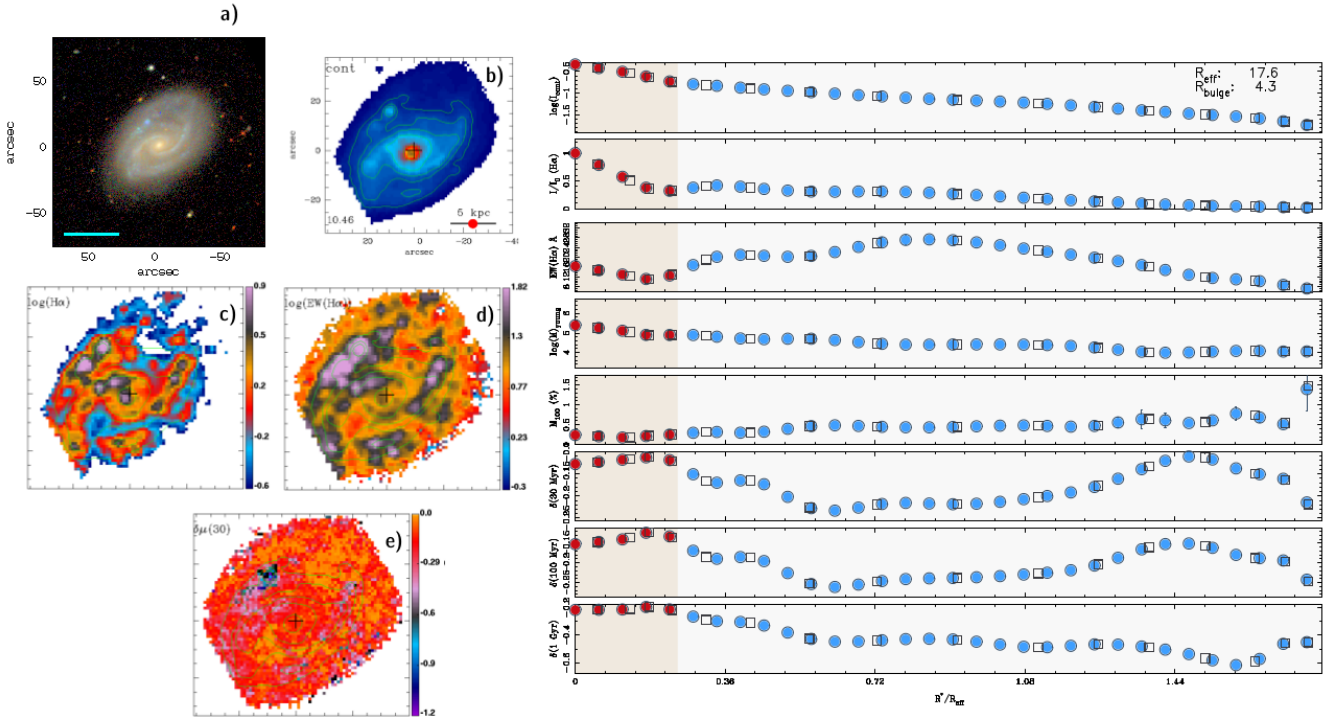

Figure A.60: Maps and radial profiles of UGC09476.

UGC12224

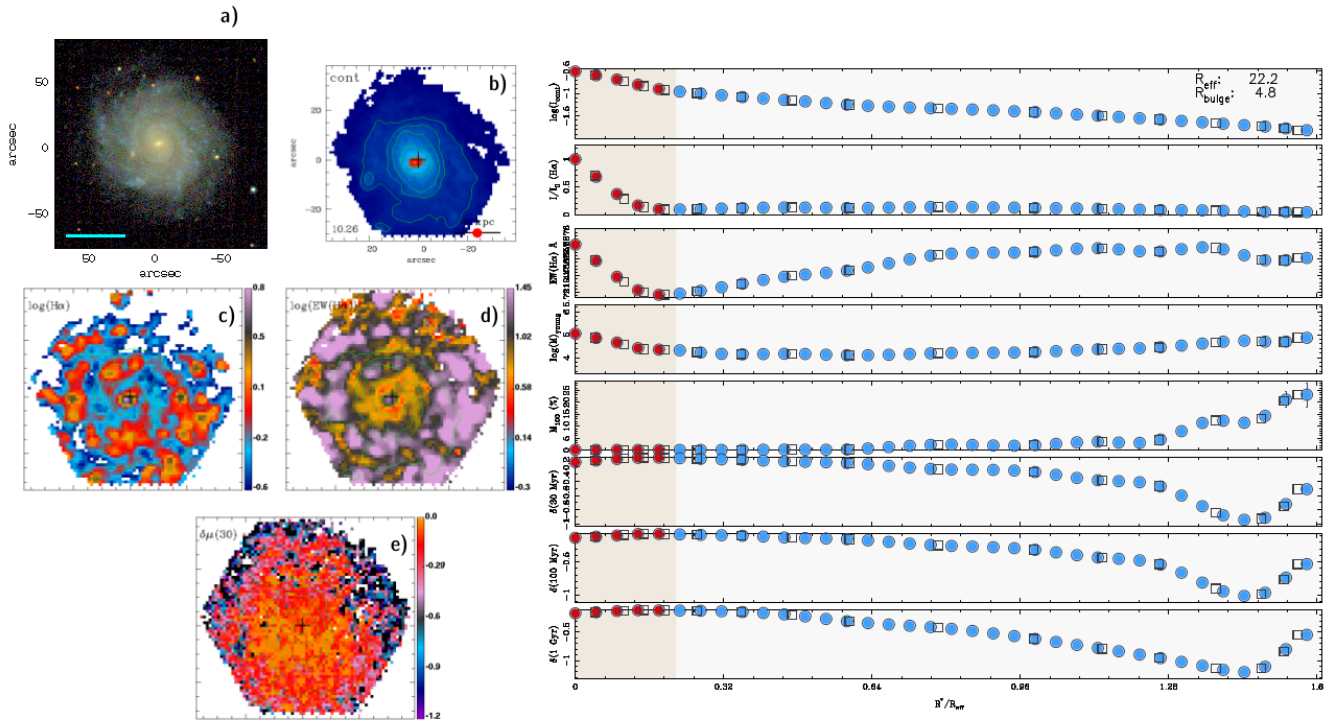

Figure A.61: Maps and radial profiles of UGC12224.

Appendices

Appendix B.

SBP Decomposition

IC0776

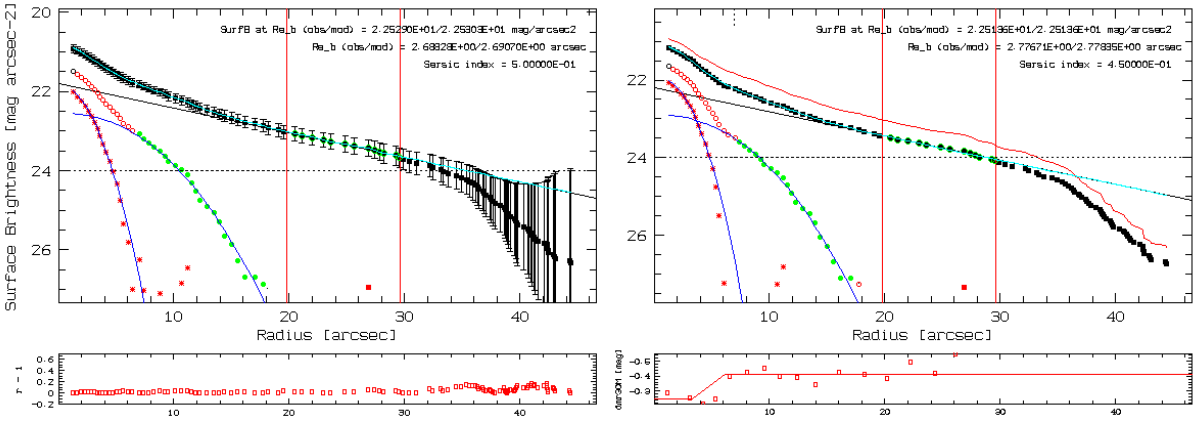

Figure B.1: Photometric decomposition of IC0776.

IC4566

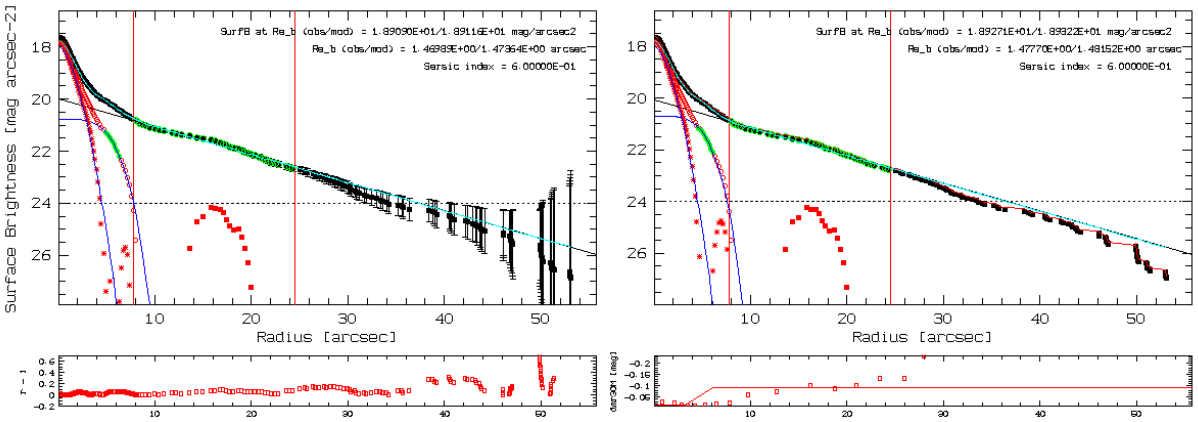

Figure B.2: Photometric decomposition of IC4566.

NGC0001

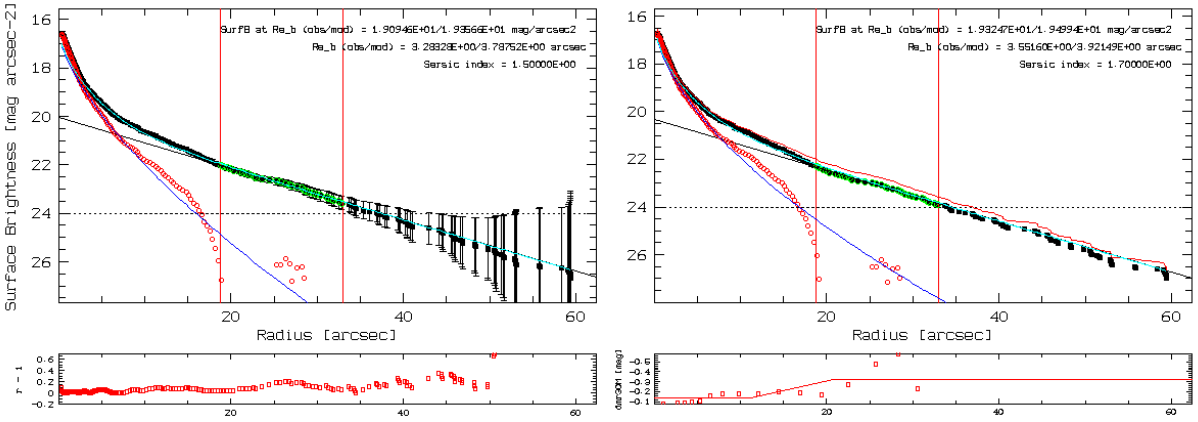

Figure B.3: Photometric decomposition of NGC0001.

NGC0160

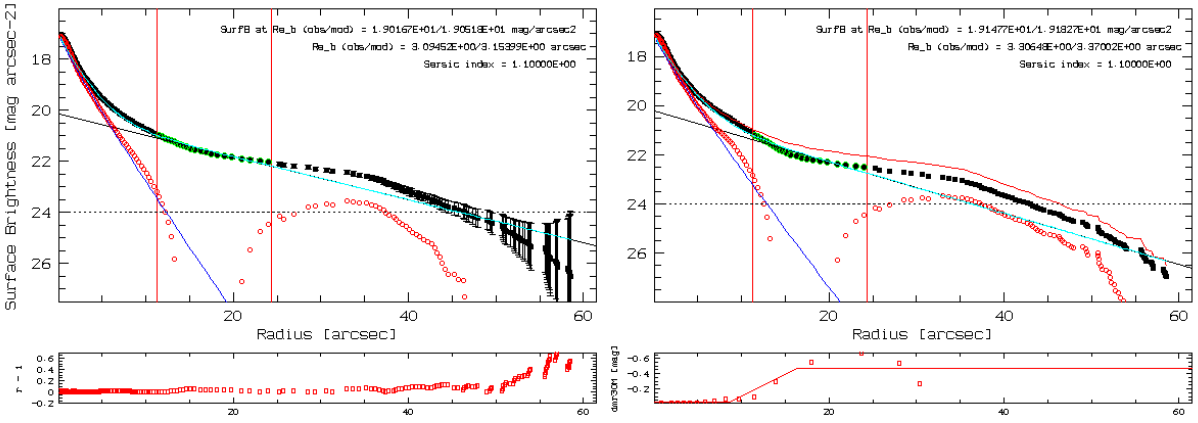

Figure B.4: Photometric decomposition of NGC0160.

NGC0165

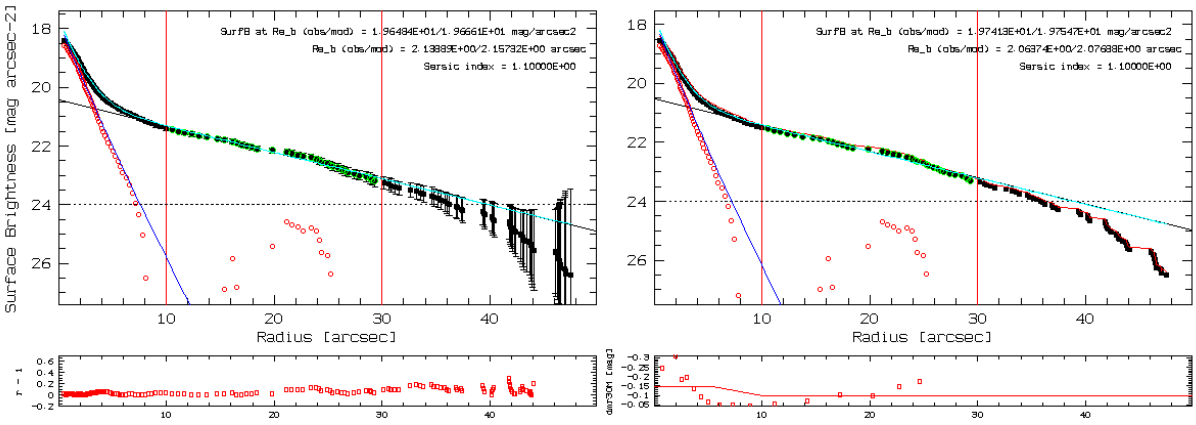

Figure B.5: Photometric decomposition of NGC0165.

NGC0171

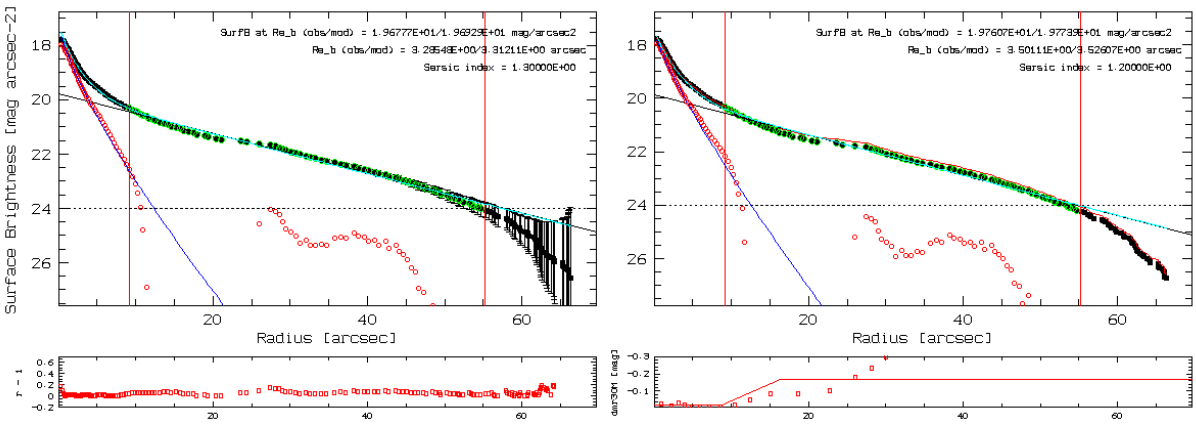

Figure B.6: Photometric decomposition of NGC0171.

NGC0180

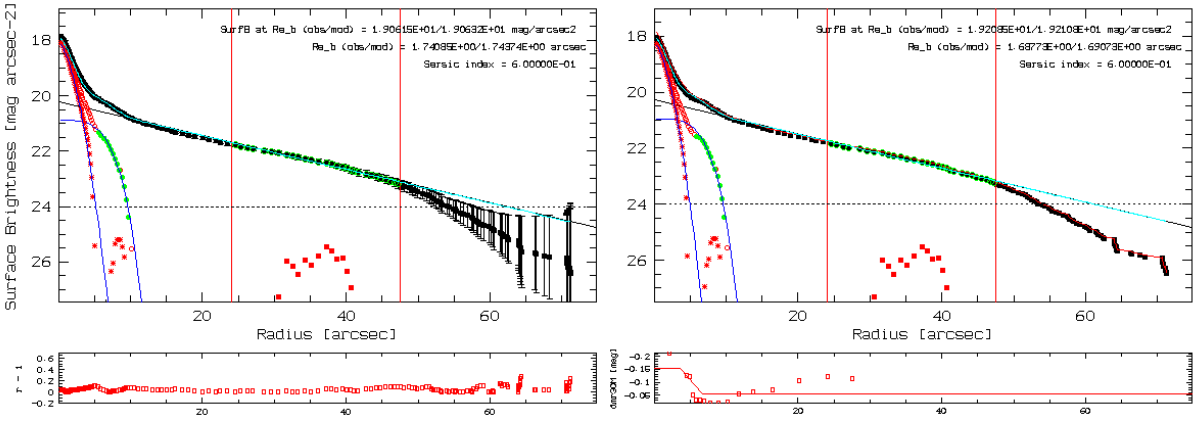

Figure B.7: Photometric decomposition of NGC0180.

NGC0214

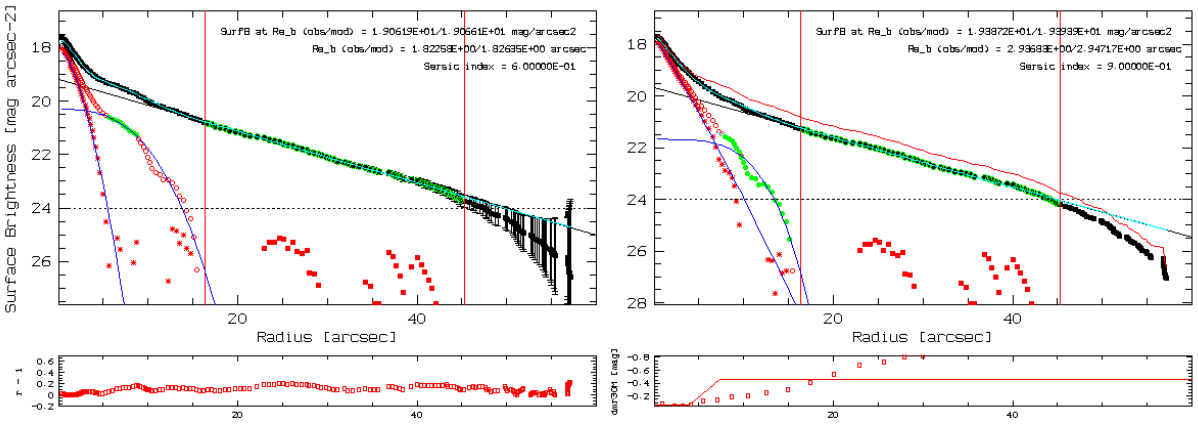

Figure B.8: Photometric decomposition of NGC0214.

NGC0237

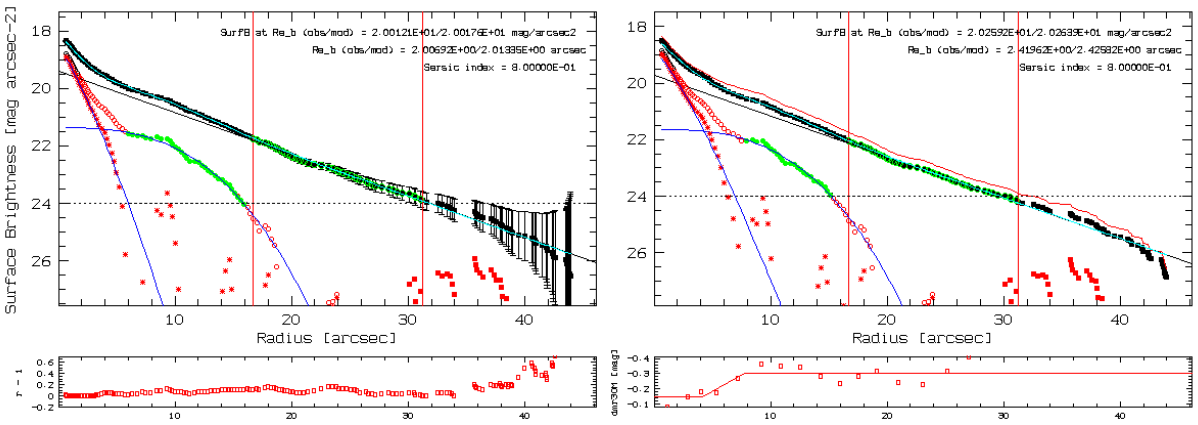

Figure B.9: Photometric decomposition of NGC0237.

NGC0257

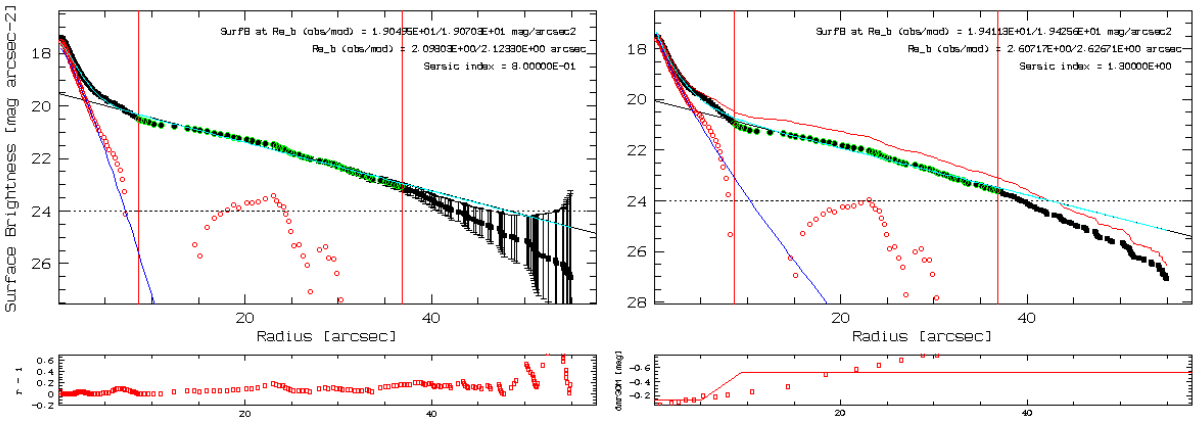

Figure B.10: Photometric decomposition of NGC0257.

NGC0477

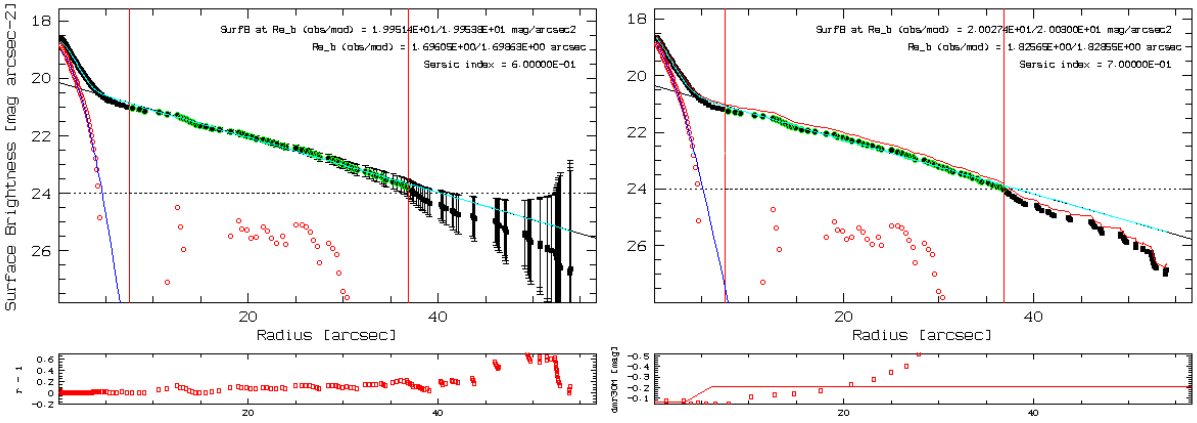

Figure B.11: Photometric decomposition of NGC0477.

NGC0776

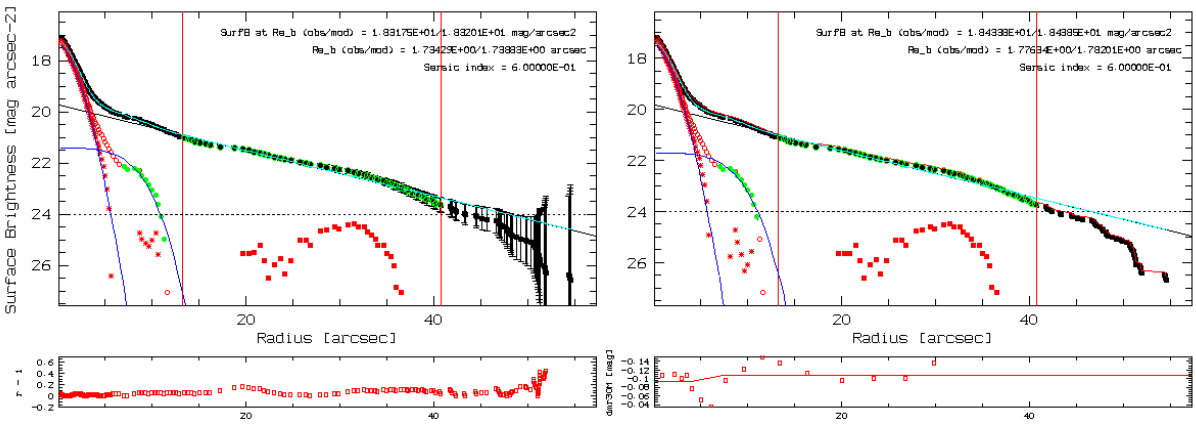

Figure B.12: Photometric decomposition of NGC0776.

NGC1093

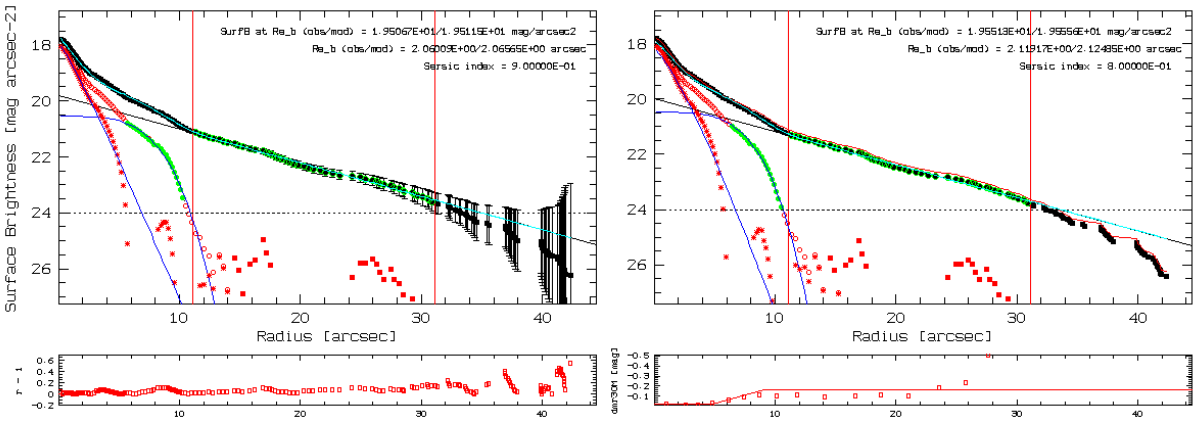

Figure B.13: Photometric decomposition of NGC1093.

NGC1645

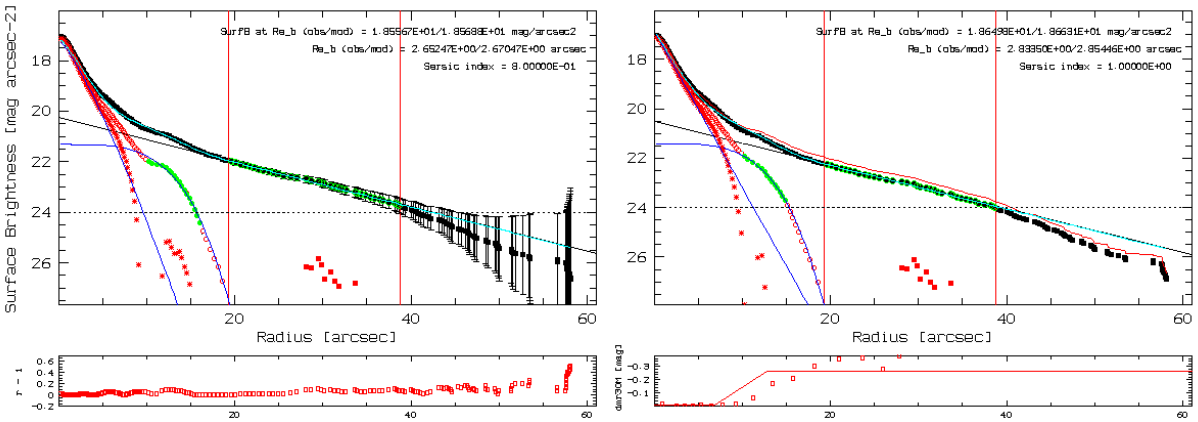

Figure B.14: Photometric decomposition of NGC1645.

NGC2253

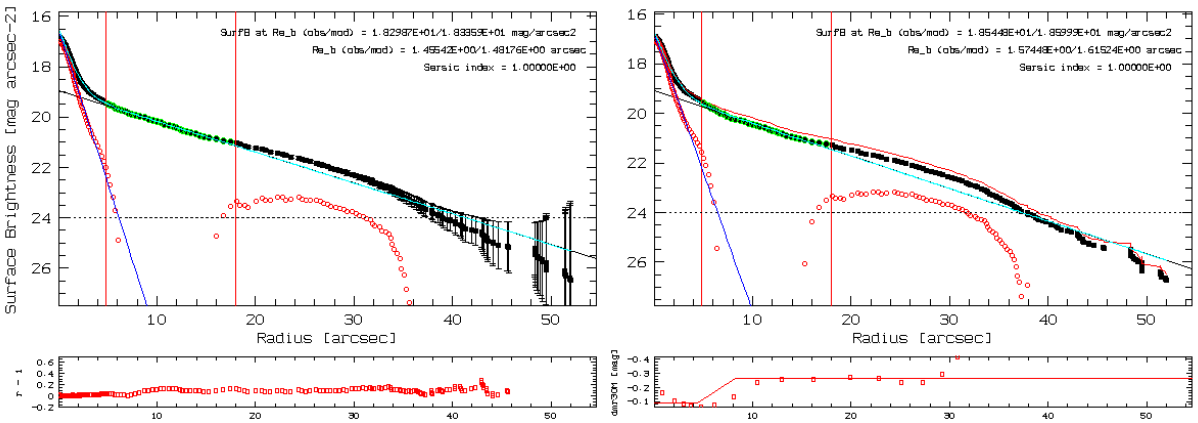

Figure B.15: Photometric decomposition of NGC2253.

NGC2347

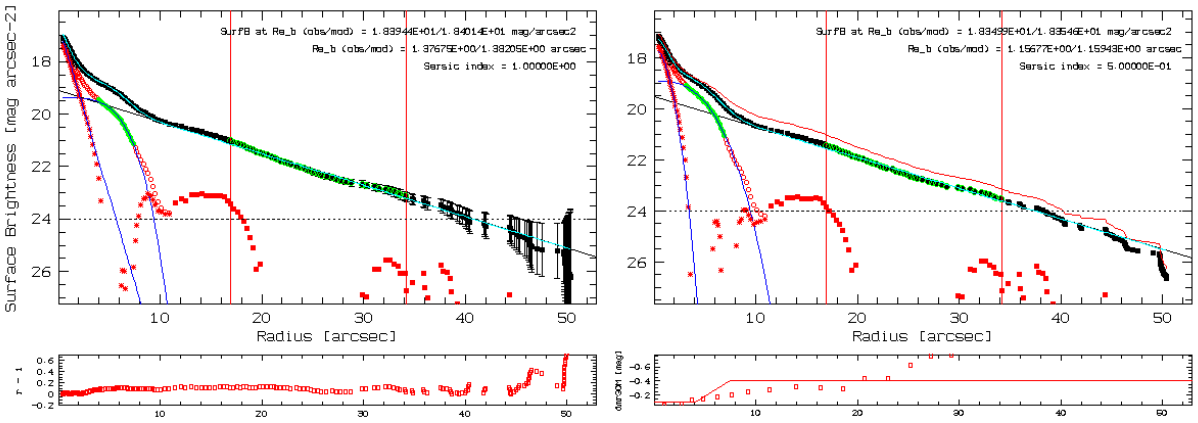

Figure B.16: Photometric decomposition of NGC2347.

NGC2639

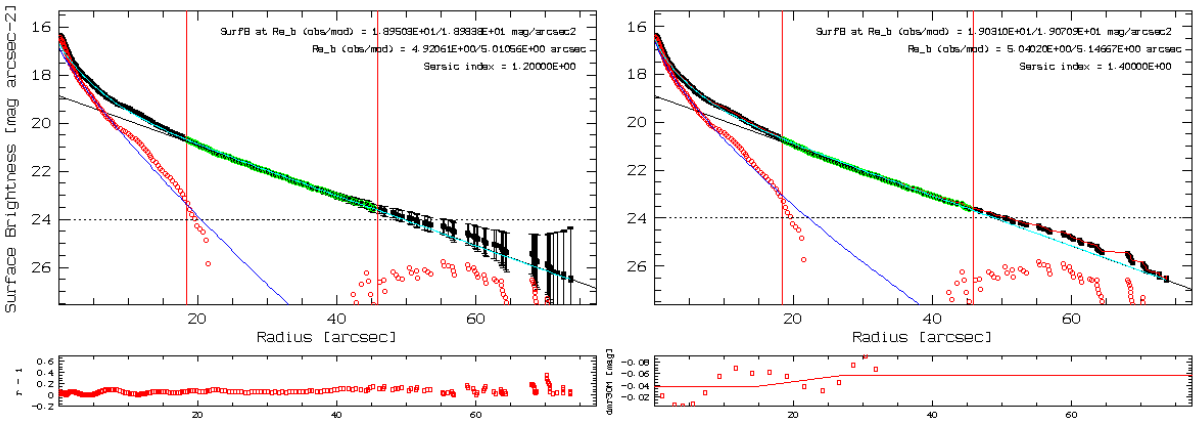

Figure B.17: Photometric decomposition of NGC2639.

NGC2730

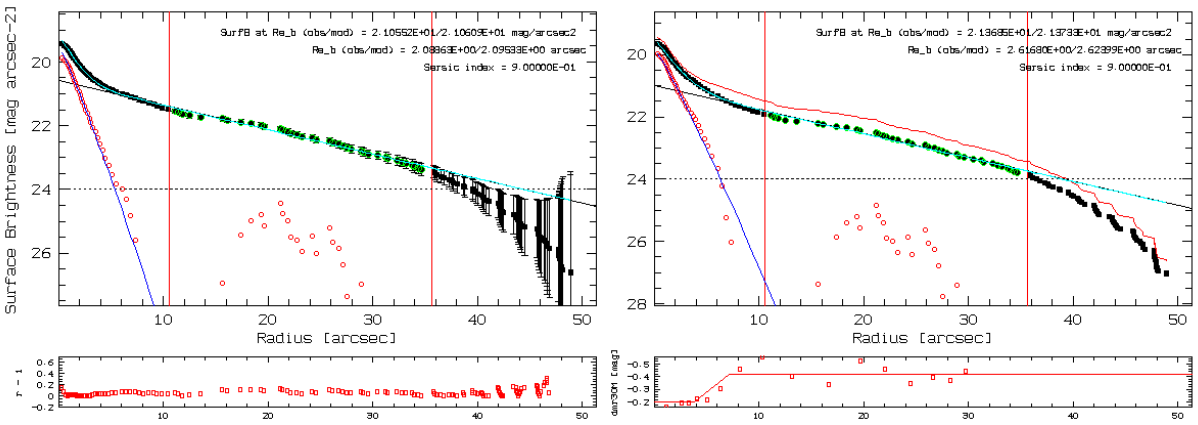

Figure B.18: Photometric decomposition of NGC2730.

NGC2906

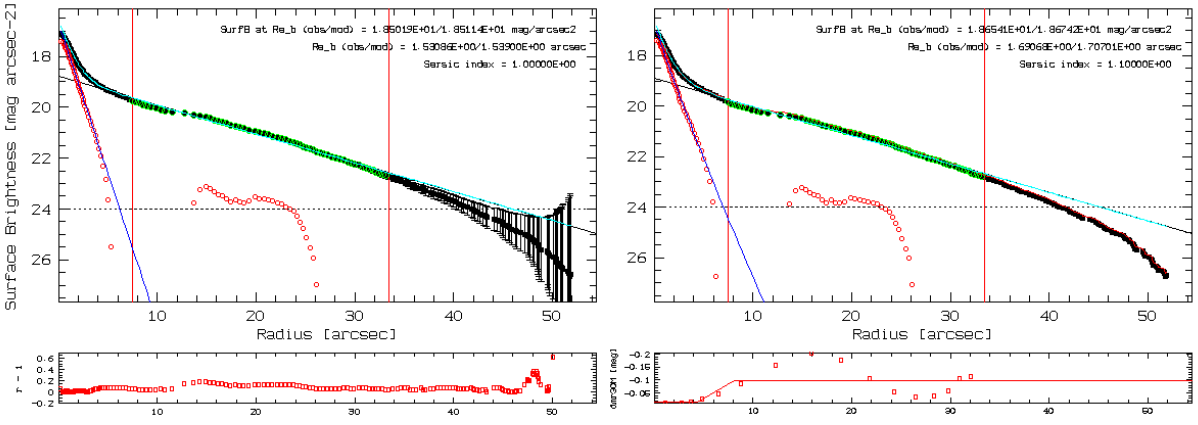

Figure B.19: Photometric decomposition of NGC2906.

NGC2916

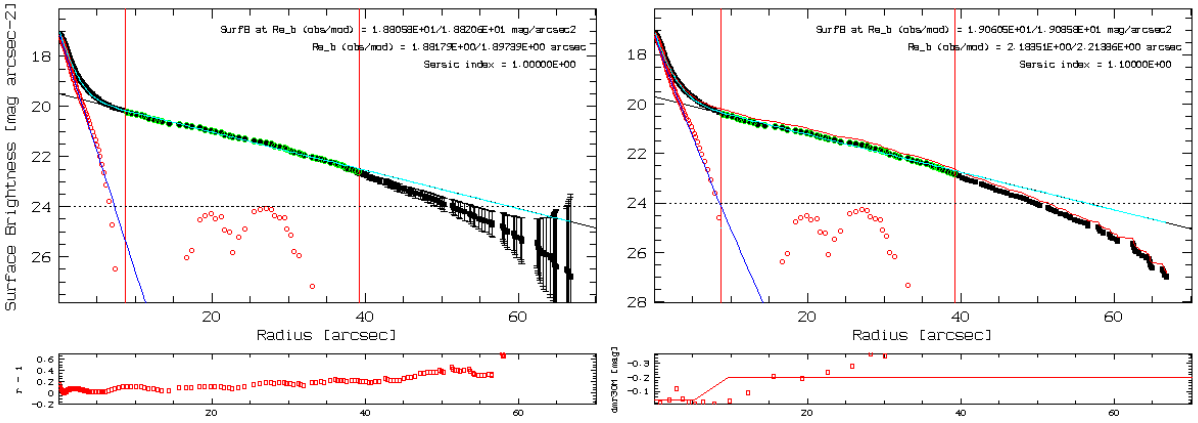

Figure B.20: Photometric decomposition of NGC2916.

NGC3300

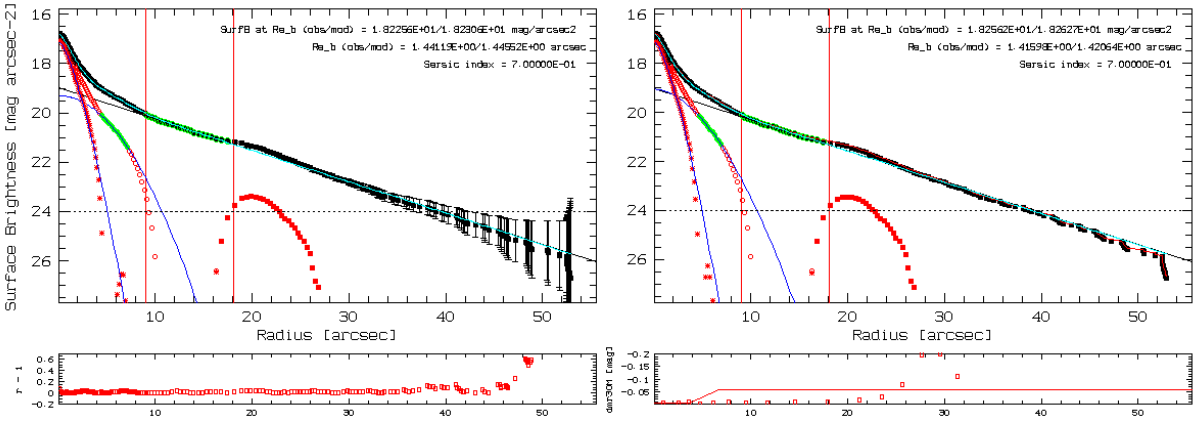

Figure B.21: Photometric decomposition of NGC3300.

NGC3381

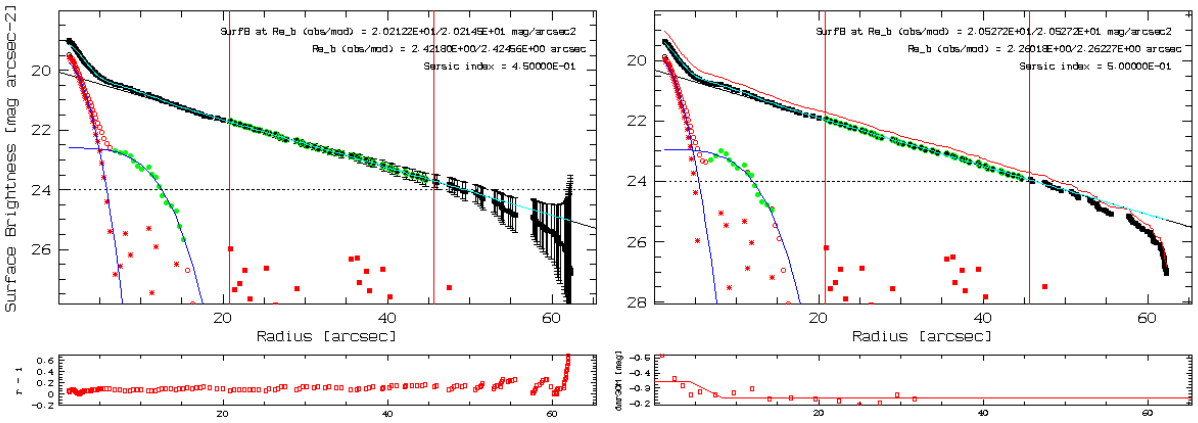

Figure B.22: Photometric decomposition of NGC3381.

NGC3614

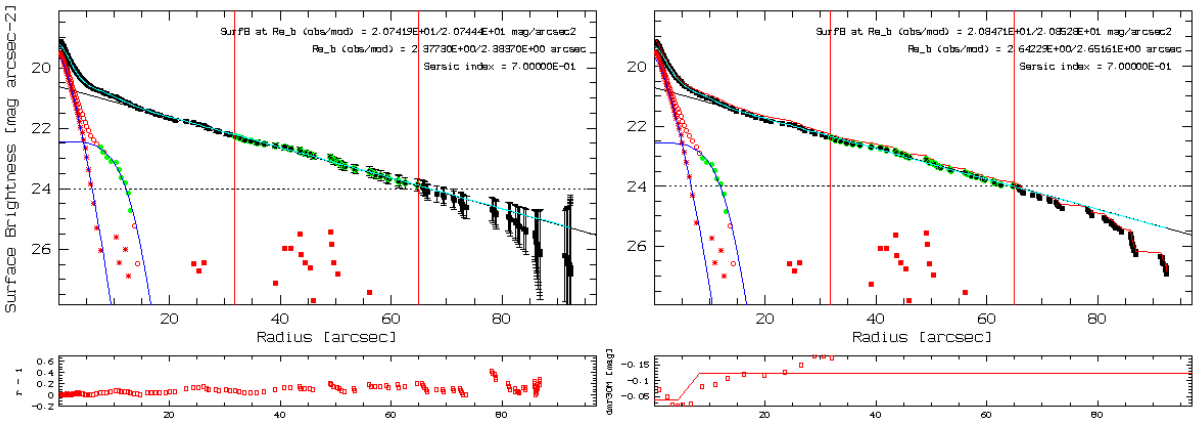

Figure B.23: Photometric decomposition of NGC3614.

NGC3687

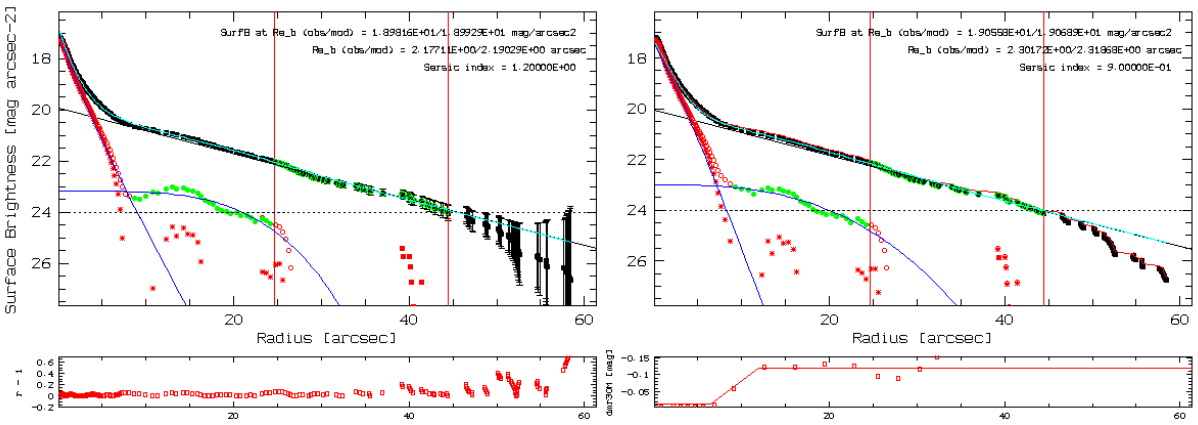

Figure B.24: Photometric decomposition of NGC3687.

NGC4003

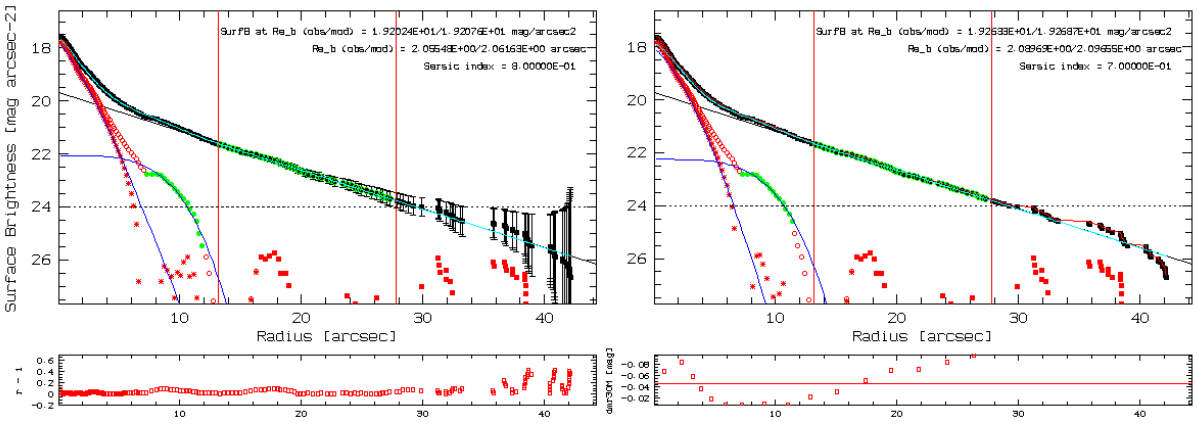

Figure B.25: Photometric decomposition of NGC4003.

NGC4047

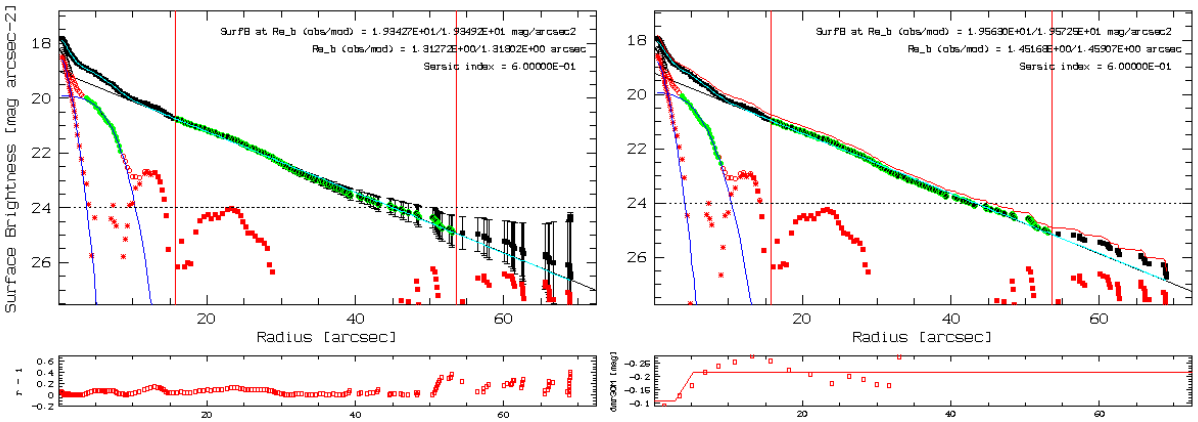

Figure B.26: Photometric decomposition of NGC4047.

NGC4185

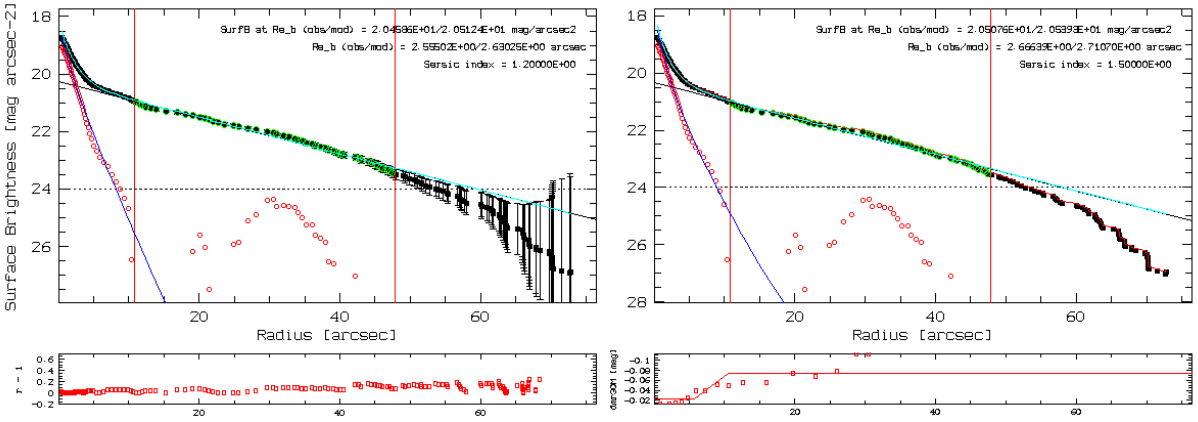

Figure B.27: Photometric decomposition of NGC4185.

NGC4210

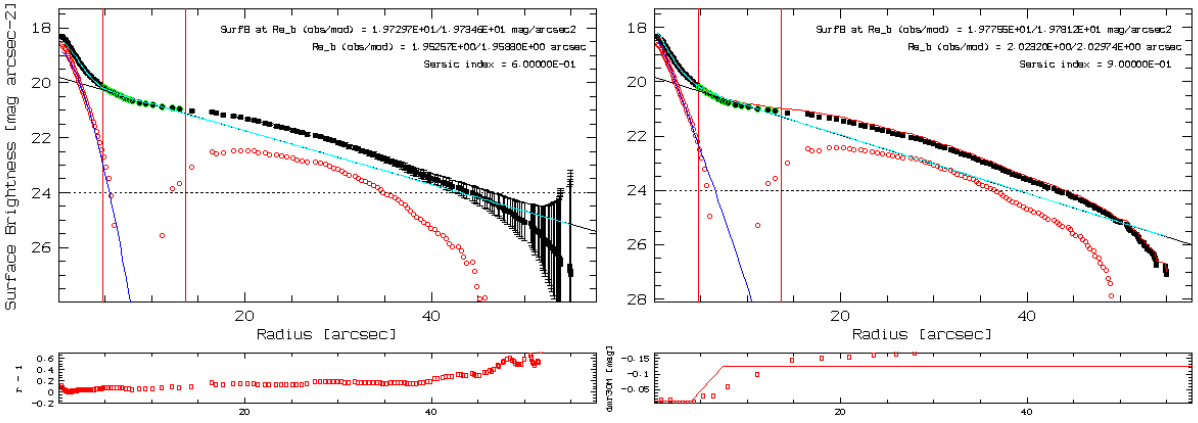

Figure B.28: Photometric decomposition of NGC4210.

NGC4961

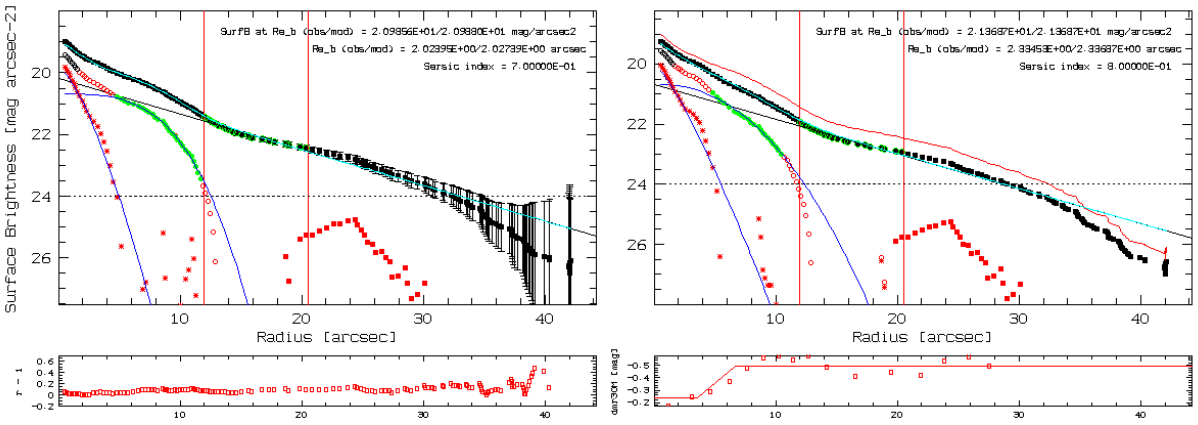

Figure B.29: Photometric decomposition of NGC4961.

NGC5000

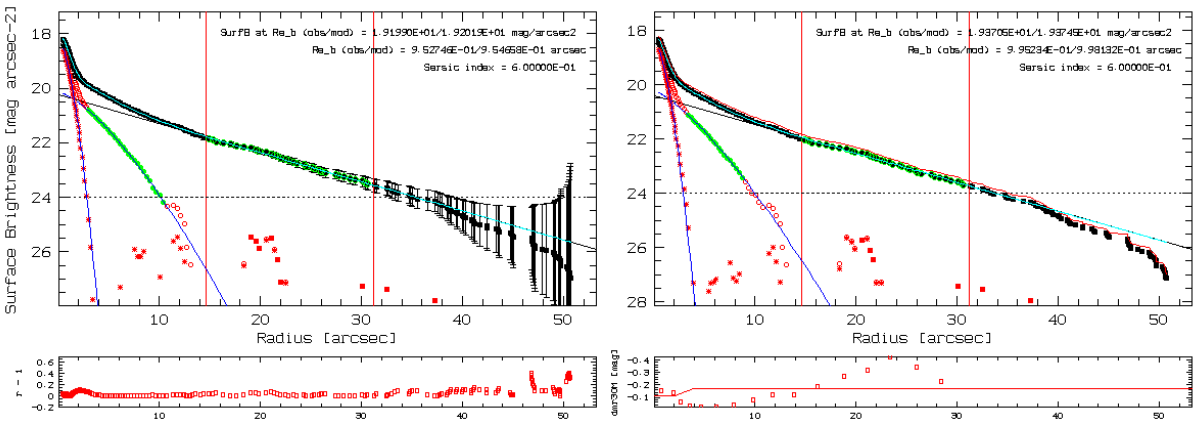

Figure B.30: Photometric decomposition of NGC5000.

NGC5016

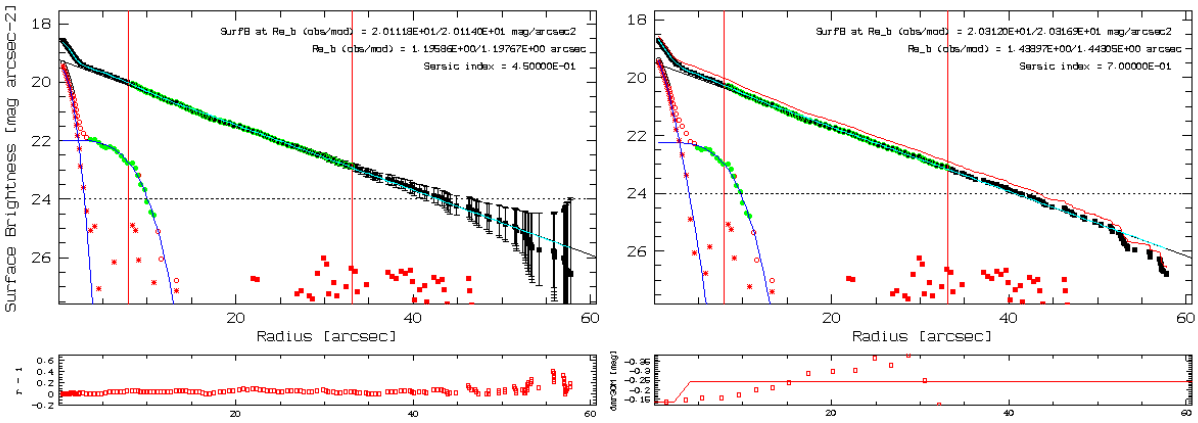

Figure B.31: Photometric decomposition of NGC5016.

NGC5205

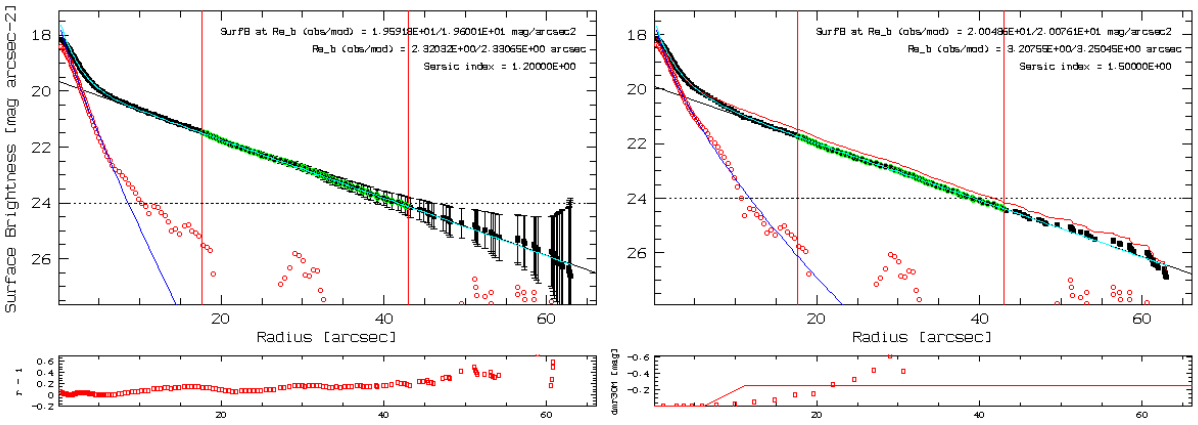

Figure B.32: Photometric decomposition of NGC5205.

NGC5320

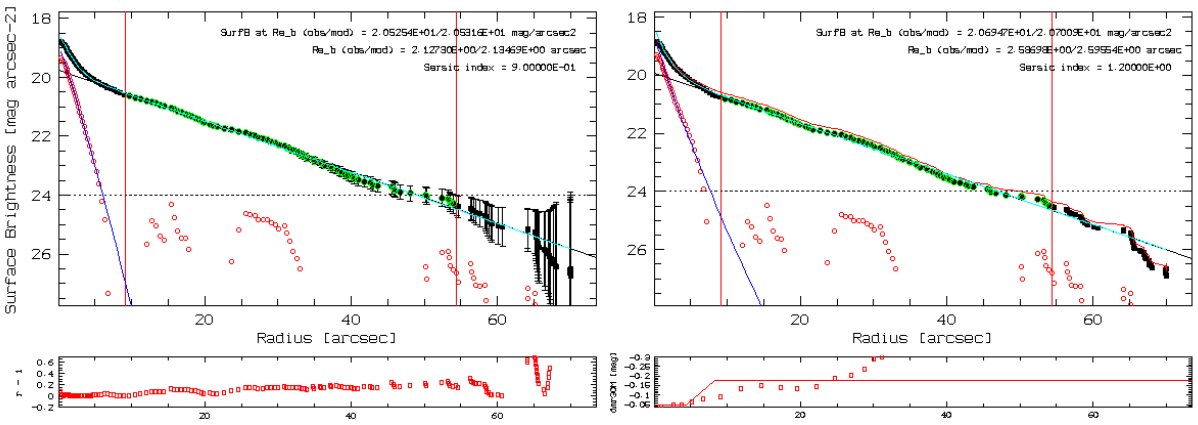

Figure B.33: Photometric decomposition of NGC5320.

NGC5378

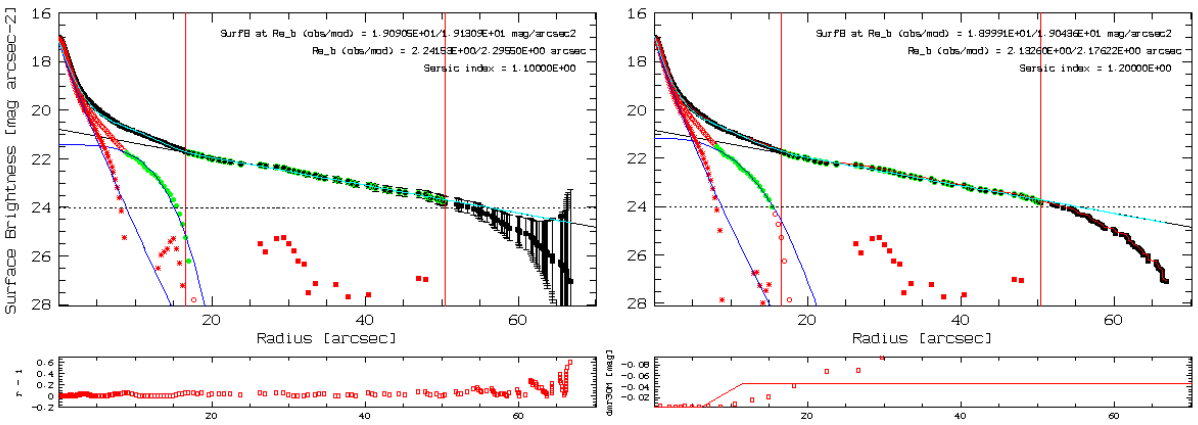

Figure B.34: Photometric decomposition of NGC5378.

NGC5406

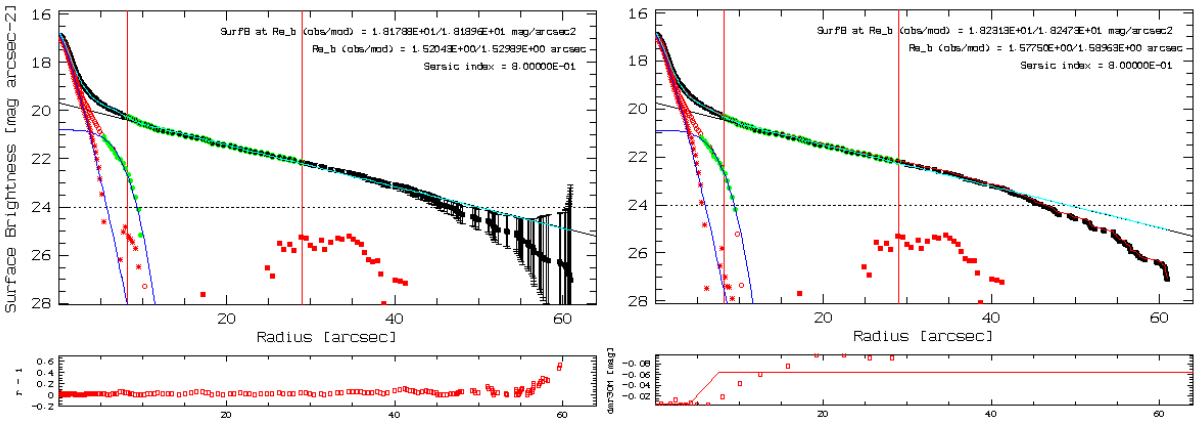

Figure B.35: Photometric decomposition of NGC5406.

NGC5480

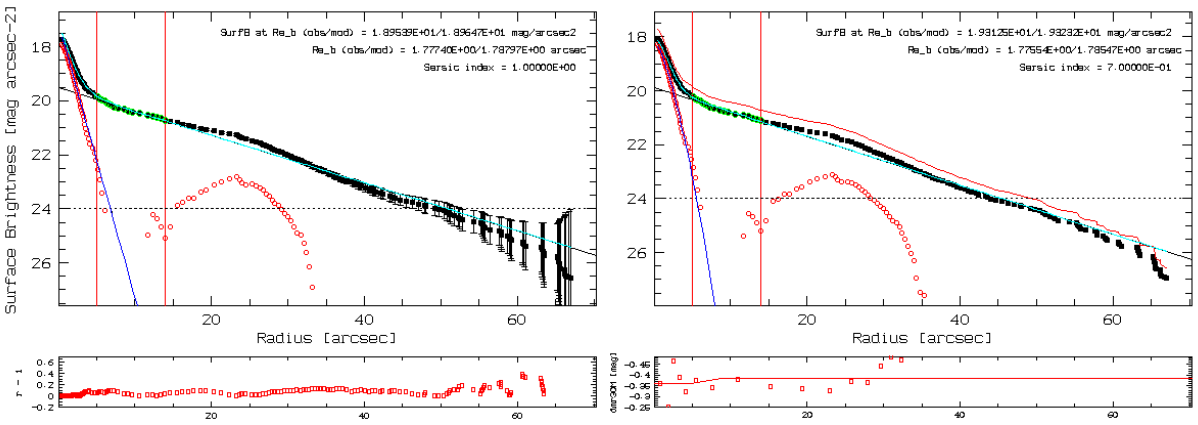

Figure B.36: Photometric decomposition of NGC5480.

NGC5614

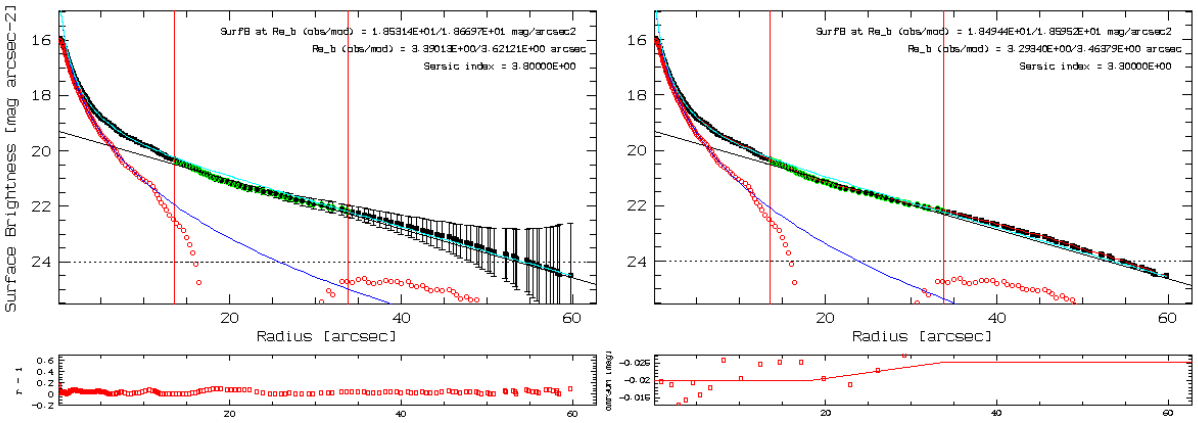

Figure B.37: Photometric decomposition of NGC5614.

NGC5656

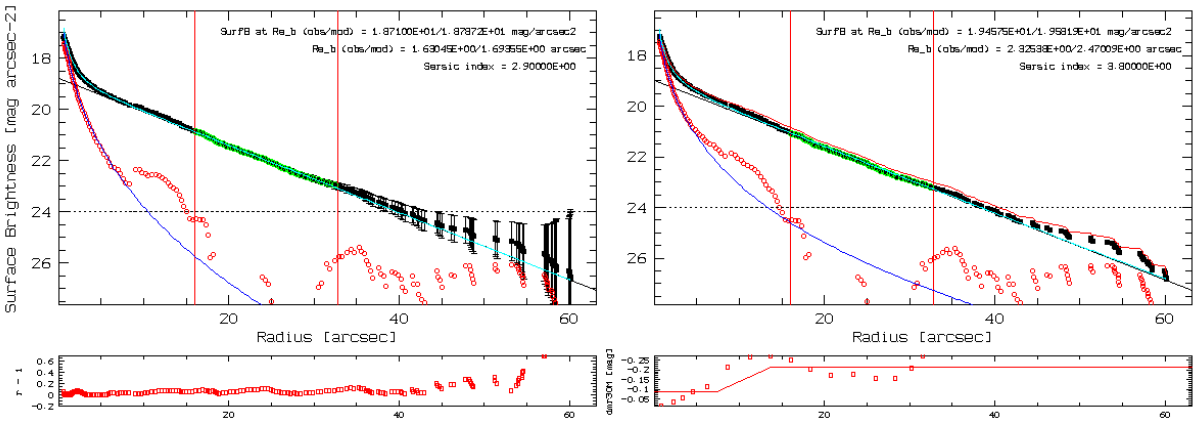

Figure B.38: Photometric decomposition of NGC5656.

NGC5735

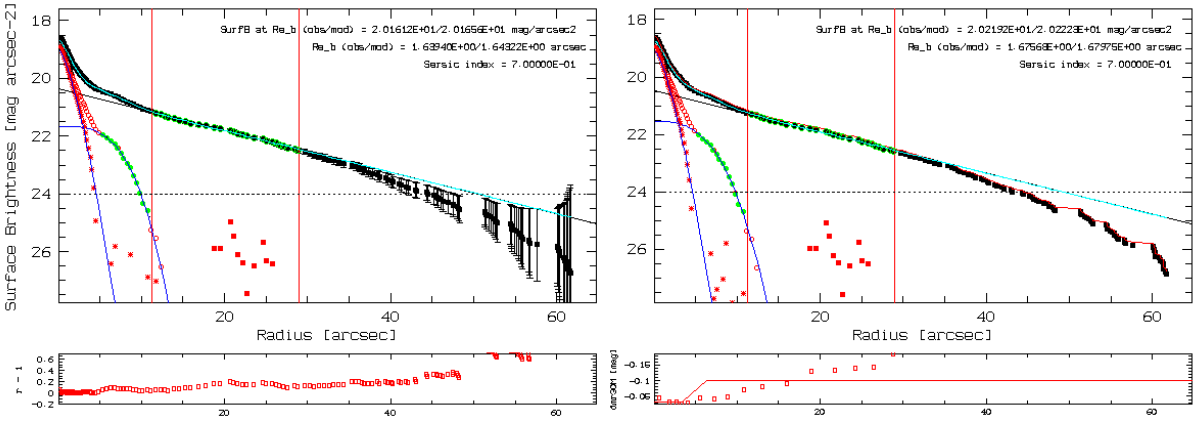

Figure B.39: Photometric decomposition of NGC5735.

NGC5772

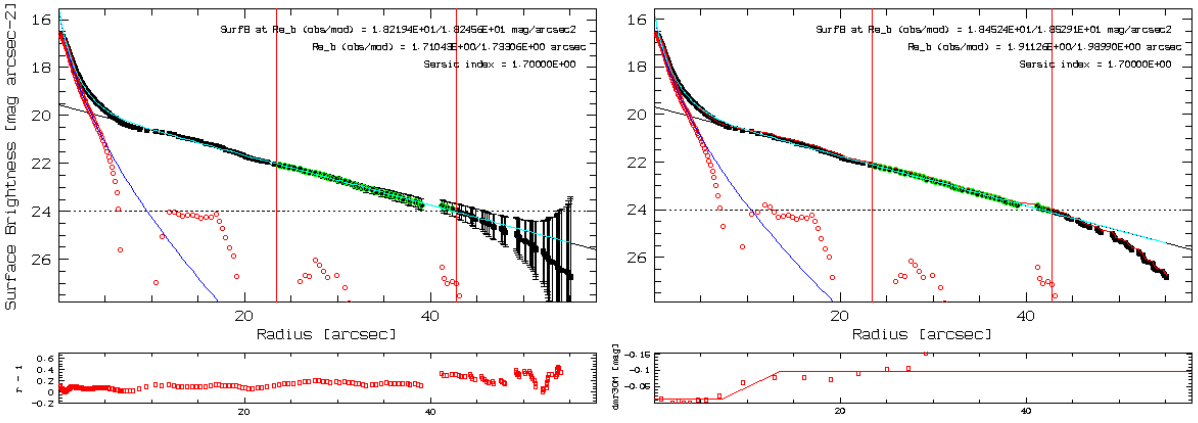

Figure B.40: Photometric decomposition of NGC5772.

NGC5829

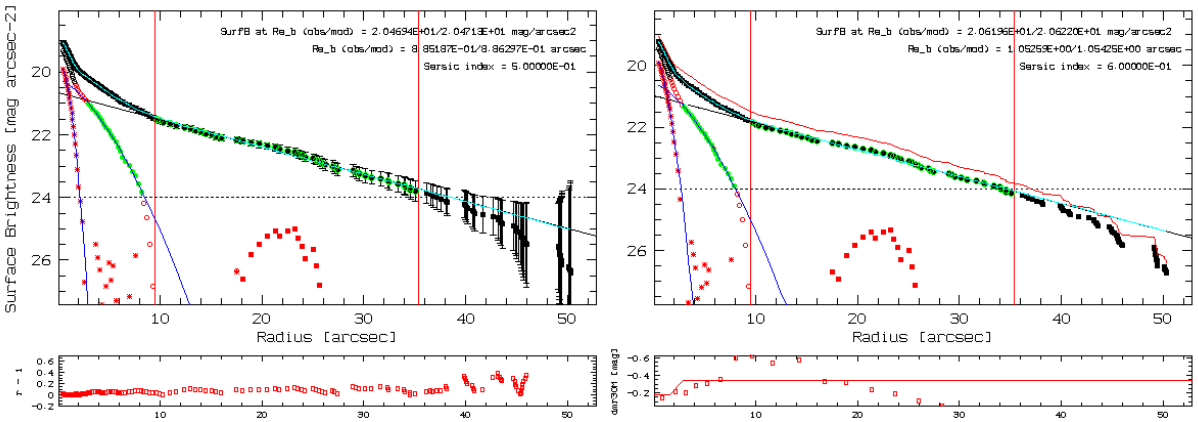

Figure B.41: Photometric decomposition of NGC5829.

NGC6004

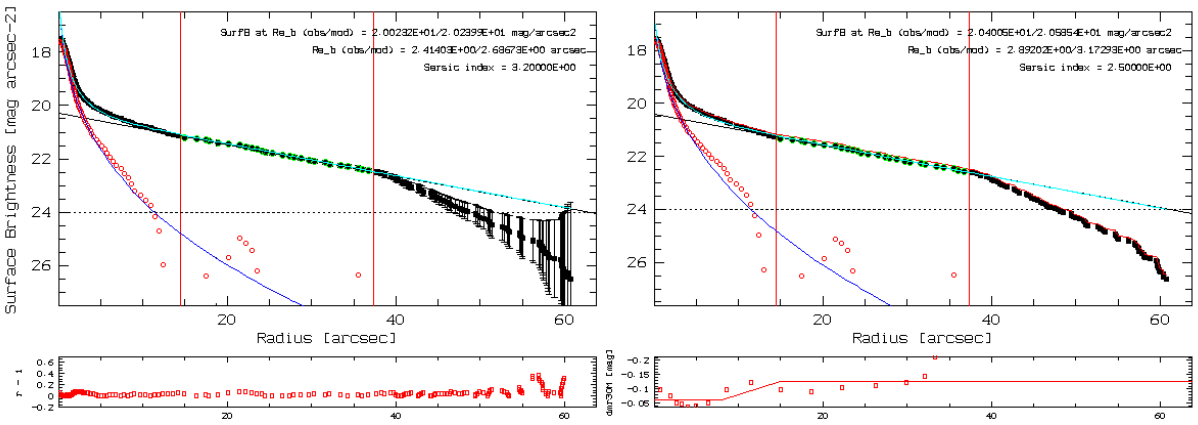

Figure B.42: Photometric decomposition of NGC6004.

NGC6032

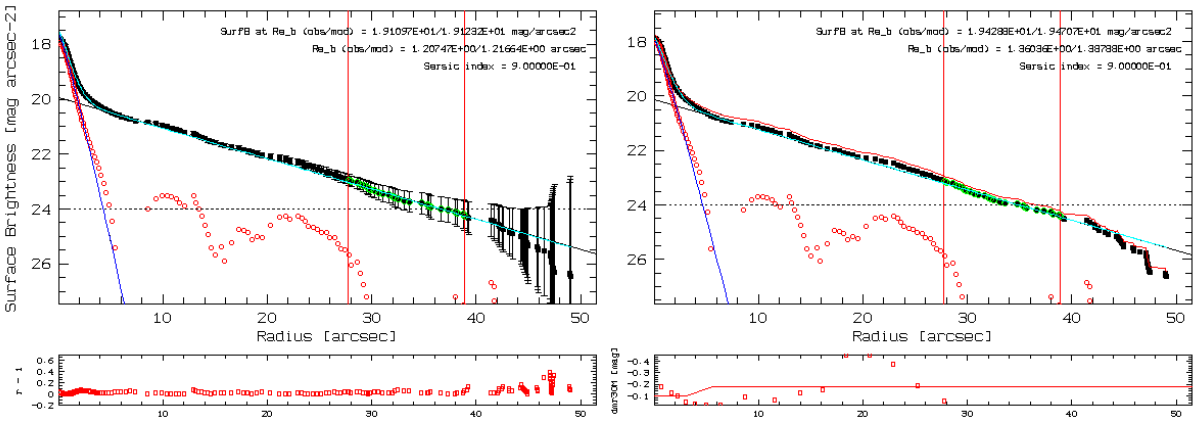

Figure B.43: Photometric decomposition of NGC6032.

NGC6186

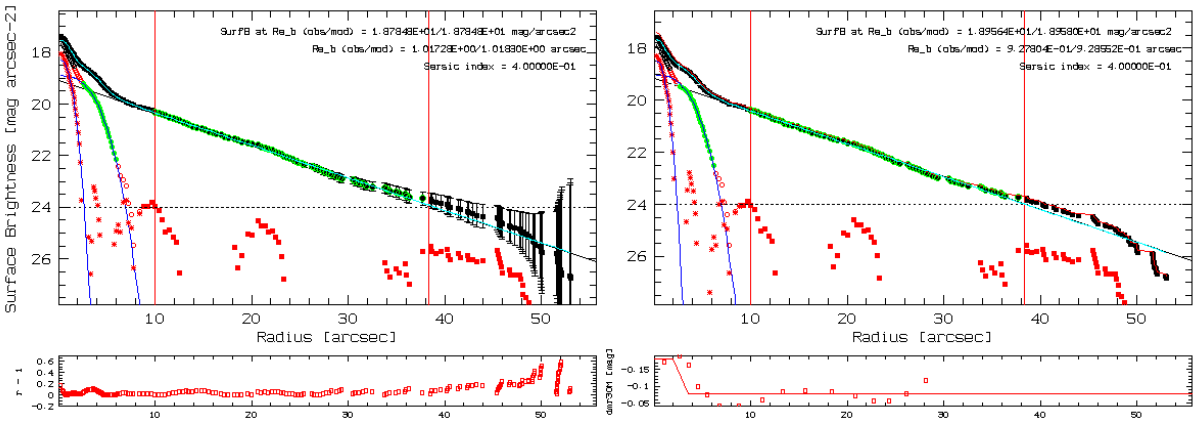

Figure B.44: Photometric decomposition of NGC6186.

NGC6278

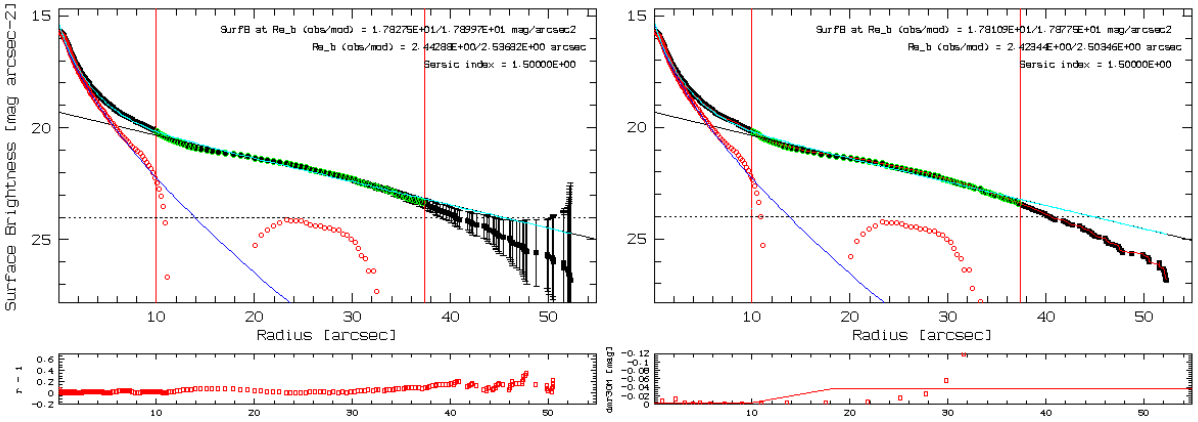

Figure B.45: Photometric decomposition of NGC6278.

NGC6941

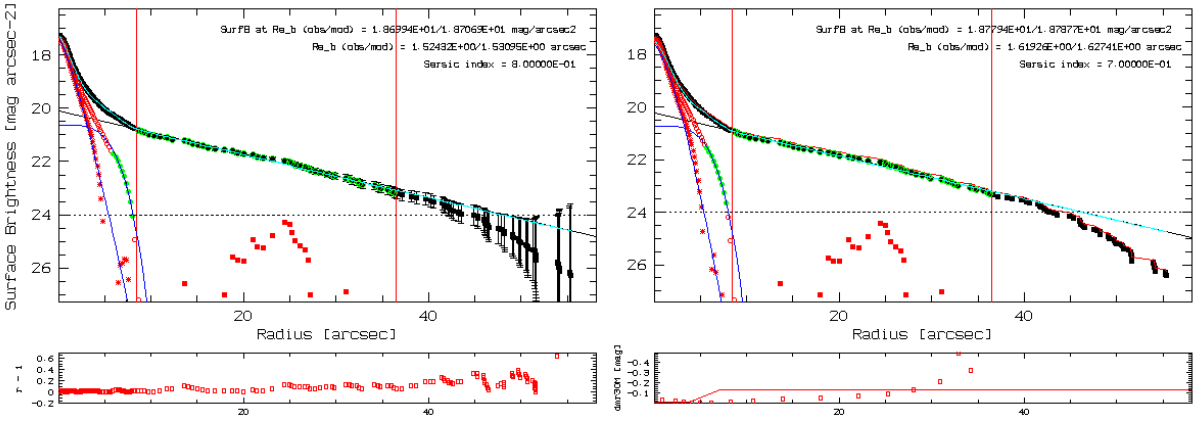

Figure B.46: Photometric decomposition of NGC6941.

NGC7321

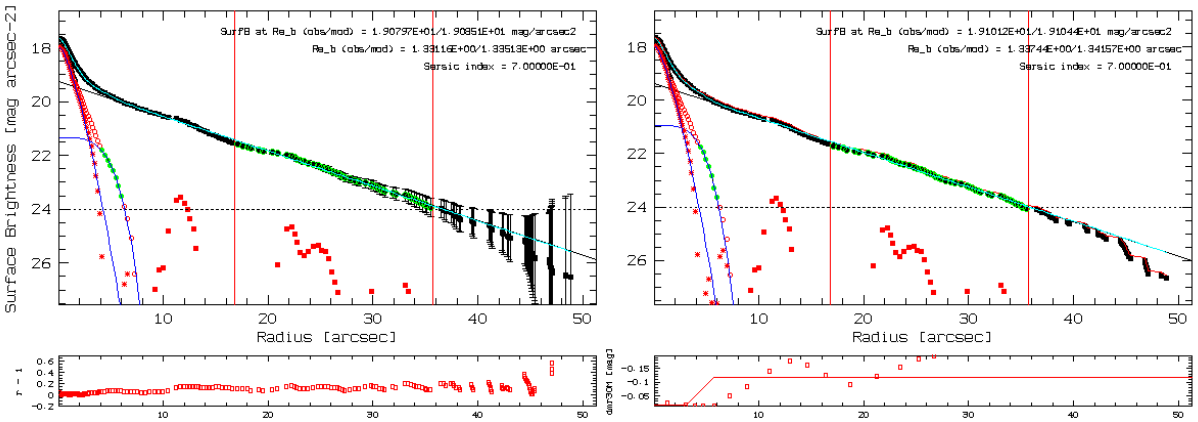

Figure B.47: Photometric decomposition of NGC7321.

NGC7489

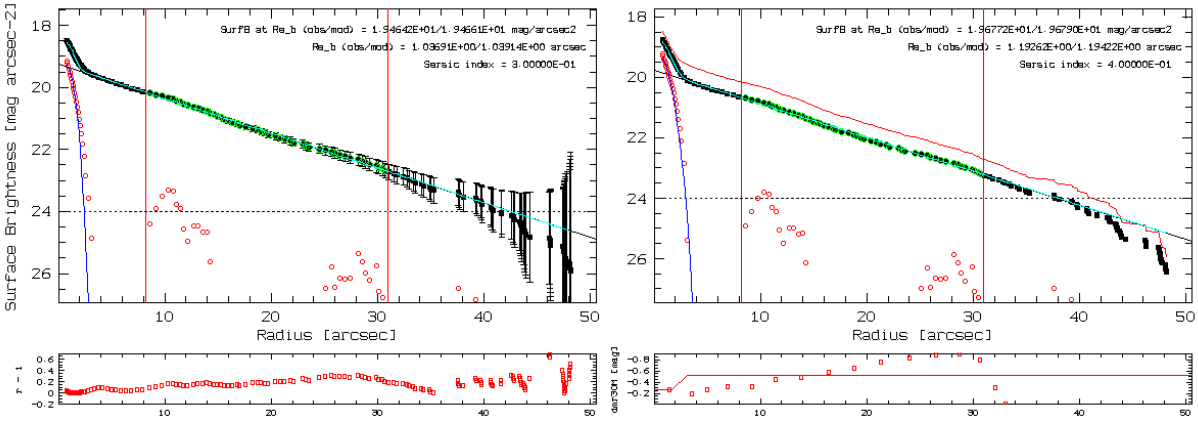

Figure B.48: Photometric decomposition of NGC7489.

NGC7625

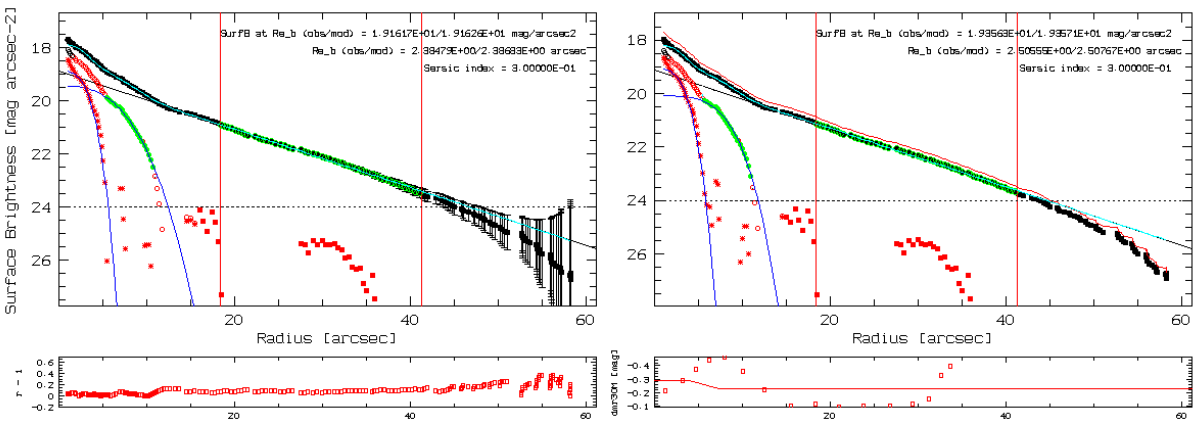

Figure B.49: Photometric decomposition of NGC7625.

NGC7653

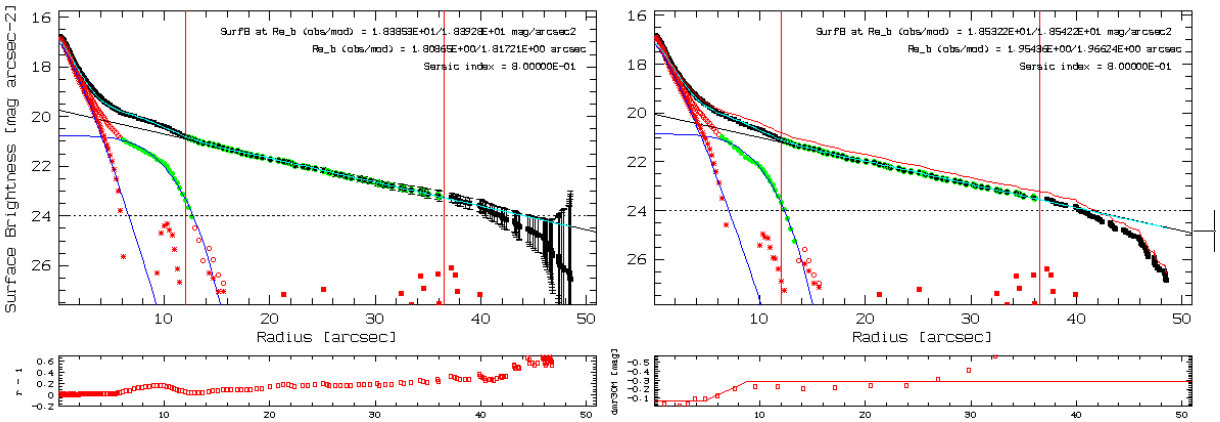

Figure B.50: Photometric decomposition of NGC7653.

NGC7691

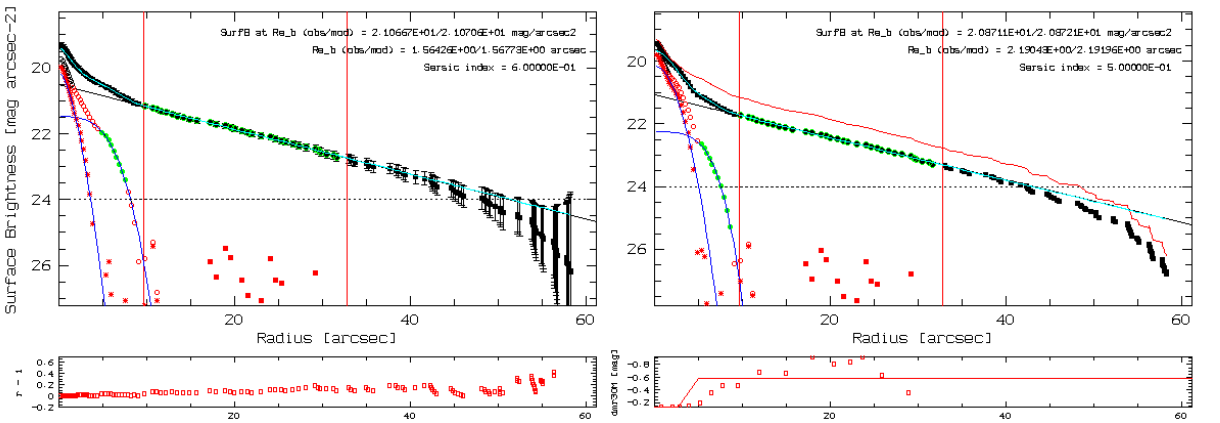

Figure B.51: Photometric decomposition of NGC7691.

NGC7716

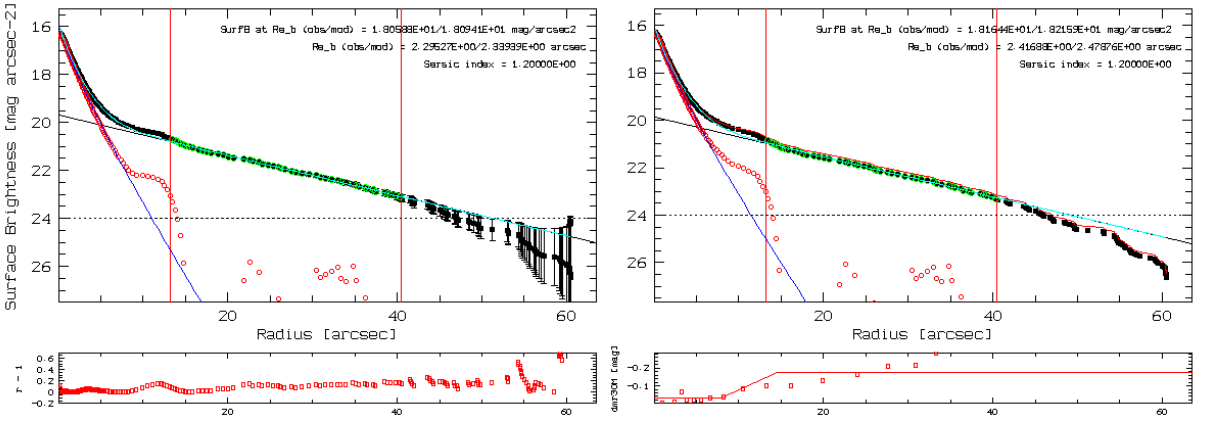

Figure B.52: Photometric decomposition of NGC7716.

NGC7738

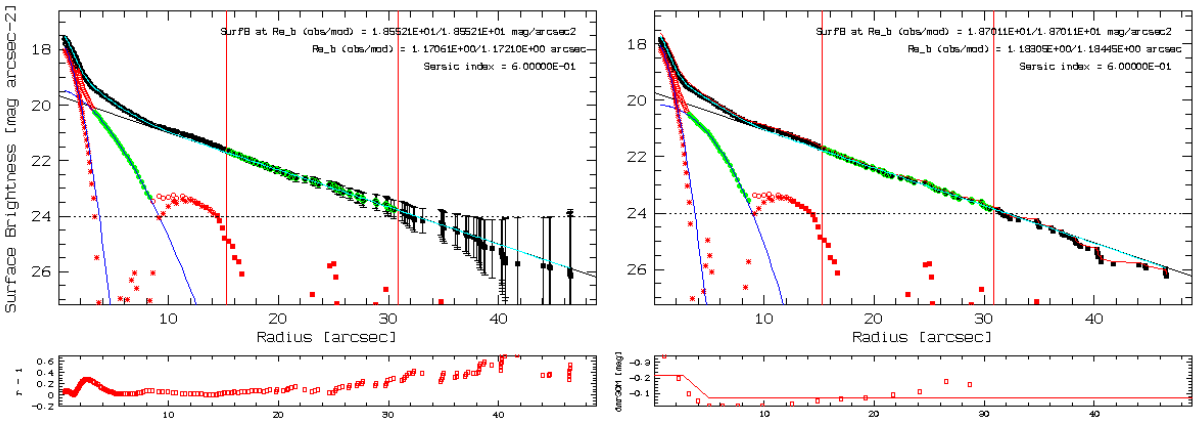

Figure B.53: Photometric decomposition of NGC7738.

NGC7819

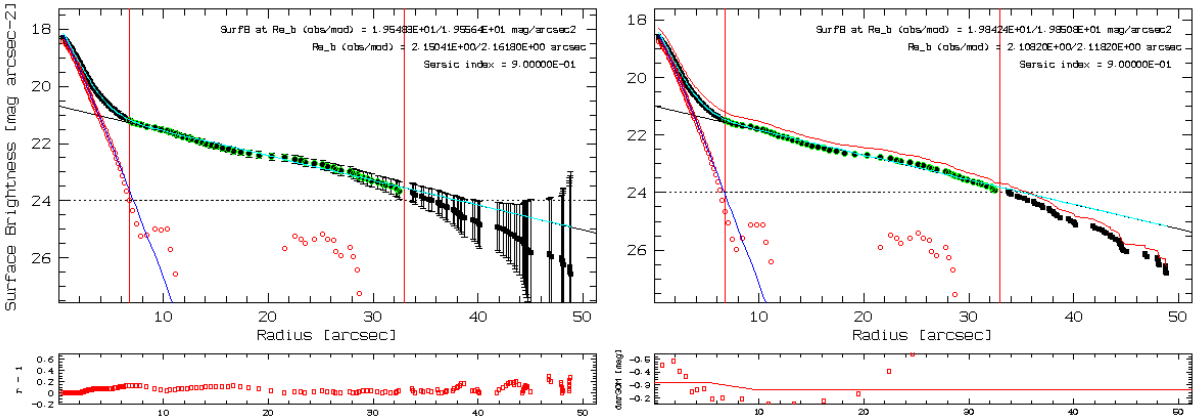

Figure B.54: Photometric decomposition of NGC7819.

UGC07012

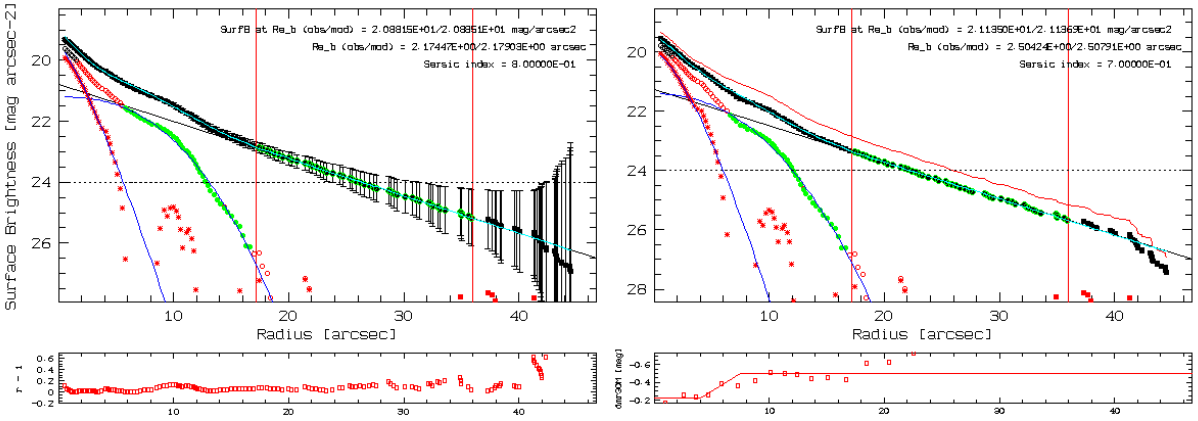

Figure B.55: Photometric decomposition of UGC07012.

UGC08234

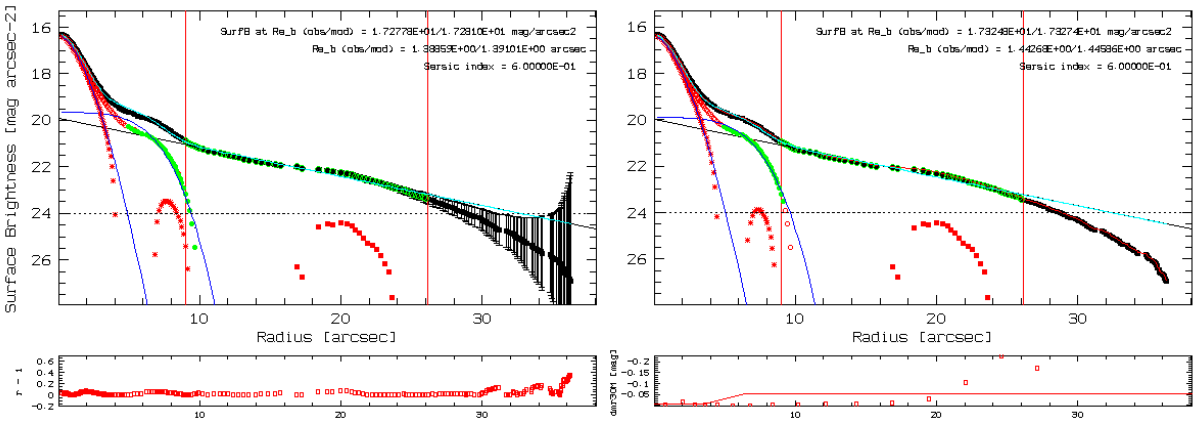

Figure B.56: Photometric decomposition of UGC08234.

UGC08733

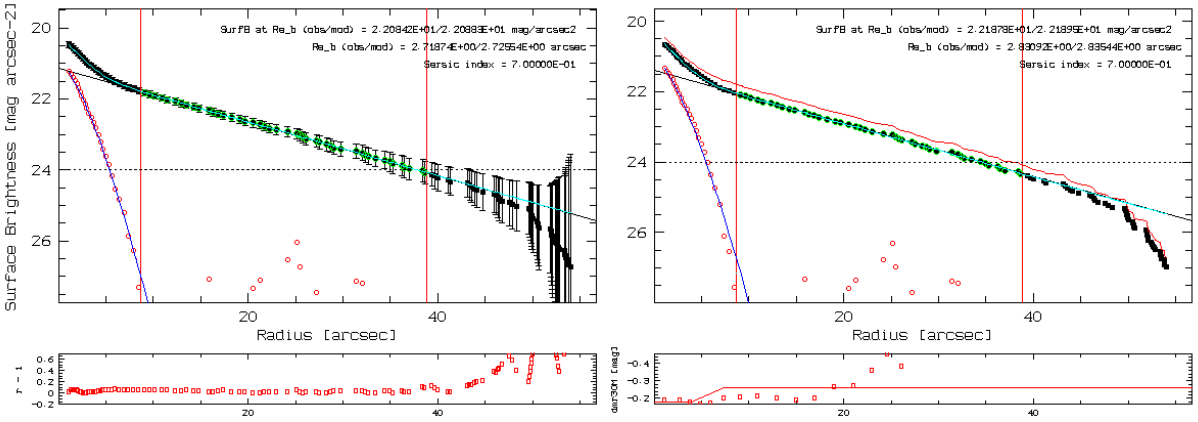

Figure B.57: Photometric decomposition of UGC08733.

UGC09067

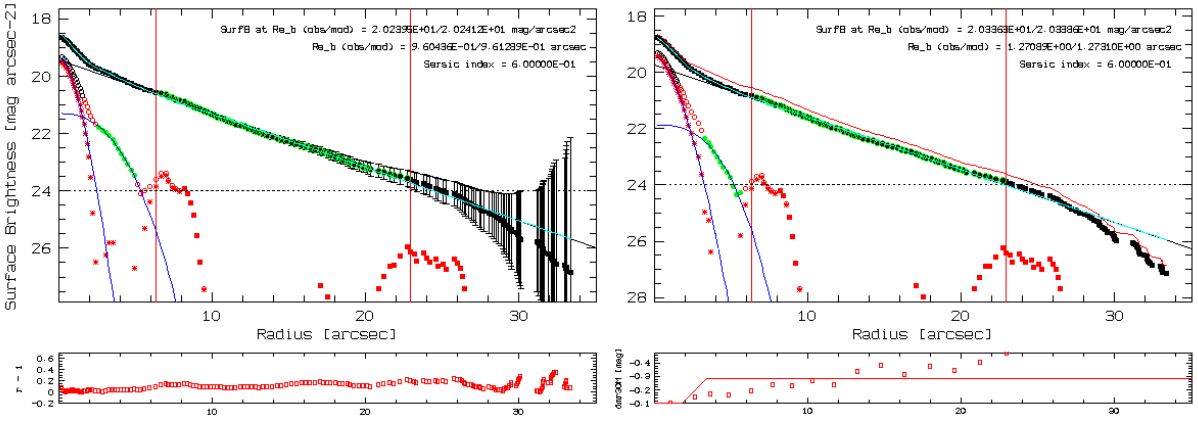

Figure B.58: Photometric decomposition of UGC09067.

UGC09291

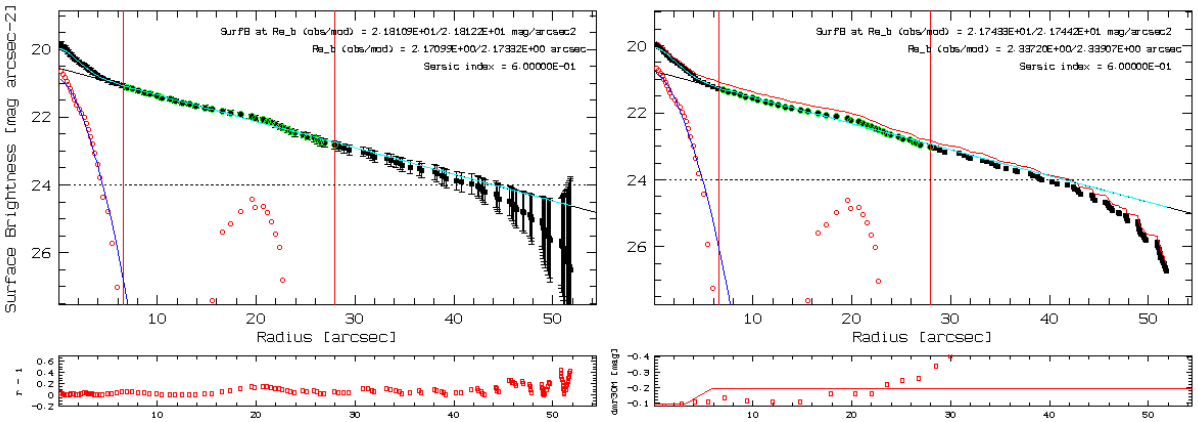

Figure B.59: Photometric decomposition of UGC09291.

UGC09476

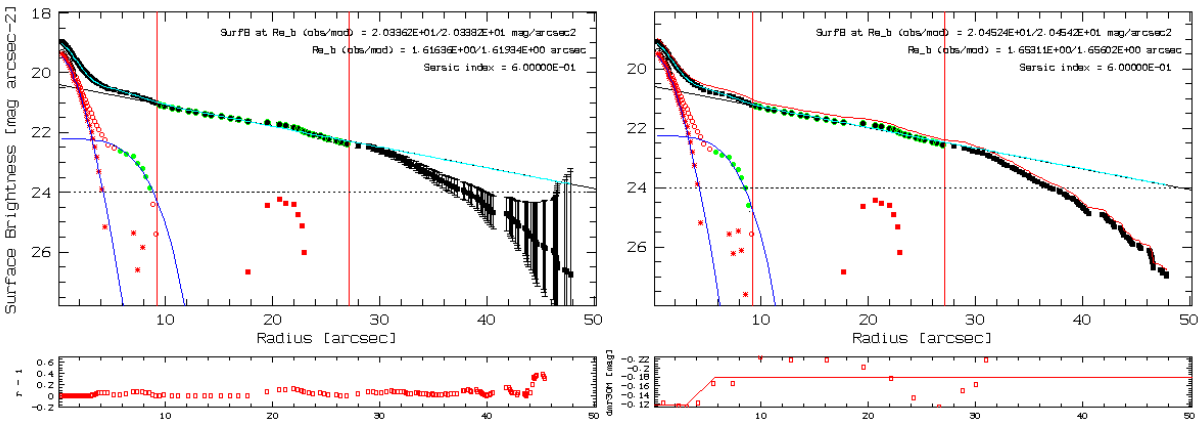

Figure B.60: Photometric decomposition of UGC09476.

UGC10796

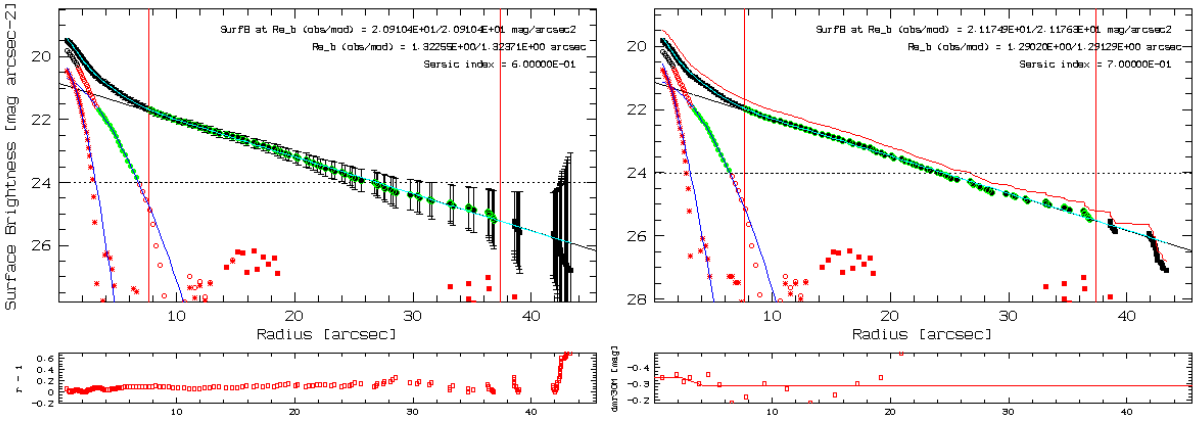

Figure B.61: Photometric decomposition of UGC10796.

UGC12224

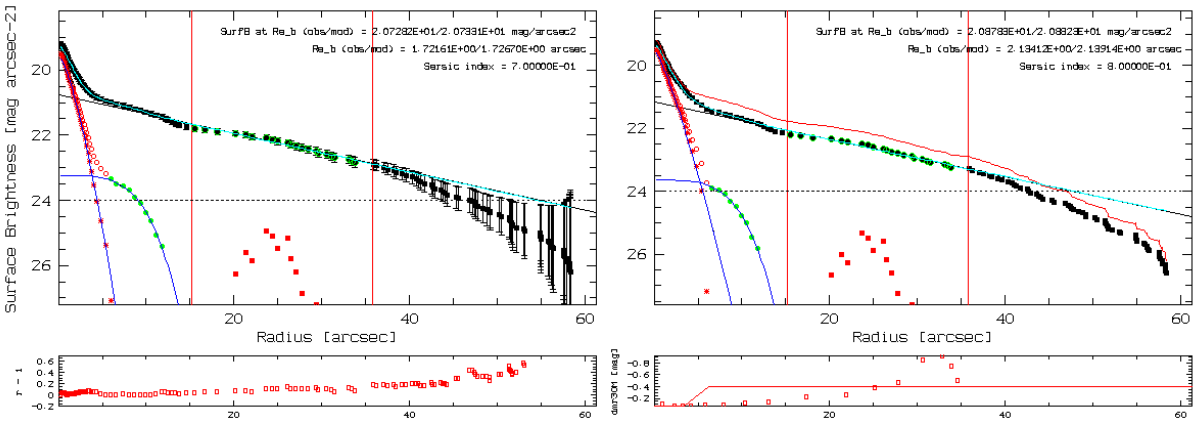

Figure B.62: Photometric decomposition of UGC12224.

Appendices

Appendix C.

Metallicity Maps and Radial Profiles

IC0776

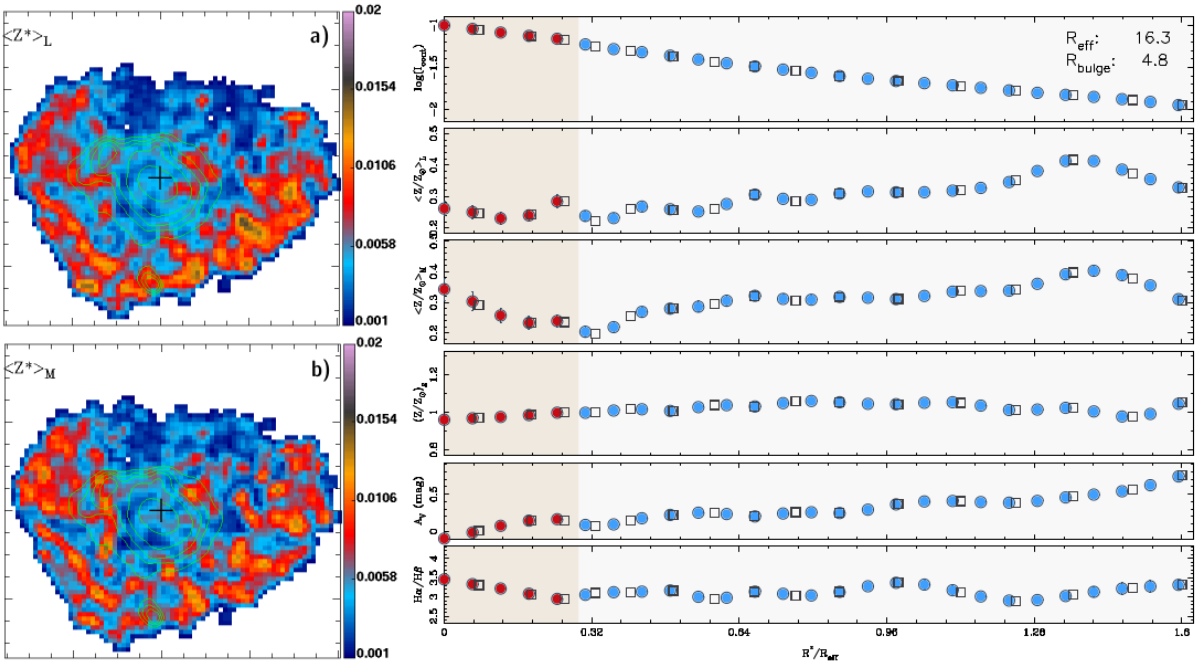

Figure C.1: Metallicity maps and radial profiles of IC0776.

IC4566

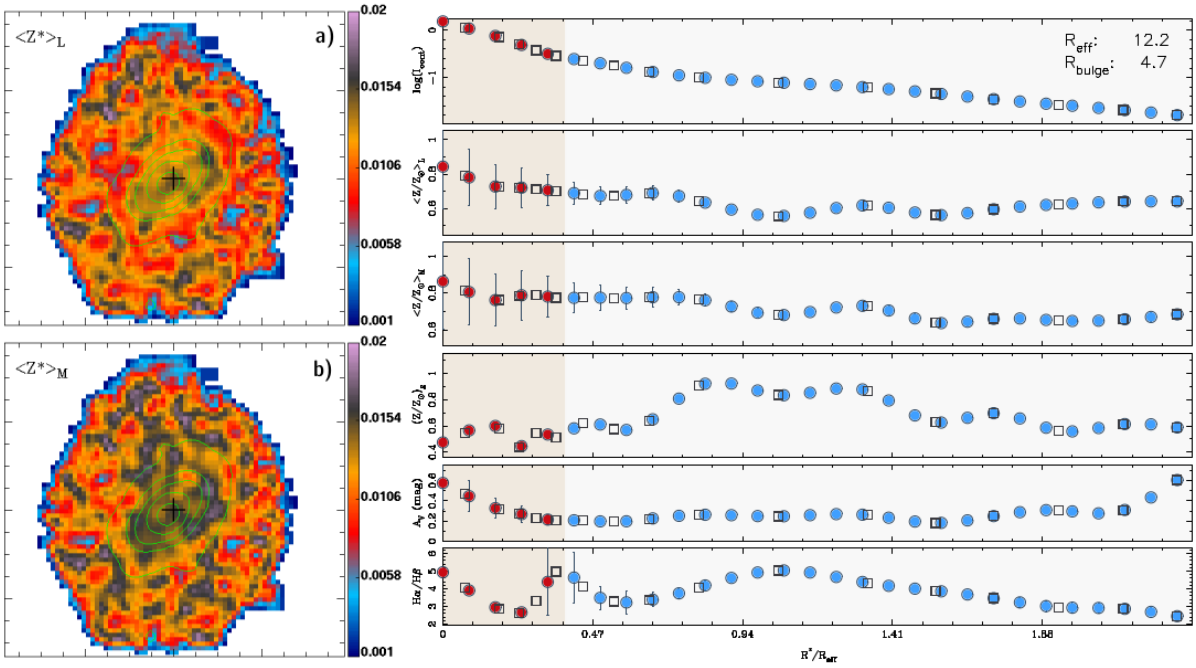

Figure C.2: Metallicity maps and radial profiles of IC4566.

NGC0001

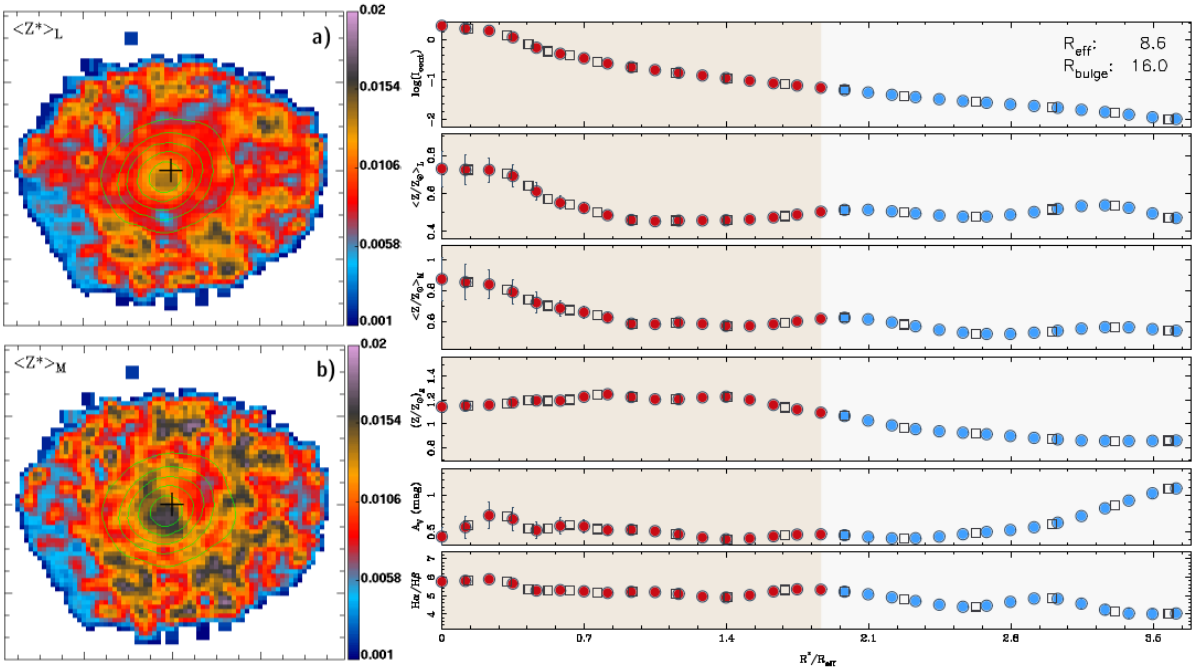

Figure C.3: Metallicity maps and radial profiles of NGC0001.

NGC0160

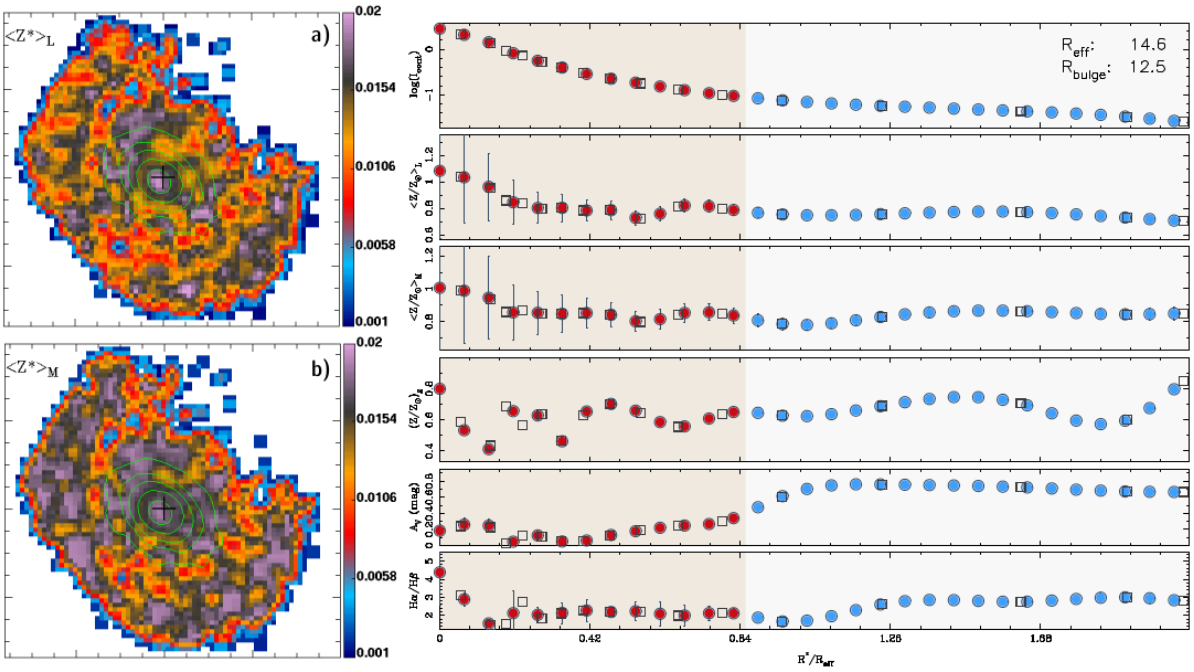

Figure C.4: Metallicity maps and radial profiles of NGC0160.

NGC0165

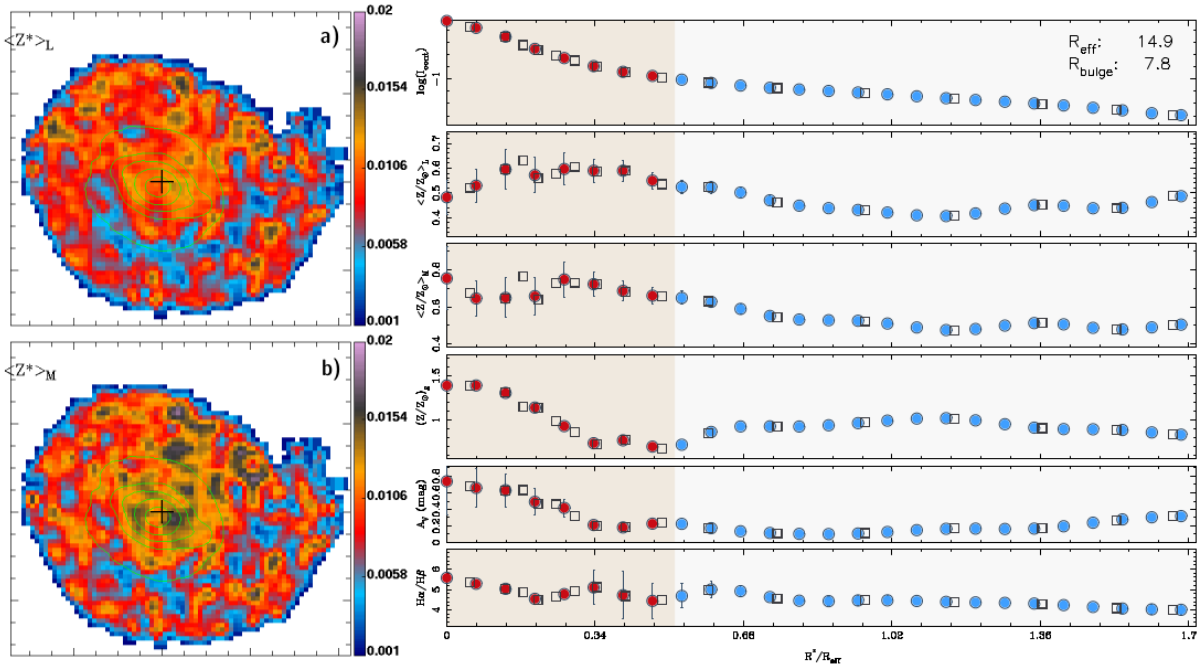

Figure C.5: Metallicity maps and radial profiles of NGC0165.

NGC0171

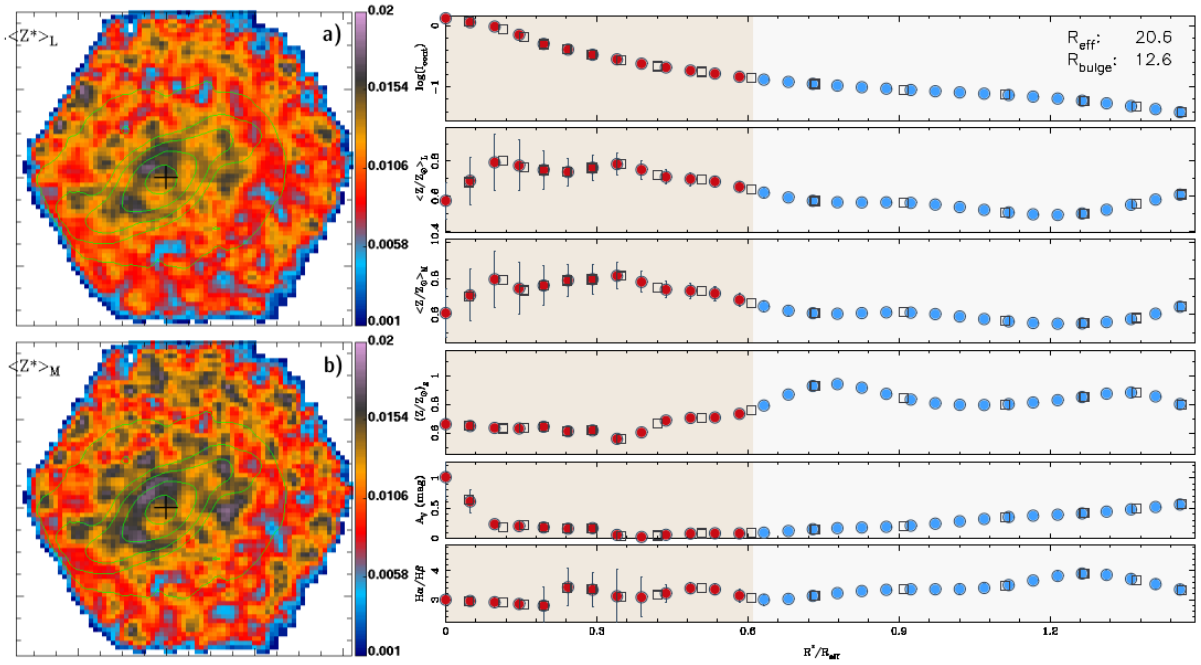

Figure C.6: Metallicity maps and radial profiles of NGC0171.

NGC0180

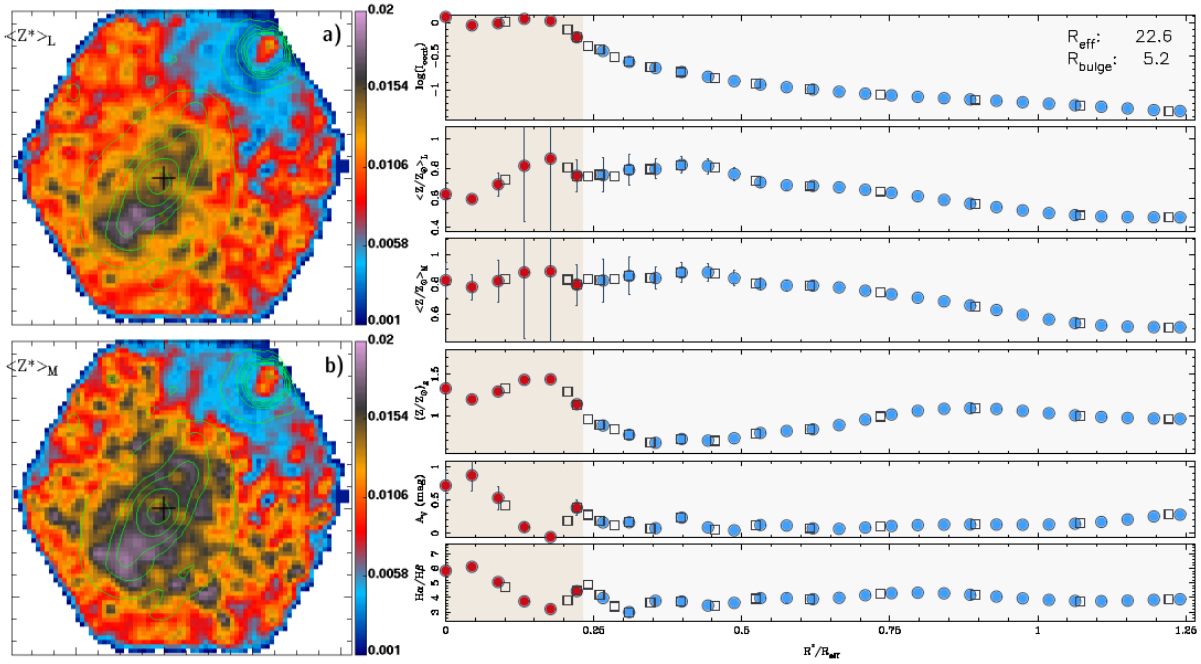

Figure C.7: Metallicity maps and radial profiles of NGC0180.

NGC0214

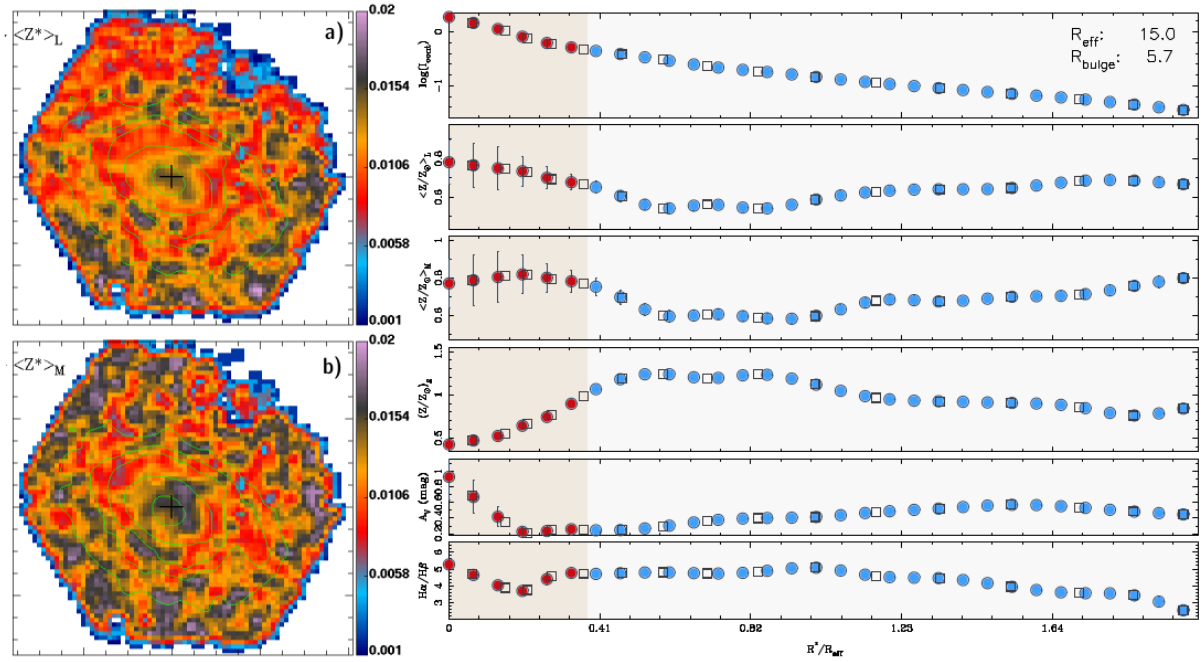

Figure C.8: Metallicity maps and radial profiles of NGC0214.

NGC0237

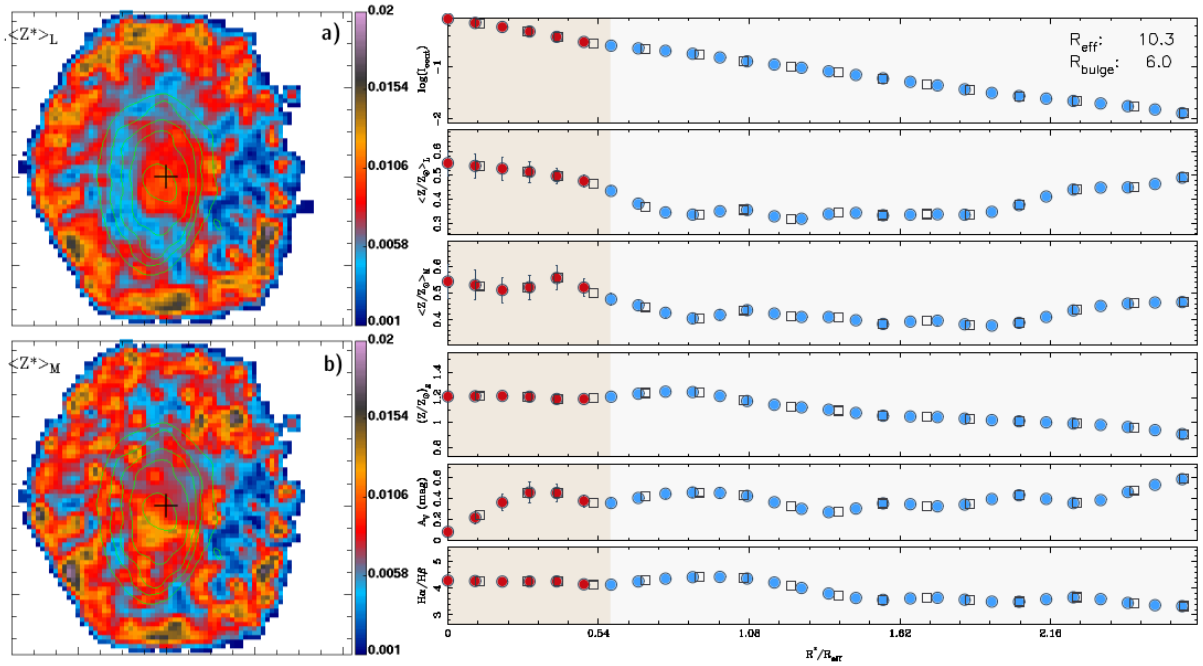

Figure C.9: Metallicity maps and radial profiles of NGC0237.

NGC0257

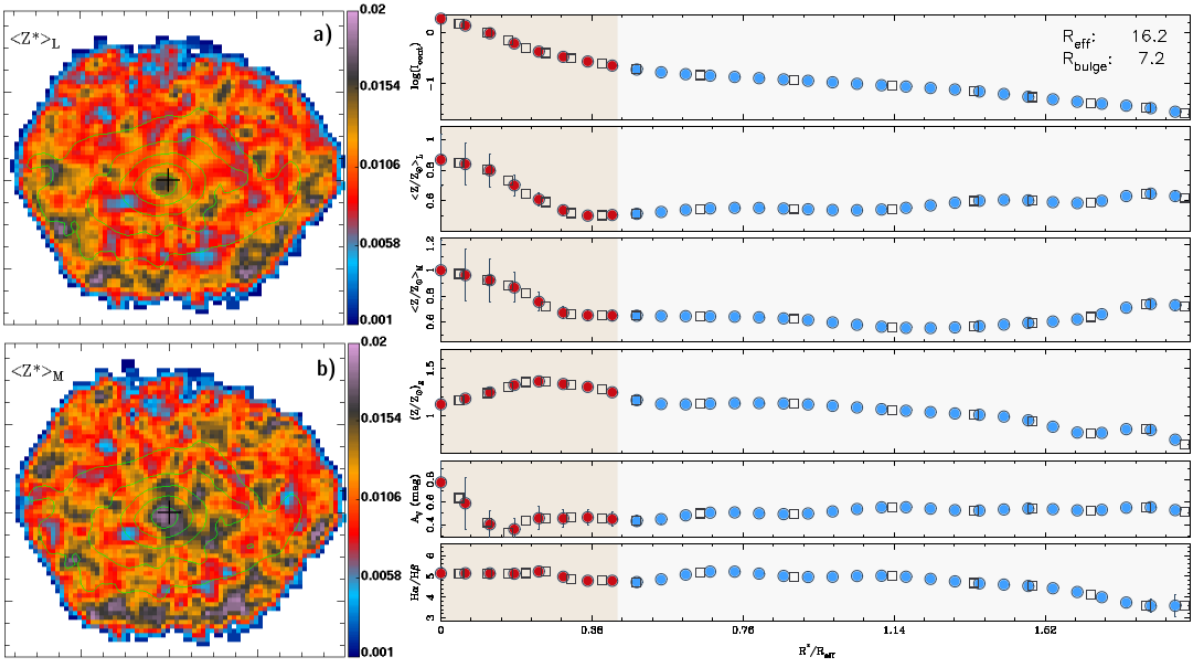

Figure C.10: Metallicity maps and radial profiles of NGC0257.

NGC0477

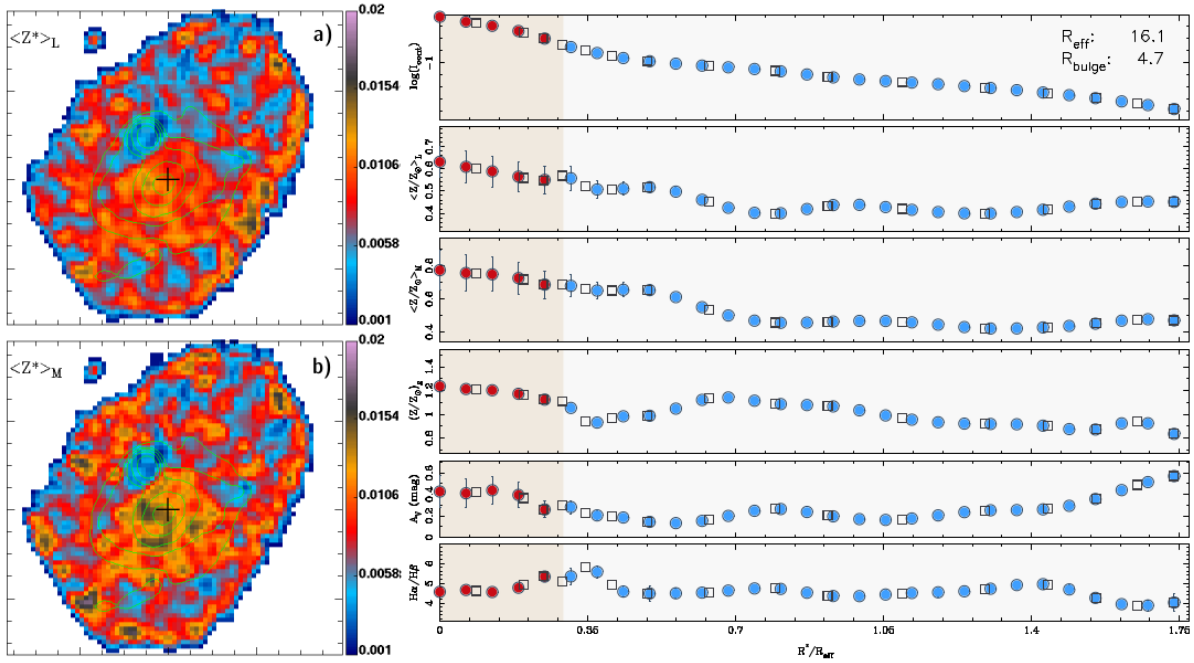

Figure C.11: Metallicity maps and radial profiles of NGC0477.

NGC0776

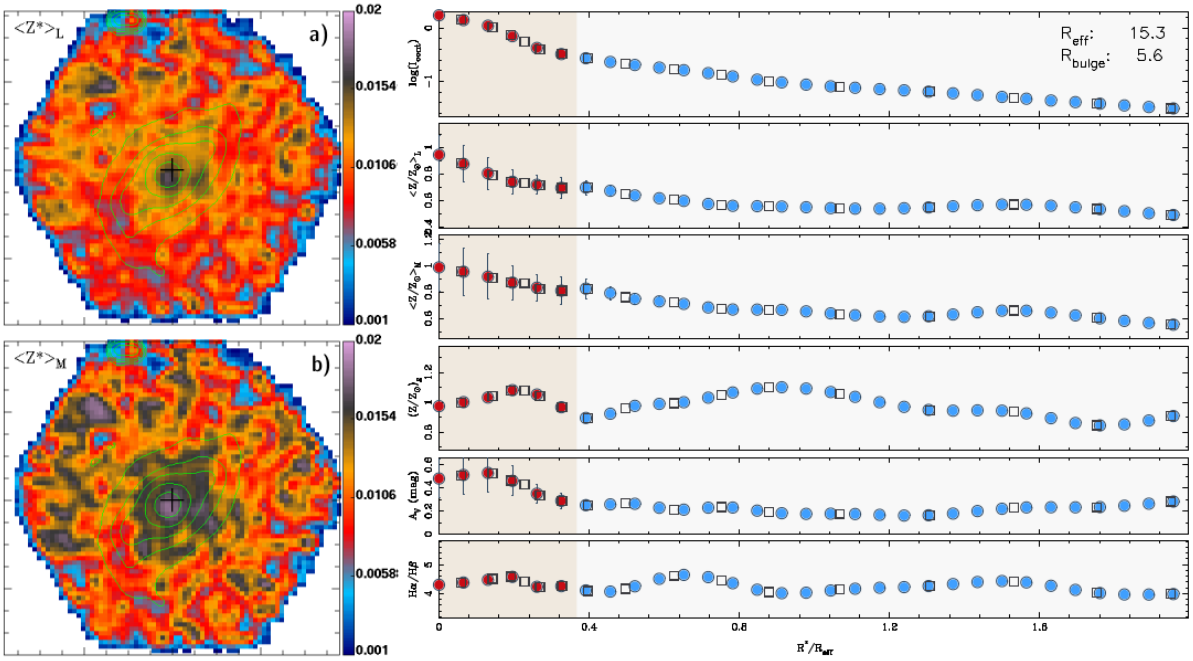

Figure C.12: Metallicity maps and radial profiles of NGC0776.

NGC1093

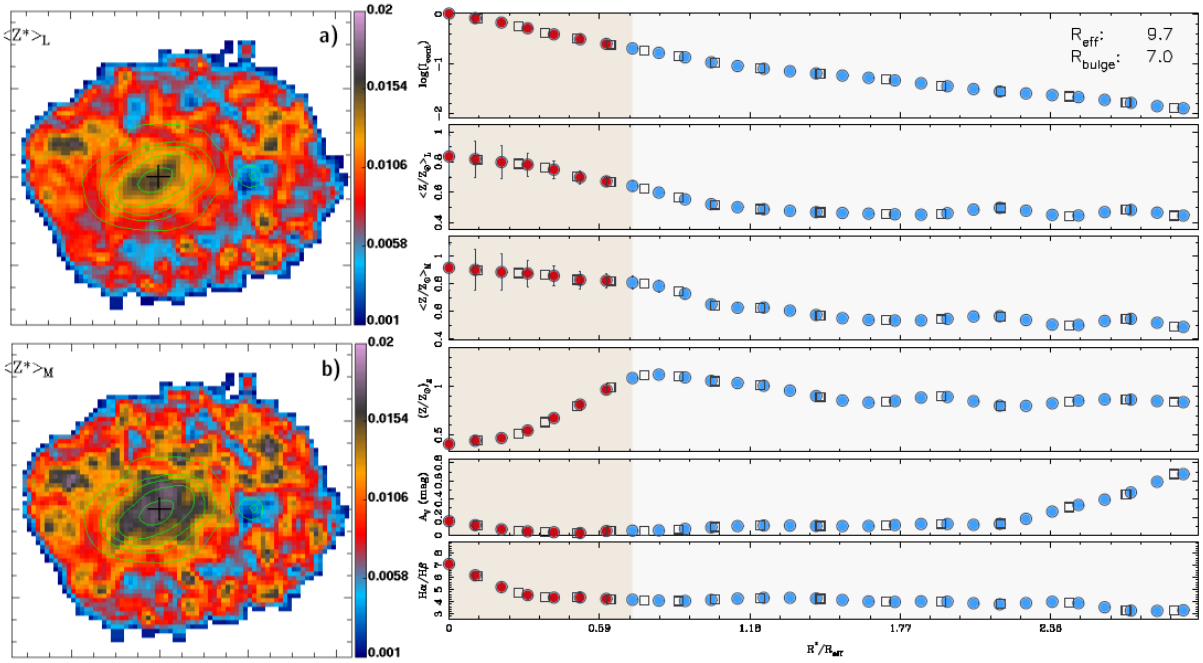

Figure C.13: Metallicity maps and radial profiles of NGC1093.

NGC1645

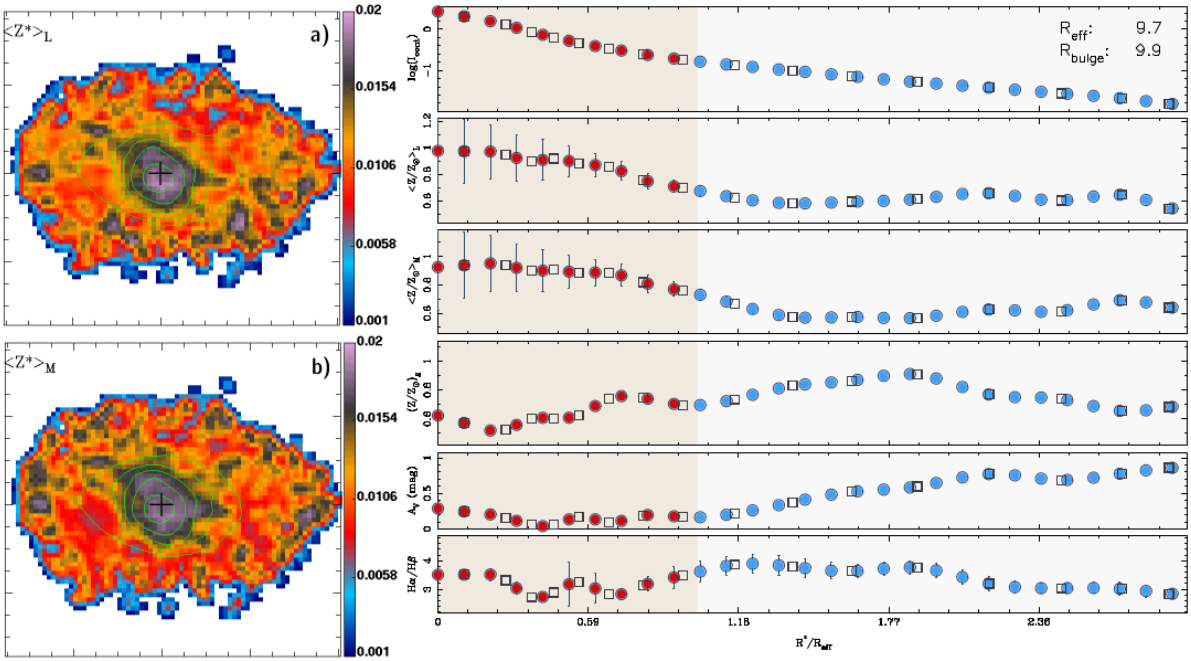

Figure C.14: Metallicity maps and radial profiles of NGC1645.

NGC2253

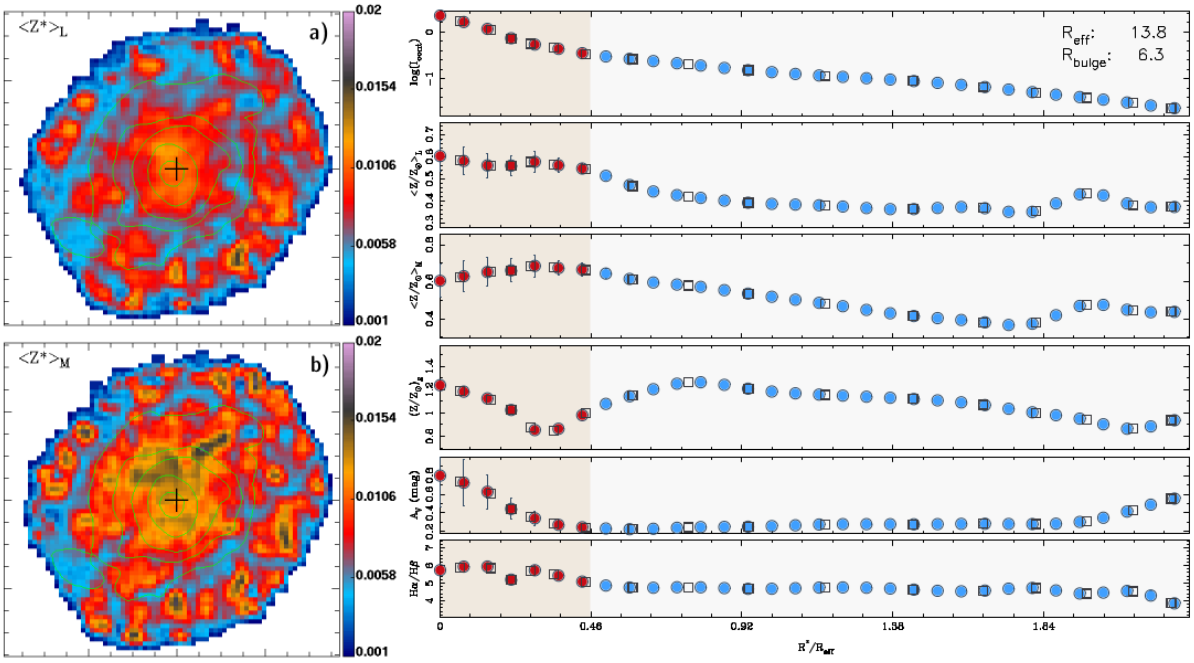

Figure C.15: Metallicity maps and radial profiles of NGC2253.

NGC2347

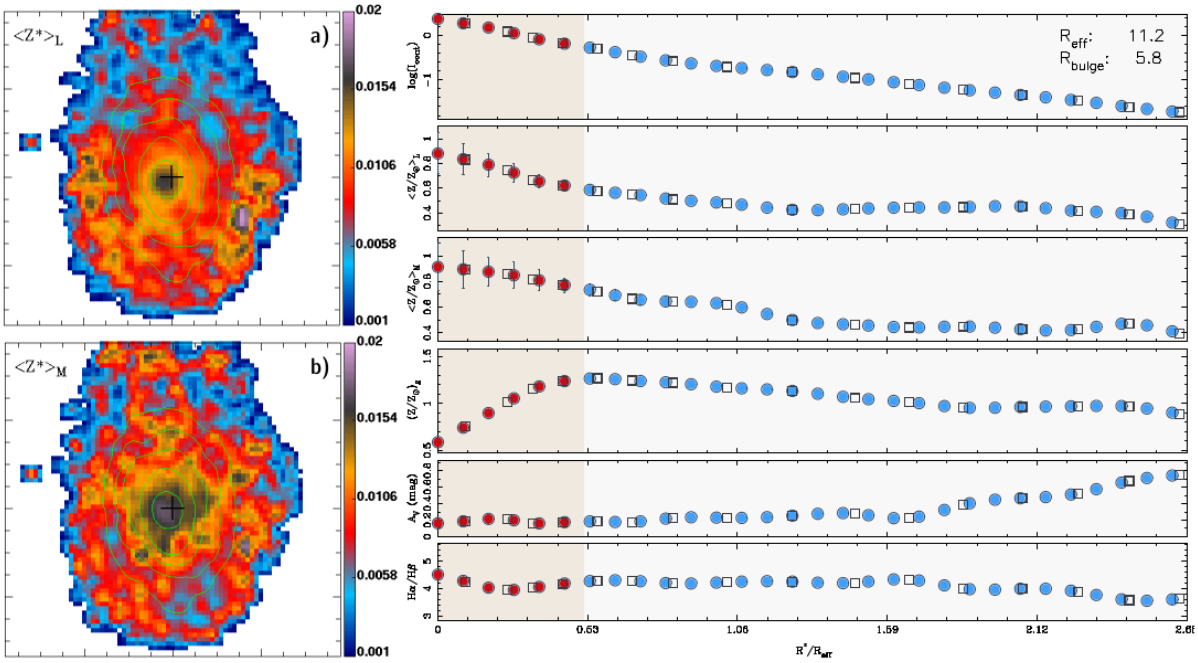

Figure C.16: Metallicity maps and radial profiles of NGC2347.

NGC2639

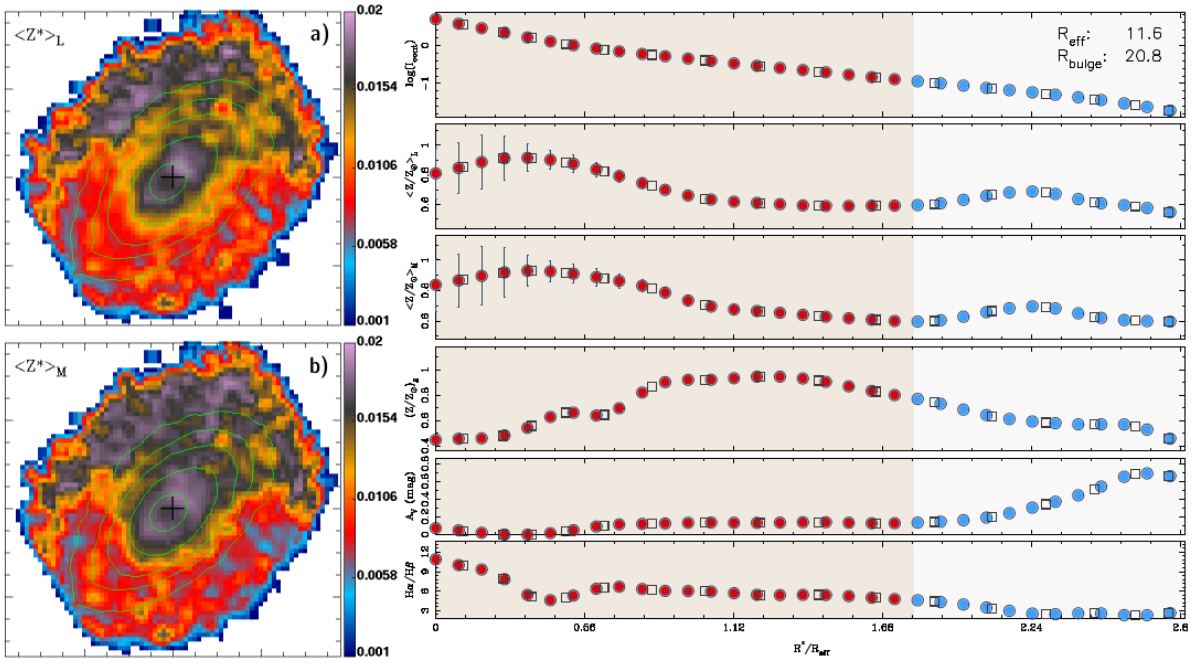

Figure C.17: Metallicity maps and radial profiles of NGC2639.

NGC2730

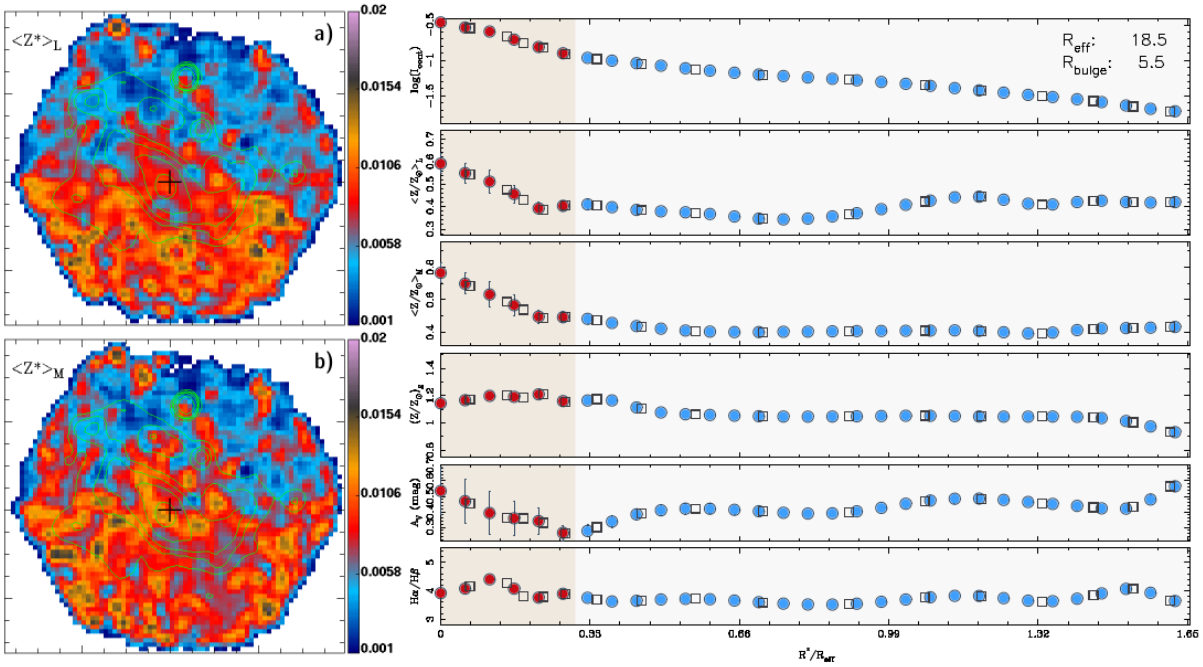

Figure C.18: Metallicity maps and radial profiles of NGC2730.

NGC2906

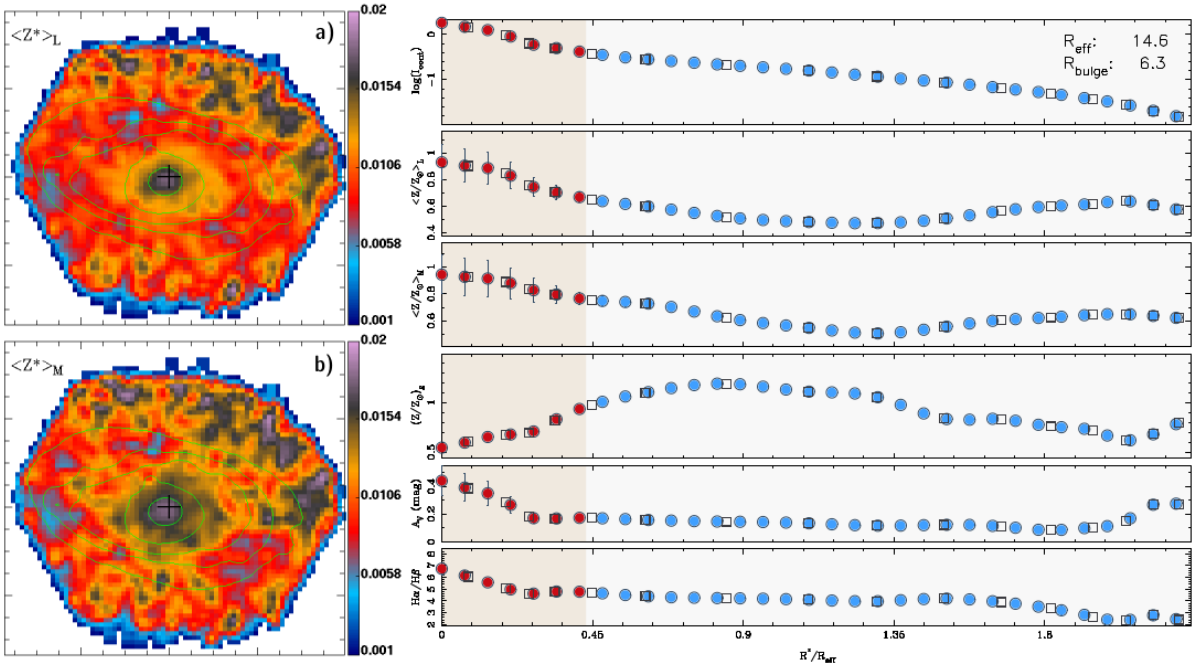

Figure C.19: Metallicity maps and radial profiles of NGC2906.

NGC2916

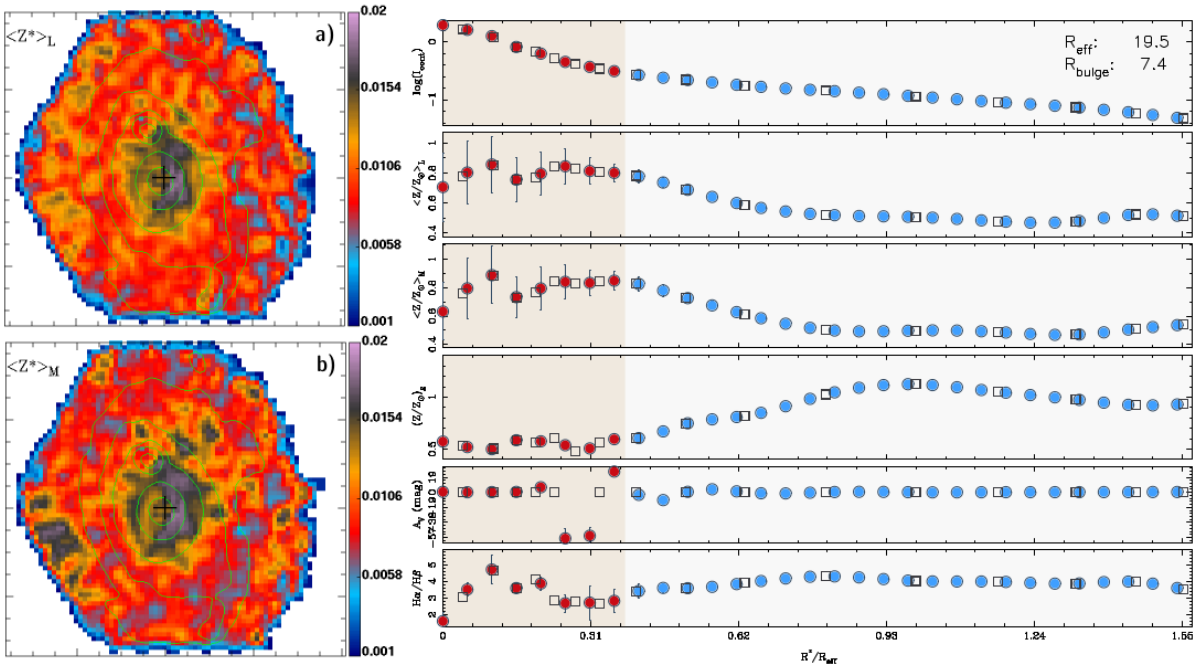

Figure C.20: Metallicity maps and radial profiles of NGC2916.

NGC3300

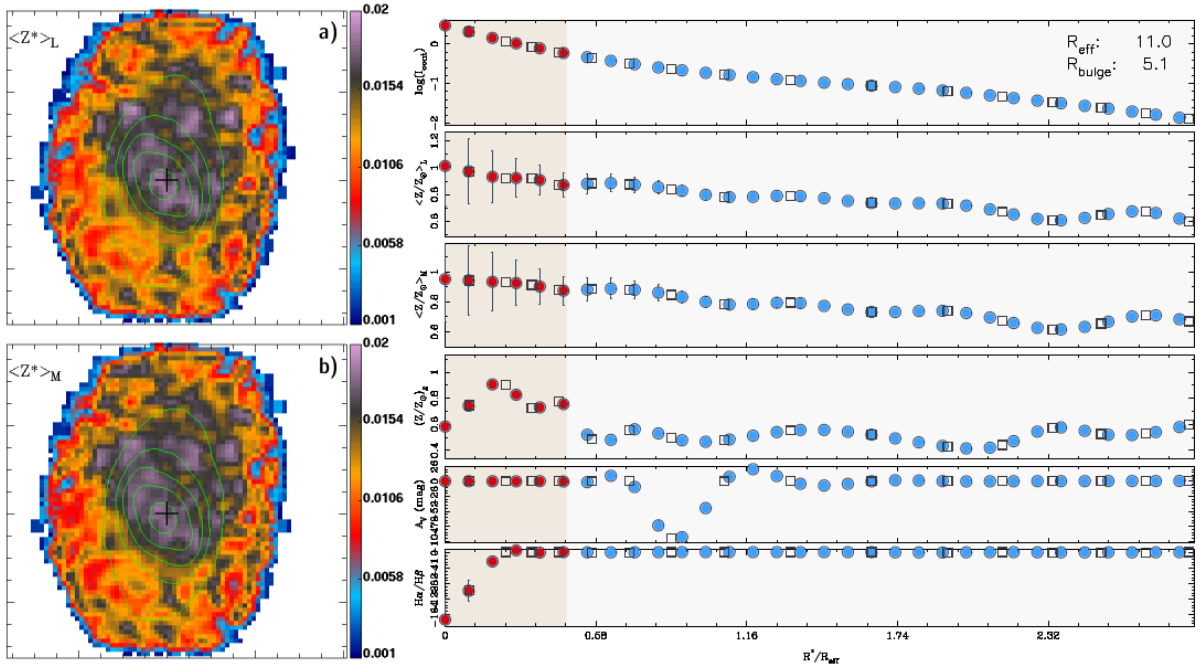

Figure C.21: Metallicity maps and radial profiles of NGC3300.

NGC3381

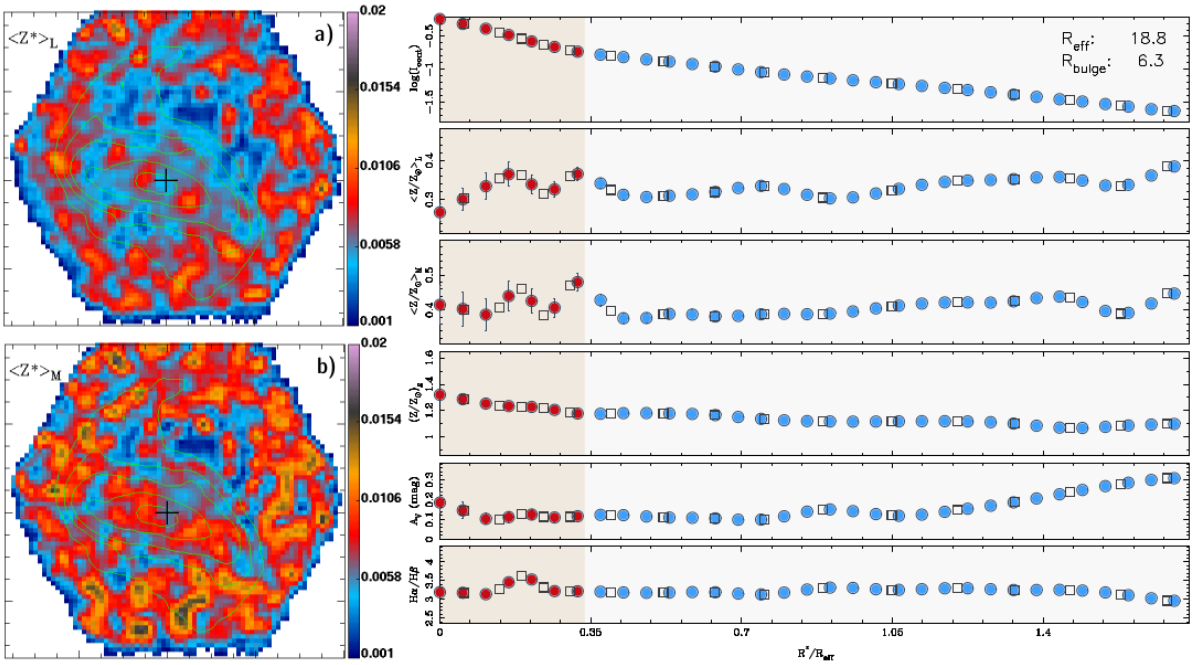

Figure C.22: Metallicity maps and radial profiles of NGC3381.

NGC3614

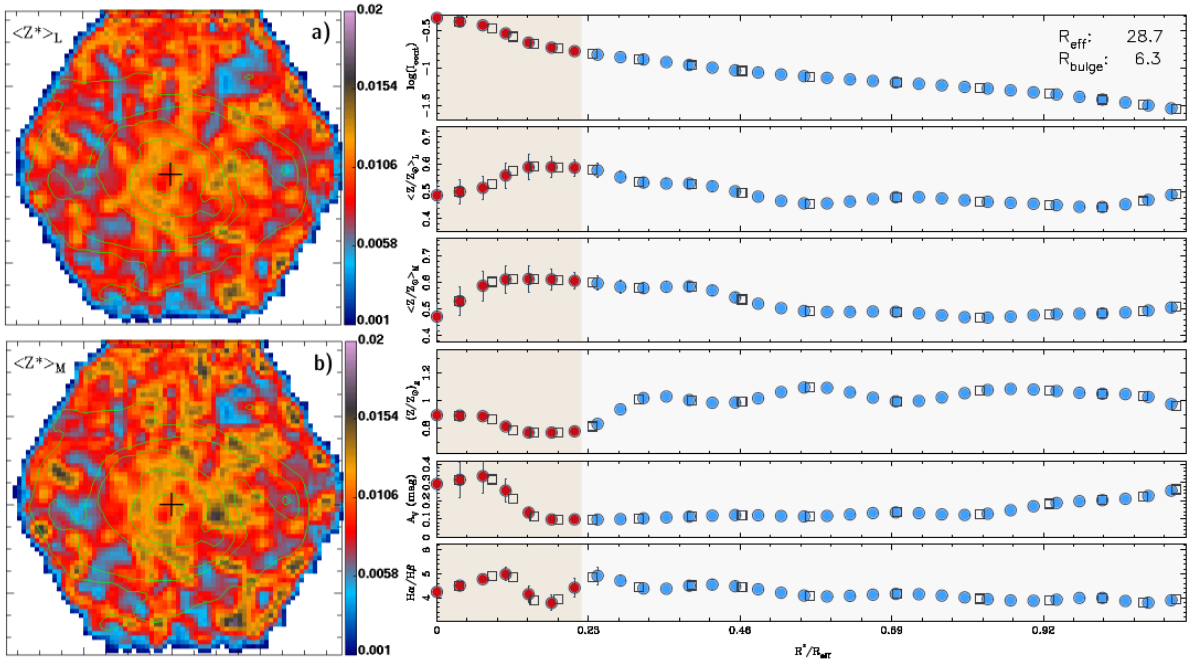

Figure C.23: Metallicity maps and radial profiles of NGC3614.

NGC3687

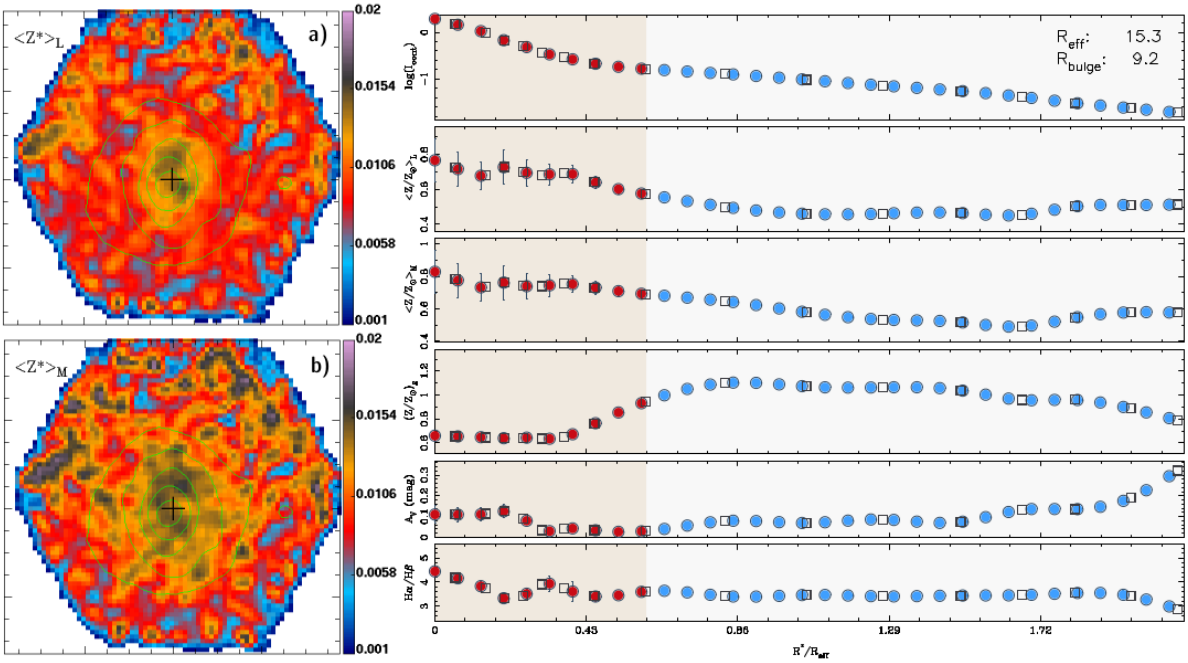

Figure C.24: Metallicity maps and radial profiles of NGC3687.

NGC4003

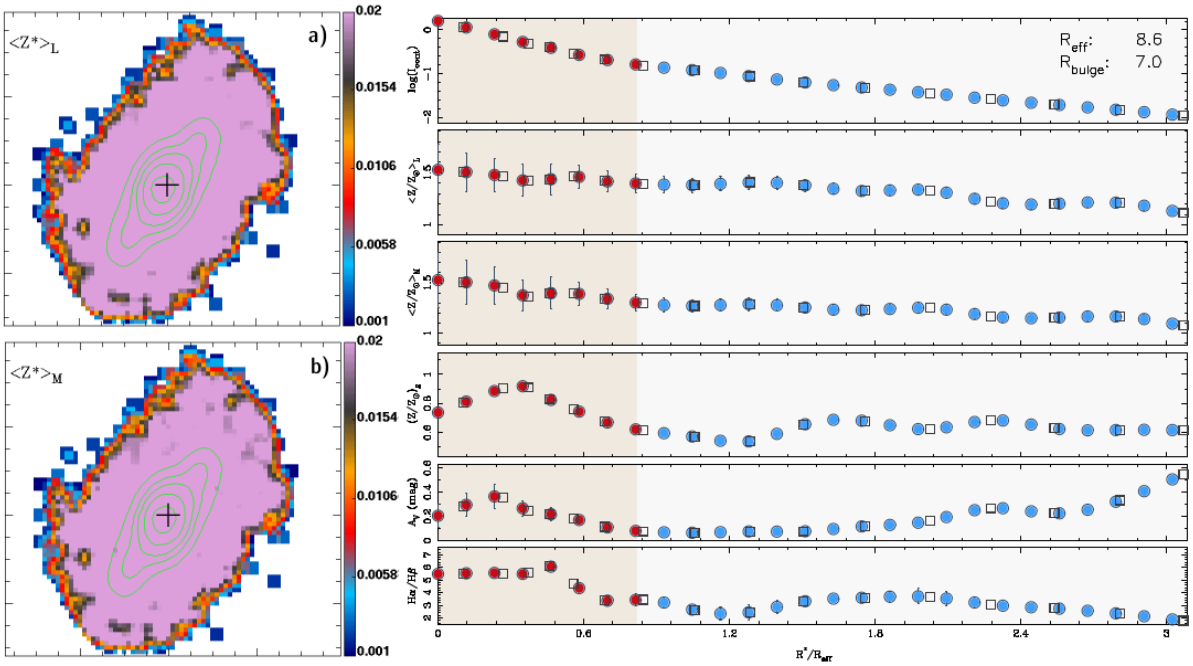

Figure C.25: Metallicity maps and radial profiles of NGC4003.

NGC4047

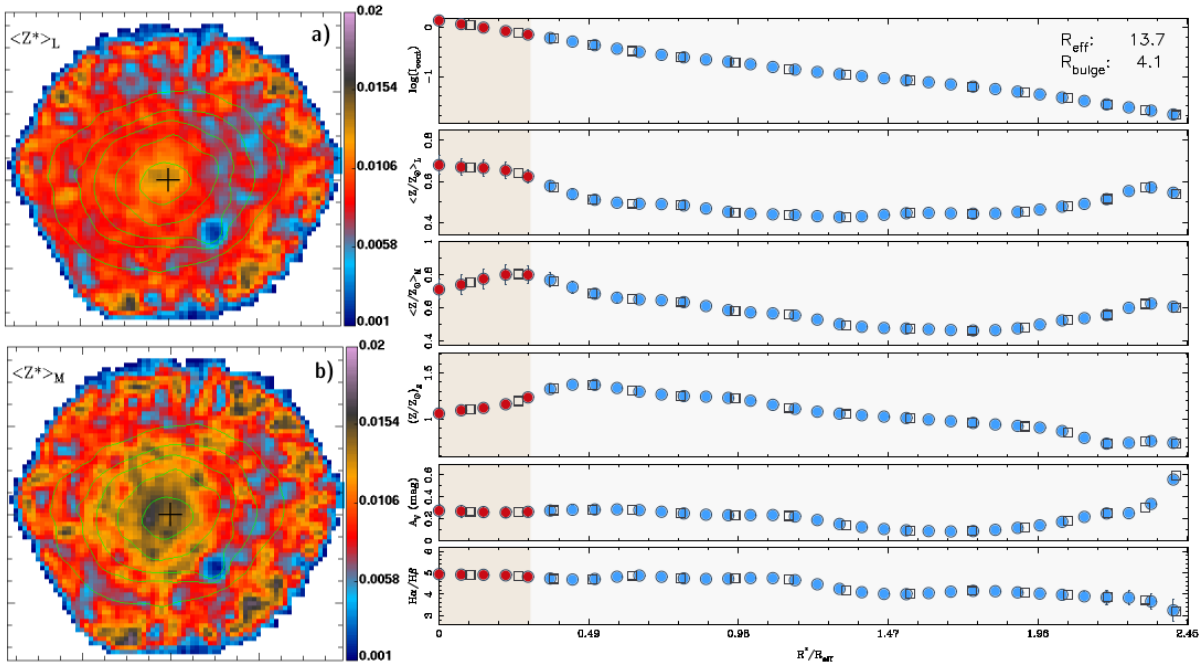

Figure C.26: Metallicity maps and radial profiles of NGC4047.

NGC4185

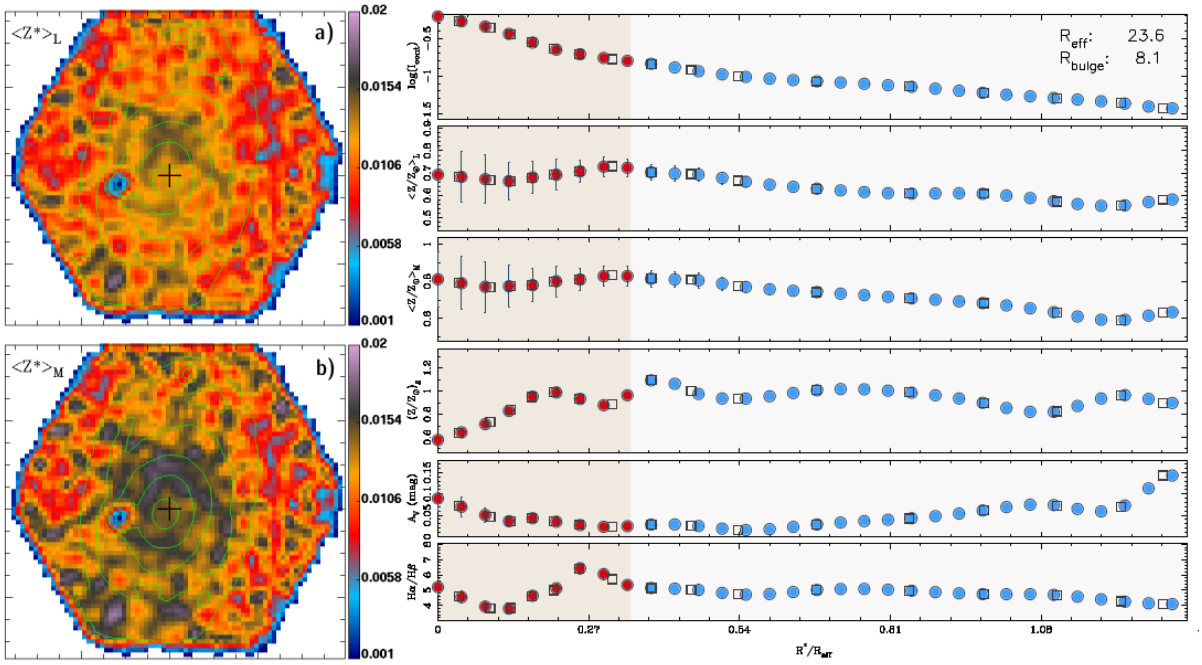

Figure C.27: Metallicity maps and radial profiles of NGC4185.

NGC4210

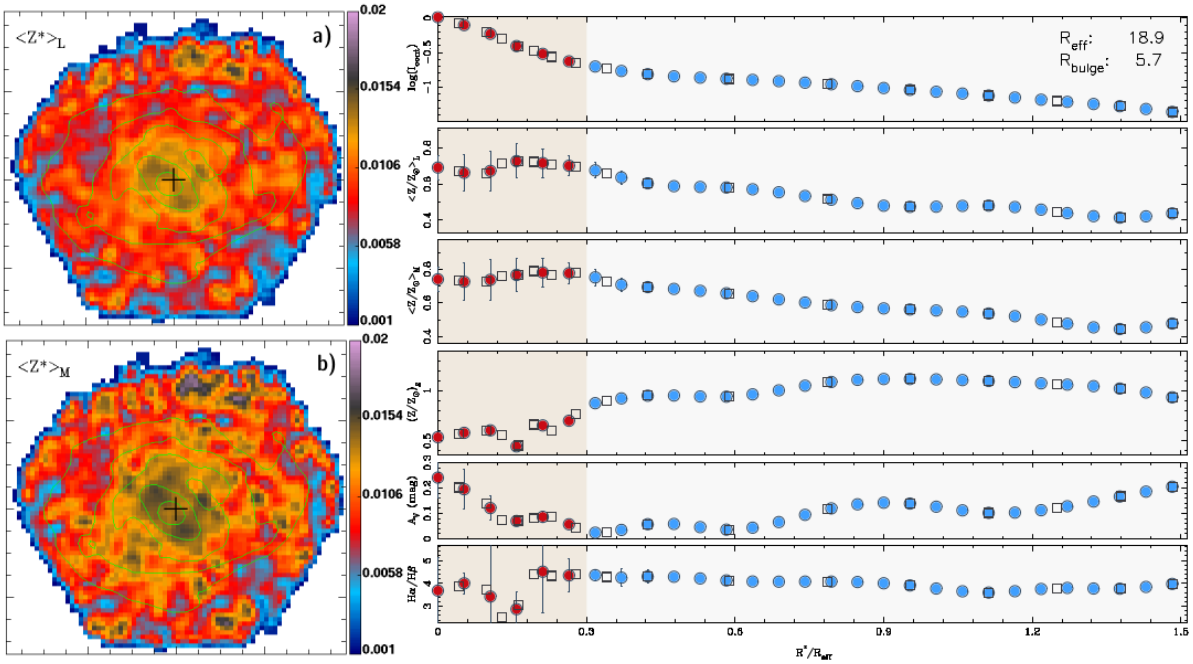

Figure C.28: Metallicity maps and radial profiles of NGC4210.

NGC4961

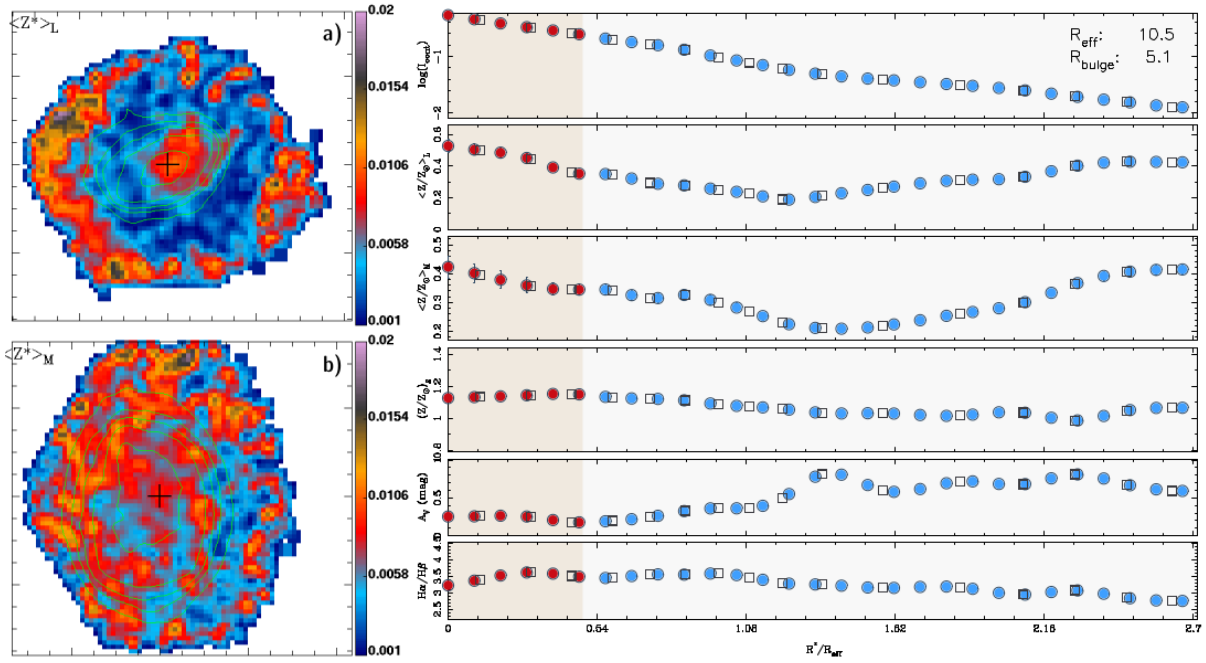

Figure C.29: Metallicity maps and radial profiles of NGC4961.

NGC5000

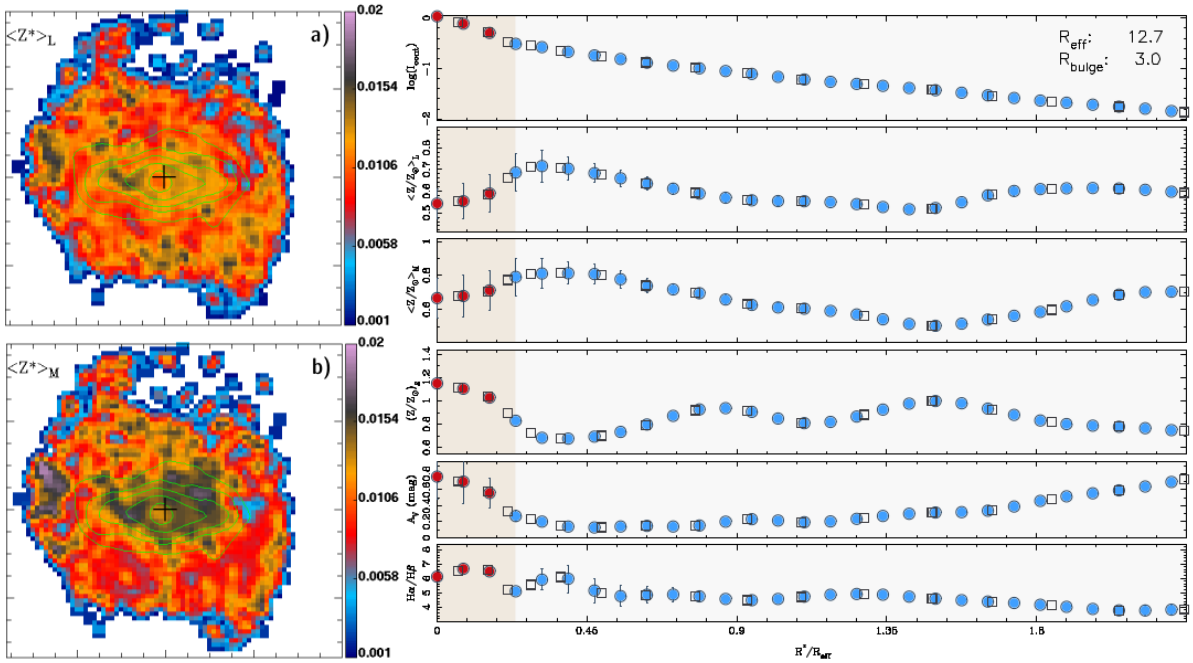

Figure C.30: Metallicity maps and radial profiles of NGC5000.

NGC5016

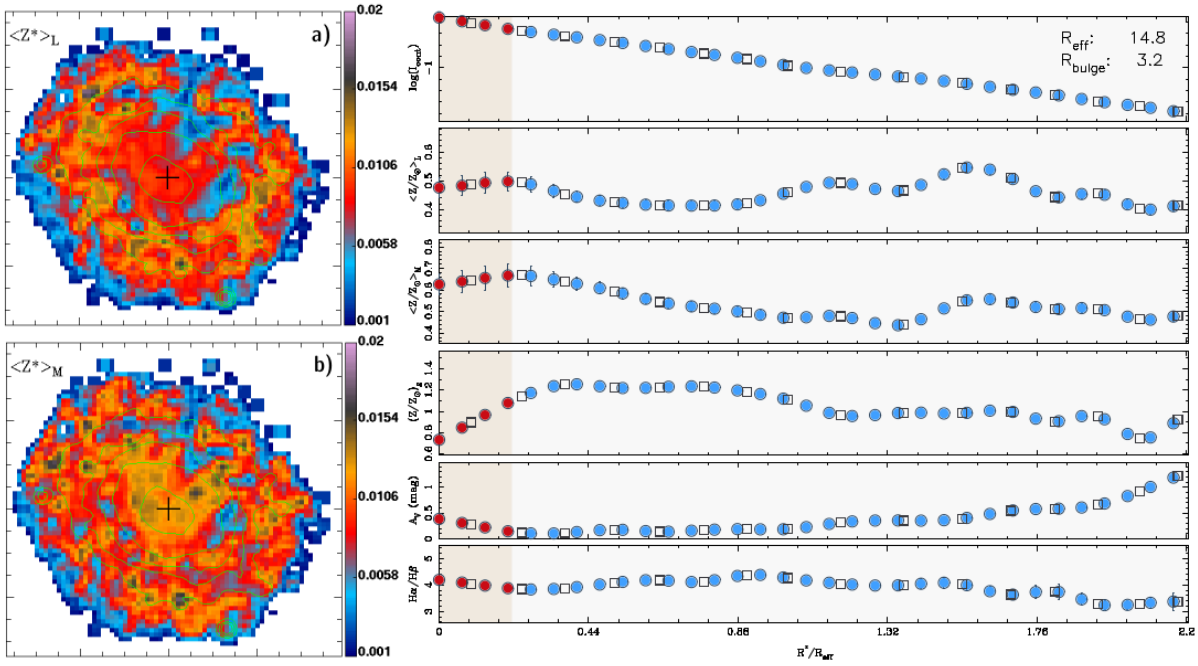

Figure C.31: Metallicity maps and radial profiles of NGC5016.

NGC5205

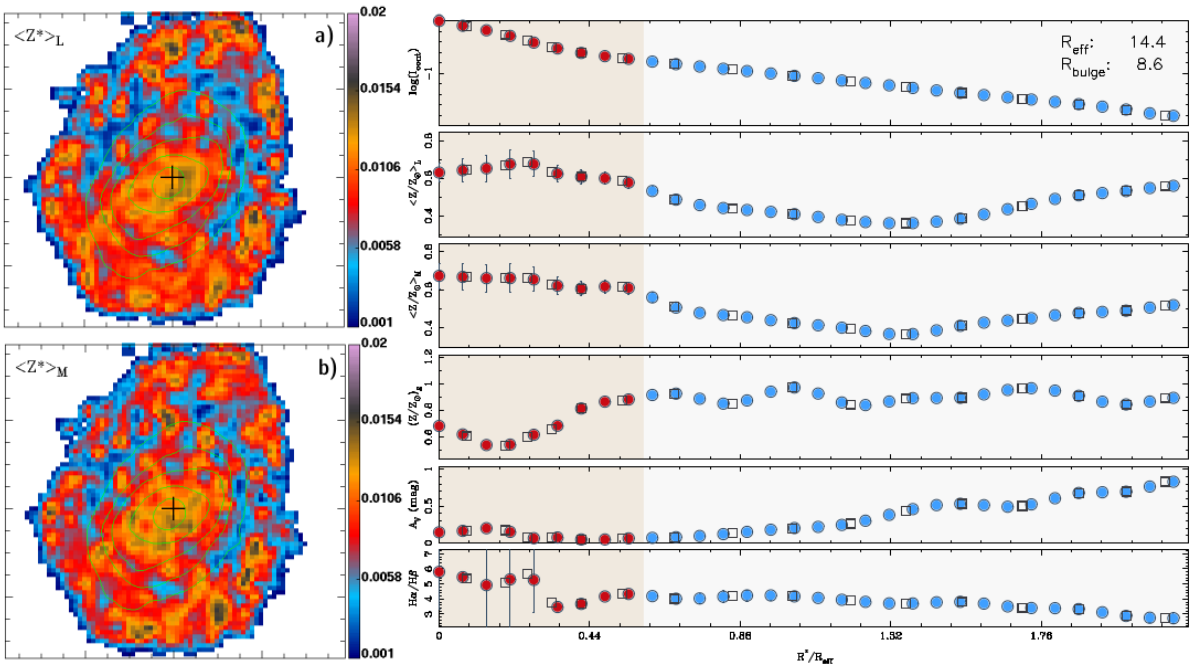

Figure C.32: Metallicity maps and radial profiles of NGC5205.

NGC5320

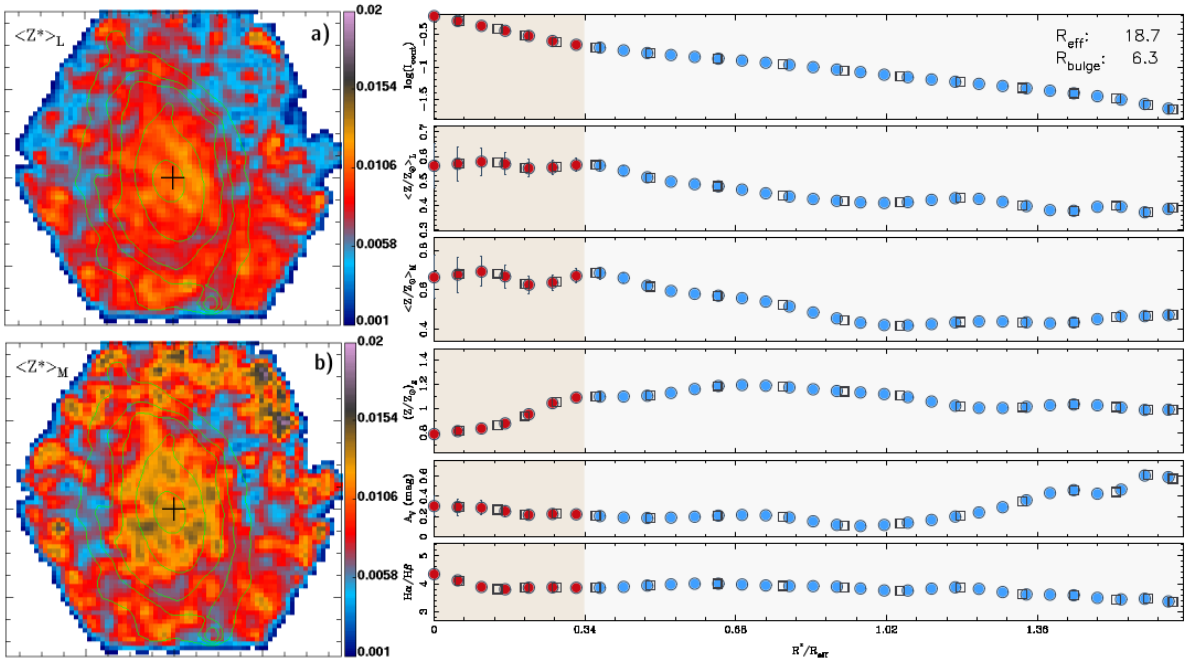

Figure C.33: Metallicity maps and radial profiles of NGC5320.

NGC5378

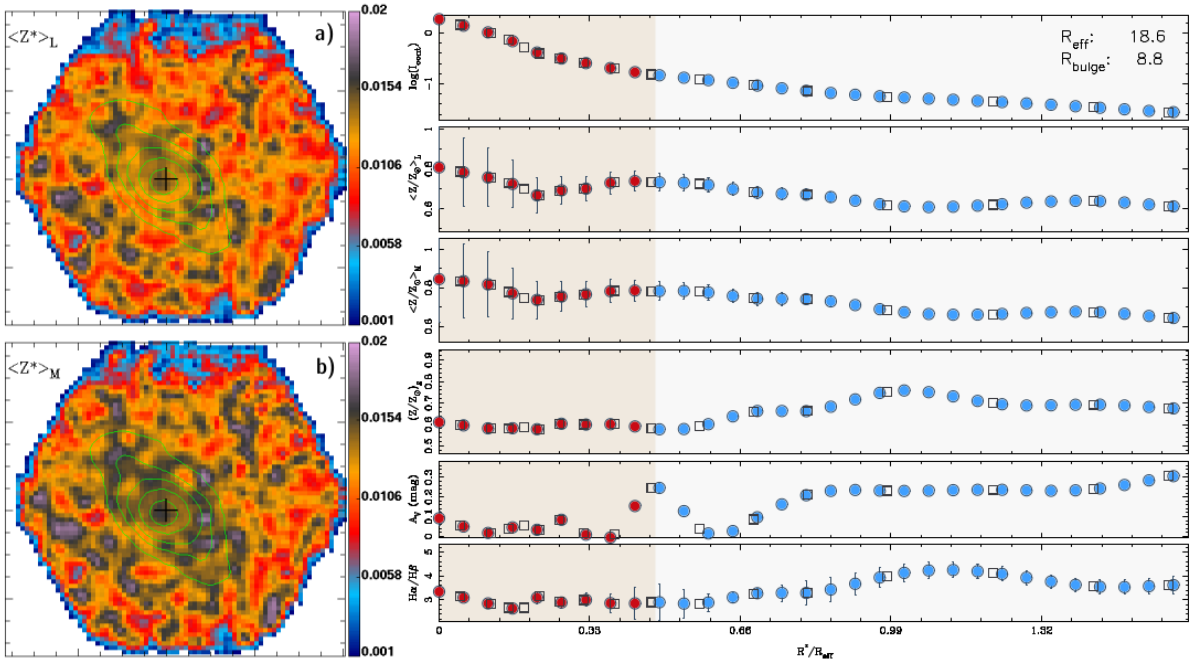

Figure C.34: Metallicity maps and radial profiles of NGC5378.

NGC5406

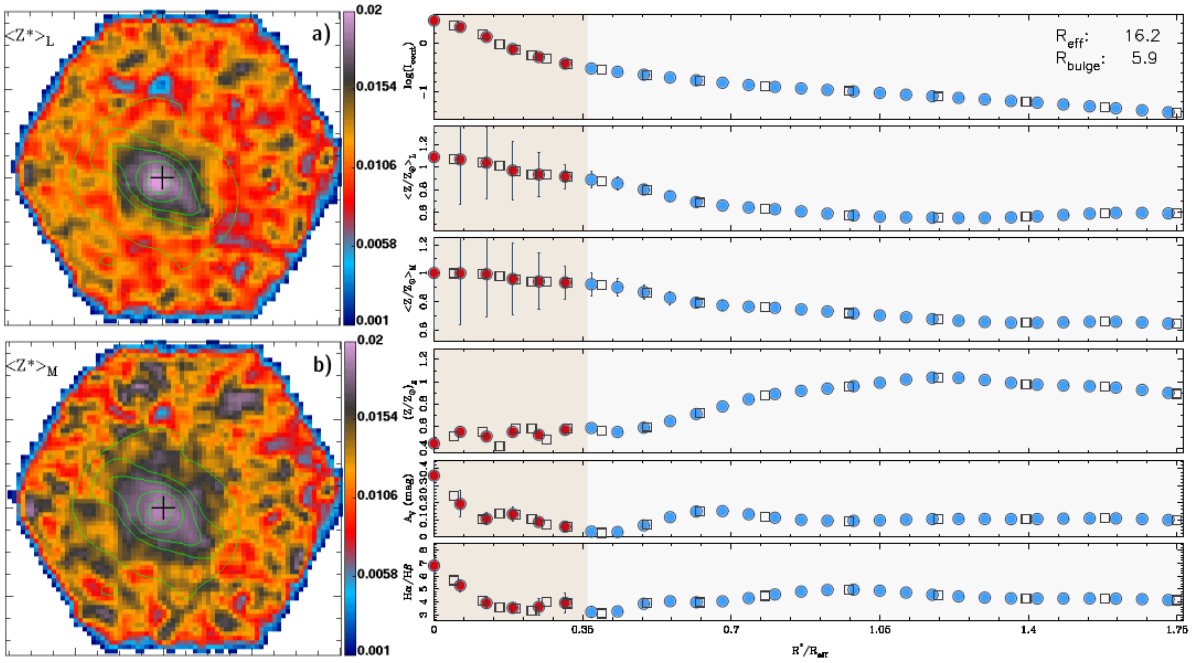

Figure C.35: Metallicity maps and radial profiles of NGC5406.

NGC5480

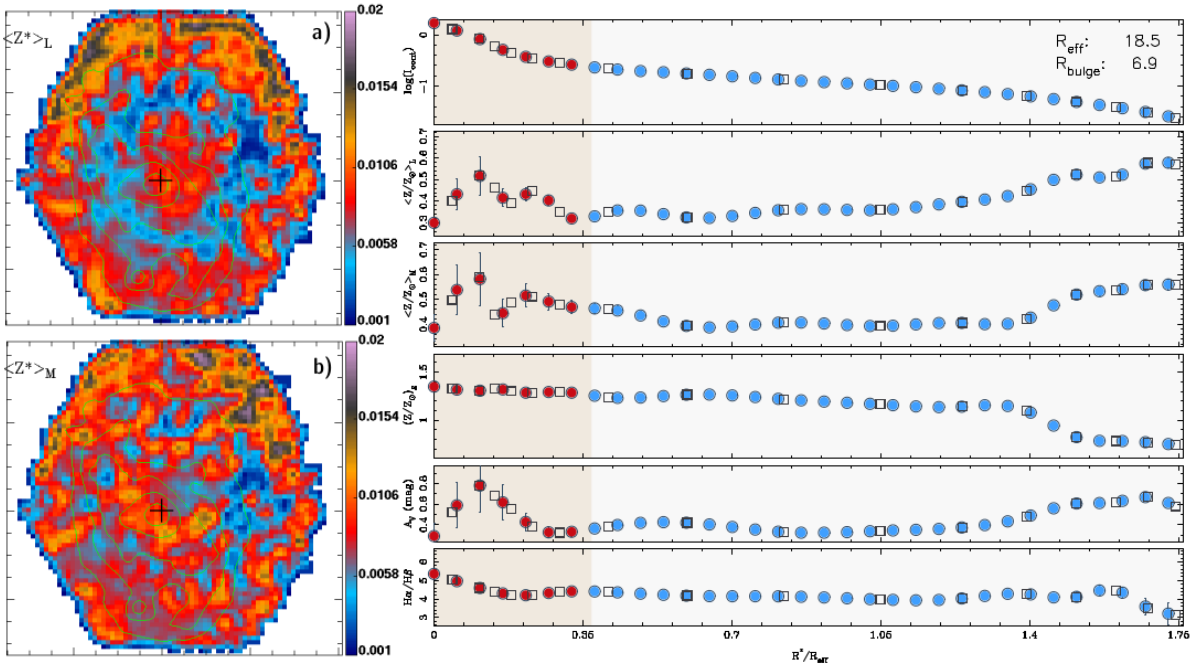

Figure C.36: Metallicity maps and radial profiles of NGC5480.

NGC5614

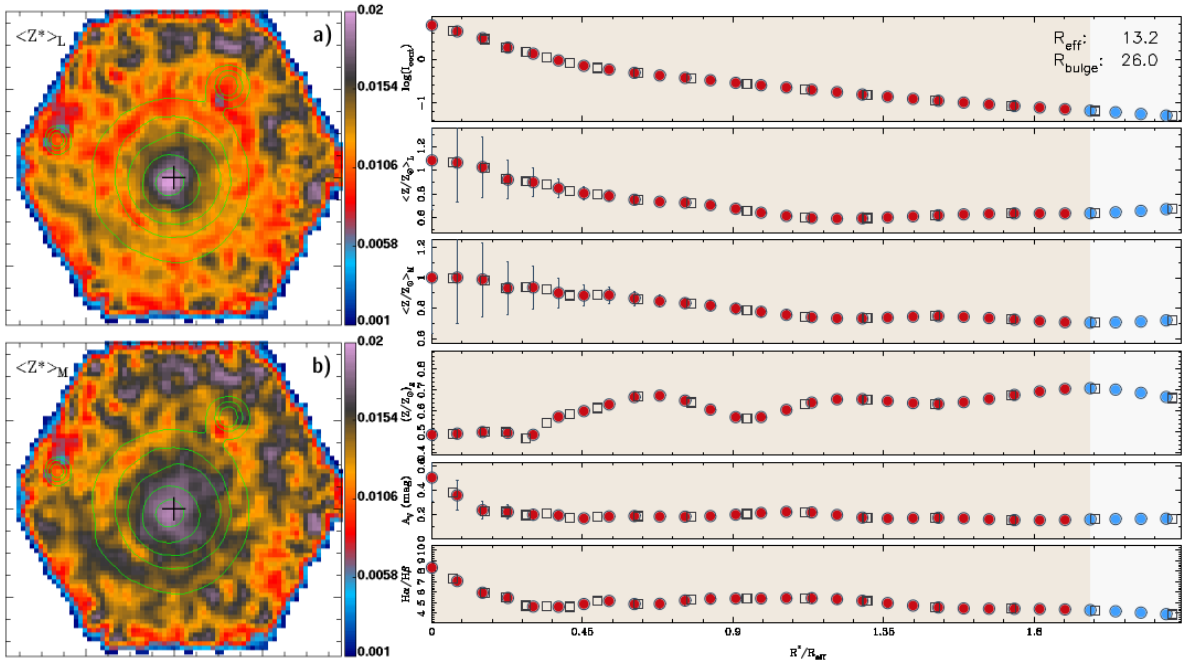

Figure C.37: Metallicity maps and radial profiles of NGC5614.

NGC5656

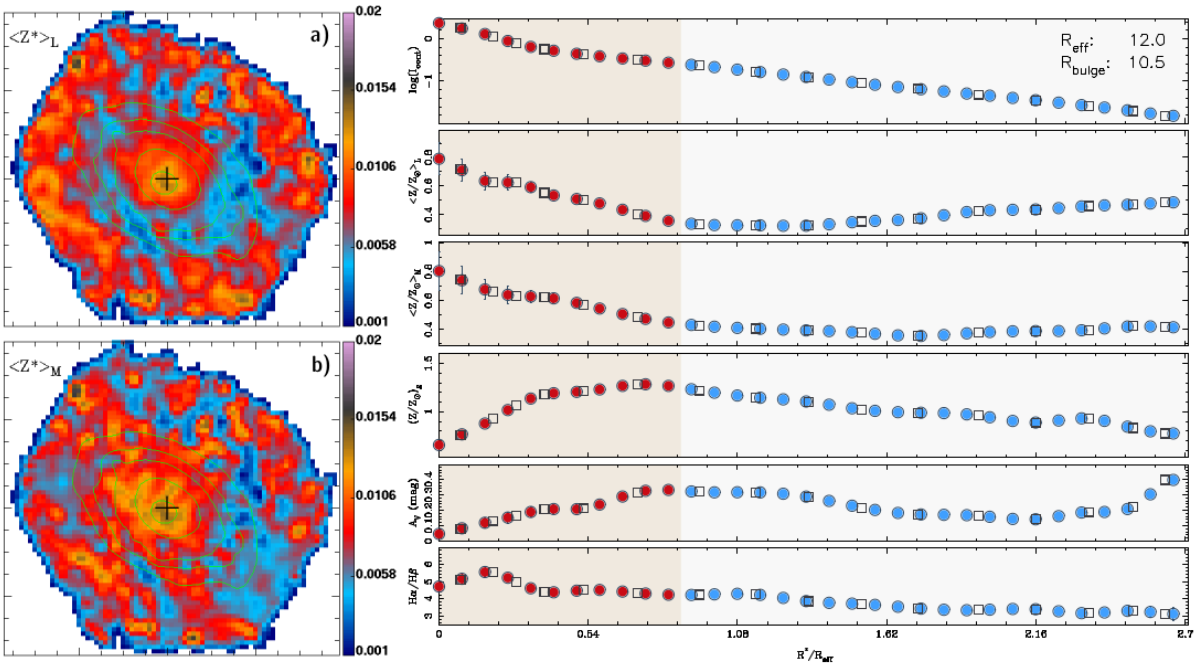

Figure C.38: Metallicity maps and radial profiles of NGC5656.

NGC5735

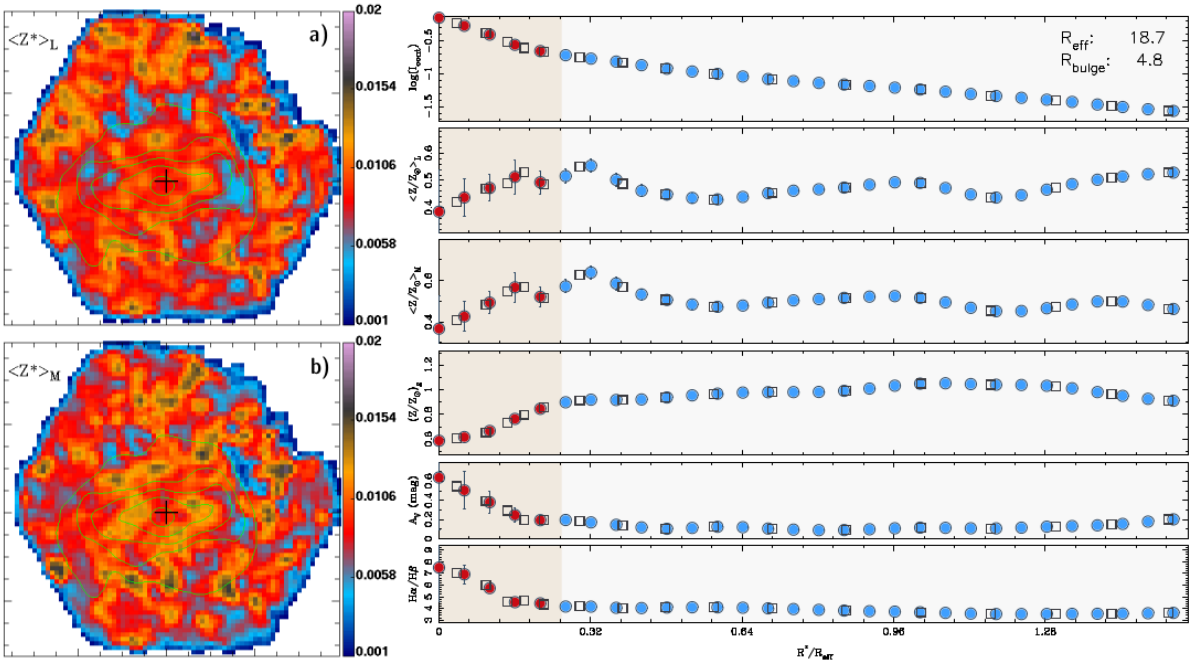

Figure C.39: Metallicity maps and radial profiles of NGC5735.

NGC5772

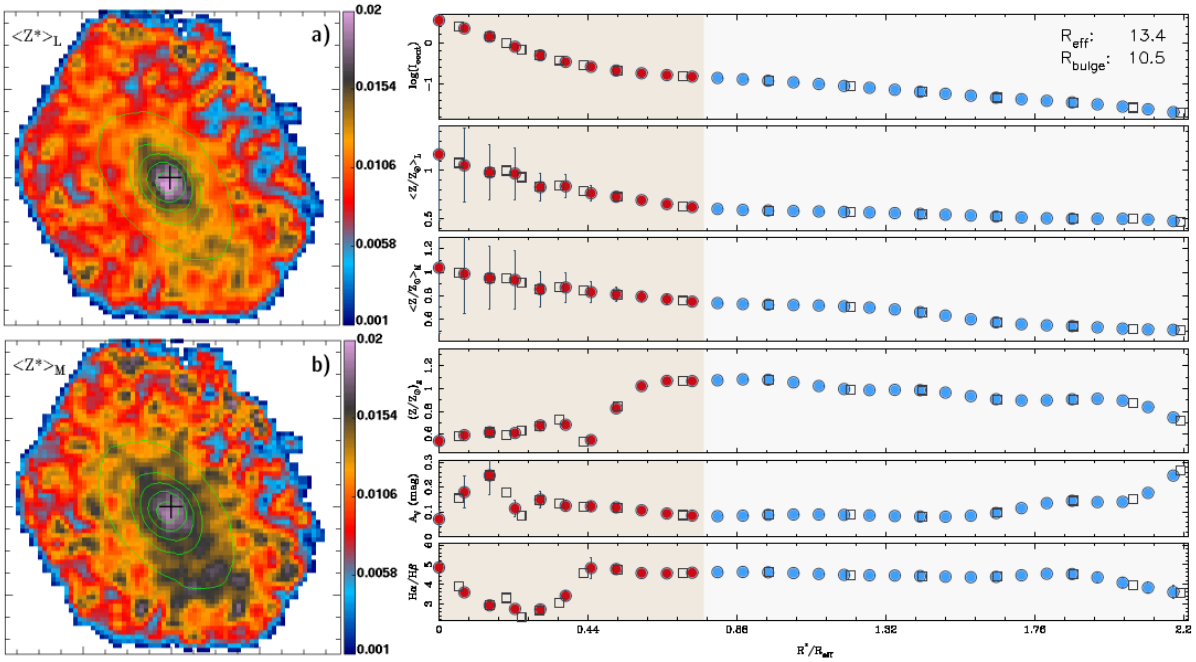

Figure C.40: Metallicity maps and radial profiles of NGC5772.

NGC5829

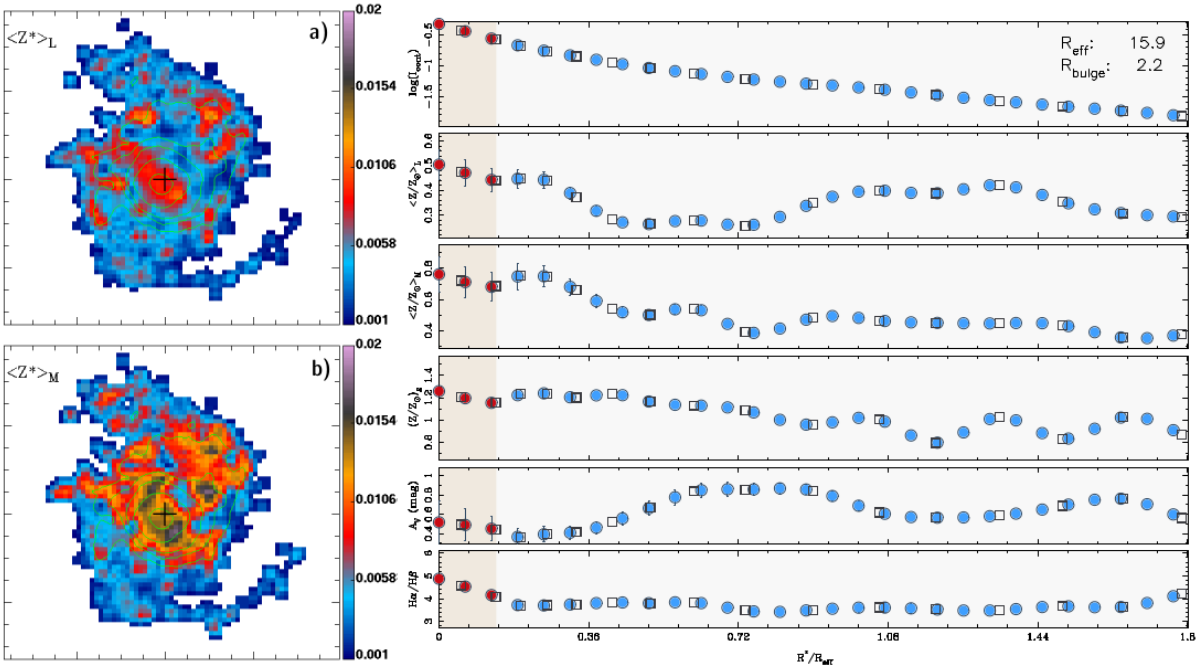

Figure C.41: Metallicity maps and radial profiles of NGC5829.

NGC6004

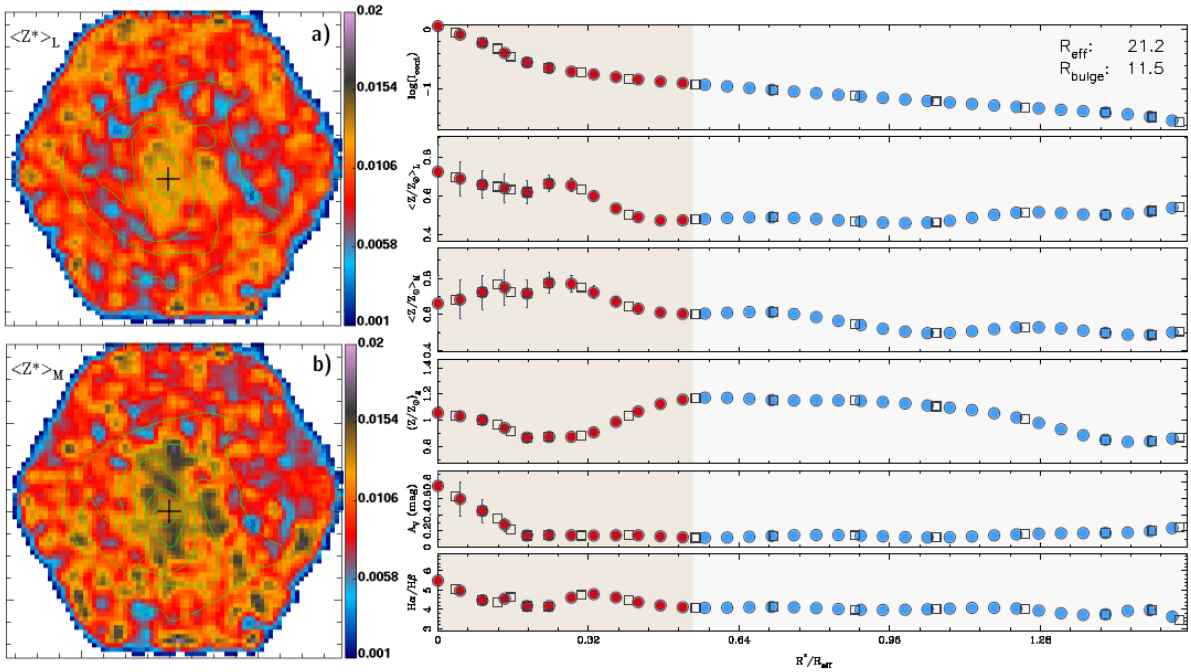

Figure C.42: Metallicity maps and radial profiles of NGC6004.

NGC6032

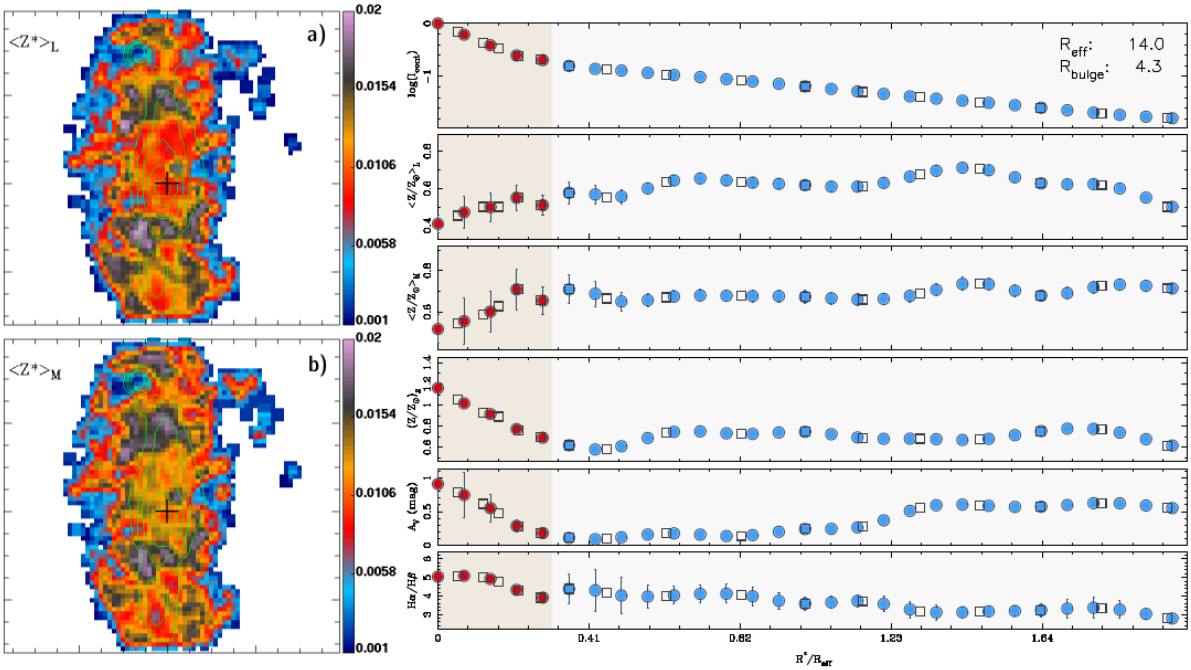

Figure C.43: Metallicity maps and radial profiles of NGC6032.

NGC6186

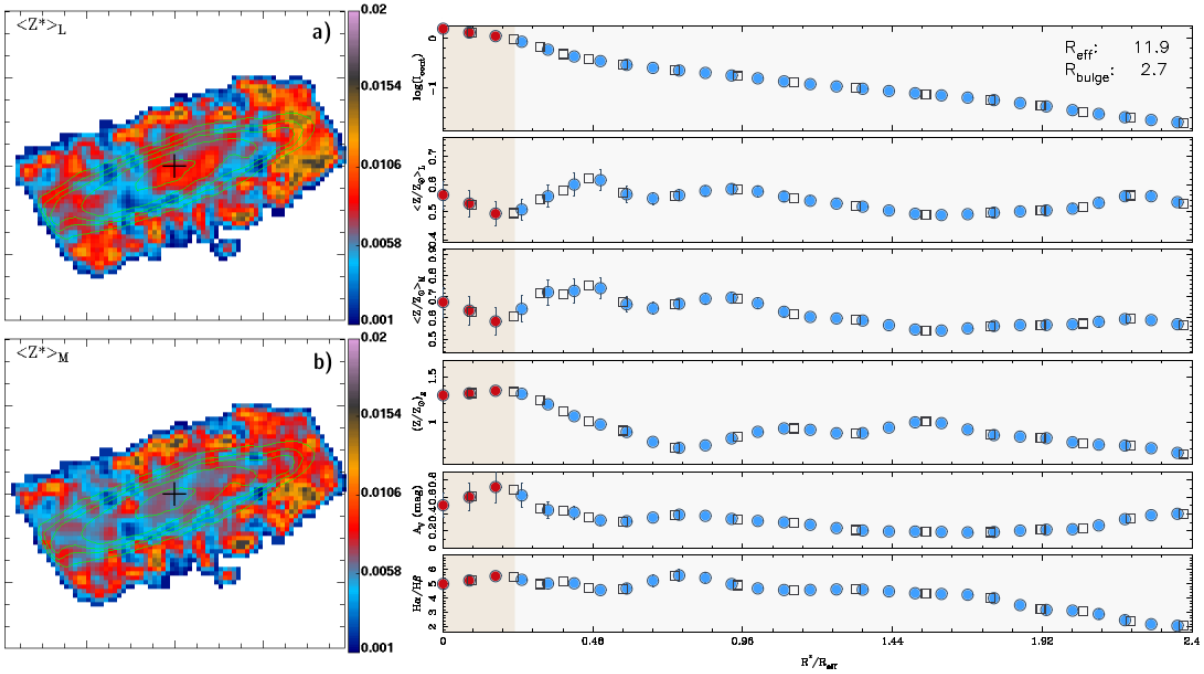

Figure C.44: Metallicity maps and radial profiles of NGC6186.

NGC6278

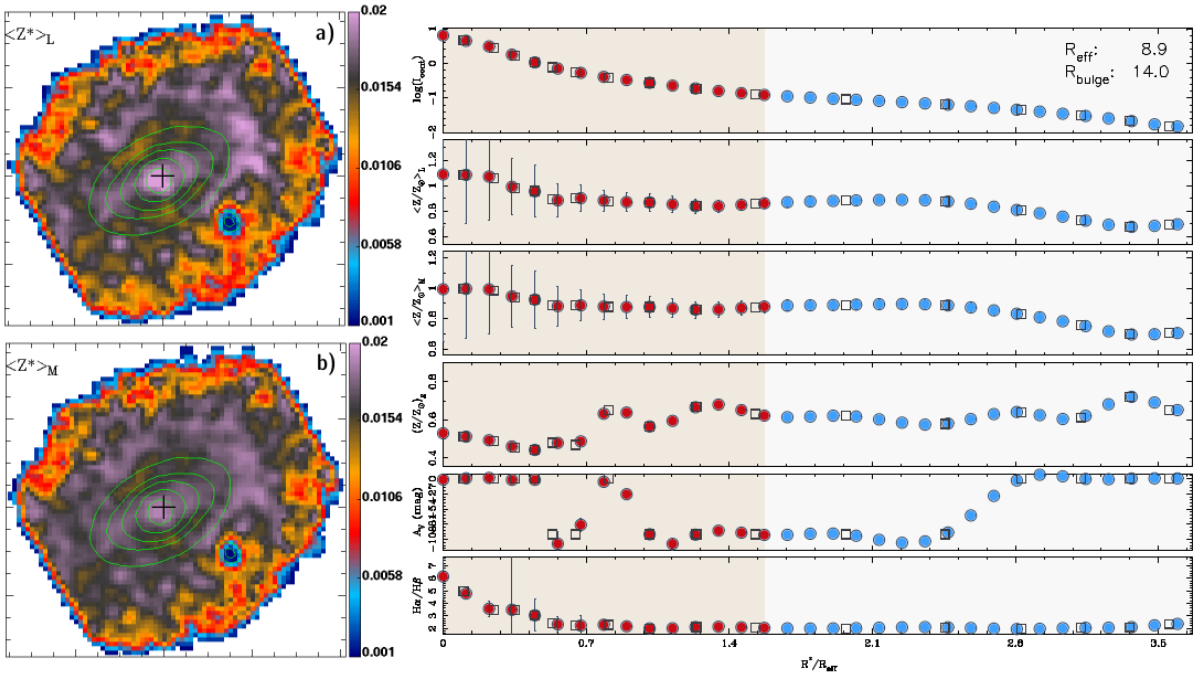

Figure C.45: Metallicity maps and radial profiles of NGC6278.

NGC6941

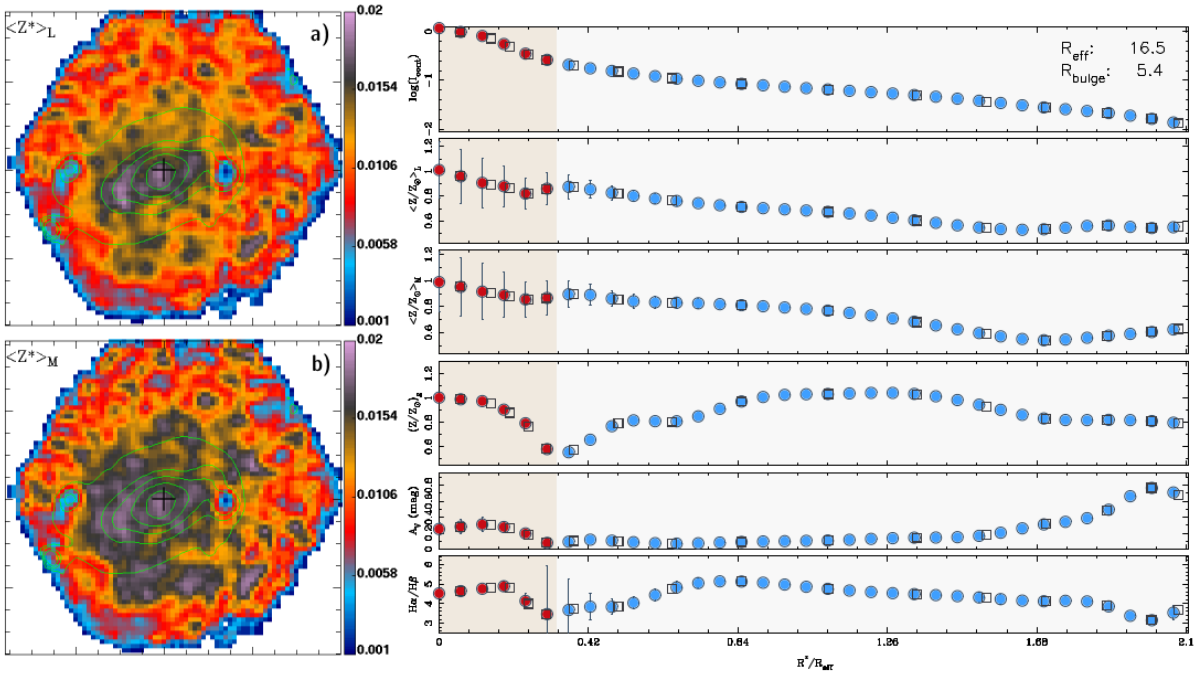

Figure C.46: Metallicity maps and radial profiles of NGC6941.

NGC7321

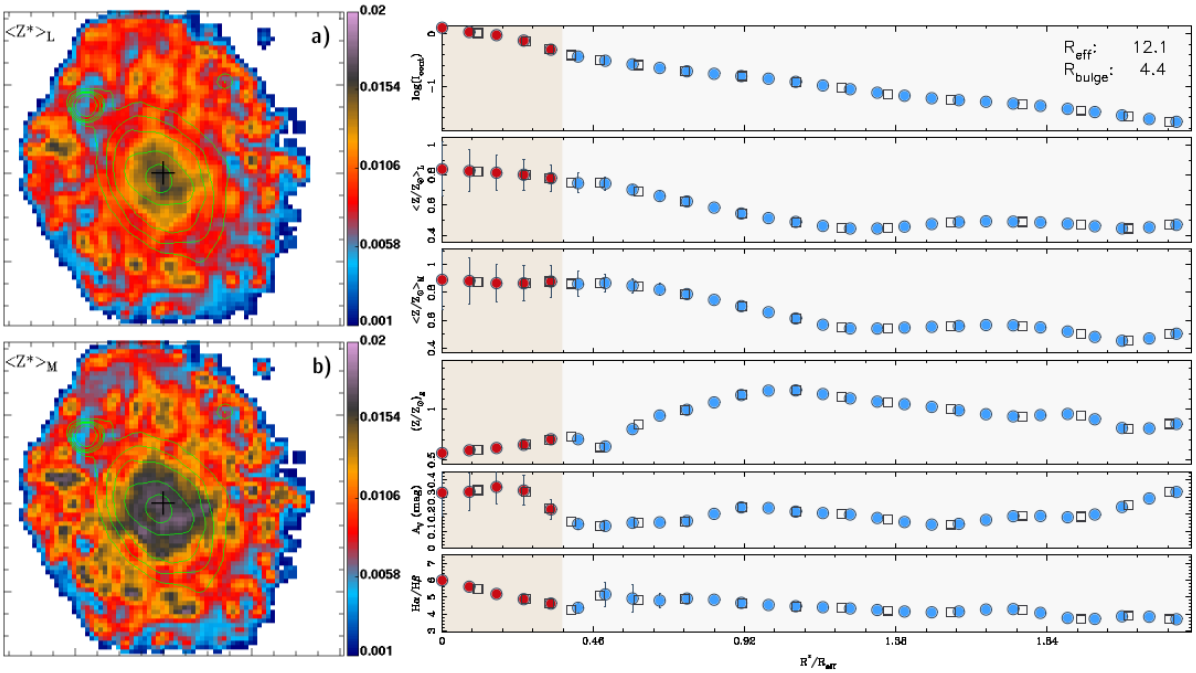

Figure C.47: Metallicity maps and radial profiles of NGC7321.

NGC7489

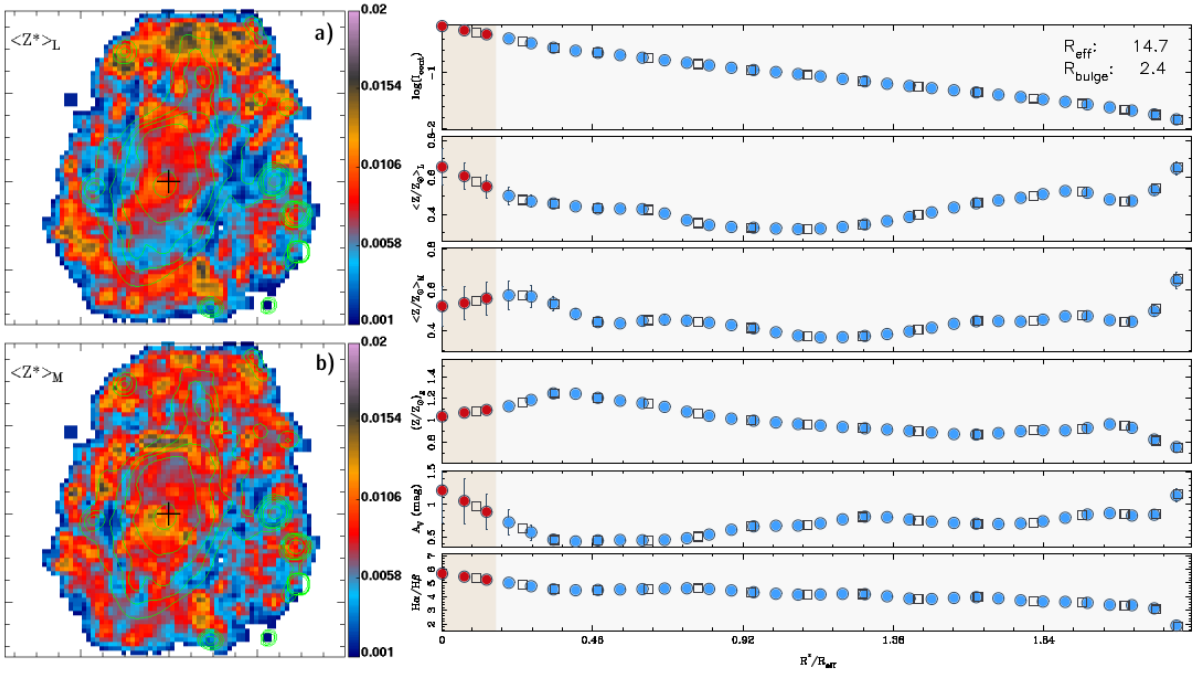

Figure C.48: Metallicity maps and radial profiles of NGC7489.

NGC7625

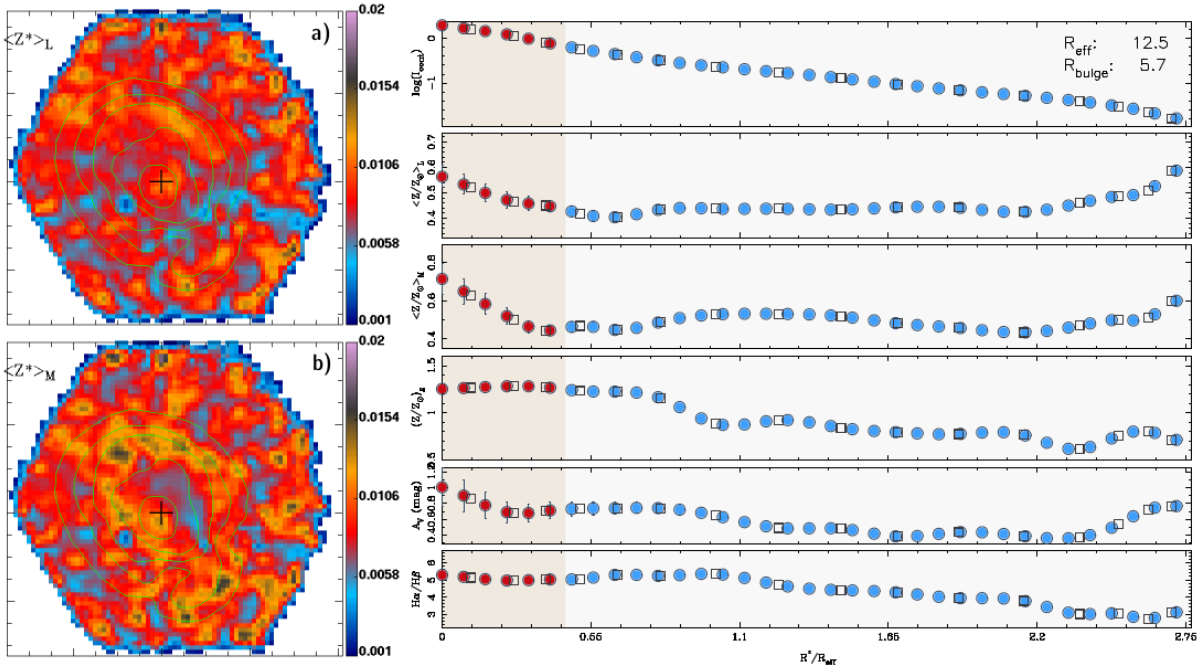

Figure C.49: Metallicity maps and radial profiles of NGC7625.

NGC7653

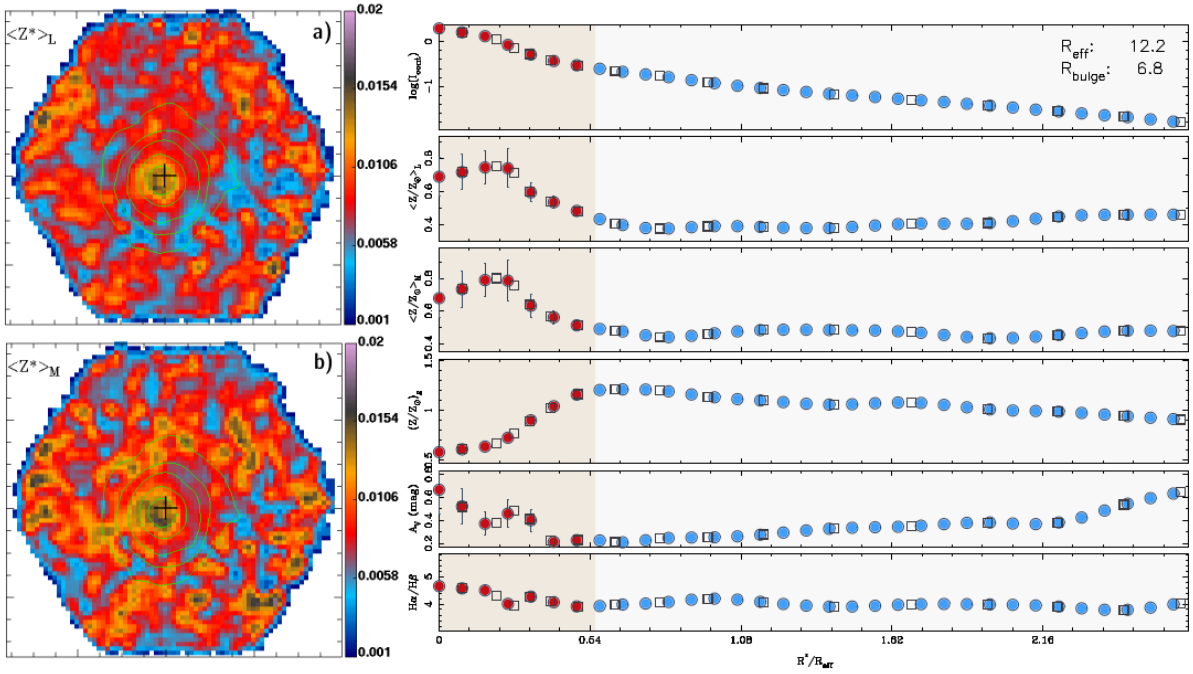

Figure C.50: Metallicity maps and radial profiles of NGC7653.

NGC7691

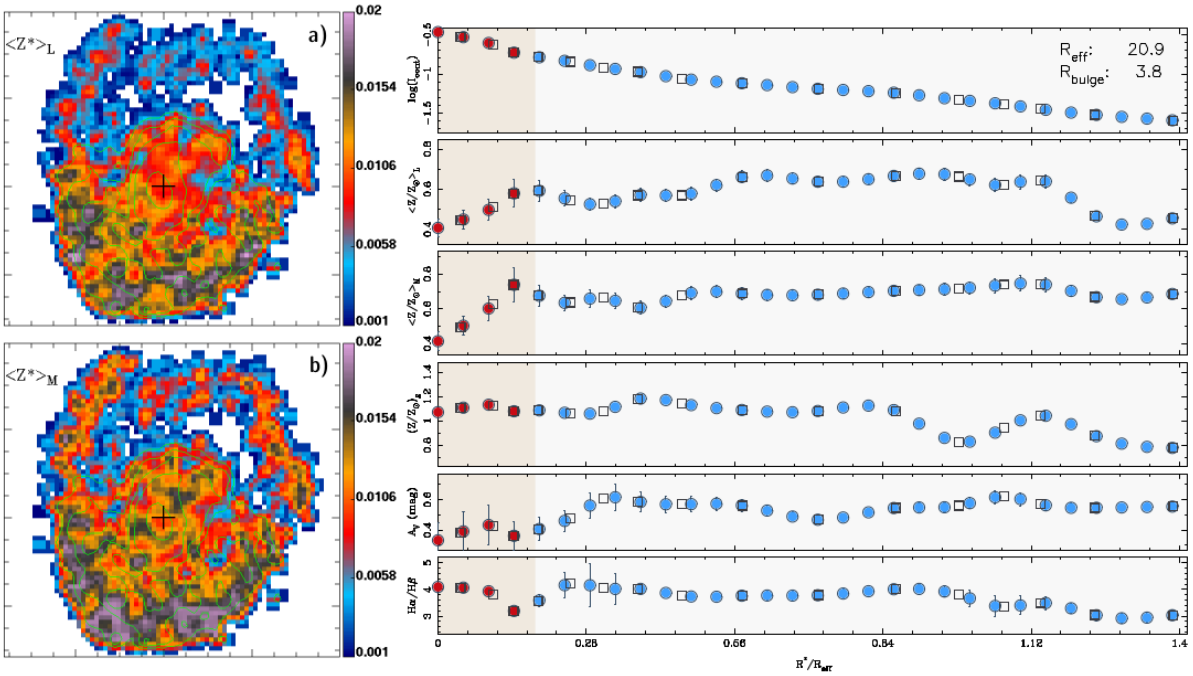

Figure C.51: Metallicity maps and radial profiles of NGC7691.

NGC7716

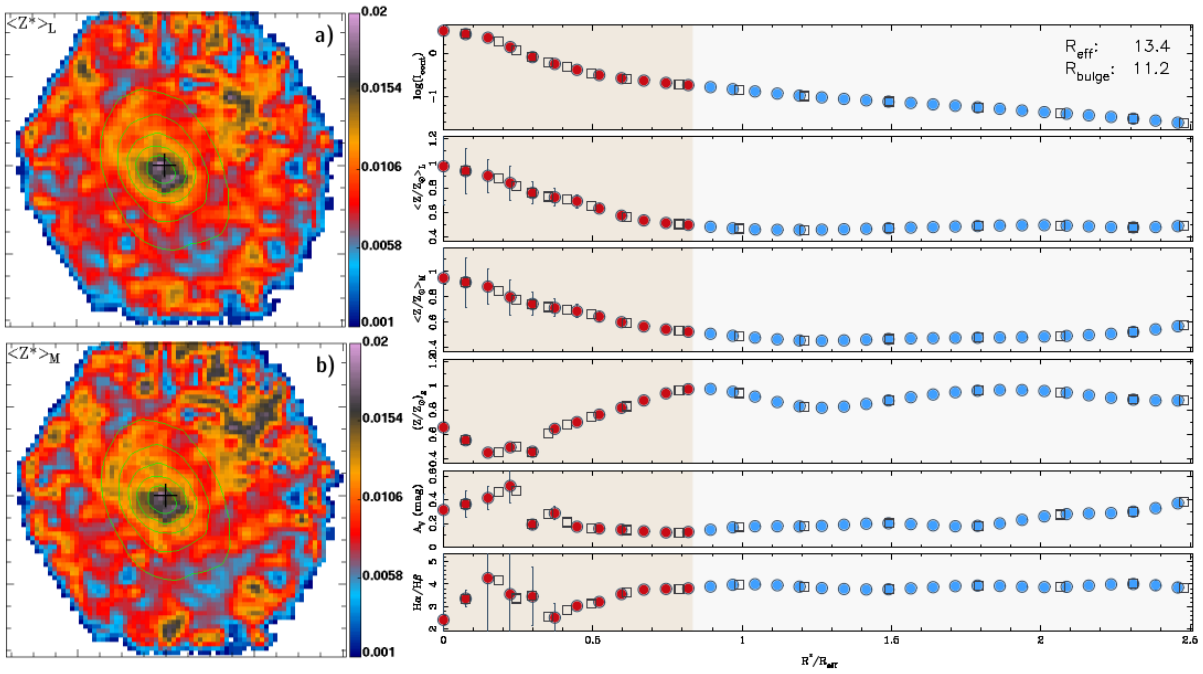

Figure C.52: Metallicity maps and radial profiles of NGC7716.

NGC7738

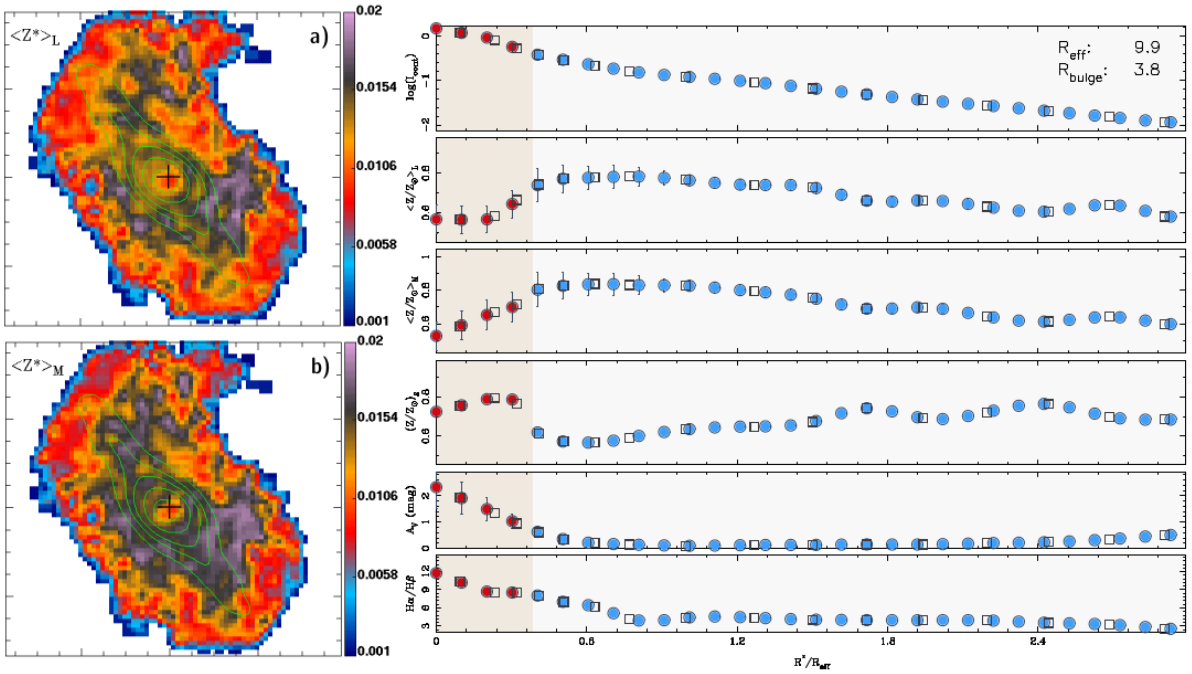

Figure C.53: Metallicity maps and radial profiles of NGC7738.

NGC7819

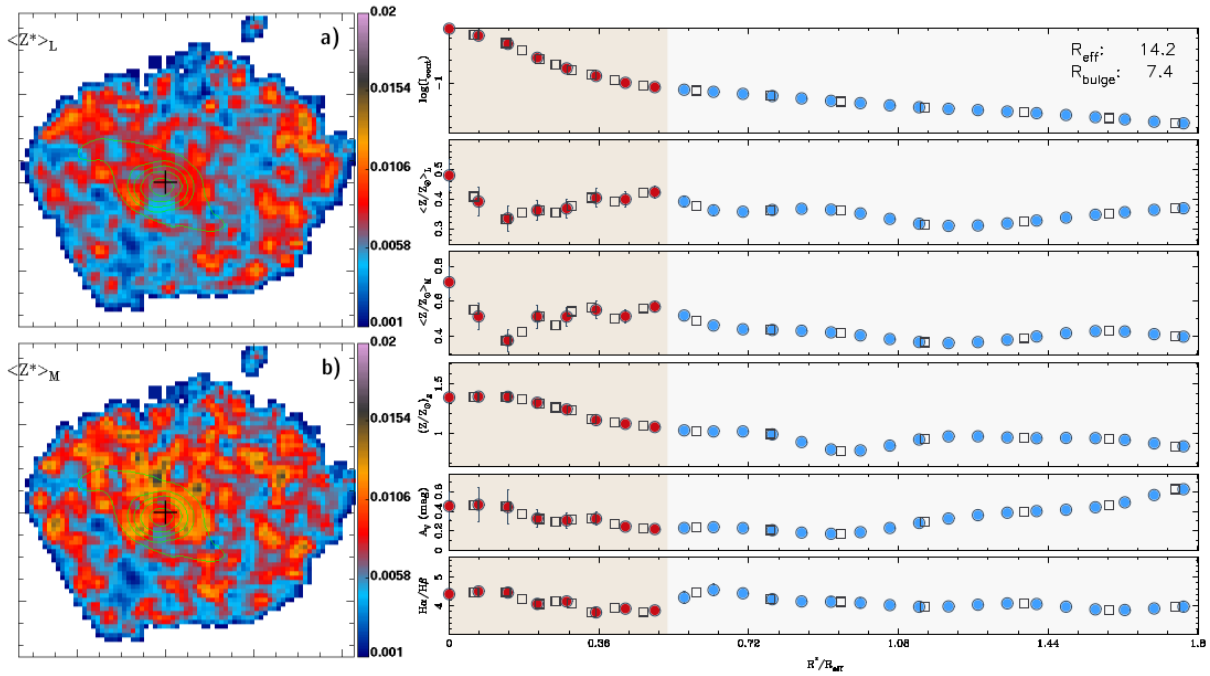

Figure C.54: Metallicity maps and radial profiles of NGC7819.

UGC07012

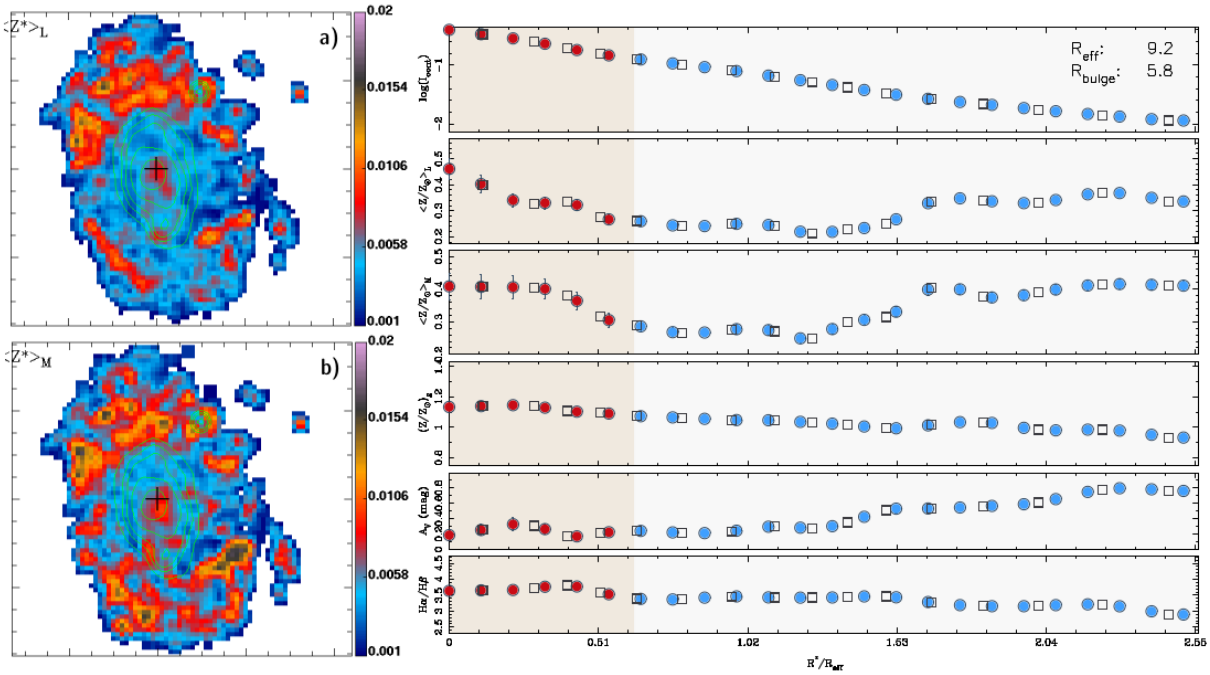

Figure C.55: Metallicity maps and radial profiles of UGC07012.

UGC08234

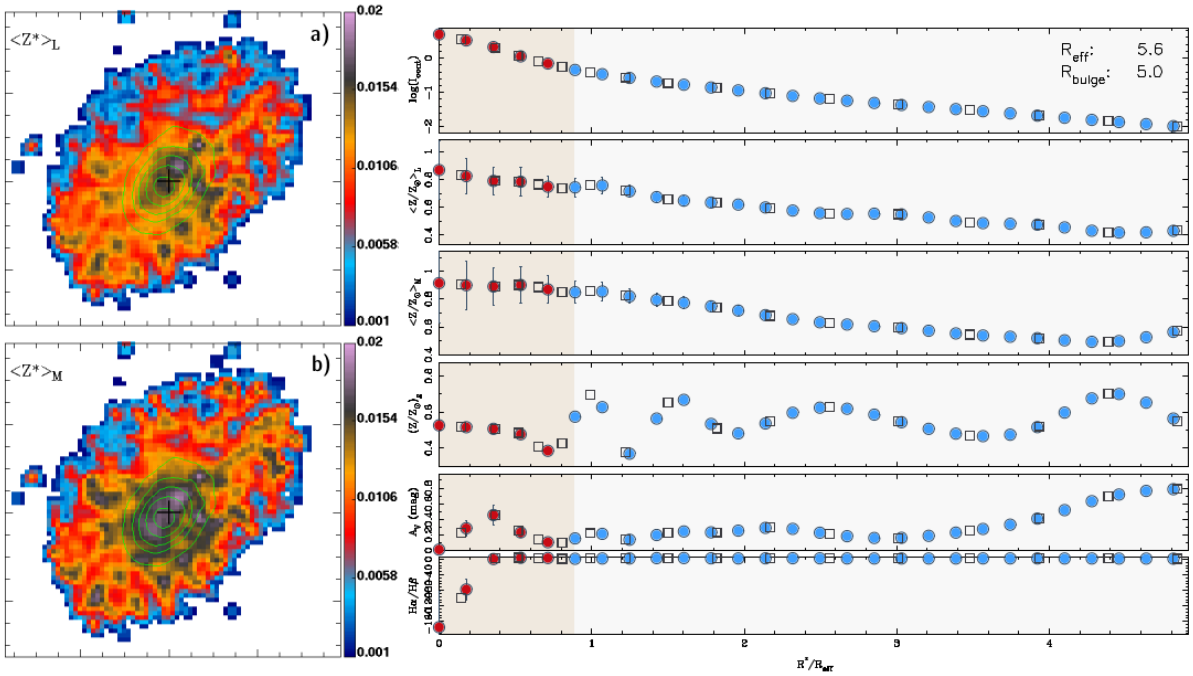

Figure C.56: Metallicity maps and radial profiles of UGC08234.

UGC08733

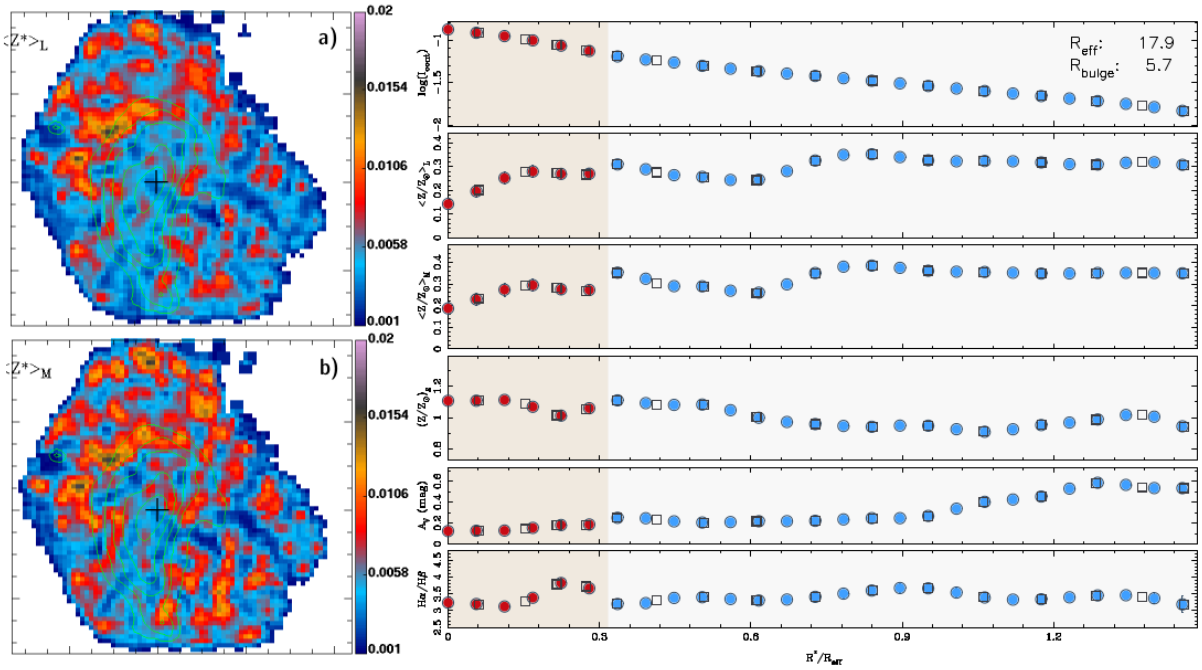

Figure C.57: Metallicity maps and radial profiles of UGC08733.

UGC09067

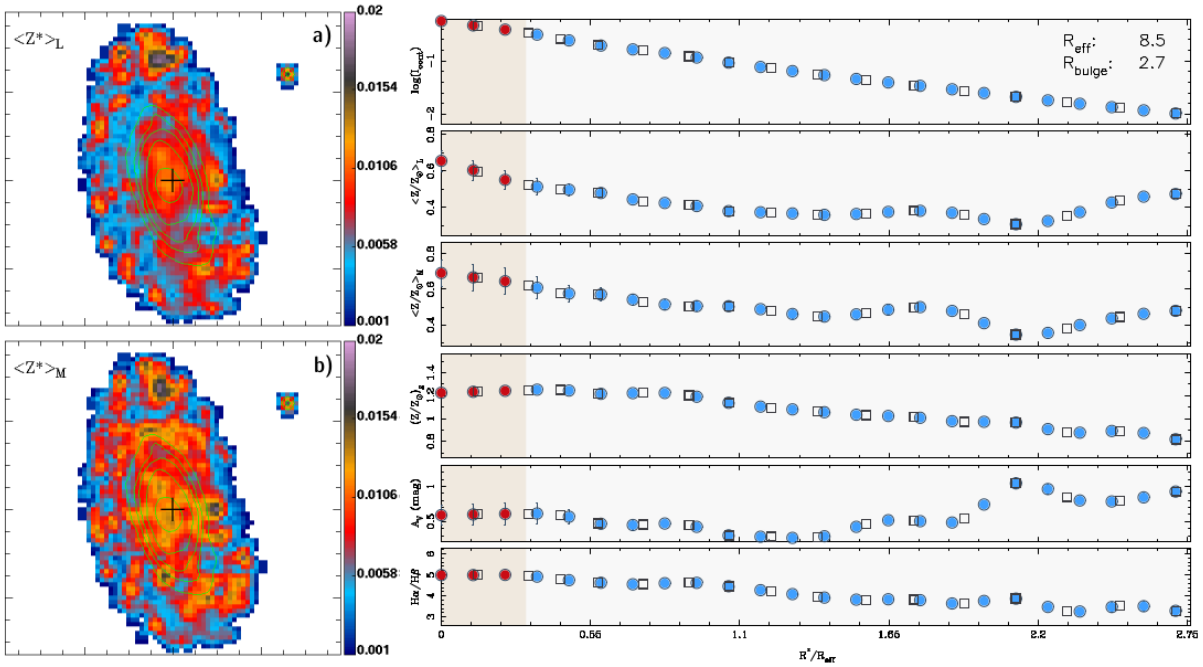

Figure C.58: Metallicity maps and radial profiles of UGC09067.

UGC09291

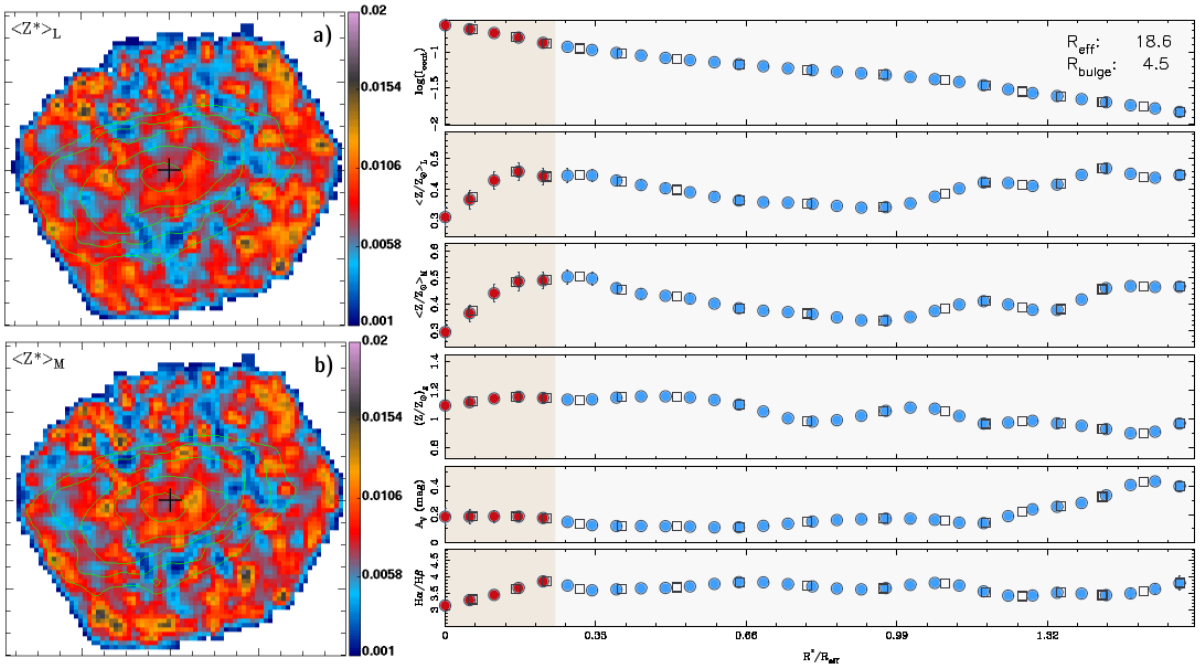

Figure C.59: Metallicity maps and radial profiles of UGC09291.

UGC09476

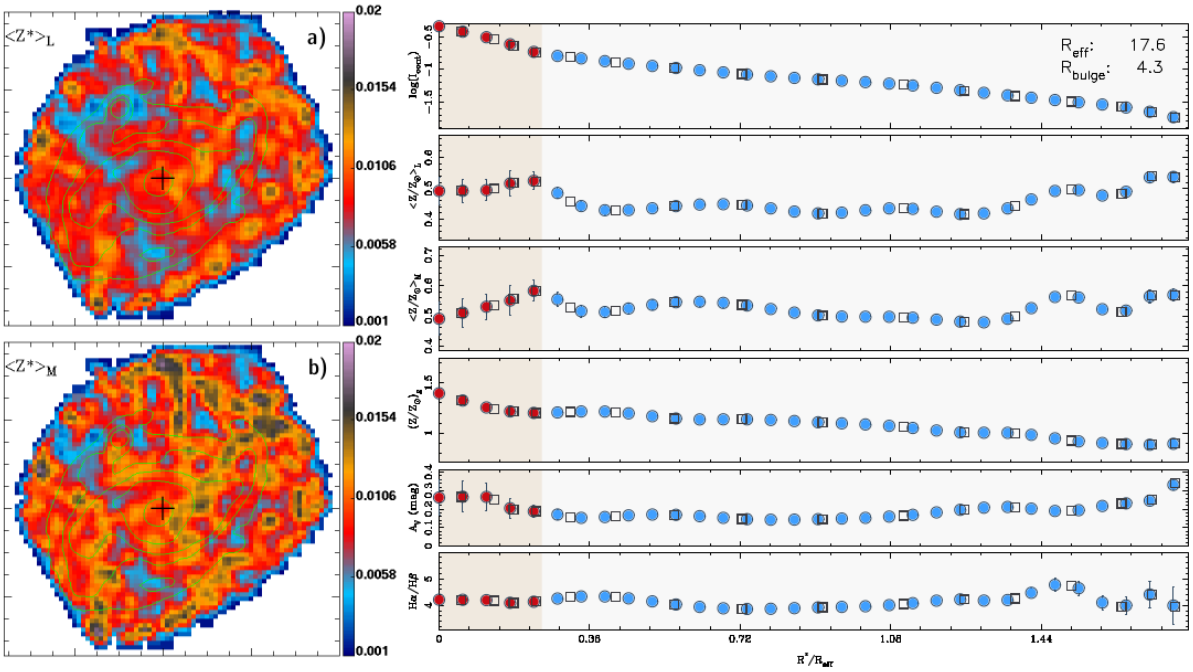

Figure C.60: Metallicity maps and radial profiles of UGC09476.

UGC12224

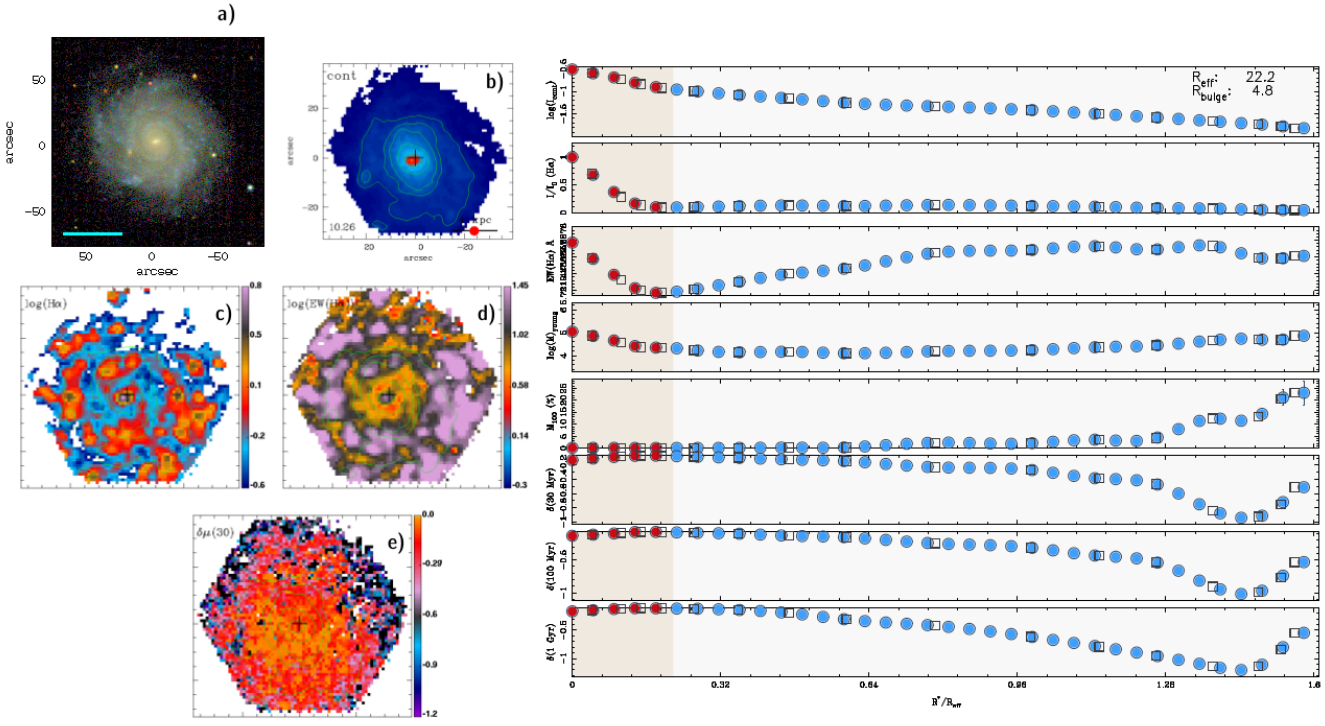

Figure C.61: Maps and radial profiles of UGC12224.

Appendices

Appendix D.

Classes

Here the reader can find the galaxy sample separated by the classes previously defined. In the tables is listed: signal of the (lum.-wei.) mean metallicity and age gradients ($< Z_{B*m} >$ and $< A_{B*m} >$, respectively), mean stellar metallicity ($< Z_{B*} >$), mean stellar age ($< A_{B*} >$), total absolute magnitude ($< AbsMag >$), mean $H\alpha$ equivalent width ($< EW(H\alpha)_B >$) and mean mass fraction of stars younger than 100 Myr ($< M_{100\%} >$) – in the bulge, with the exception of the $< AbsMag >$. Following are the true color images of the galaxies of the respective Class. Tables and Figs. are divided by two red lines: bellow the red line are the objects that present more discrepant values for mean age and metallicity of the respective class.

Class 4

Galaxy	Z_{B*m}	A_{B*m}	$< Z_{B*} >$	$< A_{B*} >$	$< AbsMag >$	$< EW(H\alpha)_B >$	$< Z_{gB} >$	$< M_{100\%} >$
NGC0023	-	+	0.56	6.19	-22.284	28.39	0.99	0.38
NGC2730	-	+	0.48	4.85	-20.661	19.19	1.18	0.28
NGC3057	-	+	0.3	3	-18.808	31.25	1.03	0.73
NGC5480	-	+	0.4	3.9	-20.537	39.56	1.31	0.75
NGC7819	-	+	0.4	5.1	-20.83	39.66	1.25	0.49
UGC10796	-	+	0.31	1.71	-19.284	29	0.98	2.98
NGC0776	-	+	0.8	10.28	-21.812	14.29	1.02	0.13

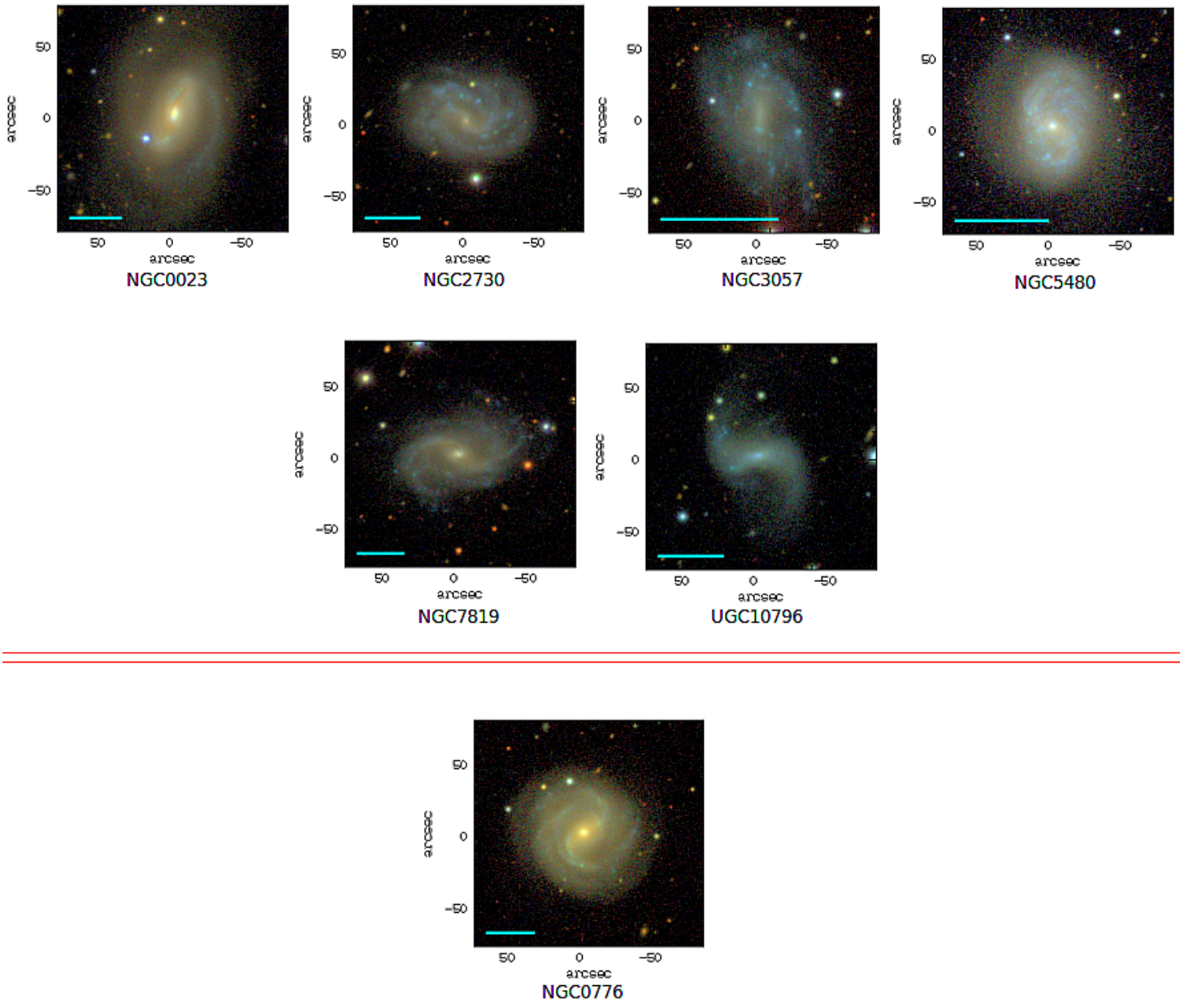

Figure D.1: Class 4 Sample.

Class 1

Galaxy	Z_{B*m}	A_{B*m}	$< Z_{B*} >$	$< A_{B*} >$	$< AbsMag >$	$< EW(H\alpha)_B >$	$< Z_{gB} >$	$< M_{100\%} >$
NGC0165	+	+	0.56	7.48	-21.35	17.73	1.05	0.26
NGC5000	+	+	0.56	9.08	-21.454	15.92	1.09	0.22
NGC6032	+	+	0.49	9.52	-21.132	25.16	0.91	0.12
NGC7738	+	+	0.59	8.23	-21.861	32.28	0.76	0.37
IC0776	+	+	0.25	3.84	-18.957	53.02	0.98	0.48
UGC08733	+	+	0.24	3.3	-19.329	17.43	1.08	0.37

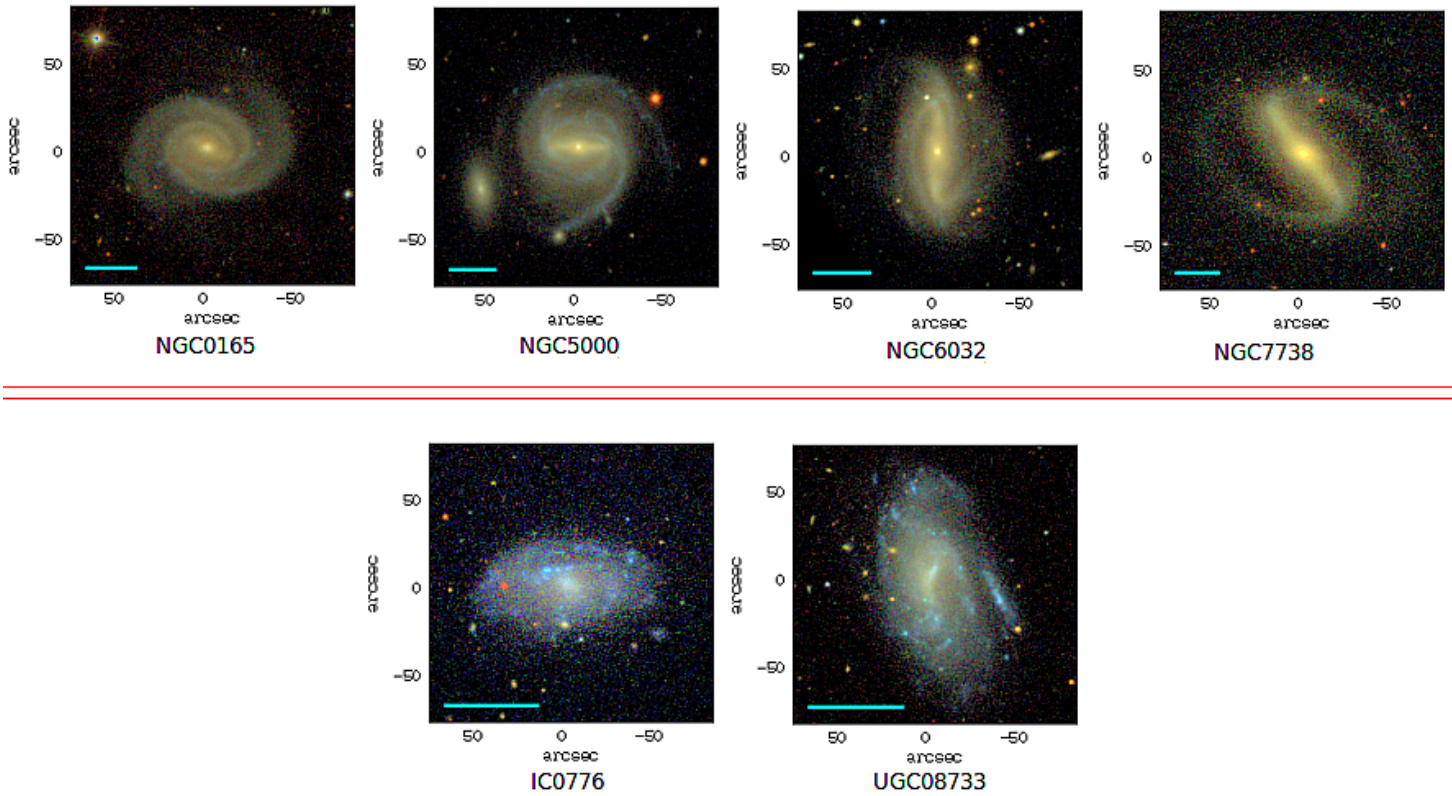

Figure D.2: Class 1 Sample.

Class 3

Galaxy	Z_{B*m}	A_{B*m}	$< Z_{B*} >$	$< A_{B*} >$	$< AbsMag >$	$< EW(H\alpha)_B >$	$< Z_{gB} >$	$< M_{100\%} >$
NGC0180	+	-	0.72	8.91	-22.111	16.43	1.31	0.33
NGC2916	+	-	0.8	8.77	-21.906	1.27	0.55	0.15
NGC3614	+	-	0.55	7.75	-20.787	4.58	0.83	0.06
NGC4185	+	-	0.69	11.09	-21.672	2.91	0.83	0.04
NGC4210	+	-	0.7	9.89	-20.825	1.15	0.59	0.03
NGC5016	+	-	0.49	8.97	-20.862	21.25	0.91	0.14
NGC5735	+	-	0.46	9.67	-21.18	4.55	0.7	0.07
NGC7691	+	-	0.48	5.34	-21.012	10.29	1.1	0.24
UGC09476	+	-	0.5	6.23	-20.749	13.55	1.28	0.22
UGC12224	+	-	0.46	6.09	-20.626	12.22	1.2	0.15
NGC3381	+	-	0.33	4.64	-19.825	73.01	1.24	0.61
UGC09291	+	-	0.4	5.8	-20.29	8	1.13	0.17

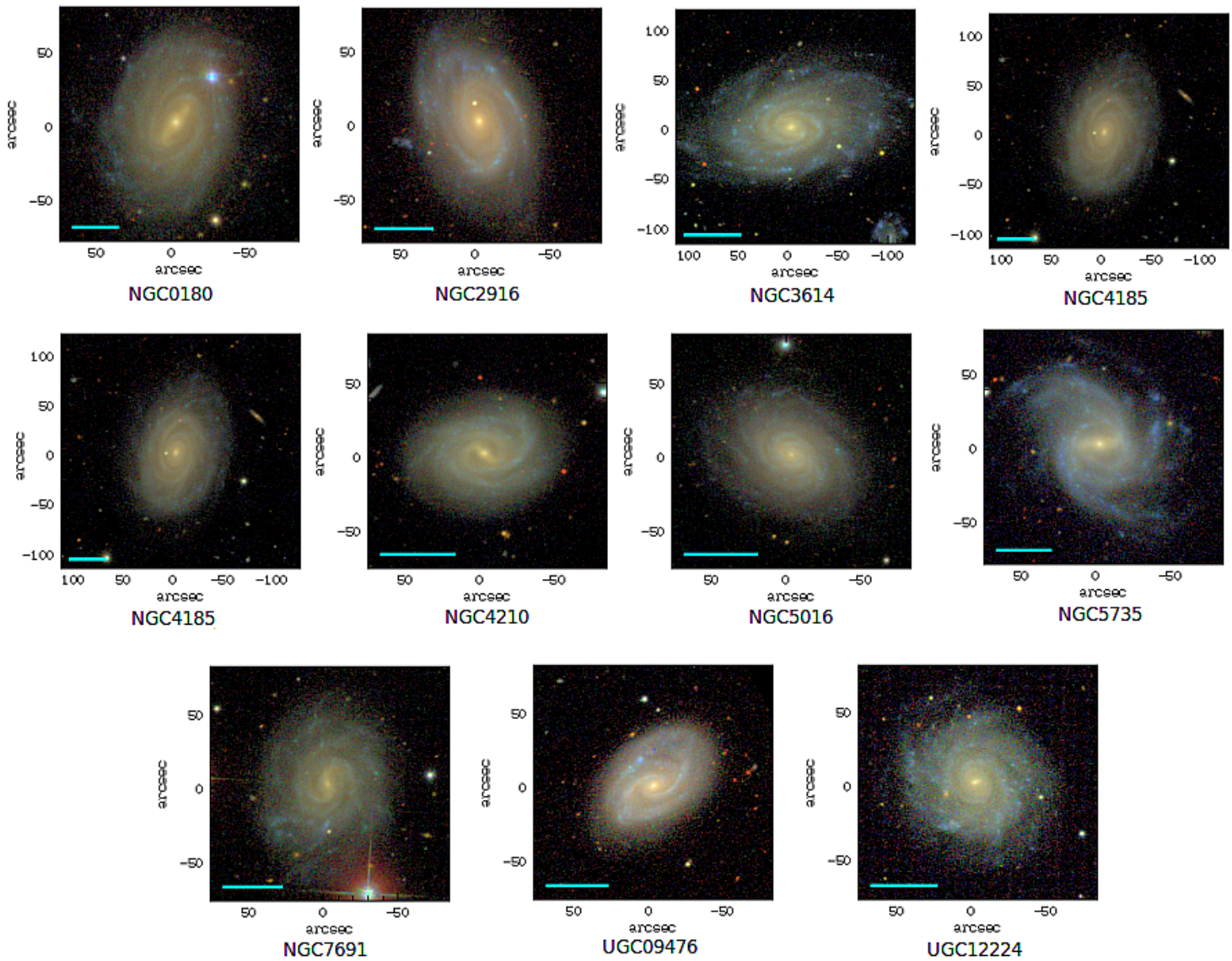

Figure D.3: Class 3 Sample part1.

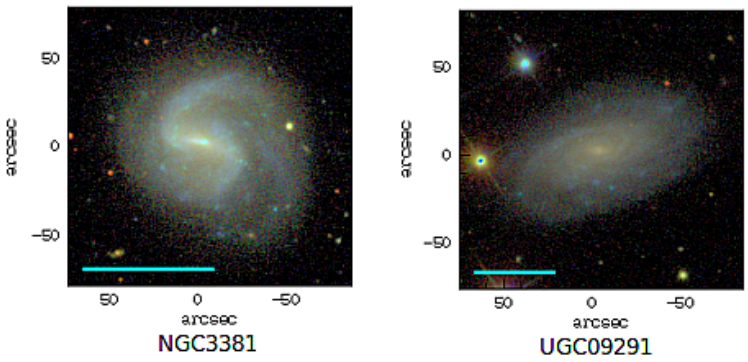

Figure D.4: Class 3 Sample part2.

Class 2

Galaxy	Z_{B*m}	A_{B*m}	$< Z_{B*} >$	$< A_{B*} >$	$< AbsMag >$	$< EW(H\alpha)_B >$	$< Z_{gB} >$	$< M_{100\%} >$
IC1256	-	-	0.62	8.73	-21.147	11.42	1.09	0.1
IC4566	-	-	0.76	12.5	-21.71	1.33	0.52	0.04
NGC0160	-	-	0.85	10.56	-21.958	0.81	0.61	0.12
NGC0171	-	-	0.72	10.16	-21.666	2.01	0.65	0.09
NGC0214	-	-	0.73	10.1	-22.043	3.71	0.62	0.11
NGC0257	-	-	0.67	7.22	-22.001	10.67	1.27	0.25
NGC0477	-	-	0.59	8.38	-21.468	11.25	1.19	0.14
NGC1093	-	-	0.77	9.88	-21.399	4.14	0.62	0.04
NGC1645	-	-	0.88	10.45	-21.671	1.27	0.64	0.05
NGC2253	-	-	0.57	8.34	-21.439	10.17	1.04	0.15
NGC2347	-	-	0.75	10.64	-21.886	8.62	0.95	0.13
NGC2639	-	-	0.73	10.63	-22.089	4.6	0.75	0.08
NGC2906	-	-	0.81	11.57	-20.712	2.37	0.71	0.03
NGC3300	-	-	0.94	11.64	-21.269	0.18	0.76	0.04
NGC3687	-	-	0.68	9.22	-20.658	2.34	0.71	0.03
NGC4003	-	-	1.46	8.44	-21.769	4.98	0.78	0.06
NGC4047	-	-	0.66	8.18	-21.667	10.4	1.14	0.18
NGC5205	-	-	0.63	7.77	-19.895	1.86	0.69	0.03
NGC5320	-	-	0.57	9.35	-20.851	4.11	0.91	0.06
NGC5378	-	-	0.73	11.98	-21.096	1.1	0.59	0.02
NGC5406	-	-	1	12.9	-22.321	0.77	0.52	0.02
NGC5614	-	-	0.73	9.69	-22.414	2.43	0.61	0.04
NGC5656	-	-	0.55	7.22	-21.452	10.88	1.08	0.17
NGC5772	-	-	0.85	12.27	-21.997	3.34	0.75	0.04
NGC5829	-	-	0.47	6.55	-21.347	12.6	1.2	0.17
NGC6004	-	-	0.6	8.21	-21.682	10.11	0.99	0.13
NGC6154	-	-	0.93	12.17	-21.788	0.95	0.53	0.04
NGC6186	-	-	0.53	9.03	-21.109	34.62	1.32	0.2
NGC6278	-	-	0.92	12.87	-21.454	0.53	0.56	0.01
NGC6941	-	-	0.91	12.1	-22.216	2.84	0.88	0.06
NGC7321	-	-	0.81	11.13	-22.317	3.23	0.63	0.05
NGC7489	-	-	0.6	6.84	-22.269	16.22	1.07	0.54
NGC7653	-	-	0.64	7.34	-21.503	6.19	0.81	0.13
NGC7716	-	-	0.71	9.17	-20.794	2.81	0.69	0.08
UGC08234	-	-	0.8	7.16	-22.596	0.23	0.48	0.02
UGC09067	-	-	0.6	8.95	-21.688	12.35	1.23	0.18
NGC0001	-	-	0.55	5.88	-21.433	15.45	1.19	0.22
NGC0237	-	-	0.52	6.07	-20.875	11.91	1.2	0.23
NGC4961	-	-	0.45	4.4	-19.985	15.4	1.14	0.47
NGC7625	-	-	0.5	4.75	-20.141	37.18	1.27	0.44
UGC07012	-	-	0.35	3.53	-19.622	28.92	1.12	0.33

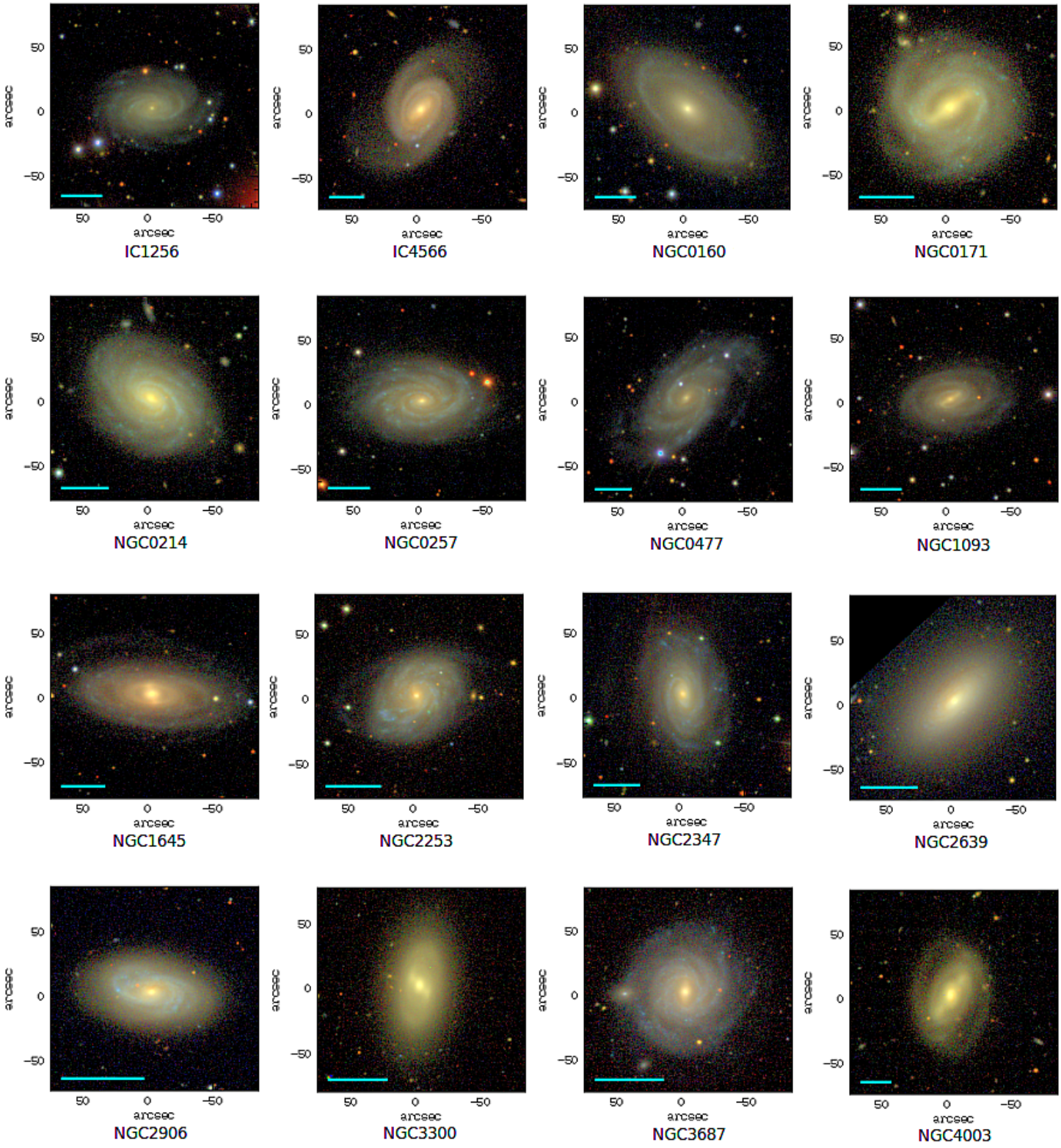

Figure D.5: Class 2 Sample part1.

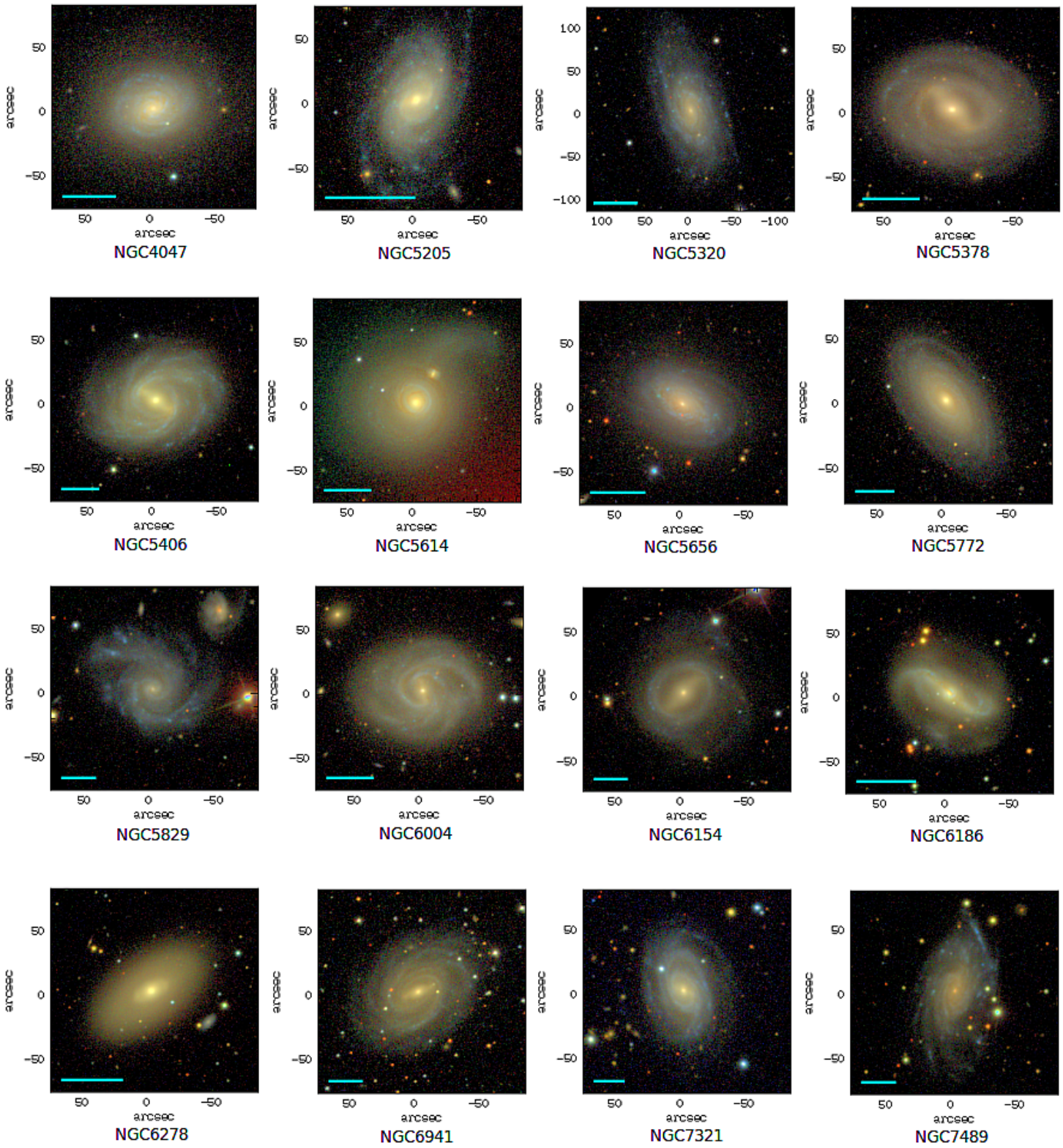

Figure D.6: Class 2 Sample part2.

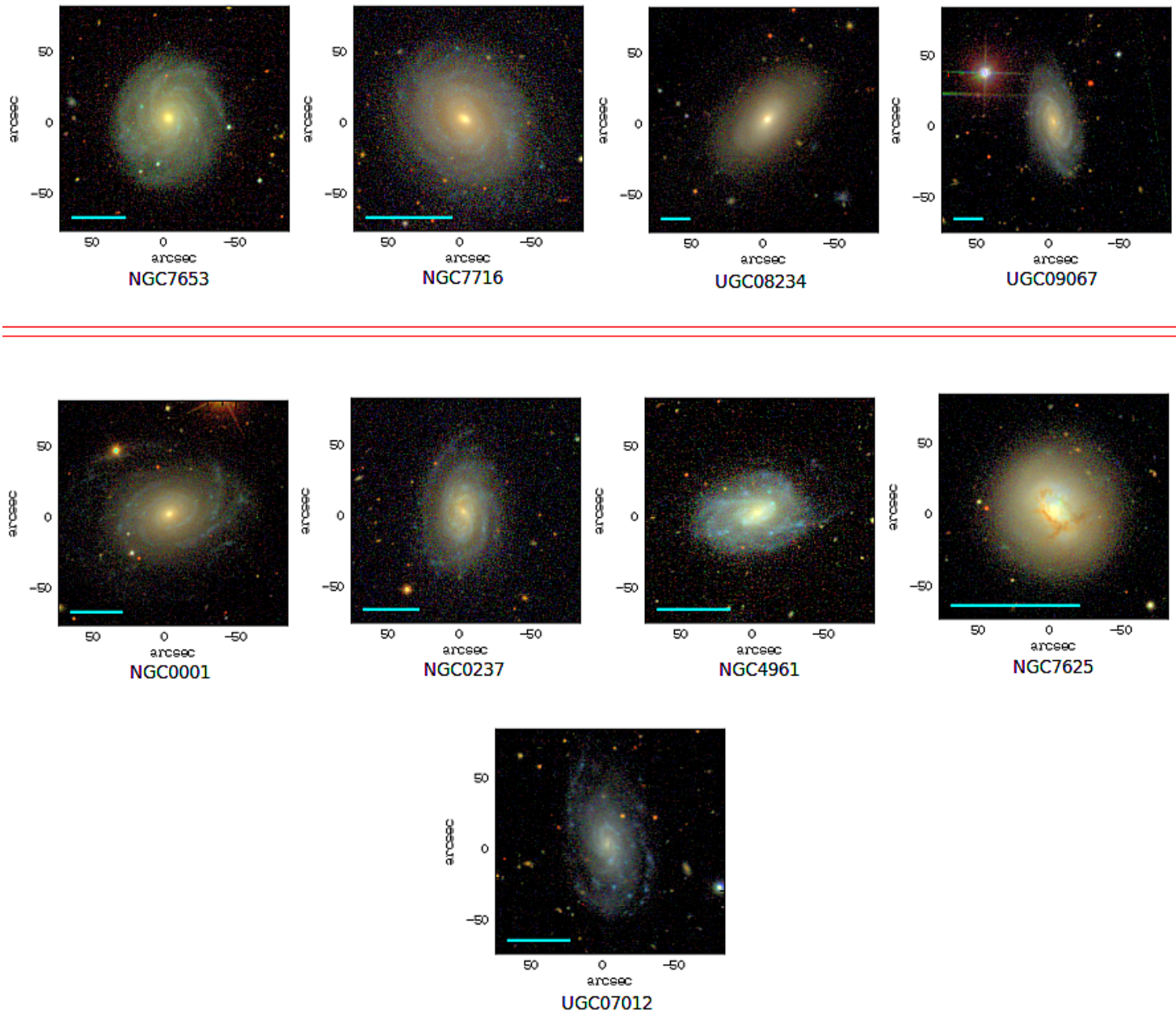

Figure D.7: Class 2 Sample part3.